

Winter 2018

CONTROL OF GAS METAL ARC WELDING USING PROCESS SENSING AND LASER ARC STABILIZATION FOR ADDITIVE MANUFACTURING

Dale Brush
Montana Tech

Follow this and additional works at: https://digitalcommons.mtech.edu/grad_rsch



Part of the [Electrical and Electronics Commons](#), and the [Power and Energy Commons](#)

Recommended Citation

Brush, Dale, "CONTROL OF GAS METAL ARC WELDING USING PROCESS SENSING AND LASER ARC STABILIZATION FOR ADDITIVE MANUFACTURING" (2018). *Graduate Theses & Non-Theses*. 191.
https://digitalcommons.mtech.edu/grad_rsch/191

This Thesis is brought to you for free and open access by the Student Scholarship at Digital Commons @ Montana Tech. It has been accepted for inclusion in Graduate Theses & Non-Theses by an authorized administrator of Digital Commons @ Montana Tech. For more information, please contact sjuskiewicz@mtech.edu.

CONTROL OF GAS METAL ARC WELDING USING PROCESS SENSING
AND LASER ARC STABILIZATION FOR ADDITIVE MANUFACTURING

by
Dale Brush

A thesis submitted in partial fulfillment of the
requirements for the degree of

Master of Science in Electrical Engineering

Montana Technological University

2018



Abstract

The goal of the present research was to bridge the gap between powder-based and wire-based additive manufacturing (AM) processes using gas metal arc welding (GMAW). Powder-based AM processes typically can produce components with high geometric resolution (small features), but at low deposition rates. Wire-based AM processes typically can produce components with low geometric resolution, but at high deposition rates. AM with GMAW is a wire-based AM process in the wire arc additive manufacturing (WAAM) category of AM. To bridge the gap between powder-based and wire-based AM processes, GMAW's deposition rate has to be reduced, allowing small features to be built.

The method proposed to build small features with GMAW was to develop a system, called GLADiS (GMAW laser assisted deposition integrated system), to perform an improved metal deposition strategy. The improved metal deposition strategy was composed of four components: single droplet deposition (SiDD), noncontact arc starting, electrode extension minimization, and laser arc stabilization. SiDD would allow single molten metal droplets to be deposited anywhere on a build plane rather than running continuous weld beads. SiDD would only be possible using an alternative, noncontact arc starting technique. Minimizing the electrode extension would allow the deposition rate to be reduced, while still maintaining sufficient current for droplet/substrate coalescence. Using a laser to stabilize the arc would ensure that individual droplets would be transferred to the correct location on the substrate.

Results showed that GLADiS was capable of building extremely thin walls using SiDD. In addition, minimizing the electrode extension was found to improve droplet/substrate coalescence. The final system used a 532nm laser to assist in arc starting and to stabilize the arc. Linear wall specimens made of steel could be produced at a 0.1lb/hr deposition rate and with a wall thickness of 0.1in or less.

Weld metal deposits produced by the SiDD process were found to have a microstructure composed of extremely small grains, indicating that it would have excellent strength and toughness. In addition, only a small number of voids were found in the deposits.

Keywords: gas metal arc welding (GMAW), additive manufacturing (AM), wire arc additive manufacturing (WAAM), laser arc stabilization

Dedication

I wish to thank my mom and dad for all their love and support throughout my education. I would also like to thank my siblings, Parker, Lane, and Erin, for being my roommates, colleagues, and best friends during my time in college.

Additional thanks go to all my grandparents for their endless support and encouragement. Special thanks go to my grandma, Deanie, for ensuring that I never went hungry throughout my time in college.

Acknowledgements

First off, I would like to thank my thesis committee, Dr. Bruce Madigan, Dr. Dan Trudnowski, Denis Clark, Dr. Josh Wold, and Scott Coguill, for their support. I would also like to thank the U.S. Army Research Labs for funding my research.

I would especially like to thank my advisor, Dr. Bruce Madigan, for his technical support and guidance throughout my research. In addition, I would like to give extra thanks to Denis Clark for his expertise in setting up the laser and optics. I would also like to thank Dr. Josh Wold for his help with data processing and both Dr. Josh Wold and Dr. John Morrison for their help designing the high frequency arc starter protection circuit.

I would like to thank Ryan Foley for his metallography work and, also, Nathan Huft and Tate Patterson for their help with microstructure analysis. Additional thanks go to Nathan Huft for his help setting up experimental equipment.

Lastly, I would like to thank Wayne Tuttle for his invaluable help setting up the high frequency arc starter and for sharing his knowledge of protecting devices from the high frequency arc starter.

Table of Contents

ABSTRACT	II
DEDICATION	III
ACKNOWLEDGEMENTS	IV
LIST OF TABLES.....	XIII
LIST OF FIGURES.....	XIV
LIST OF EQUATIONS	XXVI
GLOSSARY OF TERMS	XXVIII
1. INTRODUCTION	1
1.1. Gas Metal Arc Welding (GMAW)	2
1.2. Experimental Methods	2
1.3. Scope	2
1.4. Organization	3
2. ADDITIVE MANUFACTURING	5
2.1. Metal Additive Manufacturing.....	5
2.1.1. Powder-based AM.....	6
2.1.2. Wire-based AM	6
2.2. Wire Arc Additive Manufacturing (WAAM).....	7
3. GAS METAL ARC WELDING (GMAW).....	9
3.1. Advantages and Limitations.....	10
3.2. Process Variables	11
3.2.1. Welding Current and Wire Feed Speed	11
3.2.2. Electrode Extension.....	13
3.2.3. Arc Voltage	14
3.3. Electrical Characteristics	14

3.4.	<i>Forces in the Arc</i>	18
3.5.	<i>Metal Transfer Mechanisms</i>	20
3.5.1.	Short Circuiting Transfer.....	21
3.5.2.	Globular Transfer.....	21
3.5.3.	Spray Transfer	22
3.6.	<i>Summary</i>	25
4.	WAAM WITH GMAW	26
4.1.	<i>Complete Systems</i>	26
4.2.	<i>Weld Bead Control</i>	31
4.3.	<i>Geometric Investigation</i>	35
4.4.	<i>Metal Transfer Control</i>	38
4.5.	<i>Substrate Release Mechanisms</i>	47
4.6.	<i>Thermal Analysis</i>	48
4.7.	<i>Summary</i>	50
5.	THEORY OF PRESENT RESEARCH.....	51
5.1.	<i>Single Droplet Deposition (SiDD)</i>	51
5.2.	<i>Noncontact Arc Starting</i>	52
5.3.	<i>Electrode Extension Minimization</i>	54
5.4.	<i>Laser Arc Stabilization</i>	55
6.	EQUIPMENT.....	57
6.1.	<i>Computer with Analog and Digital I/O</i>	57
6.2.	<i>Wire Feeding System</i>	59
6.2.1.	WFS Encoder Characterization	60
6.2.2.	Wire Feeding System Calibration	61
6.2.2.1.	Procedure.....	61
6.2.2.2.	Results and Discussion	61
6.2.3.	Step Response	66

6.2.3.1.	Procedure.....	67
6.2.3.2.	Results and Discussion	67
6.2.4.	Frequency Response	69
6.2.4.1.	Procedure.....	69
6.2.4.2.	Results and Discussion	70
6.3.	<i>Welding Power Source</i>	<i>77</i>
6.3.1.	Step Response	78
6.3.1.1.	Procedure.....	80
6.3.1.2.	Results and Discussion	80
6.3.2.	Frequency Response	82
6.3.2.1.	Procedure.....	82
6.3.2.2.	Results and Discussion	84
6.4.	<i>Video Imaging System.....</i>	<i>90</i>
6.4.1.	Imaging System Design and Validation.....	91
6.4.1.1.	Procedure.....	92
6.4.1.2.	Results and Discussion	93
6.4.2.	Post Process Video Analysis	98
6.5.	<i>Three-Axis Motion System.....</i>	<i>100</i>
6.6.	<i>High Frequency Arc Starter</i>	<i>101</i>
6.6.1.	DAQ Protection Circuit	103
6.6.1.1.	Circuit Design	103
6.6.1.2.	Circuit Test	104
6.6.1.3.	Voltage Measurement	105
6.6.2.	High Frequency Arc Starter Connection	110
6.6.2.1.	Positive Connection	110
6.6.2.2.	Negative Connection.....	113
6.6.3.	Electromagnetic Interference.....	114
6.6.3.1.	EMI Shielding and Grounding.....	115
6.6.3.2.	Software Solution.....	118

6.6.3.3.	Laser Proximity and Mounting	119
6.6.4.	Wire Feeder	119
6.6.4.1.	Insulated Wire Feeder	121
6.6.4.2.	Insulated Wire Feeder Control	122
6.7.	<i>Laser</i>	125
6.8.	<i>Summary</i>	130
7.	CONTINUOUS WELD BEADS	132
7.1.	<i>Experimental Methods</i>	132
7.1.1.	Arc Initiation and Termination	133
7.1.2.	Parameter Space	134
7.1.3.	Wall Construction	135
7.1.4.	Pulsed Current	135
7.2.	<i>Results and Discussion</i>	140
7.2.1.	Arc initiation and Termination	140
7.2.2.	Parameter Space	141
7.2.3.	Wall Construction	143
7.2.4.	Pulsed Current	143
7.3.	<i>Summary</i>	148
8.	SINGLE DROPLET DEPOSITION	149
8.1.	<i>Experimental Methods</i>	149
8.2.	<i>Results and Discussion</i>	150
8.3.	<i>Summary</i>	157
9.	NONCONTACT ARC STARTING	158
9.1.	<i>Photoemission/laser</i>	159
9.1.1.	Experimental Methods	159
9.1.2.	Results and Discussion	161
9.2.	<i>PAW Pilot Arc</i>	162
9.2.1.	Experimental Methods	163

9.2.2.	Results and Discussion	164
9.3.	<i>Lift Start</i>	169
9.3.1.	Experimental Methods	169
9.3.2.	Results and Discussion	170
9.4.	<i>High Frequency Arc Starter</i>	170
9.4.1.	Experimental Methods	171
9.4.2.	Results and Discussion	171
9.5.	<i>Arc Starter/laser Hybrid Arc Starting Technique</i>	176
9.5.1.	Experimental Methods	176
9.5.2.	Results and Discussion	177
9.6.	<i>Summary</i>	180
10.	ELECTRODE EXTENSION AND DROPLET COALESCENCE.....	182
10.1.	<i>Experimental Methods</i>	182
10.2.	<i>Results and Discussion</i>	183
10.3.	<i>Summary</i>	188
11.	SPECIMEN BUILDS AND PARAMETER TUNING	189
11.1.	<i>Experimental Methods</i>	189
11.1.1.	PAW Pilot Arc Start Specimen (PAWS1)	190
11.1.2.	Arc Starter Specimen 1 (HFS1)	190
11.1.3.	Arc Starter Specimen 2 (HFS2)	191
11.1.4.	Arc Starter Specimen 3 (HFS3)	192
11.1.5.	Arc Starter Specimen 4 (HFS4)	192
11.1.6.	Arc Starter/laser Hybrid Specimen (HS1)	192
11.2.	<i>Results and Discussion</i>	193
11.2.1.	PAW Pilot Arc Start Specimen (PAWS1)	193
11.2.2.	Arc Starter Specimen 1 (HFS1)	195
11.2.3.	Arc Starter Specimen 2 (HFS2)	197
11.2.4.	Arc Starter Specimen 3 (HFS3)	198

11.2.5.	Arc Starter Specimen 4 (HFS4)	199
11.2.6.	Arc Starter/laser Hybrid Specimen (HS1)	200
11.3.	<i>Summary</i>	202
12.	SPECIMEN METALLURGICAL ANALYSIS.....	204
12.1.	<i>Macrographs</i>	204
12.2.	<i>Voids</i>	206
12.3.	<i>Microstructure</i>	209
12.4.	<i>Summary</i>	212
13.	PROCESS PARAMETER RANKING.....	213
13.1.	<i>Welding Current</i>	213
13.2.	<i>Shielding Gas Composition</i>	213
13.3.	<i>Drop Spacing</i>	213
13.4.	<i>Laser Power</i>	214
13.5.	<i>Electrode Composition</i>	214
13.6.	<i>Electrode Extension</i>	215
14.	CONCLUSIONS	216
14.1.	<i>Single Droplet Deposition</i>	216
14.2.	<i>Noncontact Arc Starting</i>	216
14.3.	<i>Electrode Extension and Droplet Coalescence</i>	218
14.4.	<i>Specimen Builds and Parameter Tuning</i>	218
14.5.	<i>Specimen Analysis</i>	220
14.6.	<i>Process Parameter Ranking</i>	220
14.7.	<i>Future Work</i>	221
14.7.1.	Specimen Metallurgical and Mechanical Analysis	221
14.7.2.	Residual Stress and Droplet Placement.....	222
14.7.3.	Closed-loop Control.....	222
14.7.4.	Pulsing Power Source and Arc Starting	223

14.7.5.	Laser Arc Stabilization and Photoemission/laser Arc Starting	224
14.7.6.	Wire Electrode Diameter and Composition.....	225
14.7.7.	Custom Contact Tip	225
14.7.8.	Automatic Geometry Correction	226
14.7.9.	Substrate Release Mechanism	226
14.7.10.	Geometric Capabilities	227
14.7.11.	Integrating Conventional GMAW AM and SiDD	227
15.	REFERENCES CITED.....	228
16.	APPENDIX A: ANALOG AND DIGITAL I/O CONTROL CODE	234
16.1.	<i>I/O PCI Card Control</i>	234
16.2.	<i>DAQ Function</i>	237
17.	APPENDIX B: WIRE FEEDER	238
17.1.	<i>Wire Feeder Control Code</i>	238
17.2.	<i>Wire Feeding System Calibration</i>	239
17.3.	<i>Step Response Analysis</i>	240
17.4.	<i>Time Domain Analysis</i>	241
17.5.	<i>Frequency Domain Analysis</i>	243
18.	APPENDIX C: WELDING POWER SOURCE	246
18.1.	<i>Welding Power Source Control Code</i>	246
18.2.	<i>Step Response Test</i>	247
18.3.	<i>Variable Frequency Test</i>	248
18.4.	<i>Discrete Frequency Test</i>	249
19.	APPENDIX D: VIDEO PROCESSING ALGORITHM	251
20.	APPENDIX E: MOTION CONTROL CODE	254
20.1.	<i>C++ class used for motion and wire feed control</i>	254
20.2.	<i>C++ Project for Jogging Motion System and Wire Feeder</i>	259
21.	APPENDIX F: LASER CONTROL CODE	264

22. APPENDIX G: CONTINUOUS WELD BEAD CODE	268
22.1. <i>Arc Initiation and Termination</i>	268
22.2. <i>Pulsed GMAW</i>	268
23. APPENDIX H: SINGLE DROPLET DEPOSITION CODE	270
23.1. <i>Single Droplet Deposition with Steel Wool Arc Starts</i>	270
23.2. <i>Single Droplet Deposition with PAW Pilot Arc Starts</i>	271
23.3. <i>Single Droplet Deposition with Lift Arc Starts</i>	272
23.4. <i>Single Droplet Deposition with High Frequency Arc Starts</i>	273
23.5. <i>Automatic Wire Positioning</i>	274
23.6. <i>Automated Single Droplet Deposition</i>	275

List of Tables

Table I: Wire feeder step response parameters: percent overshoot (%OS), percent undershoot (%US), step-up settling time (T_{Su}), step-down settling time (T_{Sd}), peak time (T_P), low time (T_L), rise time (T_R), and fall time (T_F).	68
Table II: Welding power source step response parameters: percent overshoot (%OS), percent undershoot (%US), step-up settling time (T_{Su}), step-down settling time (T_{Sd}), peak time (T_P), low time (T_L), rise time (T_R), and fall time (T_F).	81
Table III: Calculated and tuned pulsing parameters to achieve ODPP: peak current (I_p), peak time (t_p), background current (I_b), and background time (t_b).	144
Table IV: Measured electrode extensions	184
Table V: Summary of specimen builds	203

List of Figures

Figure 1: Schematic of the GMAW process [3].	9
Figure 2: GMAW current, WFS, and electrode extension relationship for 0.045in diameter ER70S-3 wire with 98% Ar, 2% O ₂ shielding gas. As electrode extension is reduced, more current is required for the same WFS.	12
Figure 3: GMAW terminology [3].	13
Figure 4: Practical welding constant current power source. A relatively large change in arc voltage results in a small change in welding current. Adapted from [3].	14
Figure 5: Practical welding constant voltage power source. A relatively small change in arc voltage results in a large change in welding current. Adapted from [3].	15
Figure 6: Welding arc VI characteristics and operating points. The point where the power source's VI curve intersects the welding arc's VI curve represents the operating point for a given arc length.	17
Figure 7: Forces acting on the molten metal droplet [15]. Pinch effect (Lorentz force), gravity, and plasma flow (aerodynamic drag force) act to detach droplets; surface tension and vapor jet force act to prevent droplet detachment.	18
Figure 8: Electromagnetic force acting on molten metal droplet. Electromagnetic force acts to prevent droplet detachment when current flux distribution is localized on the bottom of the droplet and acts to detach droplets when current flux is uniformly distributed around droplet surface [17].	19
Figure 9: Transition from globular to spray transfer [3]. As current is increased through the transition current, droplet transfer rate drastically increases and droplet volume drastically decreases.	22

Figure 10: Typical GMAW-P waveform. The wave form is characterized by four parameters: peak current (I_p), peak time (t_p), background current (I_b), and background time (t_b).	24
Figure 11: (left) 1000lb hemispherical head and (right) 12in diameter elbow manufactured using GMAW WAMM. Adapted from [21].	27
Figure 12: Components made from CAD models with GMAW WAAM [19].	28
Figure 13: Relationship between process parameters and final component qualities. Adapted from [22].	29
Figure 14: Simple component made with the open-source metal 3-D printing system. Adapted from [23].	30
Figure 15: +1000K metal 3-D printer from +MFG [24].	31
Figure 16: Adaptive controller block diagram. An adaptive controller has a typical feedback loop in addition to an outer loop (outside the feedback loop) capable of in-process controller parameter modification [28].	33
Figure 17: Weld bead width control depositing various bead widths on each layer [29].	34
Figure 18: WAAM with GMAW using an inclined torch [31].	35
Figure 19: (a) Inclined wall built on flat substrate and (b) horizontal wall built on substrate edge using the inclined torch GMAW WAAM technique. Adapted from [31].	36
Figure 20: (a) Semicircle and (b) box built using the inclined torch technique. Adapted from [31].	36
Figure 21: Schematic of flat position deposition welding system [32].	37
Figure 22: Inclined wall with 75° incline angle made with flat position deposition [32].	38
Figure 23: STT waveform. Adapted from [36].	39

Figure 24: RMD waveform and phases [39].....	40
Figure 25: CMT current and voltage waveforms [40].	42
Figure 26: Components manufacture with WAAM using CMT [8].....	43
Figure 27: Active metal transfer control and modified active control used for robust droplet detachment in titanium GMAW-P applications [17].	45
Figure 28: GMAW titanium welds (a) without a laser and (b) with a laser. Stabilizing the welding arc with a laser resulted in a more uniform weld bead profile. Adapted from [11].	47
Figure 29: Walls made with various inter-layer cooling times. Increasing the interlayer cooling time resulted in improved geometric accuracy [45].	49
Figure 30: Analog and digital I/O isolation modules. The isolation modules isolated the computer's PCI cards from the process side of the system.	58
Figure 31: Wire feeding system block diagram. The wire feeder was controlled by the computer through the wire feeder controller. The WFS was measured using a WFS encoder.	59
Figure 32: Sample of encoder data. The encoder output a square wave signal with a frequency proportional to the WFS.....	62
Figure 33: Processed encoder signal. The black circles indicate the zero crossings which were used to calculate the WFS.....	63
Figure 34: Wire feeder calibration test data.....	64
Figure 35: Wire feeder calibration test results. A relationship between input voltage and WFS was found by fitting a line to the experimental data.	65
Figure 36: Theoretical step response and step response parameters.....	66
Figure 37: Wire feeder step response to a 90ipm step and a 180ipm step.....	68

Figure 38: Time domain representation of the wire feeder's frequency response. As the frequency is increased from 0Hz to 8Hz, the wire feeder becomes less effective at tracking the commanded WFS.....	71
Figure 39: Noisy WFS data compared to NLLS WFS model.	74
Figure 40: NLLS modeled experiment at 4.00Hz.....	75
Figure 41: Wire feeder frequency response. The red line shows the wire feeder's corner frequency is at about 3.5Hz, indicating that the wire feeder can track a control signal up to 3.5Hz with reasonable accuracy.	76
Figure 42: Welding power source configuration. The individual welding power sources are controlled by analog and digital signals from the output isolation modules. The parallel connection of welding power sources can output a total of 0A-600A.....	77
Figure 43: Power source step response test using analog output isolation module control. The power source's step response is at least as fast as the analog output isolation modules step response.....	79
Figure 44: Power source step response using a high-speed function generator to produce the control signal.....	81
Figure 45: Time domain representation of welding power source frequency response. As the frequency is increased from 10Hz to 6kHz, the power source can no longer accurately track the control signal.....	85
Figure 46: Example of raw data from 7kHz welding power source test.	86
Figure 47: Comparison of raw data with models for commanded and measured current.	87
Figure 48: Modeled discrete frequency test.....	88

Figure 49: Bode plot showing the welding power source's frequency response. The red line shows the power source's corner frequency at 2.66kHz, indicating that the power source can track a 2.66kHz control signal with reasonable accuracy.	89
Figure 50: Shadowgraph imaging system schematic.....	90
Figure 51: Spectrum analyzer calibration test. Measured spectrum has peaks at wavelengths that correspond with theoretical spectrum.	93
Figure 52: GMAW arc light spectrum with ER70S-6 wire and 98% Ar, 2% O ₂ shielding gas. Regions where the wavelengths have low magnitudes are optimal wavelengths around which video imaging systems can be designed.....	94
Figure 53: Imaging system laser light spectrum (including zoomed in image). The center wavelength is at approximately 632.8nm.	95
Figure 54: Optical band pass filter frequency (or wavelength) response. The center wavelength is at approximately 632nm.	96
Figure 55: Spectra of imaging system including arc, laser, and filter spectra. No large spikes from the arc spectrum occur within the filter's pass band.	97
Figure 56: Raw image taken with the imaging system showing the GMAW gas nozzle, the wire electrode, and the top of the substrate.....	98
Figure 57: (Top) Raw images from high-speed video. (Bottom) Processed images from video showing electrode extension tracking.....	99
Figure 58: Three-axis motion system: (left) linear axes only and (right) linear axes configured for welding.....	100
Figure 59: High frequency arc starter circuit diagram.....	102

Figure 60: Protection circuit diagram. The 100k Ω resistors and 68mH inductors provide high impedance to the high frequency arc starter, and the MOV ensures V_{out} never exceeds 100V.....	103
Figure 61: Arc voltage measurement resistance diagram.	105
Figure 62: Arc voltage measurement and protection circuit. The distance between the wires/components on the input side up to the inductors is set to at least 1in to avoid arcing between wires.....	106
Figure 63: Arc voltage measurement and protection circuit diagram.....	107
Figure 64: Bode plot showing the voltage measurement/protection circuit's frequency response. The DC gain is -15.8dB which scales the welding power source open-circuit voltage to ADC levels. The corner frequency is 629kHz	109
Figure 65: High frequency arc starter connection to positive side of welding circuit.	110
Figure 66: Wire feeder/torch assembly insulated from frame using nylon washers.....	111
Figure 67: Work piece insulated from motion system using a polymer plate and nylon washers.	112
Figure 68: Insulation between wire/wire conduit and wire spool frame.	112
Figure 69: High frequency arc starter connection to negative side of welding circuit.	114
Figure 70: Earth ground. The test frame, positive welding lead, all of the EMI shielding, and the Galil controller body were attached to earth ground.	115
Figure 71: Shielding on welding leads. All shielding was connected to the earth ground.	116
Figure 72: Ferrite chokes and shielding installed on cables. Shielding was installed over the ferrite chokes and drain was not routed through a ferrite choke to ensure EMI induced currents could flow unimpeded to earth ground.	117

Figure 73: Comparison of steady-state and transient circuit diagrams. The self-inductance of the welding cables only becomes apparent in the transient diagram.	120
Figure 74: Custom built wire feeder. The motor is insulated from the wire feeder by the fiberglass shaft.	122
Figure 75: Wire feed trigger circuit diagram. When the computer energizes the isolation module, 9V is applied to the Galil controller's digital input, triggering wire feed. A 0.1 μ F capacitor was added to filter out EMI.	124
Figure 76: EMI prevention at Galil controller. The ferrite choke and 0.1 μ F capacitor were installed close to the Galil controller to filter out as much EMI as possible.	125
Figure 77: Laser console and optical head connected by a fiber optic and wire cable.	125
Figure 78: Laser beam divergence illustration. Even over a short distance, a 10mrad beam divergence results in a much larger spot size than the original beam diameter.	127
Figure 79: Illustration of lens equation.	128
Figure 80: Laser and optics setup schematic. The lens was mounted on a linear stage to allow spot size adjustment.	130
Figure 81: GLADiS block diagram.	131
Figure 82: Short circuiting arc start. The number in the top right-hand corner of each frame is the time stamp in milliseconds (ms), and the number in the bottom right-hand corner of each frame is frame number.	140
Figure 83: Parameter space, raw data. Data was taken using 0.045in diameter ER70S-3 wire and 98% Ar, 2% O ₂ shielding gas.	142
Figure 84: Parameter space with polynomial model. Data was taken using 0.045in diameter ER70S-3 wire and 98% Ar, 2% O ₂ shielding gas.	142

- Figure 85: First wall specimen made with continuous weld beads and constant, non-pulsed current.143
- Figure 86: Pulsed GMAW achieving ODPP. The number in the top right-hand corner of each frame is the time stamp in milliseconds (ms), and the number in the bottom right-hand corner of each frame is frame number.145
- Figure 87: Wall built with continuous weld beads using ODPP pulsing parameters with ER70S-3 wire and 98% Ar, 2% O₂ shielding gas.....147
- Figure 88: Wall built without alternating deposition direction. The wall was built with continuous weld beads traveling from right to left with ER70S-3 wire and 98% Ar, 2% O₂ shielding gas.147
- Figure 89: Voltage and current from SiDD test. Left-hand y-axis is the welding current and right-hand y-axis is the arc voltage. A droplet is formed over the first 175ms of background current, and is detached by the current pulse.151
- Figure 90: Droplet detachment. The number in the top right-hand corner of each frame is the time stamp in milliseconds (ms), and the number in the bottom right-hand corner of each frame is frame number.152
- Figure 91: SiDD test with wire feed using steel wool fuse arc starting. The number in the top right-hand corner of each frame is the time stamp in milliseconds (ms), and the number in the bottom right-hand corner of each frame is frame number.154
- Figure 92: Single droplets deposited using SiDD. The droplets are about 0.1in in diameter.155

- Figure 93: Power and total energy dissipated by the welding arc in SiDD. Power is equal to the arc voltage multiplied by the arc current; total energy is the area under the power curve and was found to be 209J.....156
- Figure 94: Laser focused on GTAW pure tungsten electrode. The center of the laser beam is focused near the tip of the tungsten electrode.....160
- Figure 95: Schematic of PAW torch [3].162
- Figure 96: SiDD with PAW pilot arc start. The number in the top right-hand corner of each frame is the time stamp in milliseconds (ms), and the number in the bottom right-hand corner of each frame is frame number.165
- Figure 97: Droplets deposited using SiDD with PAW pilot arc starts.166
- Figure 98: Weld bead deposited using SiDD with PAW pilot arc starts. The weld bead was made by depositing one drop at a time from left to right using ER70S-6 wire and 98% Ar, 2% O₂ shielding gas.167
- Figure 99: Two layers deposited using SiDD with PAW pilot arc starts. Both layers were deposited one drop at a time from right to left using ER70S-6 wire and 98% Ar, 2% O₂ shielding gas.....168
- Figure 100: High frequency arc starting sequence flow chart.173
- Figure 101: Arc current and voltage during SiDD with high frequency arc starting. After the power source is enabled at $t = 0$, the arc starter pulses seven times to initiate the arc.175
- Figure 102: Video frames of automated SiDD with hybrid arc starting. The number in the top right-hand corner of each frame is the time stamp in seconds (s), and the number in the bottom right-hand corner of each frame is frame number.178

Figure 103: Weld bead made using automated SiDD with hybrid arc starting. The weld bead was made by depositing one drop at a time from left to right using ER70S-3 wire and 98% Ar, 2% O ₂ shielding gas.....	179
Figure 104: High-speed camera frames processed using electrode extension tracking algorithm.	184
Figure 105: Relationship between electrode extension and welding current. To melt a given length of wire electrode, as electrode extension decreased, welding current increased.	185
Figure 106: Droplets deposited at electrode extensions of (top) 0.264in and (bottom) 0.136in.	185
Figure 107: Cross-section of droplet fusion zone. Cross-section was taken through the center of the droplet.	186
Figure 108: Relationship between fusion zone cross-sectional area, electrode extension, and welding current. The y-axis is the fusion zone cross-sectional area, the bottom x-axis is the electrode extension, and the top x-axis is the welding current.	187
Figure 109: Schematic of depositing a single layer using SiDD.	189
Figure 110: PAWS1 specimen manufactured using SiDD with PAW pilot arc starting using ER70S-6 wire and 98% Ar, 2% O ₂ shielding gas.	194
Figure 111: HFS1 specimen manufactured using SiDD with high frequency arc starting using ER70S-3 wire and 98% Ar, 2% O ₂ shielding gas.	195
Figure 112: Effects of excessive drop spacing. Detaching droplets are attracted to previously deposited droplets. If excessive drop spacing is used, the horizontal distance detaching droplets travel increases with every drop.....	196

Figure 113: Drop spacing comparison. A drop spacing of 0.070in produced a more uniform weld bead compared to the drop spacing of 0.073in.	197
Figure 114: HFS2 specimen manufactured using SiDD with high frequency arc starting using ER70S-3 wire and 98% Ar, 2% O ₂ shielding gas.	198
Figure 115: HFS3 specimen manufactured using SiDD with high frequency arc starting using ER70S-3 wire and 98% Ar, 2% O ₂ shielding gas.	199
Figure 116: HFS4 specimen manufactured using SiDD with high frequency arc starting using ER70S-3 wire and 98% Ar, 2% O ₂ shielding gas.	200
Figure 117: HS1 specimen manufactured using SiDD with laser hybrid arc starting using ER70S-3 wire and 98% Ar, 2% O ₂ shielding gas.	201
Figure 118: Macrograph of HFS4 cross-section number 1. Individual droplets and layers can be seen in the macrograph. No significant voids can be seen.	204
Figure 119: Macrograph of HFS4 cross-section number 2. Voids can be seen at the substrate/weld metal interface, and smaller voids can be seen in the weld metal.	205
Figure 120: Largest HSF4 specimen void at substrate interface (10x magnification). The void was likely caused by lack of fusion between droplets and the substrate.	206
Figure 121: Smaller HSF4 specimen void at substrate interface (10x magnification). The void was likely caused by lack of fusion between droplets and the substrate.	207
Figure 122: HSF4 specimen void within the weld metal (10x magnification). The void was likely caused by lack of fusion between droplets.	208
Figure 123: Microstructure of substrate/weld metal interface (10x magnification).	209

Figure 124: Microstructure of weld metal in middle layers (50x magnification). The microstructure in the middle layers is composed of equiaxed ferrite and pearlite grains that are 5 to 10 microns in size.210

Figure 125: Microstructure of weld metal in top layer (100x magnification). The top layer microstructure is composed mostly of bainite and ferrite.....211

List of Equations

Equation (1) Relation of GMAW wire feed speed to welding current	12
Equation (2) Total weld heat input	23
Equation (3) Wire feeder calibration curve	65
Equation (4) General model for wire feed speed frequency response data	72
Equation (5) Angle summation trigonometric identity	73
Equation (6) Modified wire feed speed model	73
Equation (7) Wire feed speed model substitution.....	73
Equation (8) Wire feed speed model substitution.....	73
Equation (9) Wire feed speed model with substitutions	73
Equation (10) Calculation of wire feed speed model amplitude.....	73
Equation (11) Calculation of wire feed speed model phase	74
Equation (12) High frequency arc starter protection circuit voltage output	106
Equation (13) Voltage measurement circuit resistance	106
Equation (14) Voltage measurement circuit input/output relationship (time domain)	107
Equation (15) Voltage measurement circuit transfer function.....	107
Equation (16) Voltage measurement circuit simplified transfer function	108
Equation (17) Equivalent resistance in simplified transfer function	108
Equation (18) Equivalent resistance in simplified transfer function	108
Equation (19) Voltage measurement circuit transfer function, pole-zero form.....	108
Equation (20) Voltage measurement circuit transfer function with numerical values	108
Equation (21) Self-inductance of a cylindrical, nonmagnetic conductor	119
Equation (22) Diverging laser beam diameter	127

Equation (23) Lens equation.....	129
Equation (24) Distance from laser beam origin to output window.....	129
Equation (25) Pulsing parameters: volume of wire melted per second	135
Equation (26) Pulsing parameters: droplet volume	135
Equation (27) Pulsing parameters: theoretical droplet frequency.....	135
Equation (28) Pulsing parameters: melting rate control linear relationship	136
Equation (29) Pulsing parameters: constant calculation.....	137
Equation (30) Pulsing parameters: peak time calculation.....	137
Equation (31) Pulsing parameters: total time calculation.....	137
Equation (32) Pulsing parameters: background time calculation	138
Equation (33) Pulsing parameters: background current calculation	139

Glossary of Terms

Term	Definition
A	ampere (amp), unit of current
AC	alternating current
ADC	analog-to-digital converter
AM	additive manufacturing
Ar	argon
AWG	American wire gauge
CAD	computer-aided design
CC	constant current
cm	centimeter
CMT	Cold Metal Transfer
csv	comma separated values
CTWD	contact-tip-to-work distance
CV	constant voltage
DAC	digital-to-analog converter
DAQ	data acquisition
dB	decibel
DC	direct current
DED	directed energy deposition
DIAC	diode alternating current
DMM	digital multimeter
E _A	arc voltage
EMI	Electromagnetic interference
ER70S-3	American Welding Society welding electrode designation
ER70S-6	American Welding Society welding electrode designation
etc.	etcetera
F	farad, unit of capacitance
FE	Finite Element
f _N	Nyquist frequency, half of the sampling frequency (f _s)
fps	frames per second
f _s	sampling frequency
ft	foot
G	giga, prefix (10 ⁹)
GLADiS	GMAW laser assisted deposition integrated system
GMAW	gas metal arc welding
GMAW-P	pulsed gas metal arc welding
GTAW	gas tungsten arc welding

H	henry, unit of inductance
HAZ	heat affected zone
HeNe	helium-neon
HFS1	high frequency specimen number 1
HFS2	high frequency specimen number 2
HFS3	high frequency specimen number 3
HFS4	high frequency specimen number 4
hr	hour, unit of time (60 minutes)
HS1	hybrid specimen number 1
Hz	hertz (cycles/second)
H _w	weld heat input
I _A	arc current
I _b	pulsed waveform background current
in	inch
I _p	pulsed waveform peak current
ipm	inches per minute
IR	infrared
I/O	input/output
J	joule, unit of energy
k	kilo, prefix (10 ³)
ℓ _A	arc length
laser	light amplification by stimulated emission of radiation
lb	pound, unit of force (weight)
ℓ _e	electrode extension
LLS	linear least-squares
LM	layered manufacturing
M	mega, prefix (10 ⁶)
m	milli, prefix (10 ⁻³)
micron	micrometer (10 ⁻⁶ meters)
MIMO	multiple-input, multiple-output
min	minute, unit of time (60 seconds)
Mn	manganese
MOV	metal-oxide varistor
ms	millisecond, unit of time (1000 th of a second)
n	nano, prefix (10 ⁻⁹)
NAN	not a number
Nd-YAG	neodymium-doped yttrium aluminum garnet
NLLS	non-linear least-squares

ODPP	one-drop-per-pulse
O ₂	molecular oxygen
PAW	plasma arc welding
PAWS1	plasma arc welding specimen number 1
PCB	printed circuit board
PCI	Peripheral Component Interconnection
PCX	plano-convex, type of lens
PID	proportional, integral, derivative
pixel	video picture element
quasi-CW	quasi-continuous-wave
rad	radian
RC	resistor/capacitor
RF	radio frequency
RL	resistor/inductor
RMD	Regulated Metal Deposition
RMS	root mean square
RP	rapid prototyping
RS-232	Recommended Standard 232 serial communication
S	welding travel speed
s	second, unit of time
SAW	submerged arc welding
SCR	silicon-controlled rectifier
SHG	second harmonic generator
Si	silicon
SiDD	single droplet deposition
SSR	solid-state relay
STT	Surface Tension Transfer
S/N	serial number
t _b	pulsed waveform background time
T _F	step response fall time
T _L	step response low time
T _P	step response peak time
t _p	pulsed waveform peak time
T _R	step response rise time
T _{Sd}	step response settling time, step-down
T _{Su}	step response settling time, step-up
USB	Universal Serial Bus

V	volt, unit of voltage
VDC	volt, direct current
VAC	volt, alternating current
WAAM	wire arc additive manufacturing
WFS	wire feed speed
x	times
λ	wavelength
μ	micro, prefix (10^{-6})
Ω	ohm, unit of resistance
°	degree
%OS	percent overshoot
%US	percent undershoot
±	plus or minus
3-D	three-dimensional

1. Introduction

Additive manufacturing (AM), also known as Rapid prototyping (RP), layered manufacturing (LM), or 3-D printing, is a subject that has drawn a great deal of interest in recent years, and many advancements have recently been made. AM is the process of building components by adding material only where it is needed. In contrast, subtractive manufacturing, such as machining, begins with a large block of material and removes material that is not needed.

Although a variety of different materials can be additively manufactured, the development and optimization of metal 3-D printers is an area of specific interest in recent years. In fact, an article in MIT's Technology Review magazine listed metal 3-D printing as one of the top 10 breakthrough technologies of 2018 [1].

Metal AM processes can be categorized into one of at least two groups based on the filler material form: powder-based AM processes or wire-based AM processes [2]. Typically, powder-based AM processes have low deposition rates (amount of material deposited in a length of time), but can produce components with high geometric resolution (i.e., can produce small features). In contrast, wire-based AM processes typically have high deposition rates, but produce components with lower geometric resolution.

The objective of the present research is to bridge the gap between powder-based AM processes and wire-based AM processes using a system called GLADiS. GLADiS stands for GMAW (gas metal arc welding) laser assisted deposition integrated system. The goal is to minimize the deposition rate of GMAW (a wire-based welding process) by using process control and laser arc stabilization. Lowering the deposition rate will allow higher geometric resolution to be achieved.

1.1. Gas Metal Arc Welding (GMAW)

GMAW is a consumable electrode welding process that establishes an arc between a work piece and a wire electrode. Thermal energy in the arc and in the wire electrode melts both the wire electrode and a portion of the work piece. Molten metal droplets that form on the end of the electrode are transferred by various mechanisms into the weld pool on the work piece. The electrode's melting rate is matched by the wire feed speed (WFS) which is the speed at which the wire is fed forward. The molten weld pool is protected from the atmosphere by shielding gas [3].

1.2. Experimental Methods

The GMAW process's deposition rate was reduced by developing an improved metal deposition strategy. Instead of continuously depositing metal droplets from the wire electrode, process control was used to deposit single droplets on command. The new deposition strategy was referred to as single droplet deposition or SiDD. In addition, welding process parameters were tuned to reduce the deposition rate, while still allowing sufficient welding current to form a weld pool on the work piece. A laser was also used to stabilize the welding arc and further improve the finished component's geometric resolution and accuracy.

1.3. Scope

The scope of this research was primarily to develop GMAW process control to build small geometric features. Although metallography was used to infer metallurgical properties of weld metal deposited using the SiDD technique, metallurgical and mechanical properties of the weld metal were not the primary focus.

Also, only single bead width linear wall specimens were produced. They were built by depositing single weld beads on top of one another. The geometric capabilities of SiDD were

assessed by analyzing the wall thickness, surface roughness, and overall consistency. The system's ability to produce components with complex geometric features was not investigated.

1.4. Organization

Section 2 of this thesis provides background information on AM. It mainly focuses on metal AM and presents a comparison between powder and wire-based AM processes.

Additional details on wire arc additive manufacturing (WAAM) are also included. WAAM is the AM category where GLADiS operates.

Section 3 presents a detailed description of GMAW. Process parameters, advantages/limitations, and general operating behaviors are discussed.

Section 4 contains background information on research that has been conducted relating to WAAM with GMAW. Section 4 is broken into six parts including discussions of complete GMAW WAAM systems, research focusing on weld bead control, geometric investigations, metal transfer control, substrate release mechanisms (removal of specimens from substrate), and thermal analysis.

Section 5 describes the different components of the proposed improved deposition strategy including single droplet deposition (SiDD), noncontact arc starting, electrode extension minimization, and laser arc stabilization. The theory behind each component is covered in detail.

Section 6 discusses the equipment used in GLADiS. It presents detailed information on the setup and characterization of each piece of equipment. Section 6 also details the process of integrating a high frequency arc starter into the system.

Section 7 presents experimental procedures used to achieve continuous weld beads with the system. Depositing continuous weld beads is the typical deposition method used in GMAW. Configuring the system to produce continuous weld beads allowed the system to be characterized

before moving on to the SiDD technique. Tests were performed to develop arc starting techniques, determine the system's parameter space, and investigate pulsed current strategies.

Section 8 details the experiments used to obtain single droplet deposition (SiDD). The results presented in Section 8 represent a key point in the research and were the basis for all subsequent experiments.

Section 9 presents five different arc starting techniques that were investigated. It was not possible to achieve SiDD using the standard short circuiting GMAW arc starting method. The first three techniques investigated (laser arc starts, PAW pilot arc starts, and lift arc starts) were all attempts to start the main welding arc without using a high frequency arc starter. The last two techniques involved the use of a high frequency arc starter.

Section 10 discusses the experimental procedures and results of tests performed to investigate the relationship between droplet coalescence and GMAW electrode extension.

Section 11 contains information on the six specimens built. Building methods and characteristics of the final specimens are both discussed. One specimen was built using PAW pilot arc starting, four were built using the high frequency arc starter, and one was built using a high frequency arc starter/laser hybrid arc starting technique.

Section 12 analyses metallurgical properties of one of the specimens. Because the primary focus of the research was not metallurgy of build specimens, only one specimen was used as a representation. Features such as microstructure characteristics and the presence of voids/inclusions are analyzed.

Section 13 summarizes key parameters used in GLADiS. A description of how each parameter affected the system is given. The parameters are discussed in order of importance.

2. Additive Manufacturing

Compared to most conventional manufacturing processes, AM has a lower “buy-to-fly” ratio. The buy-to-fly ratio is the ratio of the amount of material purchased to build a component to the amount of material used in the final product. Although mass production with AM can be slower than conventional manufacturing, it is capable of rapidly creating new prototypes or small production runs without the need to acquire new tools and fixturing or to develop new manufacturing procedures.

As technology progresses, 3-D printers that perform AM are becoming more available. Polymer 3-D printers are available in a variety of forms, from large commercial units to affordable desktop versions for home users. Although polymers are sufficient for many applications and can make excellent prototypes in terms of shape and fit, polymer prototypes often cannot be tested for full functionality in applications where metals are used.

2.1. Metal Additive Manufacturing

For many applications, metal AM is an attractive alternative to conventional manufacturing due to the potential for low cost and ease of making functional prototypes or small production runs. Material savings is another AM advantage, and it becomes an even more important factor for expensive materials, such as titanium, that typically have extremely high buy-to-fly ratios [2].

However, compared to polymer 3-D printers, the availability of metal 3-D printers is much more limited. Depending on the type of system used, powder-based or wire-based, the cost of metal 3-D printers can be extremely high.

2.1.1. Powder-based AM

Powder-based AM techniques use fine metal powders as the feed-stock metal, and typically, a laser or electron beam is used as the energy source. Two categories of powder-based AM include powder-feed and powder-bed processes [2]. Powder-feed processes feed a supply of powder to the location where the energy source is focused on the build plane. Powder-bed processes evenly distribute a layer of metal powder over the entire build plane, and use the energy source to melt portions of the powder in the desired pattern. Powder-based AM can produce components with excellent geometric accuracy (up to $\pm 0.04\text{mm}$) and low surface roughness (9-16 μm) because each layer is only 20-100 μm thick [2] [4] [5].

However, powder-based AM is limited by its low deposition rate. Because of the extremely small layer thickness, powder-bed AM processes typically deposit about 4.66in³/hr, which is 1.32lb/hr for steel [2]. Powder-feed AM processes, such as DED (directed energy deposition), can achieve deposition rates in steel up to 3.96lb/hr using powder as the feed-stock [2]. DED is an AM process that can use either powder or wire as the feed-stock. The low deposition rate of powder-based AM processes leads to long build times, making powder-based AM more suited for building small, but complex components.

Most powder-based AM processes are relatively inefficient in terms of energy [6] and material usage [2]. Hazardous health effects inherent to working with metal powders and the danger of explosions are additional limitations to powder-based AM processes [2].

2.1.2. Wire-based AM

Wire-based AM techniques use metal wire as the feed-stock metal and usually a laser, welding arc, or electron beam as the energy source. Compared to metal powder, wire is easier to manufacture consistently and does not have the same hazardous health effects. Deposition rates

of up to 44 lb/hr for steel are significantly greater than powder-based AM processes, making wire-based AM techniques more suited for large components [7]. Wire-based AM processes can be much more energy efficient than powder-based AM processes [6], and wire-based AM processes have material usage efficiencies of up to 100% [2].

Compared to powder-based AM processes, wire-based AM processes produce components with lower geometric accuracy and a rougher surface finish [8]. Components manufactured with wire-based AM techniques often require machining to final dimensions due to the lower geometric accuracy and rougher surface [8]. Wire-based AM processes also commonly have a high heat input which can lead to weld metal with large grain size, residual stresses, and distortion in the finished component [2].

While both powder and wire-based AM processes can use a laser or electron beam as an energy source, only wire-based AM has the option of using a welding arc, meaning significantly less expensive equipment can be used. Wire-based AM using a welding arc as the energy source is typically referred to as wire arc additive manufacturing or WAAM.

2.2. Wire Arc Additive Manufacturing (WAAM)

The advantage of using a welding arc as the energy source is that the necessary equipment costs significantly less than equipment required for laser or electron beam processes. In fact, most WAAM applications use standard, off the shelf welding equipment [8].

WAAM is suited for building medium to large sized parts with relatively low geometric complexity with deposition rates that can range from about 1.5-22 lb/hr [2] [8]. Some WAAM systems are capable of producing components with a dimension accuracy of $\pm 0.2\text{mm}$ and a surface roughness of 0.2mm [2] [9]. WAAM can be used to make components out of a variety

of different weldable materials including titanium alloys, aluminum alloys, and many alloys of steel [8].

WAAM is typically performed using either plasma arc welding (PAW), gas tungsten arc welding (GTAW), or gas metal arc welding (GMAW), though submerged arc welding (SAW) has been used [10]. The majority of WAAM applications and research have used GMAW as the welding process, largely due to GMAW's ease of automation [8].

3. Gas Metal Arc Welding (GMAW)

The basic equipment used for GMAW includes a welding power source, welding torch, work piece and torch leads, wire feeder, and a shielding gas supply [3]. The welding power source supplies electrical power to the welding torch where an arc is established between the consumable wire electrode protruding from the torch and the work piece. The arc melts the work piece and the wire electrode, which is supplied by the wire feeder, under an envelope of shielding gas. A schematic of the GMAW process can be seen in Figure 1.

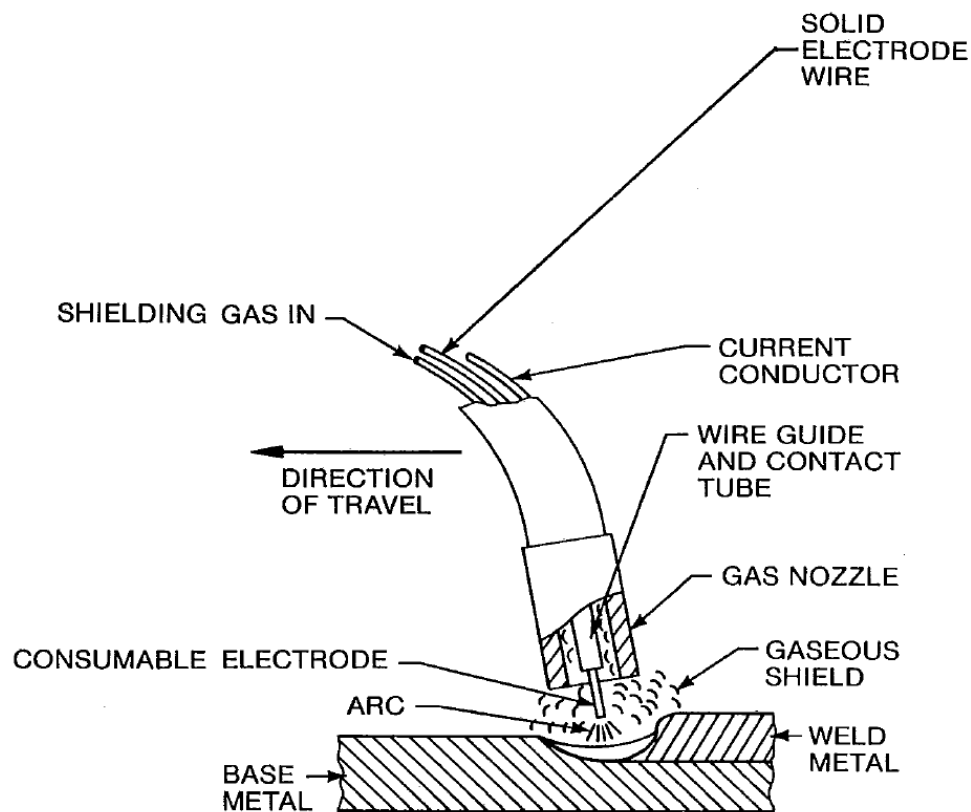


Figure 1: Schematic of the GMAW process [3].

As seen in Figure 1, GMAW uses a solid wire electrode as the filler metal. The wire electrode passes through a contact tube (contact tip), which is connected to a current conductor called the torch lead. Welding current flows through the torch lead, into the contact tip, and into the wire electrode. The welding arc is established between the electrode and the base metal (also

called the work piece or substrate). The arc melts both the electrode and the work piece, leaving behind a layer of weld metal. Molten metal is protected from the environment by a supply of shielding gas that flows through the gas nozzle.

3.1. Advantages and Limitations

GMAW has many advantages that make it an excellent choice for WAAM:

- 1) GMAW has a broad range of deposition rates making it possible to rapidly create both large and medium sized features on a component
- 2) It is readily automated because:
 - a. It uses relatively simple equipment
 - b. It typically does not require high-frequency arc starters, which are highly problematic in computer automated/robotic systems
 - c. The process is naturally self-regulated, so constant arc monitoring is unnecessary (see section 3.3) [3]
 - d. Coaxiality of the consumable electrode with the torch body results in simpler tool paths [8]
- 3) It has the ability to weld all commercial metals and alloys [3]
- 4) It can weld in all positions [3]
- 5) It is a relatively clean process that requires little post-weld cleaning [3]
- 6) Multiple different metal transfer mechanisms are available for various welding scenarios

GMAW also has a few disadvantages that hinder its use for WAAM:

- 1) GMAW lacks the ability to independently control welding current and filler metal addition (WFS)

- a. Low deposition rates are difficult to achieve without reducing the current to the point of arc instability
 - b. High deposition rates cannot be achieved without high heat input
- 2) GMAW has limited use in titanium welding
- a. Wandering arcs cause arc instability and poor weld bead quality [11]
 - b. High surface tension makes droplet transfer unpredictable [12]
- 3) Conventional short circuiting arc starts generally produce spatter, regardless of the transfer mechanism being used

3.2. Process Variables

There are many parameters associated with the GMAW process. The primary variables of interest are welding current, wire feed speed (WFS), electrode extension, and arc voltage.

3.2.1. Welding Current and Wire Feed Speed

Welding current, or arc current (I_A), is the primary source of melting. Thermal energy is generated by the collision of electrons and ions in the arc with the electrode and work piece material. Higher currents result in more collisions, and more heat is generated.

For GMAW the welding current is nearly always in the DCEP (direct current electrode positive) polarity. That means that electrons flow from the work piece (negative side) to the wire electrode (positive side). Attempting to weld using GMAW in the DCEN (direct current electrode negative) polarity leads to arc instability and spatter generation [3].

The wire feed speed (WFS) is the speed at which the wire is fed forward into the arc. It is one of two parameters that can be adjusted on a typical GMAW power source control panel. The WFS and welding current are related to each other by the Lesnewich equation [13]:

$$WFS = aI_A + b\ell_e I_A^2 \quad (1)$$

where:

WFS = wire feed speed in ipm (proportional to deposition rate)

a = constant of proportionality for anode or cathode heating (in/[min·A])

b = constant of proportionality for electrical resistance heating (min⁻¹·A⁻²)

ℓ_e = electrode extension (in)

I_A = welding current (arc current) (A)

Equation (1) shows that if the WFS is increased, the welding current must also increase at a given electrode extension. Figure 2 graphically shows the current and WFS relationship at various electrode extensions.

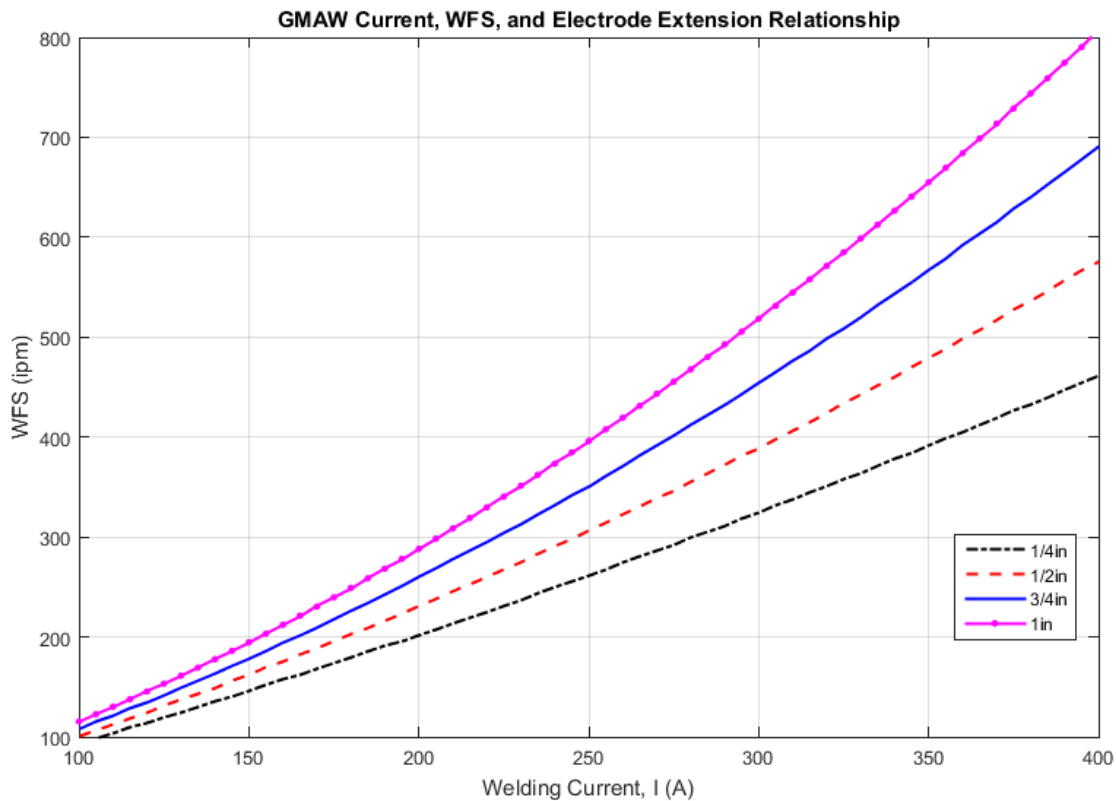


Figure 2: GMAW current, WFS, and electrode extension relationship for 0.045in diameter ER70S-3 wire with 98% Ar, 2% O₂ shielding gas. As electrode extension is reduced, more current is required for the same WFS.

The graph in Figure 2 was made by plotting (1) over a range of currents for electrode extensions of 1/4in, 1/2in, 3/4in, and 1in. Values used for a and b of $a = 0.867\text{in}/[\text{min}\cdot\text{A}]$ and $b = 2.87(10^{-3})\text{min}^{-1}\cdot\text{A}^{-2}$ are applicable to 0.045in diameter ER70S-3 wire with 98% Ar, 2% O₂ shielding gas [14].

It can be seen that by decreasing the electrode extension, the same WFS (or deposition rate) can be achieved at a higher current.

3.2.2. Electrode Extension

The electrode extension, as well as other GMAW dimensional parameters, are shown by the schematic in Figure 3.

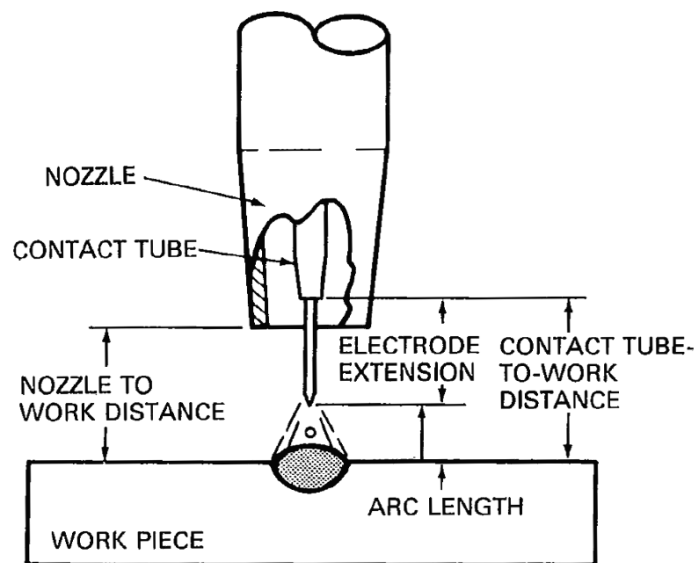


Figure 3: GMAW terminology [3].

The electrode extension is the length of wire that extends from the contact tip as seen in Figure 3. Other parameters include the contact tube-to-work distance (contact-tip-to-work distance) or CTWD, the arc length (ℓ_A), and the nozzle to work distance (NTWD).

The reason that longer electrode extensions require higher WFSs at the same current (as seen in Figure 2) is due to electrical resistance heating. In fact, the second term on the right-hand

side of (1) deals directly with resistive heating. If a long electrode extension is used, resistive heating in the electrode causes an increase in electrode melting rate for a given current [3].

3.2.3. Arc Voltage

Arc voltage is the parameter that determines the arc length. In typical GMAW applications, voltage is the other adjustment in addition to WFS that can be made on the welding power source control panel. Most GMAW power sources are constant voltage (CV), which means that they attempt to maintain a constant voltage throughout a welding process.

3.3. Electrical Characteristics

There are two basic types of welding power sources: constant current (CC) and constant voltage (CV). The VI characteristics (voltage versus amperage plot) of a practical welding CC power source can be seen in Figure 4.

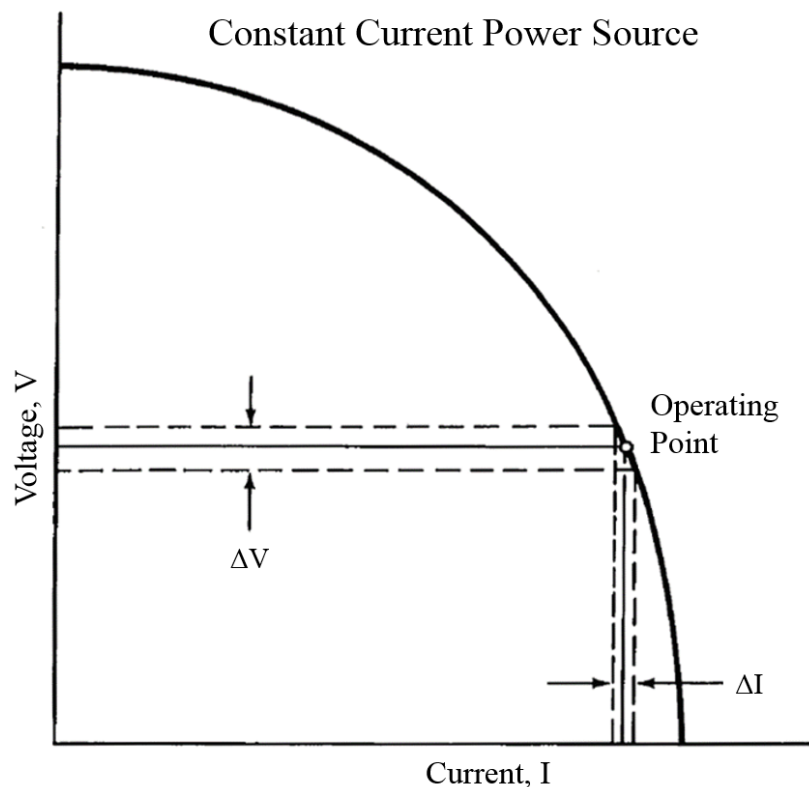


Figure 4: Practical welding constant current power source. A relatively large change in arc voltage results in a small change in welding current. Adapted from [3].

As seen in Figure 4, a practical welding CC power source does not necessarily output a constant current, especially at high voltages. It can be seen that when operating at the operating point, a large change in voltage (ΔV) results in a small change in welding current (ΔI). CC power source VI characteristics are exploited by manual welding operations where the arc length is controlled by adjusting the hand-held torch position (e.g., GTAW). Because arc voltage is related to arc length, when the arc length increases, the arc voltage increases. When the arc length is manually controlled, it can be difficult to maintain a constant arc length. With a CC power source, relatively large variations in arc length, and therefore arc voltage, will result in only minor variation in current.

The VI characteristic of a practical welding CV power source can be seen in Figure 5.

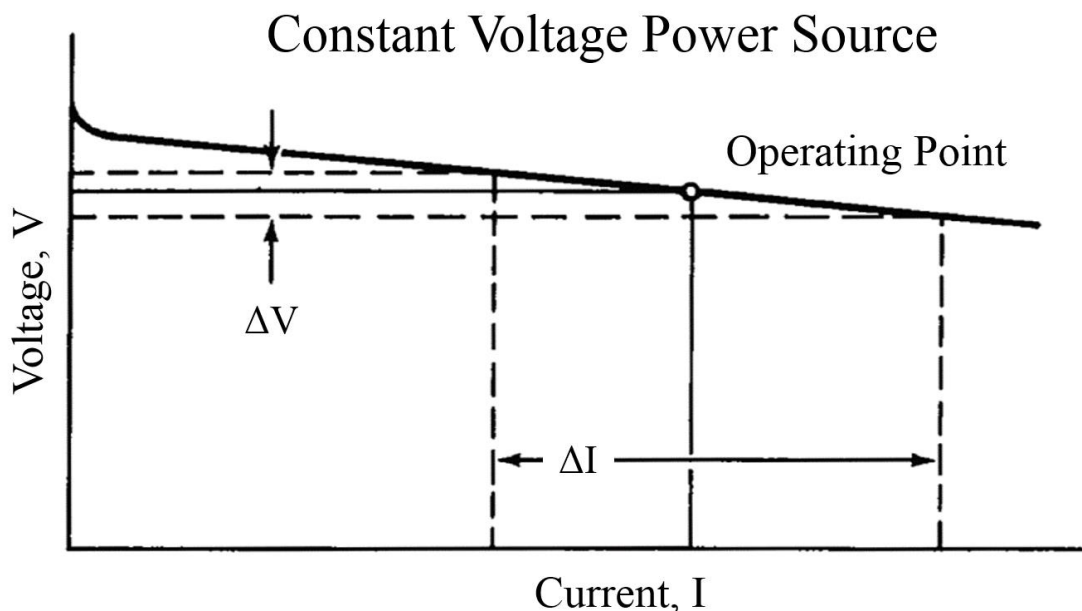


Figure 5: Practical welding constant voltage power source. A relatively small change in arc voltage results in a large change in welding current. Adapted from [3].

As seen in Figure 5, the VI characteristics of a CV power source are much different from a CC power source. It can be seen that with a practical welding CV power source, a small change in arc voltage (ΔV) results in a significant change in welding current (ΔI). CV power

sources are generally used by wire-fed welding processes (e.g., GMAW) that do not allow manual arc length control by torch position adjustment. CV power sources allow wire-fed welding processes to self-regulate.

Self-regulation is the phenomenon that maintains a constant arc length in wire-fed welding processes. As wire is fed towards the work piece, the arc length and, therefore, arc voltage decrease. Looking at Figure 5, a small decrease in arc voltage results in a large increase in welding current. Because welding current is the primary parameter that produces melting, the increase in arc current will melt the wire electrode back towards the contact tip. As the wire melts back, the arc length/arc voltage increases and the welding current decreases correspondingly. The cycle of increasing and decreasing current with decreasing and increasing arc length, respectively, keeps the arc length nearly constant, and therefore, self-regulation exists.

Using a CV power source also allows GMAW to automatically start its arc without any special technique. To start the arc, wire is fed forward towards the work piece with the power source energized. When the wire comes into contact with the work piece, a short circuit is created, and the voltage drops. Because the power source is CV, it attempts to bring the voltage back to the set-point by drastically increasing the current. The extremely high current is too much for the wire electrode to conduct. Resistive heating melts the wire, electromagnetic forces crush the molten wire and expel molten wire fragments, and the arc is started. GMAW arc starts are relatively violent due to high currents and strong electromagnetic forces, and spatter is typically generated.

At steady-state, a stable operating point exists where the arc voltage, welding current, and arc length are nearly constant. Operating points are defined by comparing the power source's VI characteristics with the welding arc's VI characteristics as seen in Figure 6.

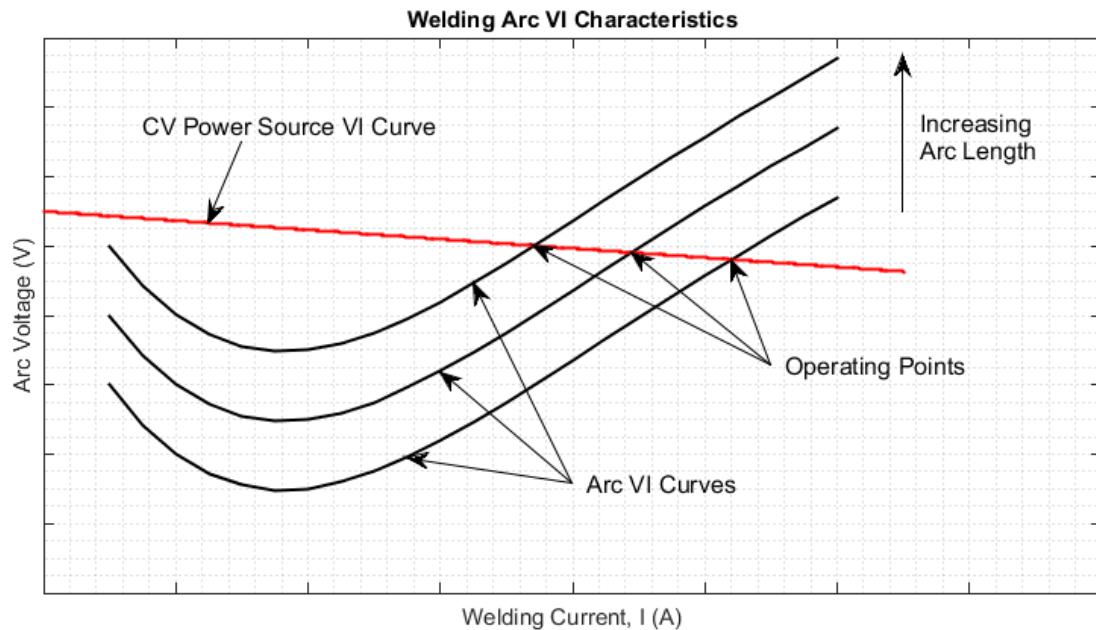


Figure 6: Welding arc VI characteristics and operating points. The point where the power source's VI curve intersects the welding arc's VI curve represents the operating point for a given arc length.

Figure 6 shows representative VI curves for three different arc lengths. Increasing the arc length shifts the VI curve upwards. Notice that at low welding currents, an increase in current results in a decrease in voltage. The decrease in voltage indicates that arc resistance is a function of current. As more current flows, the resistance significantly drops, and the voltage drops correspondingly. However, at a certain current, increases in current begin to also increase the voltage. Above this current, the arc behaves more like a resistor with a constant value.

The location where the power source's VI curve intersects the arc's VI curve represents the operating point for a given arc length. Operating points represent conditions for a stable arc.

3.4. Forces in the Arc

In GMAW, the mechanism that transfers metal from the wire electrode to the weld pool is dictated by forces acting on molten metal droplets in the arc. For DCEP polarity in Ar-based shielding, three main forces always act to pull droplets off the electrode: Lorentz force (electromagnetic pinch force), gravitational force (assuming flat position welding), and aerodynamic drag force from plasma flow [15]. To detach a droplet, the detachment forces must overcome two forces holding the droplet to the electrode: surface tension force and vapor jet force [15]. A diagram showing the forces can be seen in Figure 7.

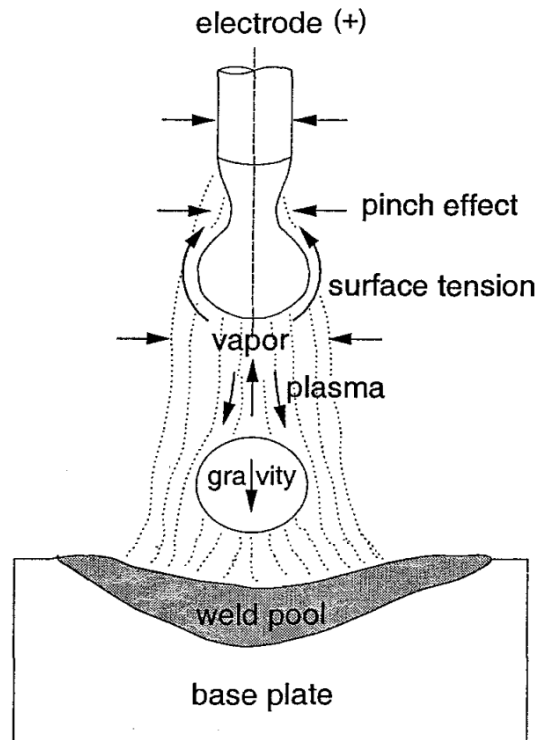


Figure 7: Forces acting on the molten metal droplet [15]. Pinch effect (Lorentz force), gravity, and plasma flow (aerodynamic drag force) act to detach droplets; surface tension and vapor jet force act to prevent droplet detachment.

As seen in Figure 7, aerodynamic drag force from plasma flow and gravity are both shown pulling the droplet from the electrode to the work piece (base plate). Although the

Lorentz force (pinch effect) does not act downwards, the pinching effect pinches droplets off the electrode and can be the dominant force within the arc.

The dominant force that holds droplets to the electrode is surface tension. Depending on the electrode composition, surface tension can be difficult to overcome. For example, titanium has a strong surface tension, making droplet transfer difficult. Because of titanium's strong surface tension, GMAW has limited uses in titanium welding.

Another factor that affects surface tension is the shielding gas composition. Adding active gases to shielding, such as O_2 , can reduce the surface tension and facilitate droplet transfer [3].

Although it is minimal, the other force that prevents droplets from detaching from the electrode is the vapor jet force. Momentum of metal vapors ejecting from the molten metal surface causes the vapor jet force.

Another important force that is not shown in Figure 7 is an electromagnetic force that can act in either an upward or a downward direction. The direction that the electromagnetic force acts is a function of the current flux distribution on the molten droplet [16] [17] as illustrated in Figure 8.

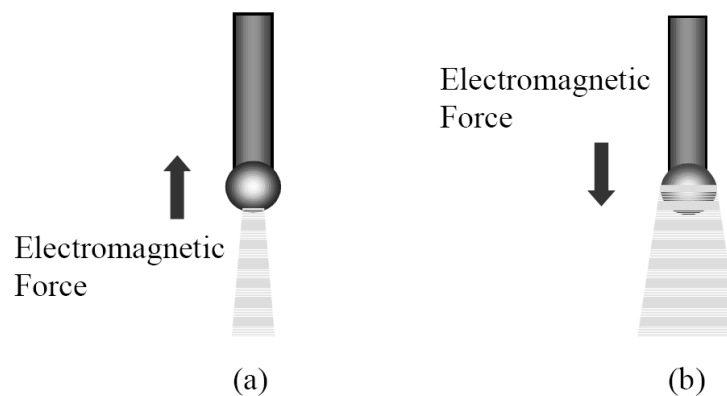


Figure 8: Electromagnetic force acting on molten metal droplet. Electromagnetic force acts to prevent droplet detachment when current flux distribution is localized on the bottom of the droplet and acts to detach droplets when current flux is uniformly distributed around droplet surface [17].

Figure 8 shows two different current flux distributions. In (a), the current flux distribution is localized on the bottom of the droplet. In (b), the current flux is more evenly distributed around the droplet's surface (i.e., uniform current emission from droplet surface). When the current flux distribution is localized on the bottom of the droplet, the electromagnetic force acts upwards, keeping the droplet from detaching [17]. When the current flux distribution is more uniform, the electromagnetic force acts downwards, helping to detach the droplet [17].

Two primary factors affect the current flux distribution: current magnitude [17] and shielding gas composition [16]. Low currents tend to produce current flux distributions that localize on the bottom of the droplet and can actually lift the droplet upwards [17]. Higher currents produce more uniform current flux distributions around the droplet's surface and promote droplet detachment [17].

The other factor affecting current flux distribution, shielding gas composition, is equally important. For example, CO₂ shielding gas causes current to emit from a small location on the bottom of the droplet [16]. Because the current flux distribution is localized on the bottom of the droplet, the electromagnetic force lifts the droplet upwards [16]. However, using Ar rich shielding gas promotes uniform current emission over the droplet's surface, and the electromagnetic force acts to detach the droplet [16].

3.5. Metal Transfer Mechanisms

GMAW has three basic, useful metal transfer mechanisms: short circuiting transfer, globular transfer, and spray transfer. The transfer mechanism is determined by the process parameters including magnitude and type of welding current, electrode diameter, electrode composition, electrode extension, and shielding gas composition [3].

3.5.1. Short Circuiting Transfer

In short circuiting transfer, wire is continuously fed at a constant WFS, and a constant voltage (CV) power source attempts to maintain a constant arc voltage. When the wire makes contact with the weld pool, a short circuit occurs, and the voltage drops to near zero. Because the power source is constant voltage, it surges the current in attempt to bring the voltage back to the set-point. The current surge is more current than the wire electrode can conduct, causing the wire to increase in temperature from resistive heating and melt. In addition, the current surge causes a strong Lorentz force that pinches off the end of the wire. Most of the molten wire is drawn into the weld pool by surface tension, but some molten wire is ejected as spatter due to the strong electromagnetic forces present. No metal is transferred through the arc gap [3]. Once the wire breaks contact with the weld pool, the power source drops the current to bring the voltage back to the set-point value, and the process repeats. Short circuiting can occur from 20 to over 200 times per second [3], generating spatter on every cycle.

3.5.2. Globular Transfer

At slightly higher current levels compared to short circuiting transfer, the electrode's melting rate from heating in the arc begins to match the WFS without having to make contact with the weld pool. As the wire electrode continues to melt, a molten droplet forms and is held on the end of the electrode by surface tension. Globular transfer occurs when the droplet grows large enough (larger than the electrode diameter) that gravitational force exceeds the surface tension force, and the droplet falls into the weld pool. Typically, droplet transfer occurs at a rate of a few drops per second. Because gravity is the governing force in globular transfer, globular transfer is usually limited to flat position welding [3].

A common problem with globular transfer is when the arc length is short, molten droplets on the end of the electrode occasionally make contact with the weld pool. Weld pool contact results in a short circuit, followed by a surge of current with enough electromagnetic force to cause the molten droplet to explode, producing large amounts of spatter. Short circuiting of molten droplets can be prevented by using a large arc length, but using a large arc length (high voltage) can lead to lack of fusion, poor penetration, arc wander, and excessive weld metal deposition. Globular transfer's disadvantages limit its practical use in production applications [3].

3.5.3. Spray Transfer

The other useful transfer mechanism, besides short circuiting transfer, is spray transfer. As current and WFS is further increased from globular transfer, it reaches a threshold known as the transition current. Below the transition current, the transfer mechanism is globular transfer; above the transition current, the transfer mechanism is spray transfer as illustrated in Figure 9.

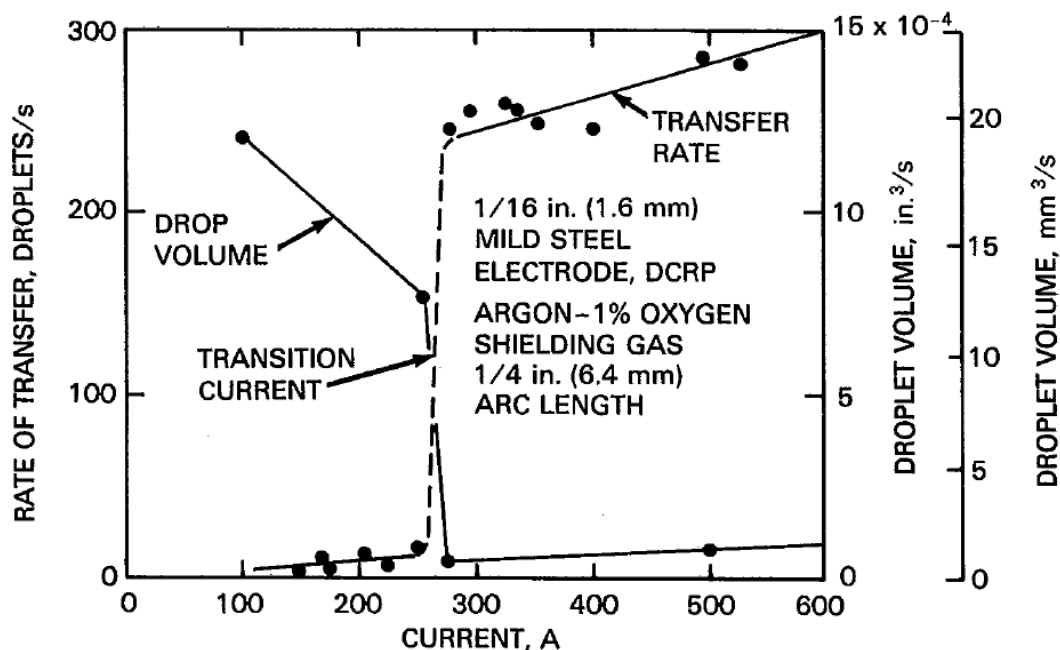


Figure 9: Transition from globular to spray transfer [3]. As current is increased through the transition current, droplet transfer rate drastically increases and droplet volume drastically decreases.

Figure 9 shows plots of both droplet frequency (transfer rate) and droplet volume as current is increased through the transition region. At the transition current, droplet detachment frequency (left y-axis) increases from a few drops per second to hundreds of drops per second. Also at the transition current, the droplet volume (right y-axis) decreases by about 10x.

In spray transfer, the current is high enough to produce a strong Lorentz force that overcomes surface tension forces and accelerates molten metal droplets off the tip of the electrode. True spray transfer can only be achieved in argon-rich shielding environments with additions of active shielding gases to 1) reduce surface tension that holds droplets on the end of the electrode [3] and 2) promote uniform current emission over the droplet surface [16]. Spray transfer can be characterized by droplets with a diameter less than the electrode diameter [3].

The high current and WFS associated with spray transfer lead to good weld penetration and high deposition rates. Because the droplets are small compared to the arc length, short circuiting never occurs in spray transfer, and relatively no spatter is generated [3].

Although the droplets in spray transfer are not significantly affected by gravity, the large and highly fluid weld pool associated with the high deposition rate, limits spray transfer's ability to weld out of position (i.e., horizontal, vertical, or overhead positions). Spray transfer is also not capable of welding thin metals due to its high current and high heat input [3].

In arc welding, heat input is the amount of energy dissipated by the arc in a given length of weld. Heat input is given by (2):

$$H_w = \frac{E_A I_A}{S} \quad (2)$$

where:

H_w = total weld heat input (J/in)

E_A = arc voltage (V)

I_A = arc current (welding current) (A)

S = welding travel speed (in/s)

It can be inferred from (2) that high welding currents and/or low welding travel speeds result in high heat inputs.

Most limitations of spray transfer have now been eliminated with the introduction of pulsed GMAW, or GMAW-P. In GMAW-P, the arc is maintained at a low current level, where a molten droplet begins to form, but is not detached from electrode. Periodically, the current is increased (pulsed) to a level well above the transition current. The current pulse creates a strong Lorentz force that pinches the molten droplet off the end of the electrode [3].

A typical GMAW-P waveform is composed of four basic parameters: background current (I_b), peak current (I_p), background time (t_b), and peak time (t_p) as shown in Figure 10.

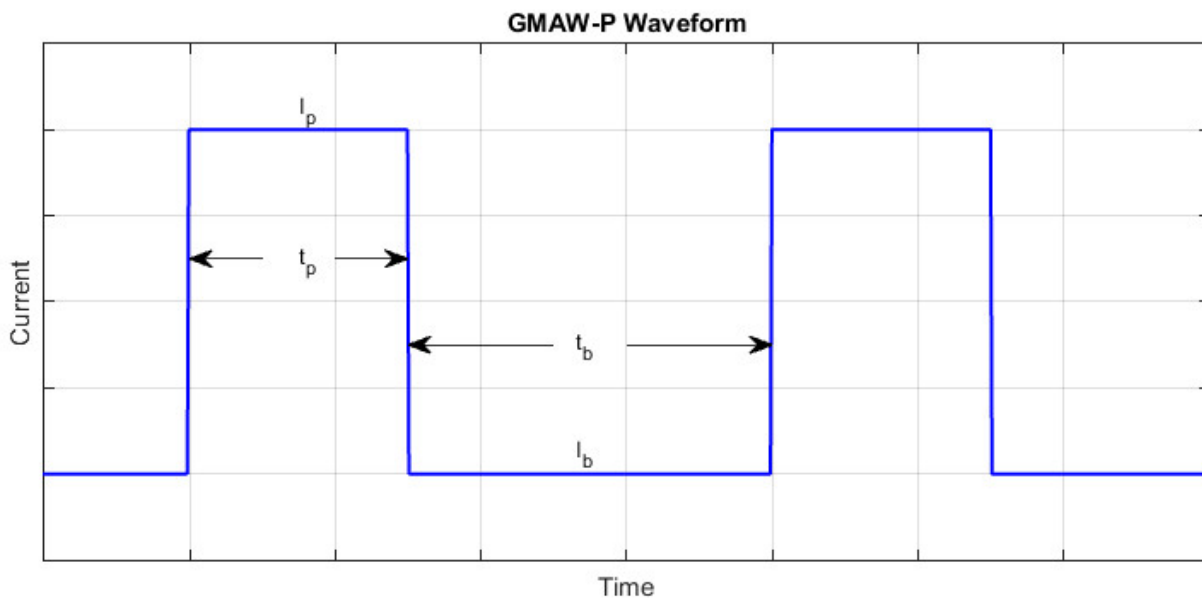


Figure 10: Typical GMAW-P waveform. The wave form is characterized by four parameters: peak current (I_p), peak time (t_p), background current (I_b), and background time (t_b).

GMAW-P parameters can be adjusted to produce a much lower average current than conventional spray transfer. The low average current leads to a low heat input and gives

GMAW-P the ability to weld at much lower deposition rates. The low heat input and deposition rate allow GMAW-P to weld thin sheets, as well as weld in any position [3].

GMAW-P is commonly performed with synergic power supplies that automatically adjust I_b , I_p , t_b , and t_p to match the desired WFS [3]. Commonly, the parameters are tuned to produce one-drop-per-pulse (ODPP) [18]. However, depending on the electrode composition, ODPP (or any other consistent droplet transfer) can be hard to achieve.

3.6. Summary

GMAW is a highly effective welding process with endless applications. Many different operation modes can be achieved by tuning the associated parameters.

GMAW has many advantages that make well suited for AM applications. Although there are several disadvantages, extensive research has been conducted to mitigate them.

4. WAAM with GMAW

Methods have been developed to control many different aspects of WAAM with GMAW such as weld bead profile, finished part geometry and surface quality, weld metal microstructure, and even substrate release energy. Substrate release energy is the amount of energy required to remove a finished component from the substrate on which it was built. Metal AM processes typically begin a component build by depositing the first layer on a piece of metal referred to as the substrate. When the build is complete, the component must be removed from the substrate by machining, cutting, or in some cases, impacting the component to break it free from the substrate. Each substrate removal technique has an associated energy, referred to as the substrate release energy.

Although not specific to WAAM, other GMAW advancements have been made that can be exploited to further improve WAAM techniques.

4.1. Complete Systems

Additively manufacturing components with GMAW began with simple component geometries such as cylinders [19]. The early work used simple motion systems to control the torch or component position [19]. The motion systems required manually programming motion paths to produce the desired geometry, limiting the geometric complexity of components [19].

In the late 1980s, Babcock & Wilcox Company developed a technique called shape melting that used a robot to control a GMAW torch and a rotational table to manipulate the component [20]. The shape melting system used proprietary algorithms relating weld bead shape and process parameters to control the weld bead shape and maintain geometric accuracy [20]. Temperature sensors and a water cooling system were also employed to maintain temperature control of the component being built [20]. The addition of precise temperature control gave

more control over the resulting microstructure and allowed high-strength alloys to be deposited without the risk of cracking [20].

The shape melting system was capable of quickly producing large components with excellent mechanical properties [20]. It was also capable of building multi-compositional components, which was not possible using other manufacturing techniques [20]. Figure 11 shows some examples of components manufactured using the shape melting process.

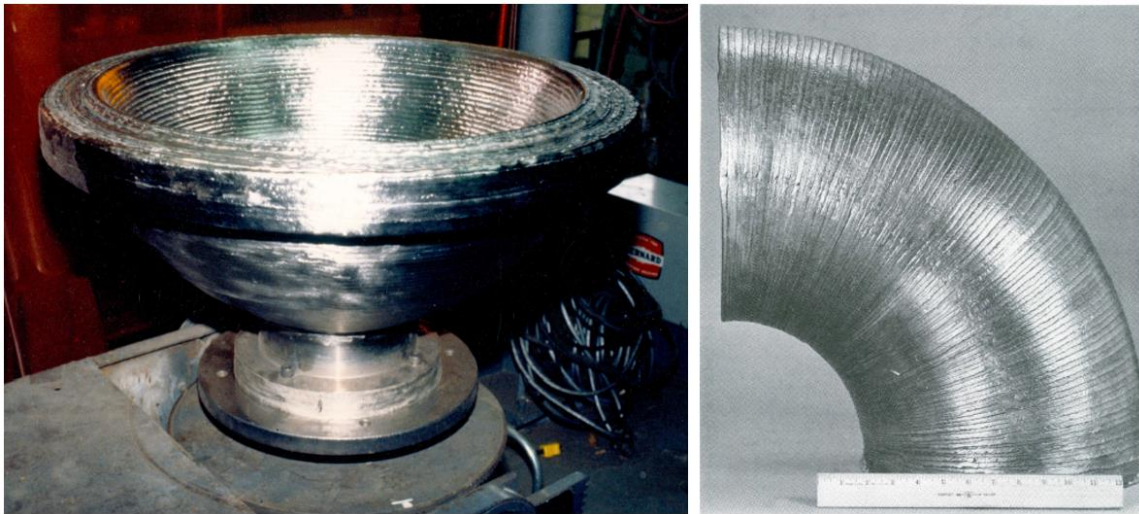


Figure 11: (left) 1000lb hemispherical head and (right) 12in diameter elbow manufactured using GMAW WAMM. Adapted from [21].

Both components in Figure 11 are shown in the as-shape melted condition, demonstrating the excellent surface quality of the finished components [20].

Although the shape melting process was successful at producing high quality components, precise programming was required to control the torch and component positions [20]. In the late 1990s, a robotic system was developed that could produce components from a CAD model [19]. Figure 12 shows examples of components build from CAD models using the robotic system.

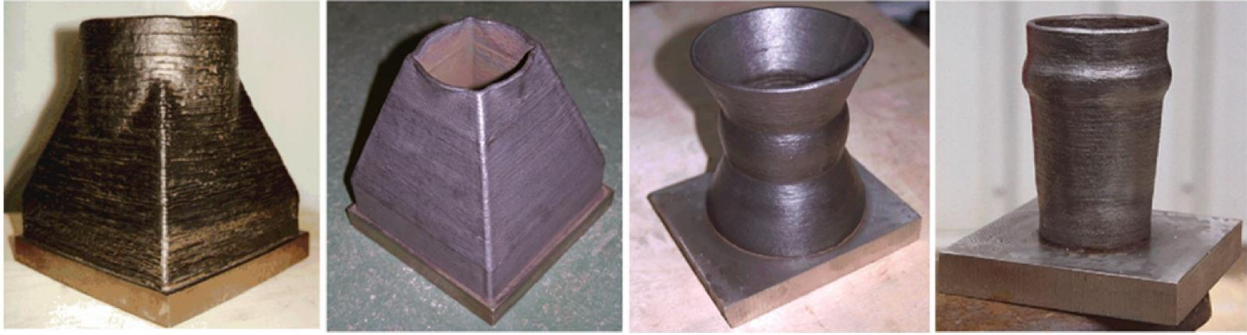


Figure 12: Components made from CAD models with GMAW WAAM [19].

Being able to produce components directly from a CAD model made it possible to quickly produce relatively complex solid metal prototypes from a design, without having to write new motion programs [19].

Zhang et al. conducted research at the University of Kentucky to develop a more advanced GMAW rapid prototyping (RP) system. Their system was also designed to build parts from a CAD model. Part of their research focused on improving geometric accuracy of the finished parts by optimizing slicing and deposition strategies from the CAD model. The other part of their research focused on using process control to optimize the deposited metal's microstructure and, therefore, mechanical properties. Process control was also used to improve geometric accuracy. Process parameters such as current, voltage, and wire feed speed (WFS) were used to control the size, flux, and thermal state of the metal droplets. Figure 13 shows how process parameters relate to the qualities of the finished component [22].

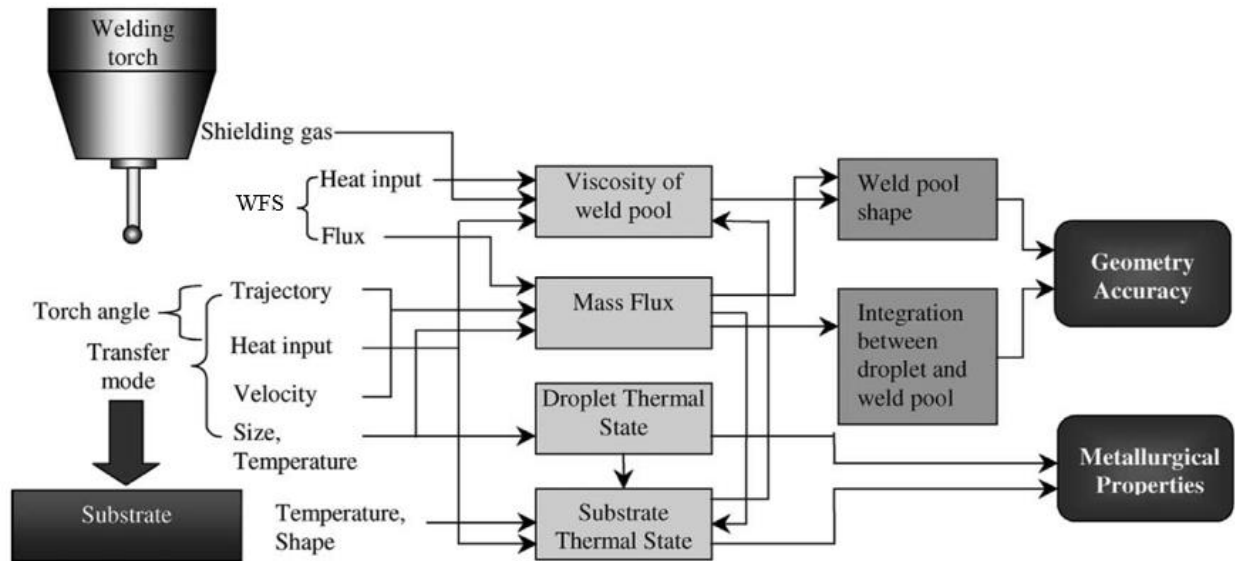


Figure 13: Relationship between process parameters and final component qualities. Adapted from [22].

Zhang created a planning algorithm for process parameters that could compensate for aspects inherent to GMAW and welding in general. The algorithm could modify welding parameters to deposit a range of layer heights. Controlling the layer height allowed components to be manufactured at any height, not just an integer multiple of a single layer height. It could also control the weld deposit's width so that filling a solid part could be completed without gaps using an integer number of weld beads. Additionally, the planning algorithm contained start and end control to allow the weld bead profile at starts and ends of each weld pass to be similar in form to the rest of the weld [22].

In more recent years, efforts have been made to develop low cost metal 3-D printers. Typically, proprietary commercialized metal 3-D printers, as well as the components they manufacture, are highly expensive. Anzalone et al. worked on developing an open-source GMAW metal 3-D printer for less than \$2000. Part of the goal in creating an inexpensive open-source metal 3-D printer was to help push innovation and development of metal 3-D printing. Their entire system was built using items that could be easily purchased online and/or locally,

and it was controlled by free software [23]. Figure 14 shows an image of a simple component made with the open-source metal 3-D printing system.



Figure 14: Simple component made with the open-source metal 3-D printing system. Adapted from [23].

As seen in Figure 14, the resulting system was capable of producing components from a CAD model, all at a cost of 1/100th of other metal 3-D printers [23]. However, it can be seen that a lack of precise weld bead control can lead to gaps between weld beads. Gaps between weld beads occur when the desired width of a feature is not divisible by an integer number of weld bead widths.

Perhaps the latest complete WAAM system using GMAW is the +1000K Arc Metal Deposition (AMD™) Machine from +MFG (Plus Manufacturing). The +1000K, shown in Figure 15, is a commercially available metal 3-D printer that uses the GMAW process to deposit a variety of alloys.



Figure 15: +1000K metal 3-D printer from +MFG [24].

The +1000K is capable of depositing steel up to 44lb/hr, and can be configured with four deposition heads to deposit four different materials/compositions on a single component [25]. Currently, the +1000K can deposit E70 steel, 300 series stainless steel, 6000 series aluminum, and titanium in a one cubic meter build chamber [25]. It has continuous temperature monitoring with a built-in chiller and quench tank to control the component's in-process thermal state [25].

4.2. Weld Bead Control

All characteristics of a completed WAAM component are functions of welding process parameters such as travel speed (S), arc current (I_A), arc voltage (E_A), wire feed speed (WFS), heat input (H_w), shielding gas composition, electrode extension (ℓ_e), contact-tip-to-work distance (CTWD), arc length (ℓ_A), etc. The affected component characteristics include surface finish, geometric accuracy and resolution, microstructure, and mechanical properties. Extensive research has focused on controlling characteristics of finished component through process control. Much of the process control research has focused specifically on controlling the profile of individual continuous weld beads in multilayer additive manufacturing.

Although all welding parameters have an effect on the shape of the weld bead, it has been found that welding current (arc current) is the major influence [26]. For multilayer single-pass additive manufacturing with GMAW, it has been found that currents higher than 200A can cause instability and pool overflow in upper layers, and the optimal current is between 100A and 180A [26].

In 2002, Doumanidis and Kwak conducted research focusing on controlling weld bead geometry as well as weld metal microstructure. They controlled the weld bead geometry using a multivariable adaptive controller, and they controlled weld metal microstructure using a technique known as thermal scanning [27].

The multiple-input, multiple-output (MIMO) controller had two inputs and two outputs. The controlling process inputs were travel speed and wire feed speed (WFS). The weld bead width and height were the controlled process outputs and were measured using a laser stripe 3-D digitizer. The adaptive controller was able to perform in-process system identification and modify the controller parameters. Because the laser stripe 3-D digitizer measured the weld profile behind the welding torch, there was a delay in output measurements. To compensate for the delay, a technique called Smith prediction was employed [27]. The results of their research showed that the controller was successfully able to control the weld bead geometry [27].

Although previous research had already investigated using complex adaptive control techniques to control the GMAW process, similar research had not been conducted with the addition of thermal scanning. Thermal scanning is the process of reciprocating a heat source over a metal surface. By locally modulating the heat source's power, the desired temperature field in the component can be achieved. In their research, Doumanidis and Kwak [27] used plasma arc welding (PAW) with robotic torch positioning as the heat source for thermal

scanning. Infrared pyrometry was used to measure the temperature field in the component, and feedback control was used to obtain the desired temperature field. By precisely controlling the thermal state of the deposited weld metal, Doumanidis and Kwak were able to control the resulting microstructure [27].

Another study by Xiong and Zhang focused exclusively on controlling layer height using closed-loop adaptive control. Because of the system's continuously evolving nature (e.g., heat accumulation, interlayer temperature, surface conditions, etc.), a fixed parameter controller, such as a PID controller, was inadequate. Layer height control required an adaptive controller that could continuously modify the controller parameters using on-line system identification [28]. A block diagram of the adaptive controller can be seen in Figure 16.

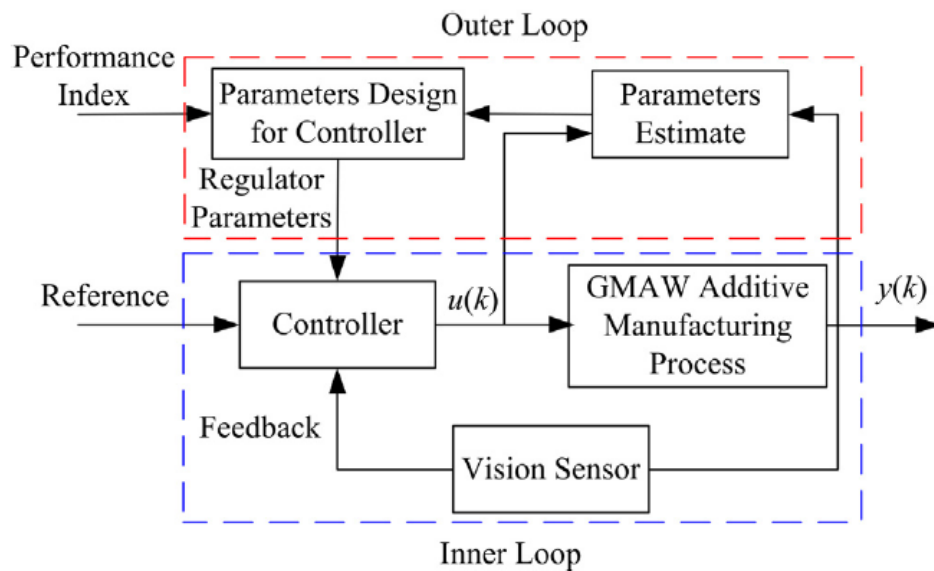


Figure 16: Adaptive controller block diagram. An adaptive controller has a typical feedback loop in addition to an outer loop (outside the feedback loop) capable of in-process controller parameter modification [28].

In Figure 16, the control input, $u(k)$, is the deposition rate, and control output, $y(k)$, is the layer height (or an indirect measure of layer height). It can be seen that the inner loop appears to be a standard feedback control loop. However, the outer loop, which is outside of the feedback

loop, estimates new model parameters from the control input/output data and calculates new controller parameters [28].

Xiong and Zhang's controller was able to control the layer height to within $\pm 0.5\text{mm}$. However, because of extreme transient conditions at the weld start and stop positions, they were not able to completely control the layer height at the beginning and end of each layer [28].

Other research has focused specifically on controlling weld bead width. Several investigations have used neural self-learning proportional summational differential (PSD) controllers to implement bead width control [29] [30]. PSD controllers have the ability to adapt to changing systems, making them much more effective than PID controllers for welding systems [30]. Figure 17 shows an example of a wall built with variable width layers using weld bead width control.



Figure 17: Weld bead width control depositing various bead widths on each layer [29].

As seen in Figure 17, PSD controllers are capable of precisely controlling weld bead width. In fact, weld bead width can be controlled with a maximum absolute error of less than 0.5mm [29].

4.3. Geometric Investigation

Other research has focused on characterizing WAAM's ability to build components with complex features such as inclined or horizontal faces. In addition to process control, torch position control and component position control can determine the complexity of finished components.

Kazanas et al. conducted research to determine the feasibility of building inclined walls with GMAW WAAM by inclining the welding torch. Inclining the torch requires a robotic arm to aim the torch at the same angle as the inclined feature so that each weld pass is positioned directly over the previous pass [31]. A schematic of the inclined torch technique can be seen in Figure 18.

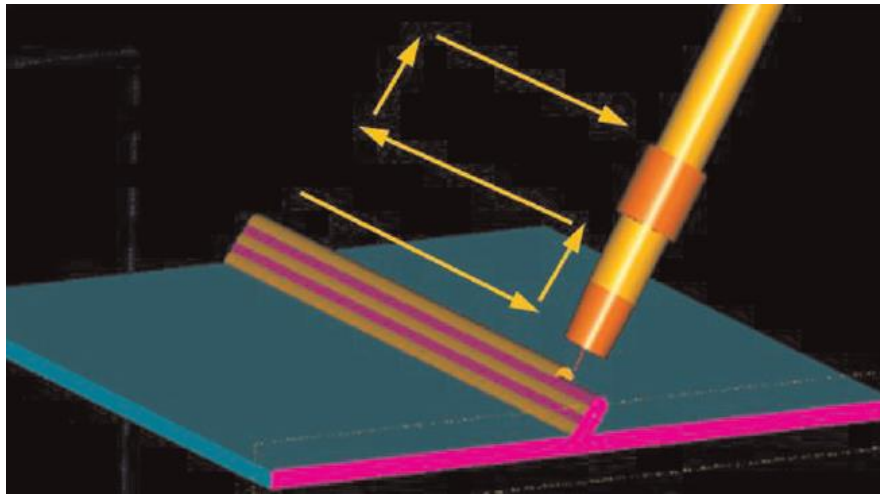


Figure 18: WAAM with GMAW using an inclined torch [31].

As seen in Figure 18, the torch is inclined at the same angle as the inclined wall. After each pass, the torch is offset in the build direction [31].

Kazanas found that inclined walls could be built on a flat substrate surface with an inclined angle up to 85° as measured from the surface normal. They also found that horizontal

walls could be built on the edge of a substrate [31]. Figure 19 shows (a) the 85° inclined wall built on a flat substrate surface, and (b) the horizontal wall built on the edge of a substrate.



Figure 19: (a) Inclined wall built on flat substrate and (b) horizontal wall built on substrate edge using the inclined torch GMAW WAAM technique. Adapted from [31].

Figure 19 shows that features can be built at any angle with an inclined torch. In fact, Kazanas was able to build completely enclosed specimens using the inclined torch technique as seen in Figure 20.

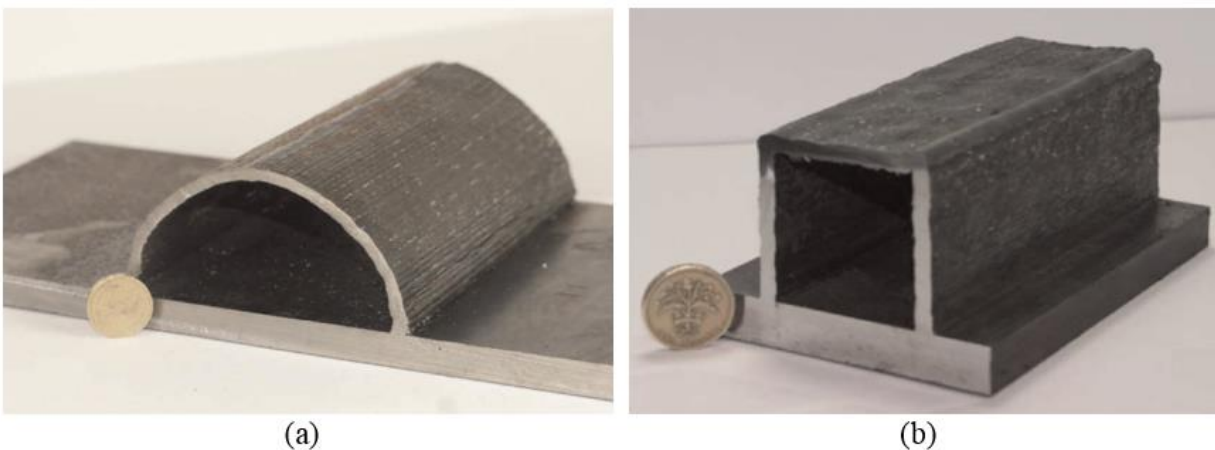


Figure 20: (a) Semicircle and (b) box built using the inclined torch technique. Adapted from [31].

As seen in Figure 20, components exhibiting various build angles can be built using the inclined torch technique.

Although GMAW WAAM can produce features on a component at any desired angle, complex positioning equipment can be required. The inclined torch technique requires the use of a robotic torch positioning system to maintain the correct inclined torch angle [31]. An alternative approach is to use a rotational-table to manipulate the component position rather than the torch. A rotational table is an effective technique because rotating the whole component allows each feature to be welded in the flat position [32]. However, the complex positioning equipment for each technique is expensive and not always practical.

Xiong et al. conducted research to determine the limits of producing inclined, thin-walled features with flat position deposition. In flat position deposition, the welding torch is always normal to the substrate and welding is performed in the flat position. Because the angle between the welding torch and the substrate is fixed, a relatively inexpensive positioning system is all that is required [32].

In flat position deposition, inclined features must be produced by offsetting each weld pass [32]. A schematic of producing an inclined wall with flat position deposition can be seen in Figure 21.

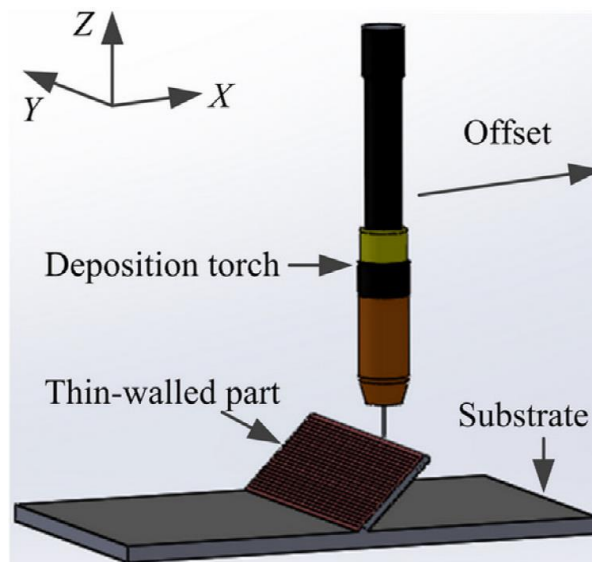


Figure 21: Schematic of flat position deposition welding system [32].

As seen in Figure 21, the torch is normal to the substrate, and the inclined wall is produced by offsetting each pass. The inter-pass offset distance determines the wall's inclined angle [32].

By tuning process parameters and adding extra control by using Cold Metal Transfer (CMT) [33], Xiong was able to achieve a 75° inclined angle, measured from the substrate normal [32]. The maximum inclined angle without a support structure was previously thought to be 45° [34]. Results of the research showed that the achievable inclined angle increased with decreasing WFS and increasing travel speed [32]. A macrograph of a sectioned portion of the 75° inclined wall can be seen in Figure 22.



Figure 22: Inclined wall with 75° incline angle made with flat position deposition [32].

As seen in Figure 22, relatively large angles were achieved with flat position deposition simply by fine-tuning the GMAW process parameters.

4.4. Metal Transfer Control

In the past 30 years, many developments have been made that have improved GMAW's appeal for WAAM. Many of the developments are associated with improving the metal transfer mechanism from the wire to the weld pool.

In 1988, Lincoln Electric developed a modified form of short circuiting transfer they called Surface Tension Transfer, or STT. STT requires the use of a standard wire feeder and a

specialized power supply, capable of extremely fast voltage/current sensing and adjustment [35].

An example of the waveform used in STT can be seen in Figure 23.

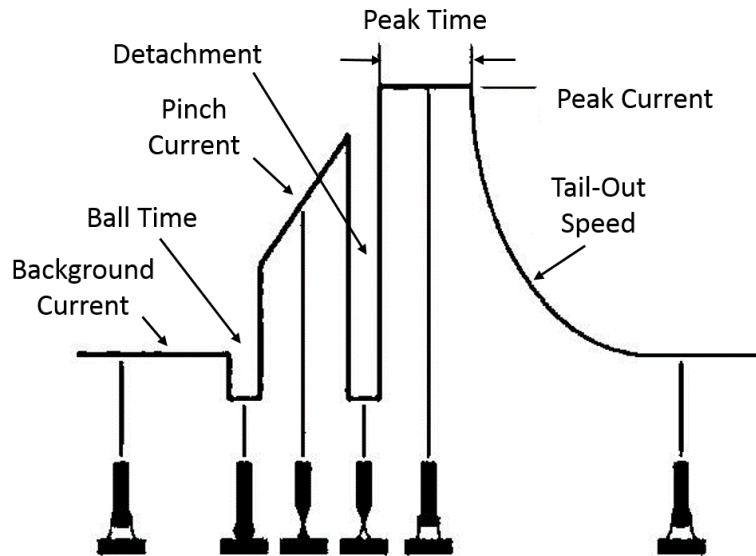


Figure 23: STT waveform. Adapted from [36].

The STT waveform is composed of six phases:

- 1) **Background Current:** A low background current is used to maintain the arc, heat the base material, and form a droplet on the end of the wire.
- 2) **Ball Time:** Just as the wire is about to make contact with the weld pool, the current is reduced to around 10A to ensure a short circuit is made.
- 3) **Pinch Current:** A pinch current is then applied to squeeze the droplet into the weld pool. At the same time, the power supply is constantly monitoring the necking of the molten metal column connecting the weld pool to the wire.
- 4) **Detachment:** When the column is about to break, the current is reduced to 45A-50A to create a gentle droplet detachment without spatter.

- 5) **Peak Time:** Once the droplet has detached, the current is increased to reestablish the arc and ensure complete droplet separation.
- 6) **Tail-Out Period:** The current is then decreased back to the background current. The Tail-Out Period can be adjusted to regulate the process heat input [36] [37].

When compared to standard short circuiting transfer, the added control of STT provides several advantages including better fusion, lower heat input, and reduced spatter. However, the complex power source required is much more expensive than a standard CV power source [35].

In 2004, Miller Electric Company developed a new modified short circuiting transfer technique they called Regulated Metal Deposition, or RMD [38]. RMD has many similarities to STT including a complex power source capable of generating specific waveforms. An example of the waveform used for RMD can be seen in Figure 24.

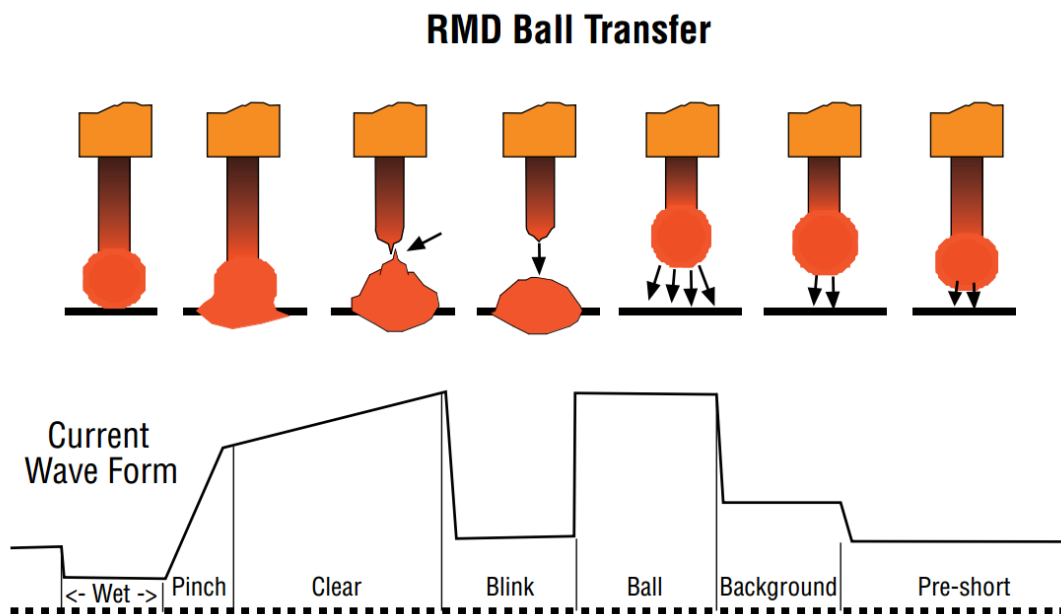


Figure 24: RMD waveform and phases [39].

As seen in Figure 12, RMD's waveform has multiple phases:

- 1) **Wet Phase:** From previous stages in the waveform, a droplet is formed on the end of the wire. Just as the droplet is about to make contact with the weld pool, the current is reduced to a low value to ensure a gentle transition of the droplet into the weld pool.
- 2) **Pinch Phase:** Once the droplet has made full contact with the weld pool, the current is rapidly increased to begin pinching off the droplet.
- 3) **Clear Phase:** In the clear phase, the current continues to increase, but at a lower rate. The current increases until the liquid column breaks, detaching the droplet into the weld pool.
- 4) **Blink Phase:** Just as the droplet detaches, the current is reduced to prevent spatter from generating.
- 5) **Ball Phase:** After a short period of time, the current is increased to reestablish the arc and start the formation of another droplet.
- 6) **Background Phase:** Once a droplet has started to form, the current is reduced to an intermediate background current to help maintain weld pool stability.
- 7) **Pre-short Phase:** The current is then reduced again to reduce the droplet growth rate and prevent globular transfer as the wire approaches the weld pool [38].

RMD has the same benefits as STT, with increased fusion, low heat input, and spatter free operation, but also requires an expensive power source [38].

About the same time RMD was developed, Fronius of Austria developed their own modified version of short circuiting transfer they called Cold Metal Transfer, or CMT. In CMT, a molten metal droplet is formed on the end of the wire. As soon as the wire makes contact with the weld pool, the current is reduced to near zero, and the wire feed is reversed to pull the wire

out of the weld pool. As the wire is retracted from the weld pool, surface tension pulls the molten droplet on the end of the wire into the weld pool. Once the droplet has detached from the wire, the current is increased to re-ignite the arc, the wire is fed forward, and the process repeats [33].

Similar to STT, CMT requires a complex power source. However, CMT also requires a more advanced wire feeding system [40]. Figure 25 shows a plot of the voltage and current waveforms used for CMT.

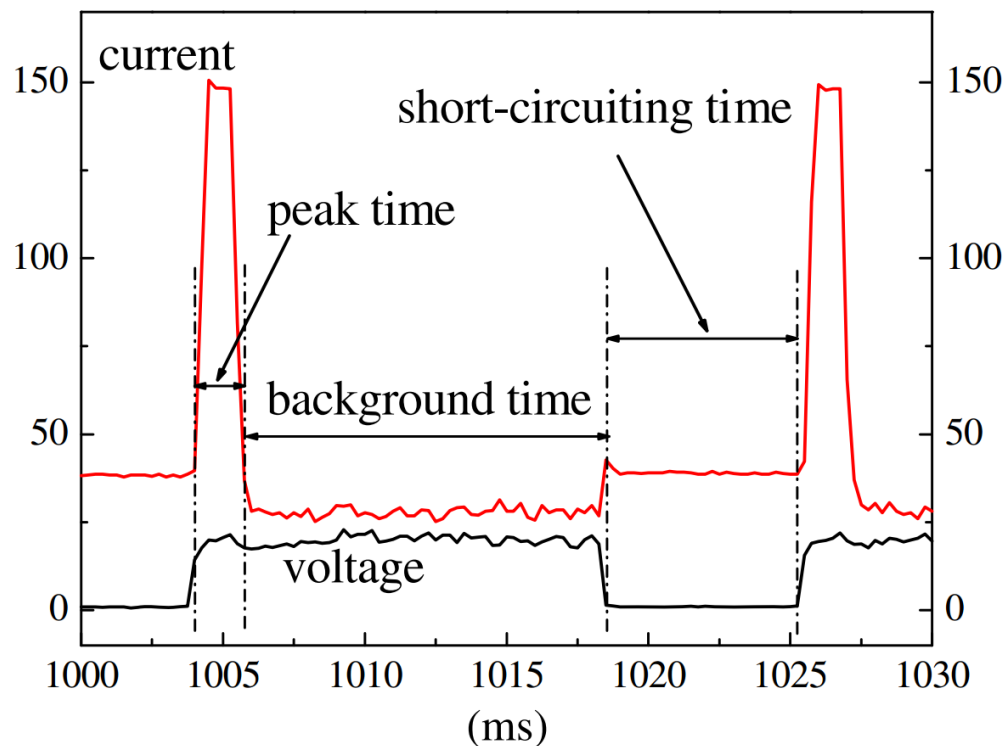


Figure 25: CMT current and voltage waveforms [40].

There are three specific time periods shown in Figure 25 that make up the CMT waveform:

- 1) **Peak time:** The peak time is a relatively large current pulse that reestablishes the arc after droplet transfer. It also forms a droplet on the end of the wire.

- 2) **Background time:** In the background time, the current drops to a low value to prevent the droplet from transferring across the arc gap while the wire is approaching the weld pool.
- 3) **Short-circuiting time:** The short circuiting time is when the wire makes contact with the weld pool. As seen in Figure 25, the voltage drops to zero and the current remain at a relatively low value. During the short circuiting time, the wire feed is reversed to detach the droplet from the end of the wire. After the short-circuiting time, the waveform repeats, starting with the peak time to re-ignite the arc [40].

CMT has many benefits that make it attractive for many applications including additive manufacturing. In fact, CMT has already been used in a number of AM applications [32] [41] [42]. Figure 26 shows some examples of components additively manufactured using WAAM with CMT.



Figure 26: Components manufacture with WAAM using CMT [8].

CMT can operate at a much lower average current and heat input compared to standard short circuiting transfer, and with a higher deposition rate [2]. A low heat input results in welds with lower residual stress as well as the ability to weld extremely thin metal or make welds on fine features [33].

Because CMT uses mechanical wire retraction at low currents rather than high current to detach droplets, it is virtually spatter-free. CMT also has an extremely stable arc because arc length detection and control are performed mechanically. The arc maintains stability through changing process and environmental conditions leading to uniform weld beads. The combination of spatter-free operation and excellent weld bead aesthetics means the surface quality of components made with CMT is exceptional [33] [43].

Research has also been conducted to improve metal transfer in pulsed GMAW. In 2001, Zhang and Li conducted research to investigate controlled metal transfer in titanium GMAW. Because molten titanium has a strong surface tension, consistent droplet transfer with standard pulsing parameters is unattainable. The goal of Zhang and Li's research was to develop new pulsing parameters that would result in a more robust (i.e. predictable and consistent) metal droplet transfer [17].

Zhang and Li had previously developed a technique they called active metal transfer control [12]. Although active metal transfer control was effective, it was not as robust as desired. They called their new technique modified active control. Modified active control used different amplitude current pulses to create droplet momentum to aid in droplet detachment. The theory was that a smaller amplitude current pulse would create an electromagnetic force acting upwards and lifting the metal droplet. Once the small current pulse was complete, the droplet would begin to fall and build momentum. As the droplet was falling, a larger current pulse with

an electromagnetic force acting downwards would force the droplet to detach from the wire electrode and fall to the weld pool. Figure 27 compares the original active metal transfer control to modified active control [17].

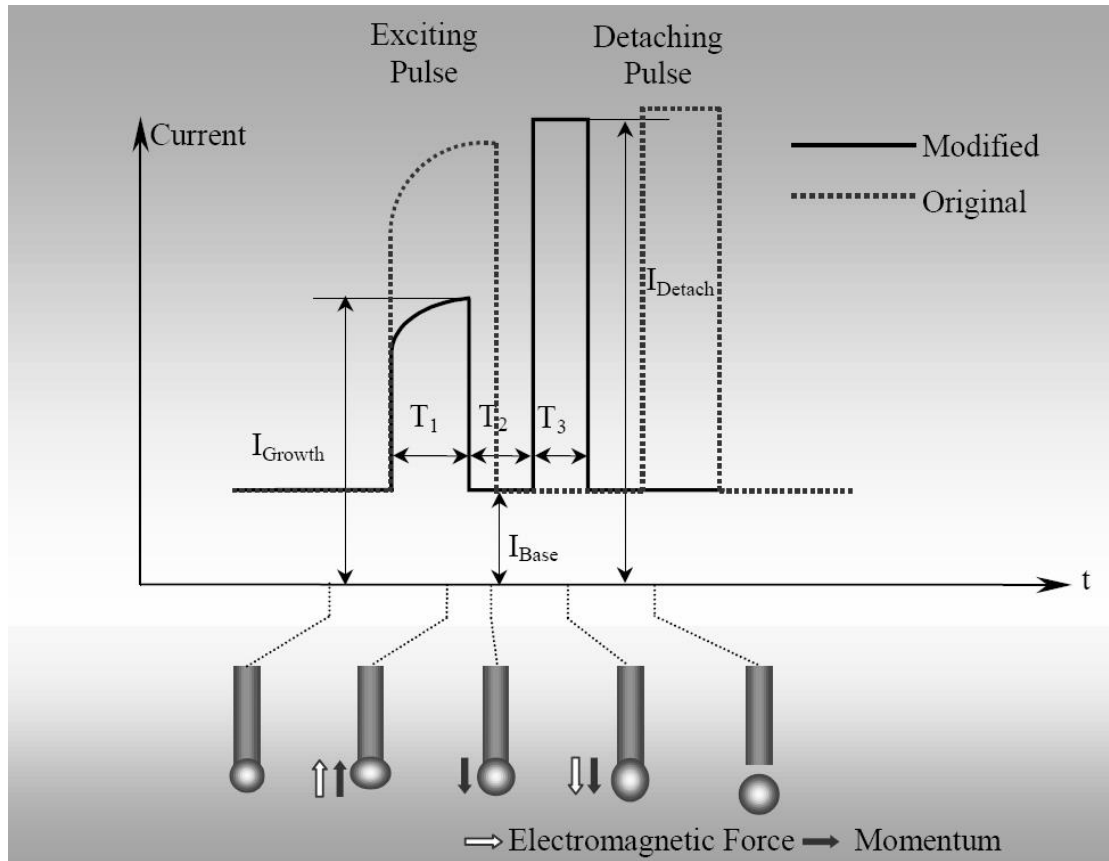


Figure 27: Active metal transfer control and modified active control used for robust droplet detachment in titanium GMAW-P applications [17].

Using a high-speed camera, Zhang and Li monitored the droplet detachment with various combinations of timing and amplitudes in the current pulses. They found that robust metal transfer was possible with the proper current pulse sequence [17].

Although much research has focused on controlling the detachment of molten metal droplets from the electrode, another aspect of metal transfer control is controlling where the molten droplets impinge on the base material.

In a typical welding arc, most of the arc discharge on the cathode is localized to a small area known as a cathode spot [11]. Although the physics behind cathode spot motion is not completely understood, it is known that cathode spots tend to wander around the cathode, likely to areas that emit electrons more easily. In GMAW (typically DCEP), the cathode is the work piece, which gives the cathode spot excessive room to move. At relatively low currents, arc instability can occur due to the wandering cathode spot [11]. Consistent transfer and placement of molten metal droplets across an unstable arc is impossible, as the droplets tend to travel to the location of arc discharge (i.e., the cathode spot).

In addition to arc instability, cathode spots can lead to excessive spatter generation. Cathode spots commonly form on top of metal droplets just entering the weld pool. Because most of the welding current is flowing through the cathode spot, a large Lorentz force is associated with the cathode spot. The Lorentz force is often great enough to crush the metal droplet and eject spatter [11].

In 2005, Shinn et al. investigated stabilizing cathode spots in titanium GMAW using a laser. Arc stability and metal transfer consistency in titanium welding can be a problem due to the more prominent cathode spot formation and motion in titanium compared to other metals. Their idea was that enhanced evaporation from laser emission would stabilize the cathode spot, fixing it to a desired location. Welds were made with an Nd-YAG laser focused on the leading edge of the weld pool. Various laser parameters including power and focus spot size were varied to characterize the laser effects [11].

Shinn's results showed that the laser had a considerable effect on the welding process. Adding the laser to the welding process resulted in reduced spatter generation as well as a much

more uniform weld bead profile. Figure 28 shows a comparison of welds made with and without the laser [11].

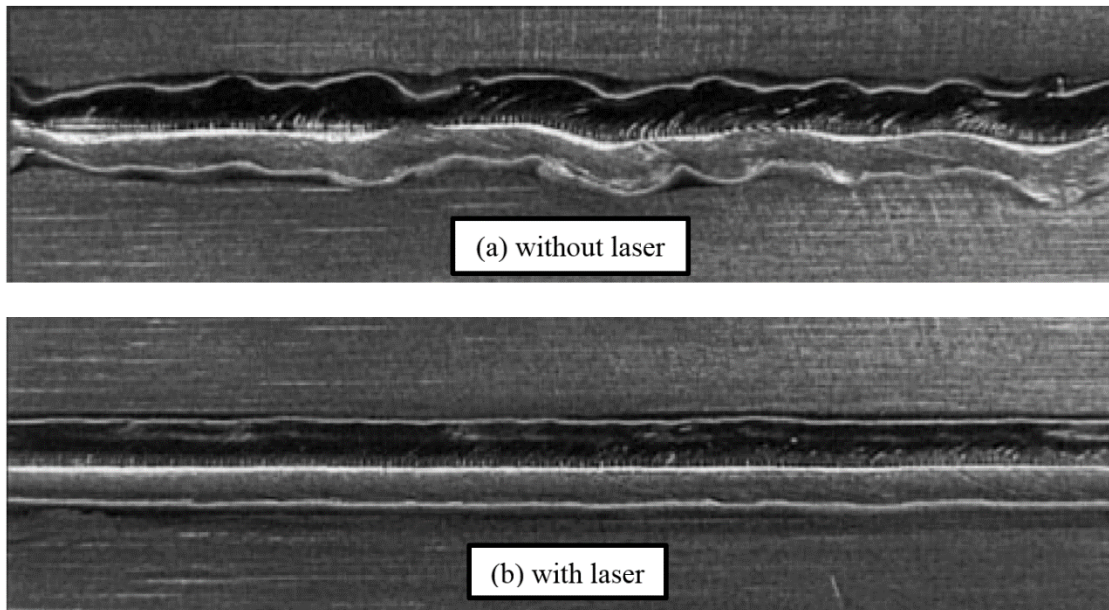


Figure 28: GMAW titanium welds (a) without a laser and (b) with a laser. Stabilizing the welding arc with a laser resulted in a more uniform weld bead profile. Adapted from [11].

As seen in Figure 28, the laser effectively eliminated weld bead irregularity caused by the wandering cathode spot.

4.5. Substrate Release Mechanisms

Haselhuhn et al. conducted research at the Michigan Technological University to develop an affordable substrate release mechanism. Their release mechanism would allow GMAW additive manufactured components to be easily removed from a reusable substrate. Typically, a component forms an extremely strong bond to the substrate on which it was built. Removing the finished component requires excessive time and energy, and often the substrate must be sacrificed in the removal process. The different substrate release mechanisms they tested included shielding gas manipulation, first layer weld parameter modification, surface coatings, and welding of dissimilar metals [44].

The method Haselhuhn used to determine the release energy was to use a modified Charpy impact tester to break specimens off the substrate and measure the corresponding impact energy. Although all tested release mechanisms significantly reduced the release energy, welding of dissimilar metals (aluminum on a steel substrate) and surface coatings were the most effective for aluminum specimens. Because surface coatings could not survive in steel welding environments, the best release mechanisms for steel specimens were shielding gas manipulation (no shielding gas on the first layer) and first layer weld parameter modification [44].

4.6. Thermal Analysis

It is common for the high deposition rates of GMAW to produce high heat inputs [45]. High heat inputs can lead to residual stresses, distortion, poor surface finish, and low geometric accuracy in deposited components [45]. A great deal of research has focused on modelling the thermal behavior of AM with GMAW through Finite Element (FE) analysis. Models are validated with experimental results to develop techniques that mitigate residual stress and distortion [42] [46] [47] [48] [49] [50] [51].

Although earlier FE analysis techniques could not handle large models due to excessive computation time, newer techniques allow large models that simulate the fabrication of larger components [42]. Simulation, backed by experimental results, have shown that adding a secondary heat source (induction heating) [48], or preheating the substrate [50] can smooth the thermal cycles and reduce induced stress and distortion.

Although FE analysis has been shown to accurately predict residual stresses and distortion, it is difficult to predict how thermal cycles affect the finished component's geometric accuracy and mechanical properties [45]. Experimentation has shown that insufficient inter-

layer cooling time can lead to poor surface finish and geometric accuracy as seen in Figure 29 [45].

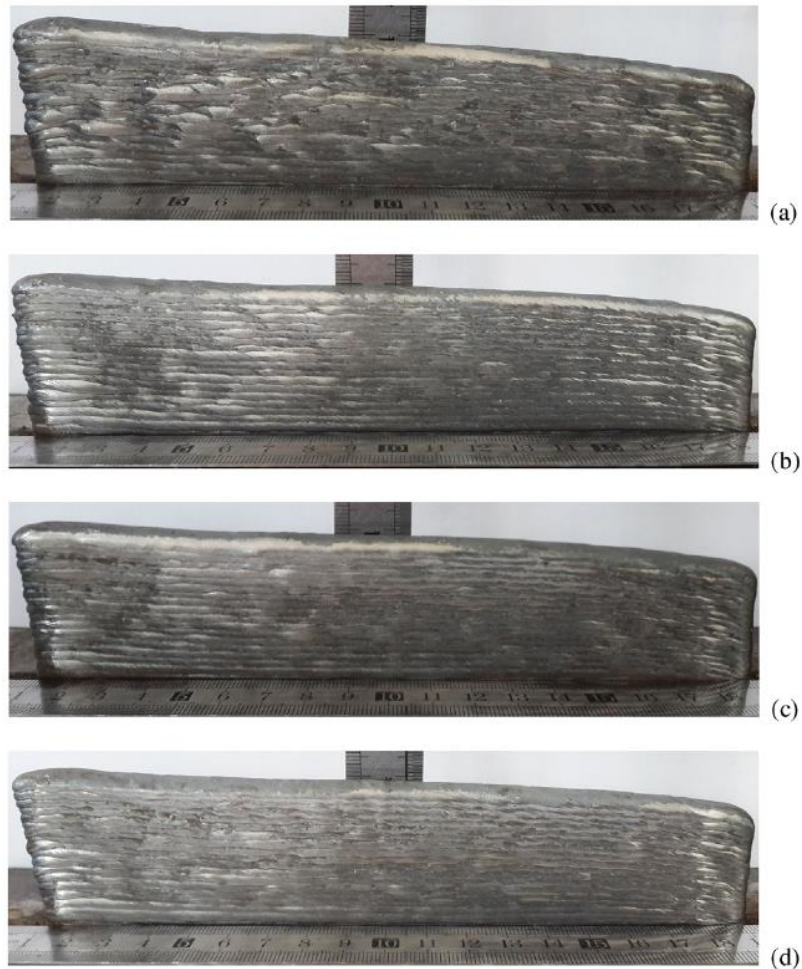


Figure 29: Walls made with various inter-layer cooling times. Increasing the interlayer cooling time resulted in improved geometric accuracy [45].

In Figure 29, the inter-layer cooling times were (a) 2 min, (b) 5 min, (c) 8 min, and (d) alternated at 2 min for odd layers and 5 min for even layers [45]. It can be seen that increasing the inter-layer cooling time from 2 min to 5 min improved the surface finish as well as the geometric accuracy (less slope from left to right), but increasing from 5 min to 8 min had little effect [45]. Alternating the inter-pass cooling time from 2 min to 5 min from layer to layer was an effective compromise between build time and finished quality [45].

4.7. Summary

Promising results from many different investigations have shown that GMAW has great potential in WAAM applications. Rapid prototyping systems using GMAW have proven to be successful at planning machine paths and are limited only by the difficulty of weld bead width and height control. Although the complexity of the GMAW process has limited the ability to precisely control weld bead profile, advanced control techniques have been successful at controlling the steady state weld bead profile. However, transient conditions at the beginning and end of each weld have limited the ability to control the weld bead profile in these locations, and geometric accuracy suffers.

Depending on the desired geometric complexity, substrate positioners can be as simple as a 3-axis platform or as complex as a robotic arm or rotational table. To save money, process control can be used to deposit relatively complex features using only simple positioning equipment. If more complex features are required, a robotic arm in conjunction with process control can be used to deposit features at virtually any angle.

Advancements in GMAW metal transfer control have improved GMAW's WAAM abilities, and have the potential to be even more influential. The introduction of CMT has already allowed GMAW to weld with both high deposition rates and low heat input, which means components can be built rapidly and with lower residual stress. Other innovations in metal transfer control, specifically focusing on titanium, have created the possibility to additively manufacture titanium using GMAW.

Researchers have attempted to control nearly every aspect of WAAM with GMAW including weld bead profile, metal transfer, geometry, substrate release energy, and thermal conditions. However, limited research (if any) has focused on producing small geometric features with GMAW.

5. Theory of Present Research

As previously stated, this research's objective is to bridge the gap between powder and wire-based metal AM using GMAW. The goal can be achieved by developing an improved GMAW metal deposition strategy that reduces the deposition rate to allow maximum geometric resolution. The improved deposition strategy is composed of four components: single droplet deposition (SiDD), noncontact arc starting, electrode extension minimization, and laser arc stabilization.

5.1. Single Droplet Deposition (SiDD)

Typical GMAW AM processes use continuous weld beads to build components layer by layer. The first problem with continuous weld beads is that extreme transient conditions at the start and end of each bead lead to poor geometric accuracy at these locations. Even with complex adaptive control techniques, weld bead profile control is extremely difficult at the start and end of a weld bead [28].

Another problem with continuous weld beads is that a component's geometric resolution is limited by the width and minimum length of the weld bead. Because GMAW typically has a relatively high deposition rate, the only way to achieve a narrower weld bead is to increase the travel speed. Increasing the travel speed is not always practical and can lead to weld beads of poor quality and profile.

As with most metal AM, a common problem with components manufacture by WAAM with GMAW is residual stresses [42]. Residual stresses are the result of thermal cycles produced by continuous weld beads and their associated high deposition rates [45].

The proposed solution is to use single droplet deposition (SiDD) to deposit individual droplets instead of continuous weld beads. A similar technique was investigated that used PAW

to build components out of steel shot [52]. Because conditions would be largely the same for each drop, and because droplets could be placed in any given location in a build plane, there would be no start and end geometric inconsistencies.

In addition, geometric resolution would be limited only by the droplet diameter. Since each droplet would be small in diameter, small features could be produced on a component.

Lastly, because droplets could be placed anywhere on a given layer, residual stresses could be minimized. Instead of allowing excessive heat to build up in any given location, distributing the droplets would also distribute the heat input.

5.2. Noncontact Arc Starting

The only way to achieve SiDD is to use an alternative arc starting technique. Recall that typical GMAW processes start the arc with short circuiting arc starts. When the wire short circuits with the work piece, a large current spike melts the electrode, and the arc is started. The extremely high currents associated with a short circuiting arc start produce strong electromagnetic forces that essentially cause the electrode to explode. In a short circuiting arc start, a large portion of the electrode is either deposited in the weld pool or ejected as spatter.

From the description of a short circuiting arc start, it is evident that SiDD would not be possible if standard short circuiting arc starts were used. SiDD relies on the ability to form a single droplet on the electrode that can be transferred to the work piece. A short circuiting arc start itself often produces much more than a single droplet.

The feasibility of performing SiDD is completely dependent on the ability to develop an alternative arc starting method. The proposed solution is to use a noncontact arc starting technique that starts the arc without short circuiting the electrode to the work piece.

When the welding electrode is not in contact with the work piece before the arc is initiated, the shielding gas in the arc gap between the electrode and the work piece acts as an insulator. In an argon rich environment, the electric field strength needed to break down the gases in the arc gap is about 15kV/in (the dielectric strength of argon). Because the power source's open-circuit voltage is rated at 75V (typical for a welding power source), the electrode would have to be, at most, 0.005in from the work piece. Not only would it be difficult to repeatedly set the electrode 0.005in or less from the work piece, but also molten metal would instantly bridge the small arc gap and short circuit before the arc could be initiated.

GTAW processes have used noncontact arc starting extensively in applications where tungsten inclusions from lift or scratch starts are unacceptable. GTAW uses high frequency arc starters, which use high frequencies to generate extremely high voltages to break down shielding gas in the arc gap. Once gases in the arc gap have broken down and become conductive, lower welding voltages can maintain the arc, and welding current can flow.

The main problem with high frequency arc starters is that their high voltages and generated EMI (electromagnetic interference) can destroy electronics connected or in proximity to the welding system. Arc starters generate voltages on the order of 10kV to 50kV. Electronics, such as volt meters, connected to the welding circuit are not made to handle such large voltages. In addition to problems associated with physical contact to the welding system, arc starters generate significant amounts of EMI that can cause serial communication errors and even damage electronics. Because of problems inherent to high frequency arc starters, GTAW is typically a manual operation where few electronics are involved, and automated/robotic GTAW processes are uncommon.

Because GLADiS would be composed of many electronic devices, the first proposed noncontact arc starting solution is to use photoemission from the laser to start the arc (see section 5.4 for photoemission details). If sufficient photoemission could be generated, the welding process's open circuit voltage could be enough to initiate the welding arc.

If sufficient photoemission cannot be generated by the laser, a different arc starting technique will be employed. Alternative arc starting techniques include using a PAW pilot arc, performing a lift start, or using a high frequency arc starter. If a high frequency arc starter is used, GLADiS will have to be built to withstand it.

5.3. Electrode Extension Minimization

If it is desired to minimize deposition rate in a typical GMAW process, the WFS is simply reduced. With a reduced WFS, the welding current would also have to be reduced to reduce the melting rate. Recall the Lesnewich equation (1) [13]:

$$WFS = aI_A + b\ell_e I_A^2 \quad (1)$$

Looking at (1), it can be seen that if WFS is reduced, I_A can be reduced to maintain the equality. However, because current is the primary parameter that causes melting of both the electrode and the work piece, it would be possible to excessively lower the current. If the current is too low, a weld pool will not form on the work piece and the filler metal will not coalesce with the work piece. Therefore, the WFS and current cannot be significantly reduced.

However, the other parameter in (1) that can be controlled is the electrode extension, ℓ_e . It can be seen that if ℓ_e is reduced significantly, the WFS can also be reduced without having to lower the current.

Part of the improved deposition strategy in GLADiS is to deposit weld metal at reduced electrode extensions. The short electrode extension could allow the deposition rate to be minimized while still maintaining sufficient current for droplet/work piece coalescence.

5.4. Laser Arc Stabilization

To be emitted from a metal surface and form a welding arc, electrons must have enough energy to overcome the work function. The work function is the amount of energy required to remove an electron from the surface. Electrons can be emitted from a metal surface by three different mechanisms. Emission mechanisms include thermionic emission, field emission, and photoemission.

Thermionic emission occurs at extremely high temperatures. When the temperature is high enough, some electrons can have sufficient energy to overcome the work function. Because thermionic temperatures are above the melting temperature of steel, thermionic emission is not a significant source of emission in consumable electrode processes like GMAW.

Field emission relies on extremely strong electric fields to pull electrons from the surface. Fields strengths of 10^8V/m to 10^9V/m can be required. Although the overall electric field strength across a typical welding arc is on the order of 10^3V/m , different regions within the arc can have much higher field strengths. In addition, extremely thin oxide layers on a metal surface with even a small voltage potential across them can result in electric field strengths sufficient for field emission.

Photoemission is typically not a significant source of electrons in welding arcs. Photoemission occurs when a photon transfers sufficient energy to an electron for the electron to overcome the work function. Metals have low quantum efficiencies, which means that few electrons are emitted per photon absorbed.

Although metals have a low quantum efficiency, the extremely large fluence of photons in a laser beam can result in considerable photoemission. In addition, the quantum efficiency can be increased by using a laser with a short wavelength. Lasers with short wavelengths have higher photon energies, and therefore, more electrons are emitted.

Recall that cathode spots form on welding cathodes and can cause arc instability with DCEP polarity. Shinn et al. used a high powered infrared laser to stabilize the cathode spot in titanium GMAW [11]. However, the principle they relied on to stabilize the cathode spot was enhanced metal evaporation caused by the laser's thermal energy [11].

The present research also proposes to use a laser for arc stabilization. However, instead of using a high powered infrared (1064nm) laser to enhance metal evaporation, a lower power, short wavelength laser (532nm) will be used to generate photoemission.

Cathode spot motion is likely due to oxides on the metal surface that have lower work functions than the bare metal. As the arc decomposes the oxides, the cathode spot moves to new oxides where electrons can be emitted more easily.

If a laser of sufficiently short wavelength is focused on the work piece below the welding electrode, it could be possible to emit enough electrons from the work piece (cathode) to hold the cathode spot in place. Because the area where the laser is focused would be the most favorable location to emit electrons due to photoemission, the cathode spot would be fixed at that location.

As seen back in Figure 28 of Section 4.4, a weld bead's uniformity is highly dictated by arc stability. In AM applications, if an unstable arc is used, the component will have poor geometric accuracy and a rough surface finish. A stable arc, however, could produce high geometric accuracy and a smooth surface.

6. Equipment

GLADiS is composed of many different devices including a computer with analog and digital I/O (input/output), wire feeding system, welding power source, high-speed video imaging system, 3-axis motion system, high frequency arc starter, and a 200W 532nm laser. All GLADiS's devices are controlled by a control system operated by the computer.

6.1. Computer with Analog and Digital I/O

A computer running Linux with a C++ programming tool chain was used to control the various devices. Communications were established with each device using USB, RS-232, or PCI analog and digital I/O.

Analog and digital I/O was provided via a DAC (digital-to-analog converter) PCI card with digital I/O and a 16-bit ADC (analog-to-digital converter) PCI card. Both were inserted into the PCI slots in the computer. The PCI cards were isolated from physical devices through isolation modules. See Appendix A for the C++ class used to control the analog and digital I/O.

For analog input, Dataforth[®] SCM5B41-03 isolation modules were used. These modules have a -10V to 10V input range and a -5V to 5V output range. The -10V to 10V input voltage range means that any input voltage has to be scaled to fall within the range. Optimally, an input signal would be scaled such that the minimum value would scale to -10V and the maximum value would scale to 10V to take full advantage of the ADC's 16-bit resolution. The analog input modules have a 10kHz band width, which means they can accurately measure signals with frequencies up to 10kHz. They can protect the ADC card from voltages up to 1500V_{RMS}, and they themselves can withstand up to 240V_{RMS} without damage. The DAQ (data acquisition system) was composed of the analog input modules, ADC card, and DAQ software.

Dataforth SCM5B49-05 modules were used for analog voltage output isolation. The analog output modules have the same input and output range of -10V to 10V, and have a bandwidth of 400Hz. Similar to the analog input modules, the analog output modules can protect the DAC card from voltages up to 1500V_{RMS}, and can withstand up to 240V_{RMS} without damage.

Digital output isolation was provided by Grayhill Inc. 70-ODC5 modules. The digital output modules are basically normally open solid state relays (SSRs) that can withstand up to 60VDC and 3.5A on the output side. They have a turn-on time of 0.02ms and a turn-off time of 0.05ms and are controlled by a 5VDC input signal. The electronics enclosure housing the analog and digital I/O modules can be seen in Figure 30.

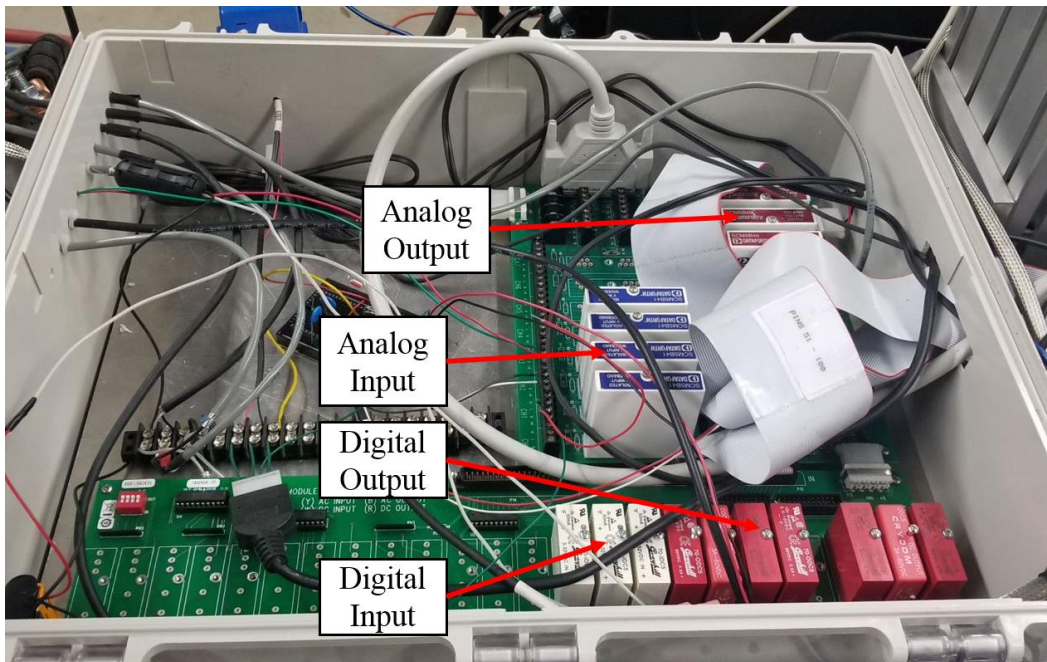


Figure 30: Analog and digital I/O isolation modules. The isolation modules isolated the computer's PCI cards from the process side of the system.

As seen in Figure 30, the isolation modules are connected to PCBs inside the electronics enclosure. The various devices are interfaced with the isolation modules through screw down terminals on PCBs.

Data acquisition was performed by writing a C++ code to sample inputs at the analog input modules. Originally, the DAQ code was written by placing parameter sampling commands within the process control code, which made the sampling frequency dependent on the process control code execution time. However, as the process control code became more complex, the DAQ code had to be modified. The new DAQ code was in the form of a C++ function that could run as a separate thread to the process control code. The DAQ thread was capable of sampling two inputs at around 20kHz. The DAQ function can be found in Appendix A.

6.2. Wire Feeding System

The original wire feeding system was composed of a wire feeder, wire feeder controller, and a wire feed speed (WFS) encoder as seen in Figure 31.

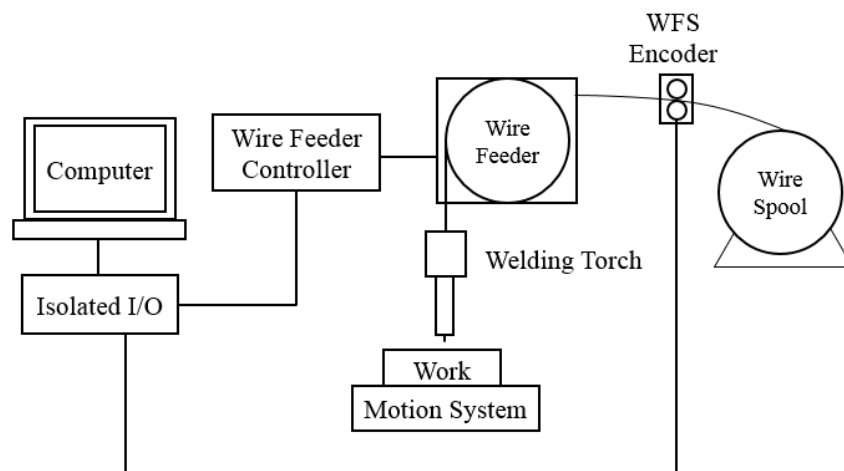


Figure 31: Wire feeding system block diagram. The wire feeder was controlled by the computer through the wire feeder controller. The WFS was measured using a WFS encoder.

The original wire feeder was a CWT[®] (Computer Weld Technology) WF-100 Capstan Wire Feeder (S/N 2560913001). It was connected to a CWT WFD-2 wire feeder controller (S/N 3860913001) that accepted an analog signal to control the WFS and two digital signals to control wire feed direction. To control the WFS, a 0V – 10V analog signal was sent from the computer’s DAC through the analog output isolation module to the wire feeder controller. The

controller was designed to linearly map the 0V – 10V signal to a nominal WFS of 5ipm – 300ipm. See Appendix B for the C++ class used to control the CWT wire feeder.

Wire was fed from a 33lb wire spool. The wire spool had a friction brake to keep consistent tension on the wire and to prevent spool momentum from slacking the wire when wire feed was stopped.

The actual WFS was measured using an optical encoder. The encoder's output signal was fed into the DAQ. Once the raw encoder signal was recorded, further processing was performed to determine the WFS. However, before the encoder could be used, its resolution (i.e. cycles per inch) had to be determined.

6.2.1. WFS Encoder Characterization

The encoder's output was a square-wave signal. The number of cycles in the encoder signal was proportional to rotational displacement of the encoder wheel and, therefore, length of wire fed through the encoder. The frequency of the encoder signal was proportional to the rotational velocity of the encoder wheel and, therefore, the WFS.

Determining the encoder's resolution required writing code to count cycles from the encoder. A hardware interrupt in C++ code was used to increment a counter on positive edges of the encoder's output signal. An MSP430G2553[®] microcontroller was used to implement the experiment.

With the encoder connected and the cycle counter code operational, a known length of wire (15 inches) was pulled through the encoder. Averaging the results of 10 trials, the number of cycles per inch was determined to be 100 cycles/inch.

6.2.2. Wire Feeding System Calibration

The first experiment was to determine the wire feeder controller's true relationship between the input voltage signal from the computer and the output WFS by developing a calibration curve. Using the calibration curve, the system could be calibrated to produce the correct WFS.

6.2.2.1. Procedure

The first step was to write a program that would start the wire feeder at a given command voltage, sample 5s of data, and stop the wire feed. The sampled data included a timestamp, the encoder's signal, and the command voltage.

An initial test showed the command voltage signal contained a large amount of noise. Further investigation using an oscilloscope showed the noise had a 0.4V amplitude. To mitigate the noise, a low-pass RC filter was placed on the analog output isolation module's output. Measurements with the oscilloscope showed that the filter effectively eliminated the noise problem.

Once the wire feeder control system was working properly, tests were performed at various wire feed speeds. Command voltages were chosen to produce wire feed speeds from about 20ipm to 300ipm in 20ipm increments for a total of 15 different tests. Once all the data were recorded, MATLAB[®] was used to process the results.

6.2.2.2. Results and Discussion

Before the actual WFS could be determined, MATLAB code had to be written to convert the encoder's signal into WFS. A sample of raw data from the encoder can be seen in Figure 32.

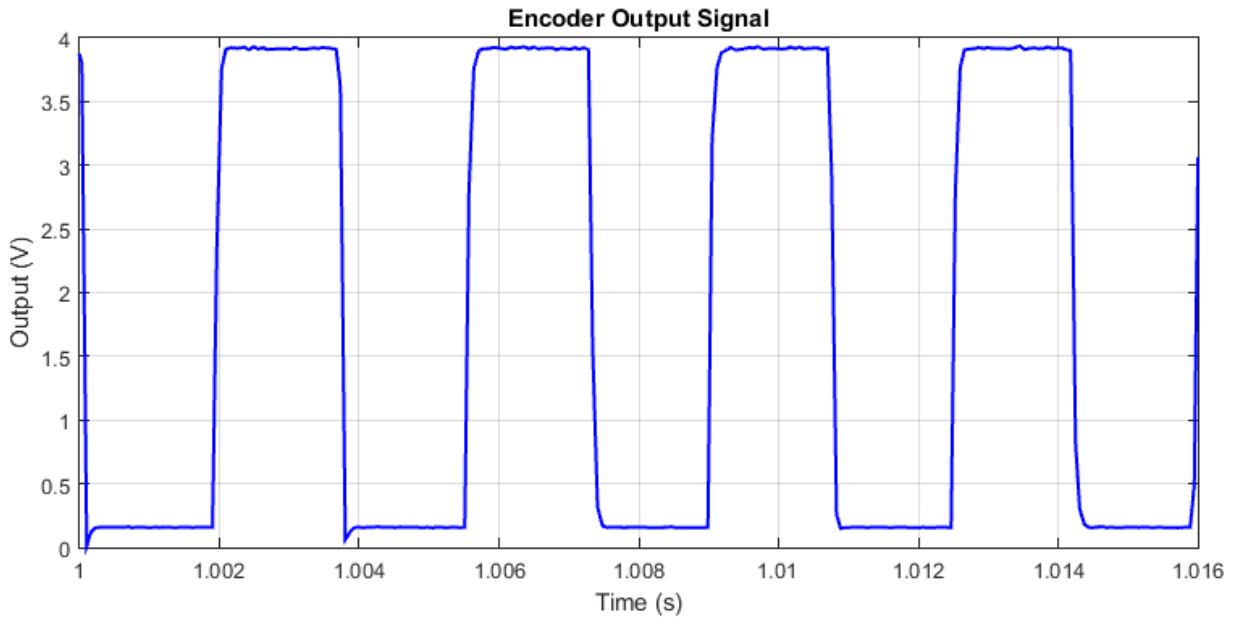


Figure 32: Sample of encoder data. The encoder output a square wave signal with a frequency proportional to the WFS.

As seen in Figure 32, the encoder signal is a square-wave signal that switches between approximately 0.2V and 3.9V. The frequency of the square wave signal is proportional to the WFS.

Time domain analysis was used to determine the WFS between each edge of the encoder's signal. Positive edges of the encoder signal are where the signal goes from a low value (logic 0) to a high value (logic 1), and negative edges are where the signal goes from a high value to a low value. The approach taken to find the WFS was to determine the time duration between each edge (positive and negative edges) of the signal and use the resolution value found in the encoder characterization test to determine WFS.

To find edges of the signal, the DC offset was first removed, resulting in a square-wave AC signal with a zero mean. The approximate locations of zero crossings were found by shifting the signal to the right by one term, multiplying the shifted signal by the unshifted signal, and finding where the product was less than zero. Products less than zero indicate that one of the

multiples was positive and one was negative which means a zero crossing must exist between the two factors.

Once approximate locations of the zero crossings were found, a linear least-squares regression analysis was performed on the five points surrounding the approximate zero crossings to interpolate a more precise zero crossing location. Figure 33 shows the encoder signal with the DC offset removed and the zero crossings located.

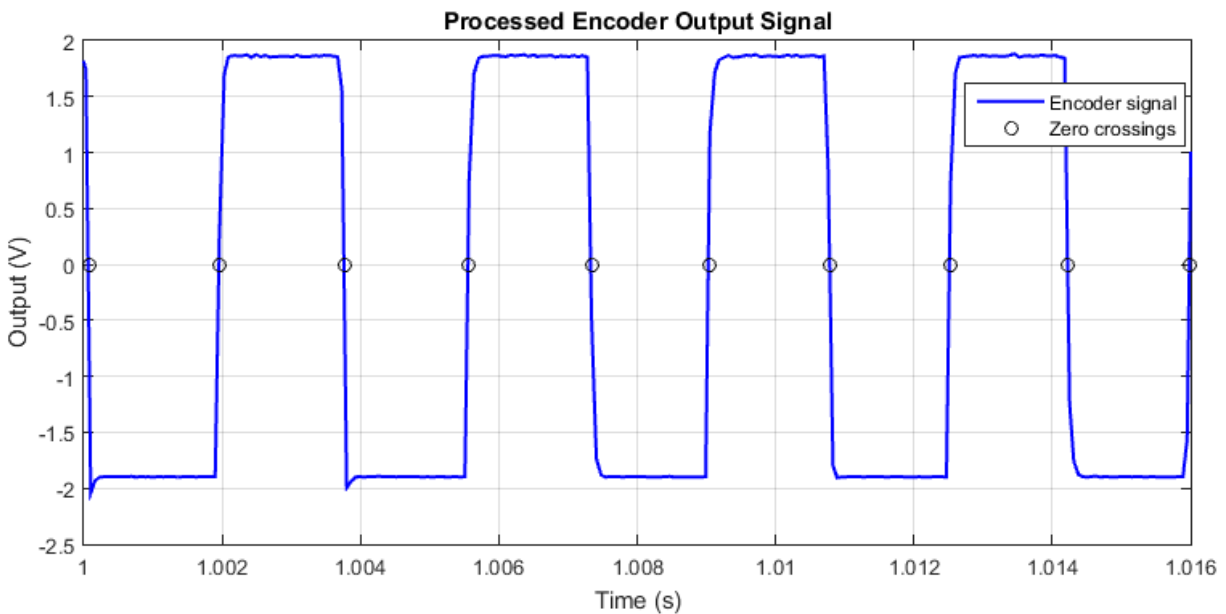


Figure 33: Processed encoder signal. The black circles indicate the zero crossings which were used to calculate the WFS.

As seen in Figure 33, the code could successfully locate the zero crossings. With the zero crossings located, the time between them could be determined and the WFS calculated.

Figure 34 shows the measured WFS and the nominal commanded WFS for each test. The nominal commanded WFS assumes a perfect linear relationship of 0V – 10V to 0ipm – 300ipm.

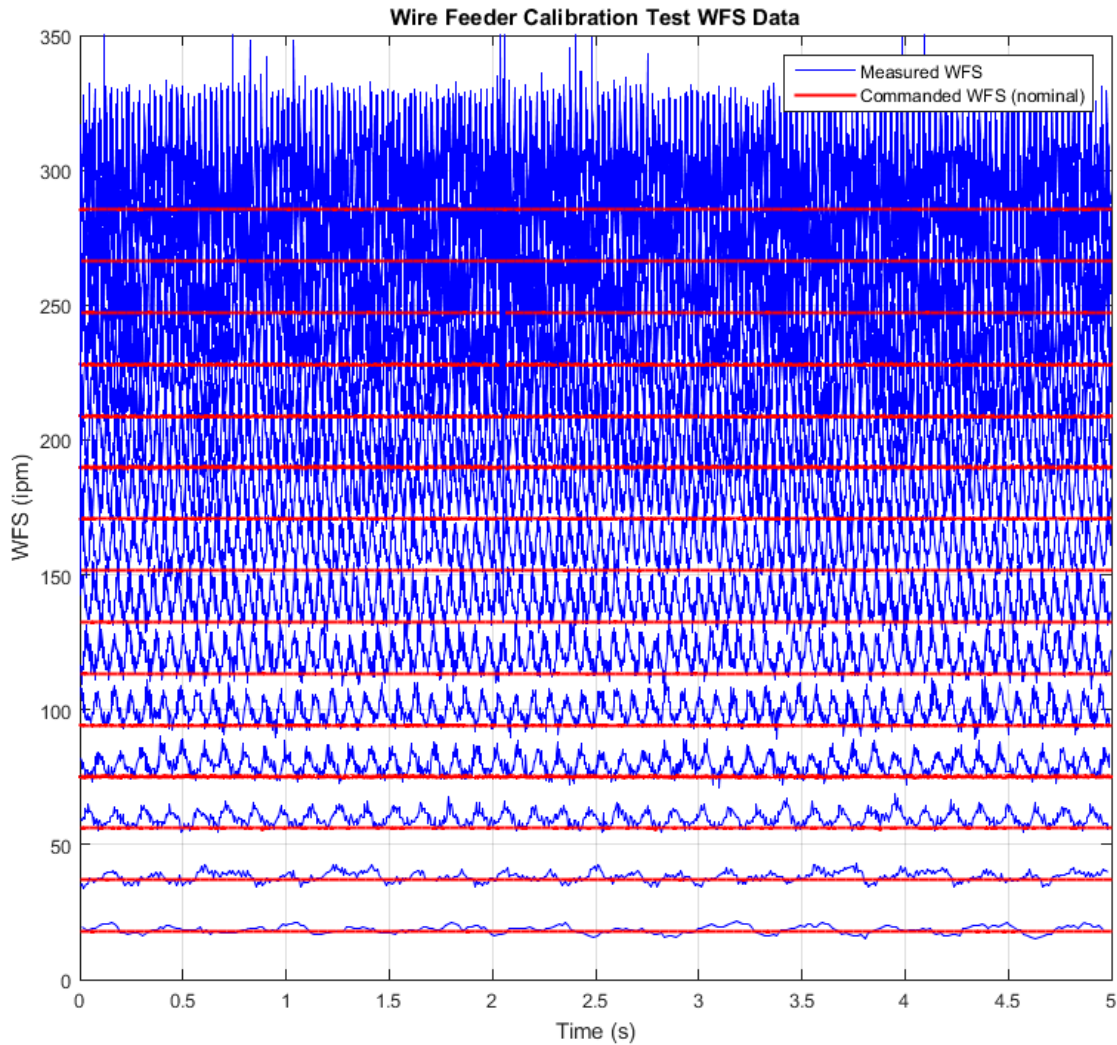


Figure 34: Wire feeder calibration test data.

It can be seen in Figure 34 that at low WFS, the commanded WFS agrees with the measured WFS. However, at higher WFS, the commanded WFS begins to deviate from the measured WFS. As the WFS increases, the level of noise in the WFS measurement also increases. The increased noise causes the data in Figure 34 to overlap above 150ipm.

With the actual command voltages and WFSs known for each test, a true relationship between command voltage and WFS could be determined. MATLAB was used to find the average WFSs and average command voltages for each test, and a LLS (linear least-squares)

model was built. Figure 35 shows the average WFSs plotted versus the average command voltages as well as the model representing the linear relationship between them.

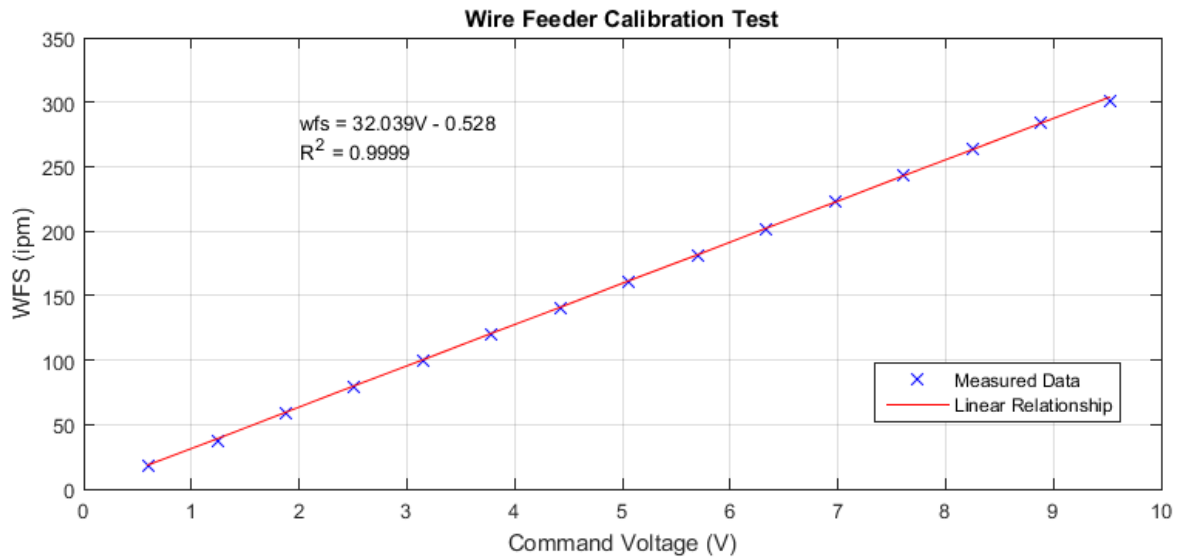


Figure 35: Wire feeder calibration test results. A relationship between input voltage and WFS was found by fitting a line to the experimental data.

As seen in Figure 35, the best fit line representing the relationship between input voltage and WFS closely matches the measured data ($R^2 = 0.9999$). The relationship between input voltage and WFS is shown in (3)

$$WFS = 32.039 \frac{ipm}{V} (v) - 0.528 ipm \quad (3)$$

where:

WFS = wire feed speed in inches per minute (ipm)

v = input voltage in volts (V)

See Appendix B for the MATLAB code used to process the wire feeding system calibration data.

6.2.3. Step Response

With the system calibrated, experiments could be performed to determine the wire feeder's step response. A step response test characterizes a system's ability to change from a low output to a high output and back. A system's step response can be quantified by the following parameters: percent overshoot (%OS), percent undershoot (%US), step-up settling time (T_{Su}), step-down settling time (T_{Sd}), peak time (T_P), low time (T_L), rise time (T_R), and fall time (T_F). Figure 36 shows an example of a theoretical step response and its parameters.

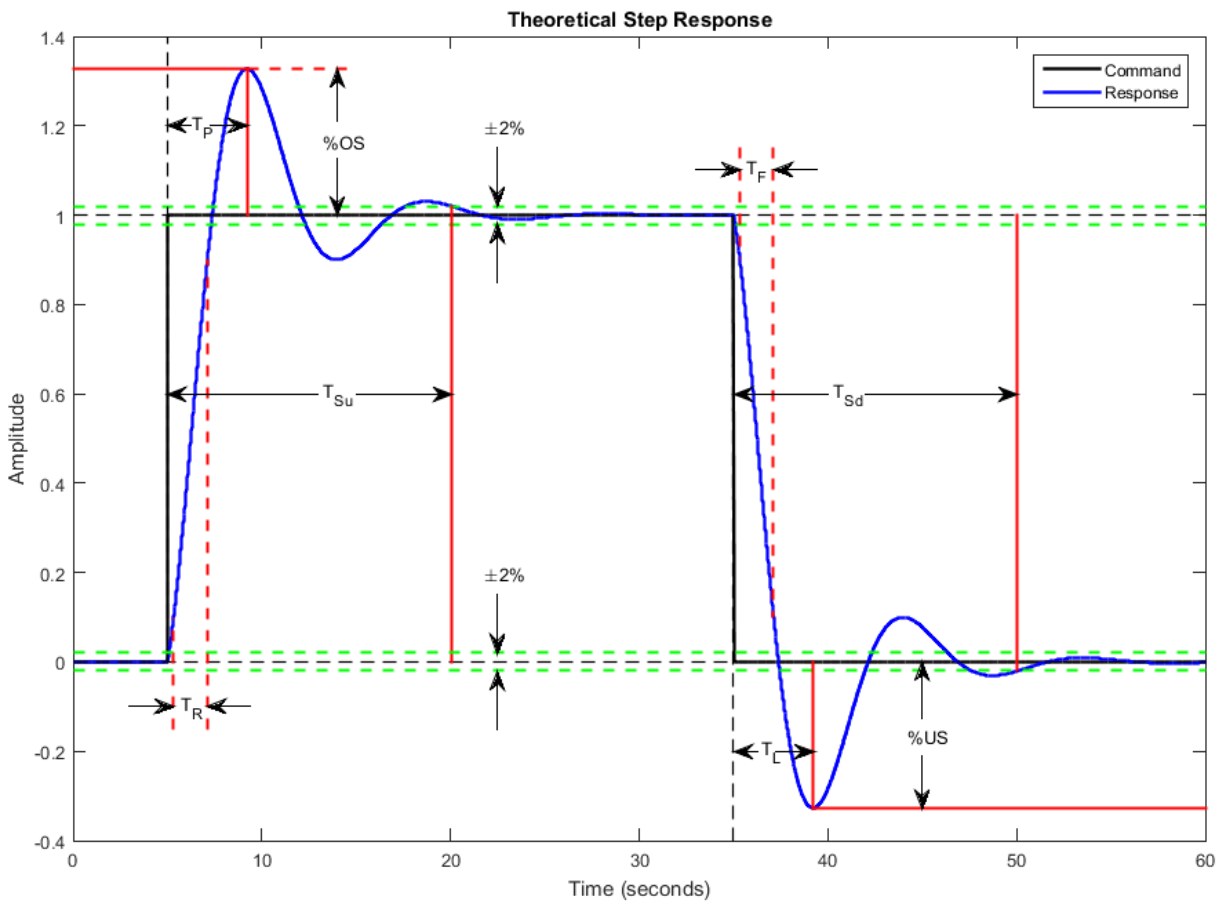


Figure 36: Theoretical step response and step response parameters.

As seen in Figure 36, at 5s the command, represented by the solid black line, steps up from the initial value of 0 to the final value of 1. At 35s the command steps from 1 back to 0. The blue line represents the system's response to the changing input.

The %OS is a measure of how far the system's response exceeds the command after the step-up, and the %US is a measure of how far the response falls below the command after the step-down. T_{Su} is a measure of how long it takes the response to settle within $\pm 2\%$ of the step size after the step-up, and T_{Sd} is a measure of how long it takes the response to settle within $\pm 2\%$ of the step size after the step-down. T_P is a measure of the time it takes before the response reaches its peak overshoot after the step-up, and T_L is a measure of the time it takes before the response reaches its lowest undershoot value after the step-down. T_{Su} and T_P are referenced from the time when the step-up occurred, and T_{Sd} and T_L are referenced from the time when the step-down occurred. T_R is a measure of how long it takes the response to increase from 10% to 90% of the step size after the step-up, and T_F is a measure of how long it takes the response to decrease from 90% to 10% of the step size after the step-down,.

6.2.3.1. Procedure

A program was written to feed wire at 10ipm for 2s, step the WFS up to 100ipm for 2s, and step the WFS back down to 10ipm for another 3s. Both the commanded and measured WFS were sampled throughout the test. The WFS was stepped from 10ipm to 100ipm instead of 0ipm to 100ipm because the WFS encoder does not output any signal at 0ipm and it cannot determine WFS direction, making it impossible to characterize the wire feeder's behavior before and after the step changes. The experiment included a step down as well as a step up so that the wire feeder's acceleration and deceleration characteristics could be compared.

Once the 90ipm step change (10ipm to 100ipm) data was recorded, the experiment was repeated for a 180ipm step change to see how the parameters were affected.

6.2.3.2. Results and Discussion

The wire feeder's step response can be seen in Figure 37.

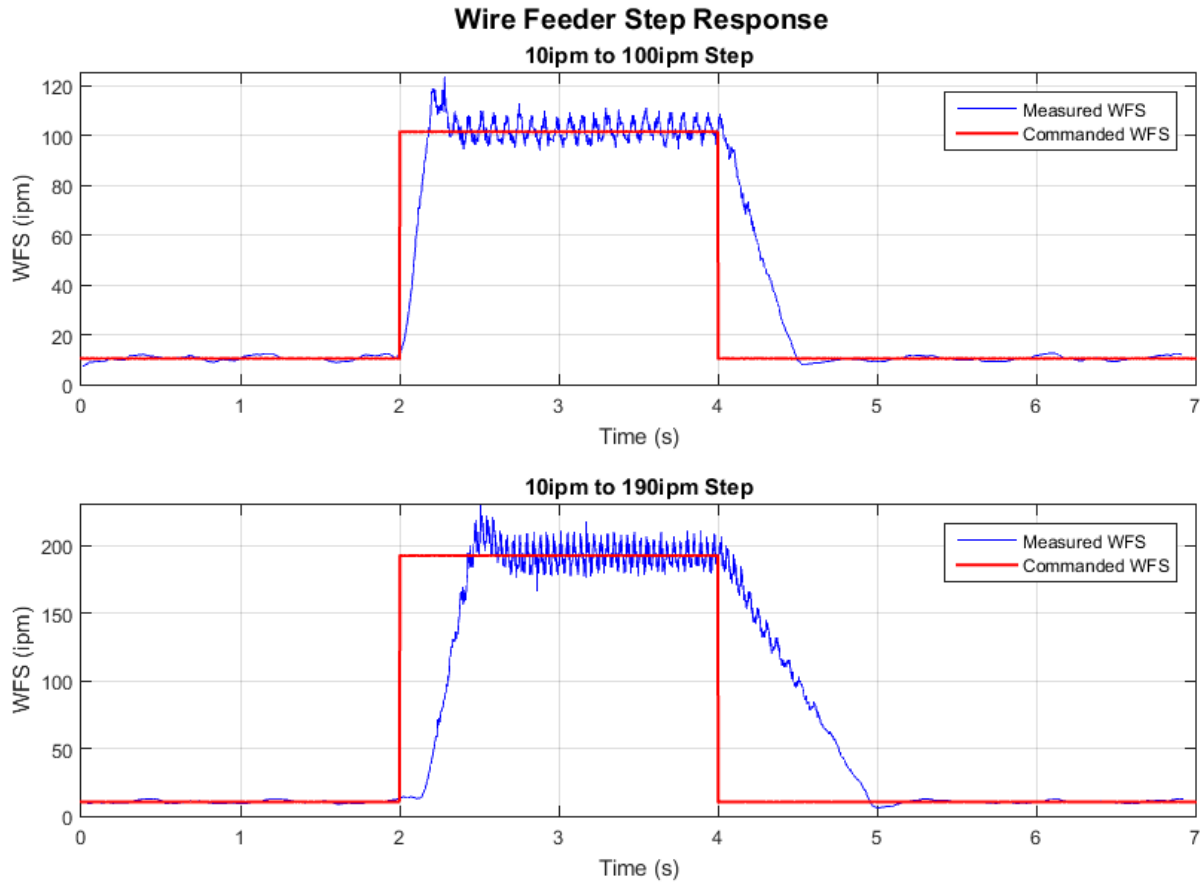


Figure 37: Wire feeder step response to a 90ipm step and a 180ipm step.

As seen in Figure 37, the wire feeder appears to behave differently at the two different step sizes. Doubling the step size resulted in nearly doubling the rise time (T_R), indicating that the wire feeding system is non-linear with a fixed acceleration. It can also be seen that it takes the wire feeder longer to slow down from a higher WFS to a lower WFS than to speed up from a lower WFS to a higher WFS. Table I contains the measured step response parameters.

Table I: Wire feeder step response parameters: percent overshoot (%OS), percent undershoot (%US), step-up settling time (T_{Su}), step-down settling time (T_{Sd}), peak time (T_P), low time (T_L), rise time (T_R), and fall time (T_F).

Step Size	%OS	%US	T_{Su} (s)	T_{Sd} (s)	T_P (s)	T_L (s)	T_R (s)	T_F (s)
90ipm	13.6%	2.5%	0.34	0.61	0.25	0.53	0.13	0.36
180ipm	9.5%	2.5%	0.68	1.05	0.54	1.00	0.25	0.73

As seen in Table I, doubling the step size resulted in approximately doubling all the parameters except for %OS. The %OS actually was less on the larger step. It can also be seen that T_F exceeds T_R by nearly three times for a given step size. Note that the values in Table I are only estimates from the noisy WFS measurements. MATLAB code used to process the step response data can be found in Appendix B.

6.2.4. Frequency Response

With the wire feeder's step response characterized, experiments could be performed to determine its frequency response.

6.2.4.1. Procedure

For the frequency response test, a function generator was used rather than the computer to drive the wire feeder controller. An oscilloscope was used to set the function generator to the desired wire feeder controller input.

Code was written to sample the input signal from the function generator and the encoder's output signal through the computer's analog input modules. A program was made to enable the wire feeder, collect 5s of data, and stream the data, along with a time stamp, to a csv file.

The first experiment was a variable frequency test where the input signal's frequency was increased from 0Hz to 8Hz by manually rotating the frequency adjustment dial on the function generator. The function generator was set to control a 33.5ipm amplitude sinusoidal WFS with a 132.5ipm DC offset. The results of the variable frequency test would be a time domain representation of the wire feeder's frequency response.

The second experiment was to record WFS data at discrete frequencies. Knowing the wire feeder's response at discrete frequencies would simplify the frequency domain analysis.

Once again, the function generator was used to control the wire feeder. The desired output was a sinusoidal WFS with approximately a 200ipm DC offset and an amplitude equal to 10% of the DC offset.

Using the same data sampling program used in the variable frequency test, the discrete frequency test was performed for 46 different frequencies ranging from 0.2Hz to 12.5Hz.

Once the data were collected, it was processed in MATLAB to determine the frequency response. Data were processed by fitting sinusoidal models to the data from each frequency test, determining the gain and phase of each model, and plotting the results in a Bode plot.

6.2.4.2. Results and Discussion

Analysis took place in both time and frequency domains. The time domain representation of the wire feeder's frequency response provides a visual sense of how the wire feeder responds to different frequencies. The frequency domain analysis provides a quantitative account of the wire feeder's frequency response.

6.2.4.2.1. Time Domain Analysis

Time domain analysis was performed using data from the variable frequency test where the frequency was swept from 0Hz to 8Hz throughout the test. Figure 38 shows the time domain representation of the wire feeder's frequency response.

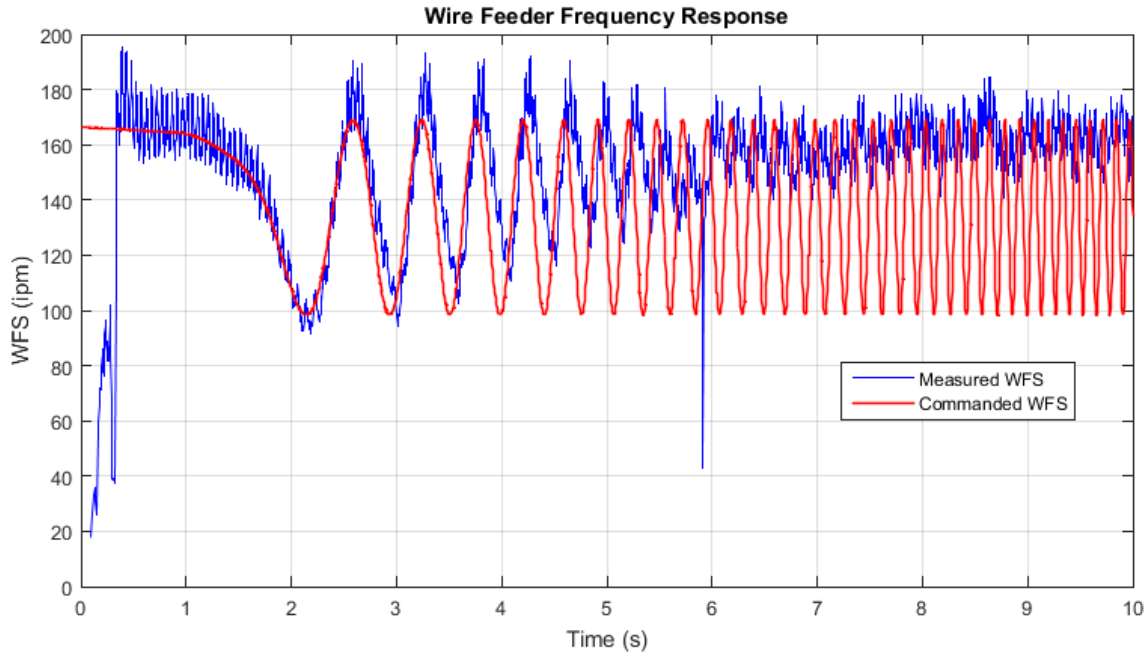


Figure 38: Time domain representation of the wire feeder's frequency response. As the frequency is increased from 0Hz to 8Hz, the wire feeder becomes less effective at tracking the commanded WFS.

As seen in Figure 38, the measured WFS appears to track the commanded WFS at low frequencies. However, as the frequency increases, the wire feeder begins to have difficulty keeping up with the commanded WFS. As expected, the measured WFS begins to lag the commanded WFS as well as decrease in amplitude. The DC offset also appears to increase at the frequency increases indicating that the wire feeder speeds up faster than it slows down, which was shown explicitly in the step response test.

It can be seen that the measured WFS signal in Figure 38 exhibits a great deal of noise. The noise is significant enough to make it impossible to take accurate measurements on the variable frequency test data.

MATLAB code used to process the data in the time domain can be seen in Appendix B.

6.2.4.2.2. Frequency Domain Analysis

The goal of the frequency domain analysis is to quantify the time domain results shown in Figure 38 by creating a Bode plot. The general approach to creating a Bode plot is to compare the amplitudes and phases of the commanded WFS and the measured WFS at various frequencies and plot the results. Although the time domain plot in Figure 38 shows the general trend of amplitude and phase as frequency is increased, a Bode plot will show exactly how much the amplitude and phase change with increasing frequency.

Because of all the measurement noise (demonstrated in Figure 38), the raw data from the discrete frequency tests could not be used directly to create an accurate Bode plot. To create the best possible Bode plot in a least-squares sense, models representing the commanded and measured WFS were fit to each data set.

Models were fit to the data using the Levenberg-Marquardt NLLS (nonlinear least-squares) algorithm. Because the WFS was sinusoidal, the general model for each experiment is given by (4):

$$\widehat{WFS}_k = A \sin(\omega t_k + \theta) + D \quad (4)$$

where:

\widehat{WFS}_k = estimated WFS (ipm)

A = amplitude (ipm)

ω = frequency (rads/s)

t_k = time (s)

θ = phase (rad)

D = DC offset (ipm)

k = indexing variable

In NLLS analysis, initial guesses have to be made for parameters that enter non-linearly in the model. Notice that the model in (4) has two parameters that enter non-linearly: frequency and phase. Because more than one parameter enters non-linearly, NLLS analysis would be required to solve for multiple parameters. Not only is using NLLS for multiple parameters computationally inefficient, but it also makes it difficult to make initial guesses for the parameters (especially when writing code to make its own initial guesses).

To make the model-fitting algorithm more efficient and the algorithm for making initial guesses more robust, the model in (4) was manipulated using the following trigonometric identity:

$$\cos(\alpha + \beta) = \cos(\alpha) \cos(\beta) - \sin(\alpha) \sin(\beta) \quad (5)$$

Using (5), (4) can be rewritten as follows:

$$\widehat{WFS}_k = A \cos(\omega t_k) \cos(\theta) - A \sin(\omega t_k) \sin(\theta) + D \quad (6)$$

Then, if

$$B = A \cos(\theta) \quad (7)$$

and

$$C = -A \sin(\theta) \quad (8)$$

(6) can be rewritten as:

$$\widehat{WFS}_k = B \cos(\omega t_k) + C \sin(\omega t_k) + D \quad (9)$$

Notice that in (9), only the frequency is entered non-linearly. B, C, and D all enter linearly. The NLLS algorithm can solve exclusively for the frequency, and B, C, and D can be solved for at each iteration of the NLLS solver using a LLS (linear least-squares) method. B and C can then be used to find amplitude (A) and phase (θ) as follows.

$$B = A \cos(\theta) \Rightarrow A = \frac{B}{\cos(\theta)} \quad (10)$$

$$C = -A\sin(\theta) = -\frac{B}{\cos(\theta)}\sin(\theta) = -B\tan(\theta) \Rightarrow -\frac{C}{B} = \tan(\theta)$$

$$\theta = \tan^{-1}\left(-\frac{C}{B}\right) \quad (11)$$

MATLAB code was written to make initial guesses and calculate final parameters for the new model. Figure 39 shows an example of data from one of the discrete frequency tests compared to the NLLS model.

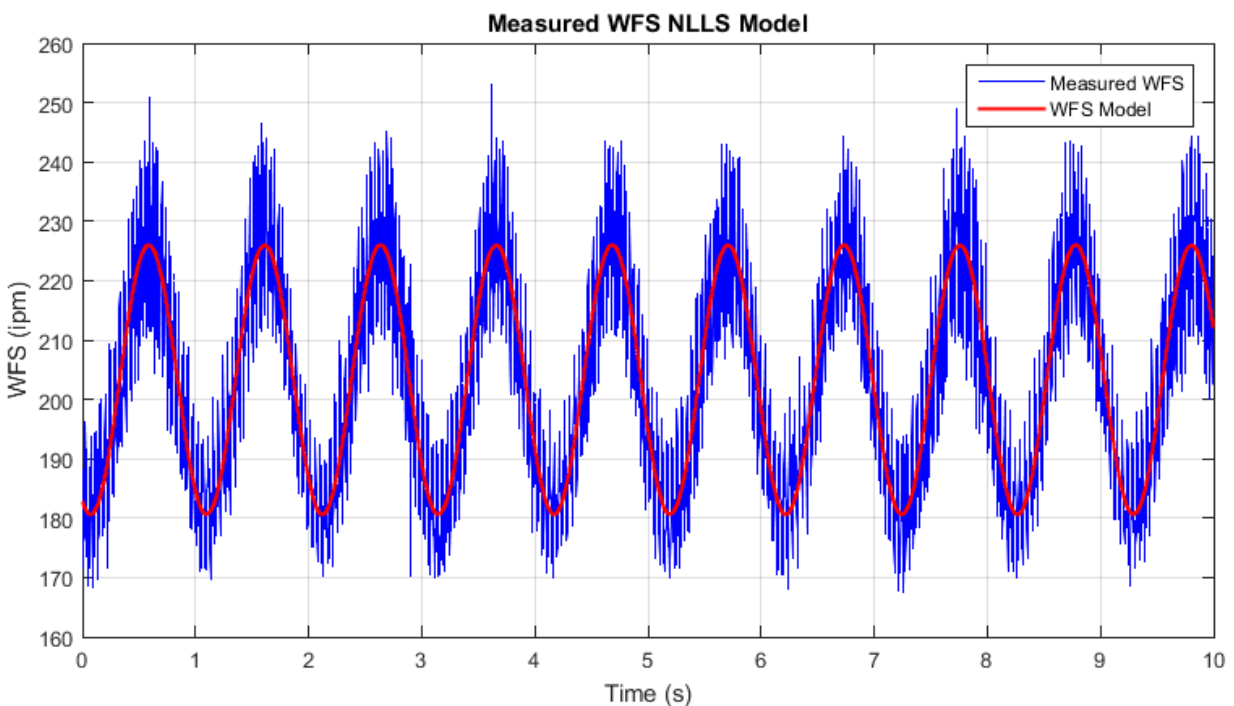


Figure 39: Noisy WFS data compared to NLLS WFS model.

As seen in Figure 39, the NLLS model appears to accurately represent the noisy measured WFS signal.

Each of the 46 different frequency tests were modeled using the NLLS procedure. Both the commanded and measured WFS were modeled for each test. An example of one of the modeled experiments can be seen in Figure 40.

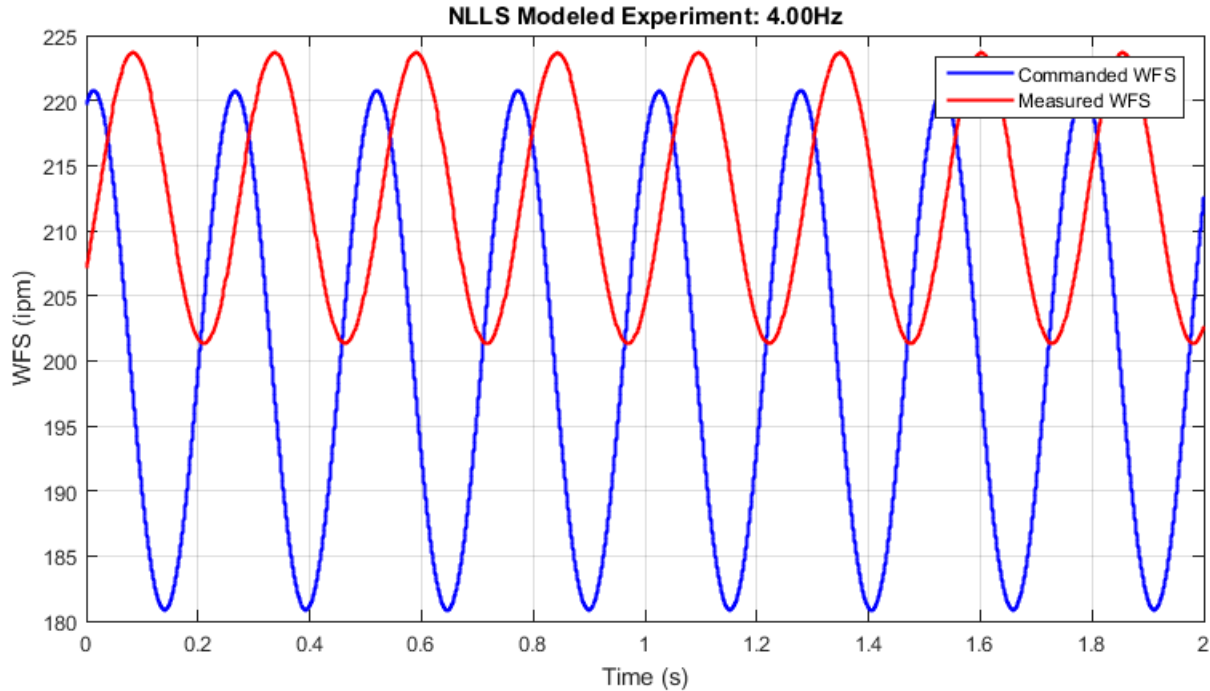


Figure 40: NLLS modeled experiment at 4.00Hz.

As seen in Figure 40, the measured WFS model shows a suppressed amplitude and a delay (phase shift) compared to the commanded WFS model. The two models also appear to have a different DC offset, which is consistent with the system's behavior at higher frequencies in the variable frequency test.

The change in amplitude and the phase shift was calculated for each test using the model parameters. The result is shown in the Bode plot in Figure 41.

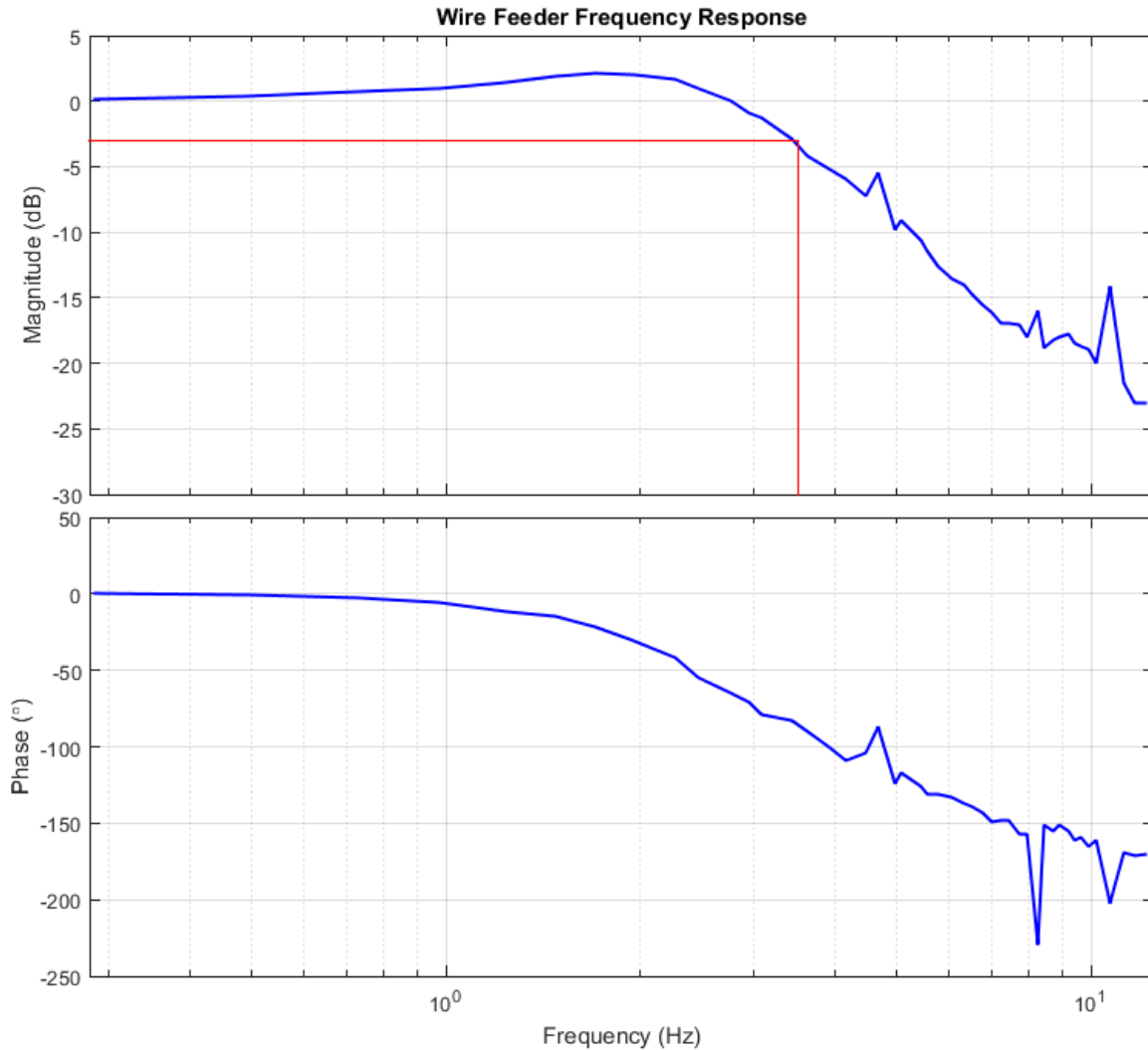


Figure 41: Wire feeder frequency response. The red line shows the wire feeder's corner frequency is at about 3.5Hz, indicating that the wire feeder can track a control signal up to 3.5Hz with reasonable accuracy.

As seen in Figure 41, the wire feeder has no change in amplitude or phase shift at low frequencies. As the frequency increases from about 0.5Hz to 2Hz, the amplitude increases. The amplitude then begins to decrease with further increase in frequency. The phase slowly decreases across the range of input frequencies.

In Figure 41, the red line shows a 3dB drop in magnitude, which occurs at about 3.5Hz. A 3dB drop indicates that the actual WFS has diminished to about 70% of the commanded WFS. The phase shift at 3.5Hz is about -83° . The interpretation of Figure 41 is that the wire feeder has

a 3.5Hz bandwidth when operating under similar wire feeding conditions to the test, meaning it can follow an input changing up to 3.5 times per second without losing more than 30% of its amplitude and it lags by less than 83° or 66ms.

The MATLAB code used to process data for the discrete frequency tests can be found in Appendix B.

6.3. Welding Power Source

The welding power source was composed of three Liburdi® Puls weld® P200-004 power sources connected in parallel (S/Ns 002701, 960901, and 091303). Each power source was controlled using analog and digital voltage signals from the computer's I/O. A schematic of the welding power source configuration can be seen in Figure 42

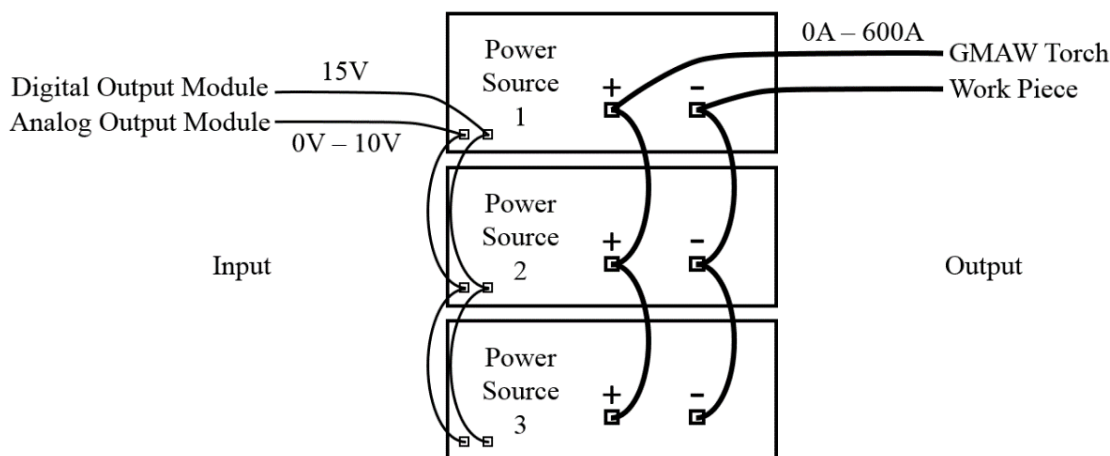


Figure 42: Welding power source configuration. The individual welding power sources are controlled by analog and digital signals from the output isolation modules. The parallel connection of welding power sources can output a total of 0A-600A.

Each individual power source in Figure 42 could supply 0A – 200A, for a total of 0A – 600A, with a 0V – 10V control input voltage. The 0V – 10V control signal came from one of the analog output isolation modules connected to the computer's DAC card. Each welding power source also had a 15V arc enable input that was connected to a digital output isolation

module controlled by the computer's digital I/O card. The C++ class used to control the welding power source can be seen in Appendix C.

The welding power source's current output was measured using a LEM[®] LT 505-S/SP4 current transducer. The current transducer had a 150kHz bandwidth and could measure currents from -1400A to 1400A. A physical connection to the welding circuit was not required because the current transducer operated using the Hall Effect. The current transducer's output was a current that had a 1:5000 ratio to its input current (from the welding power source).

To obtain data from the current transducer, the transducer's output was fed through a resistor to convert the current signal into a voltage signal that could be measured using the computer's ADC. A resistor with an approximate resistance of 83Ω was chosen to produce a voltage difference of about 0V – 10V with an input current of 0A – 0.12A, which was the 1:5000 scaled version of the 0A – 600A welding power source current. The voltage across the resistor was fed into one of the analog input isolation modules.

The welding power source's voltage was also monitored. The voltage was measured between the work piece and the welding torch (as close as possible to the arc voltage). Because the welding power source's maximum open circuit voltage was rated at 75V, and the analog input isolation modules could only read up to 10V, a voltage divider circuit was built to scale a 75V signal down to 10V. The voltage divider circuit's output was fed directly into an analog input isolation module.

6.3.1. Step Response

The first test to characterize the welding power source was a step response test. All tests were conducted using a GTAW torch connected to the power source. A GTAW torch was used to simplify the testing procedure because no wire feed would be required.

Initially, the step response test was performed similar to the wire feeder step response test, which involved using a signal from the analog output isolation module to control the step change input signal. However, after examining initial results, it was clear that the analog output isolation module's step response was inadequate due to its 400Hz rated bandwidth. Results of the initial test can be seen in Figure 43.

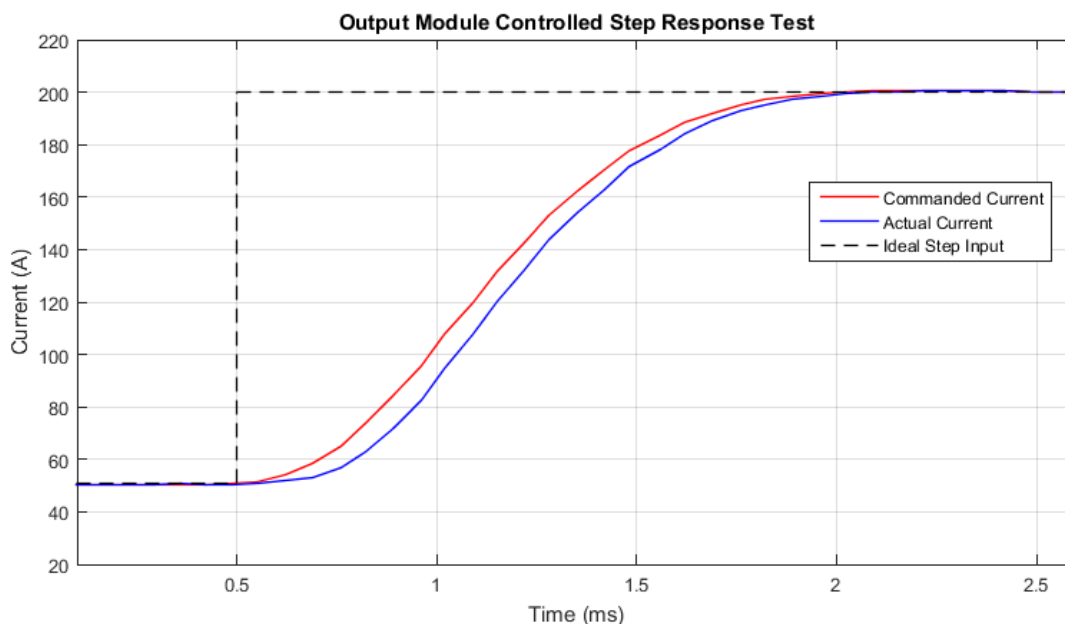


Figure 43: Power source step response test using analog output isolation module control. The power source's step response is at least as fast as the analog output isolation modules step response.

In Figure 43, the black dotted line represents what an ideal step command should look like. It can be seen that the commanded current (red signal) from the analog output isolation module does not behave like an ideal step. It takes the output module about 1.5ms to rise from the 50A command to the 200A command. The output module's speed limitation was not evident in the wire feeder step response test because the system (wire feeder) was much slower than the output module (i.e., wire feeder's 3.5Hz bandwidth versus module's 400Hz bandwidth).

Although the output module's speed was sufficient for the wire feeder step response test, it was not fast enough for the welding power source step response test. In fact, Figure 43 shows

that the welding power source can follow a step change at least as fast as the output module can, indicating that the welding power source had at least a 400Hz bandwidth (rated bandwidth of output module). Because of the output module's speed limitation, a different procedure was required to measure the welding power source's step response.

6.3.1.1. Procedure

The first step was to configure a high-speed function generator to control the welding power source. Using an oscilloscope to measure the function generator output, the function generator was set to output a square wave signal from approximately 0.8V to 5V to control a step from about 50A to 300A. The frequency and duty-cycle were adjusted such that the pulse duration (time between a positive and subsequent negative edge) was just under 2.5ms. The pulse duration was selected to allow the step-up response and the step-down response to be captured with one oscilloscope reading.

The function generator was connected to the welding power source's control input, and the oscilloscope was connected to both the function generator output and the current transducer output. Code was written to enable the arc for 10s to allow time to manually start the arc and to collect data.

6.3.1.2. Results and Discussion

The welding power source's step response can be seen in Figure 44.

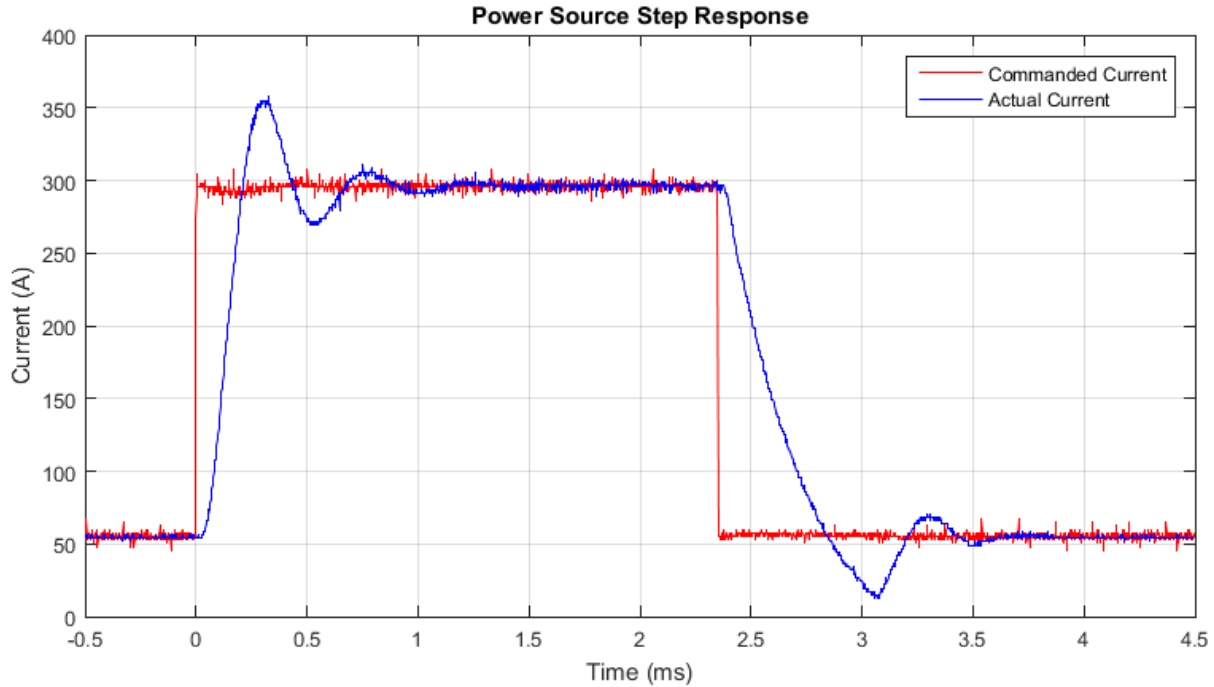


Figure 44: Power source step response using a high-speed function generator to produce the control signal.

As seen in Figure 44, the step command from the function generator (red signal) is a nearly ideal step demonstrated by nearly instantaneous step changes. The welding power source's step response is characteristic of a typical underdamped system with some overshoot and damped oscillations. Similar to the wire feeder, the welding power source responds differently to a step-up versus a step-down. Table II contains step response parameters obtained from the data in Figure 44.

Table II: Welding power source step response parameters: percent overshoot (%OS), percent undershoot (%US), step-up settling time (T_{Su}), step-down settling time (T_{Sd}), peak time (T_P), low time (T_L), rise time (T_R), and fall time (T_F).

Step Size	%OS	%US	T_{Su} (ms)	T_{Sd} (ms)	T_P (ms)	T_L (ms)	T_R (ms)	T_F (ms)
250A	24.4%	16.7%	0.87	1.19	0.31	0.72	0.13	0.36

It can be seen that T_R is nearly three times as fast as T_F . The %OS is also significantly more than the %US. Comparing the welding power source's step response parameters to the wire feeder's step response parameters shows that the rise and fall times are about 1000 times

faster for the welding power source. MATLAB code used to process the welding power source step response data can be found in Appendix C.

6.3.2. Frequency Response

The welding power source's frequency response test was performed similarly to the wire feeder's frequency response test. The function generator was once again used to provide the input control signal to the welding power source. A DAQ system was to be used to measure and record the commanded current as well as the actual current for various frequencies. With data collected over a range of frequencies, a frequency response characterization could be completed.

6.3.2.1. Procedure

It was initially speculated that the welding power source's bandwidth would be greater than 10kHz. However, the analog input isolation module connected to the current transducer's output circuit had a bandwidth of only 10kHz. In addition, the sampling frequency of the computer's DAQ system was found to be about 15.2kHz, making the Nyquist frequency (f_N) about 7.6kHz. Because of the isolation module's limited bandwidth and the 7.6kHz Nyquist frequency, it was decided that a different DAQ system (an oscilloscope) had to be used to measure a greater than 10kHz signal.

An oscilloscope was connected to both the function generator's output and the current transducer's output to visually compare the welding power source's input/output relationship. The function generator was adjusted to control the welding power source to output a sinusoidal current with a 100A DC offset and an amplitude of about 15% of the offset ($\pm 15A$). A GTAW torch was connected to the welding power source rather than a GMAW torch to simplify the characterization process. Once the computer enabled the welding power source, the arc was manually lit by using a tungsten electrode to short circuit the welding electrode to the base plate.

The same magnitude function generator signal (same amplitude and DC offset, different frequencies) and arc starting technique was used for all the experiments.

An initial visual test was performed by increasing the control signal's frequency and observing the effects on the oscilloscope display. It was observed that the amplitude of the welding power source's current was significantly suppressed compared to the commanded current amplitude at frequencies above 5kHz. Because it appeared that the welding power source's bandwidth was less than 7.6kHz (the Nyquist frequency), it was decided that the computer's DAQ system was adequate for sampling data for the frequency response tests.

6.3.2.1.1. Variable Frequency Test

The first test was a variable frequency test where the frequency was increased from about 10Hz to 6kHz by manually adjusting the frequency control on the function generator over a 10s period. The variable frequency test was performed to generate a time domain representation of the welding power source's frequency response.

The code used to collect data was written to enable the arc, wait 5s, record data for 10s, and disable the arc. The 5s wait between enabling the arc and recording data was to provide sufficient time to manually light the arc. The sampled data included a time stamp for each measurement, the commanded current from the function generator, and the measured current from the current transducer.

Once the data were collected, it could be processed in MATLAB to generate a time domain representation of the welding power source's frequency response.

6.3.2.1.2. Discrete Frequency Test

The next experiment was to test the welding power source at discrete frequencies to simplify the frequency domain analysis. The same code and procedure used in the variable

frequency test was used for each discrete frequency tested. The only difference was that only 5s of data were collected.

The experiment consisted of 33 different frequencies ranging from 1Hz to 7.5kHz (just under the Nyquist frequency). Lower frequencies were selected based on a logarithmic scale (e.g., 1Hz, 10Hz, 100Hz) because only insignificant changes in amplitude and phase were observed at low frequencies. Once a larger change in amplitude was observed, the frequencies were selected based on a linear scale in 100Hz or 250Hz increments to increase precision. When a significant drop in amplitude was observed, the precision was further increased to 50Hz increments. When the drop in amplitude between frequencies started to decrease, the precision was reduced to 500Hz increments for the rest of the experiment.

6.3.2.2. Results and Discussion

Data collected for the variable frequency test and the discrete frequency test were processed using MATLAB. See Appendix C for MATLAB code used for data processing.

6.3.2.2.1. Variable Frequency Test

Plotting results from initial tests of the DAQ system showed that at low frequencies or DC, the measured current from the current transducer circuit was 2.87% less than the commanded current. The commanded current appeared to be in agreement with the built in analog ammeters on the Puls weld power sources, indicating that the measured current was not correct. Because the error in measured current was most likely due to the resistor in the current transducer circuit, the measured current was simply scaled up by 2.87%.

The raw data from the variable frequency test can be seen in Figure 45.

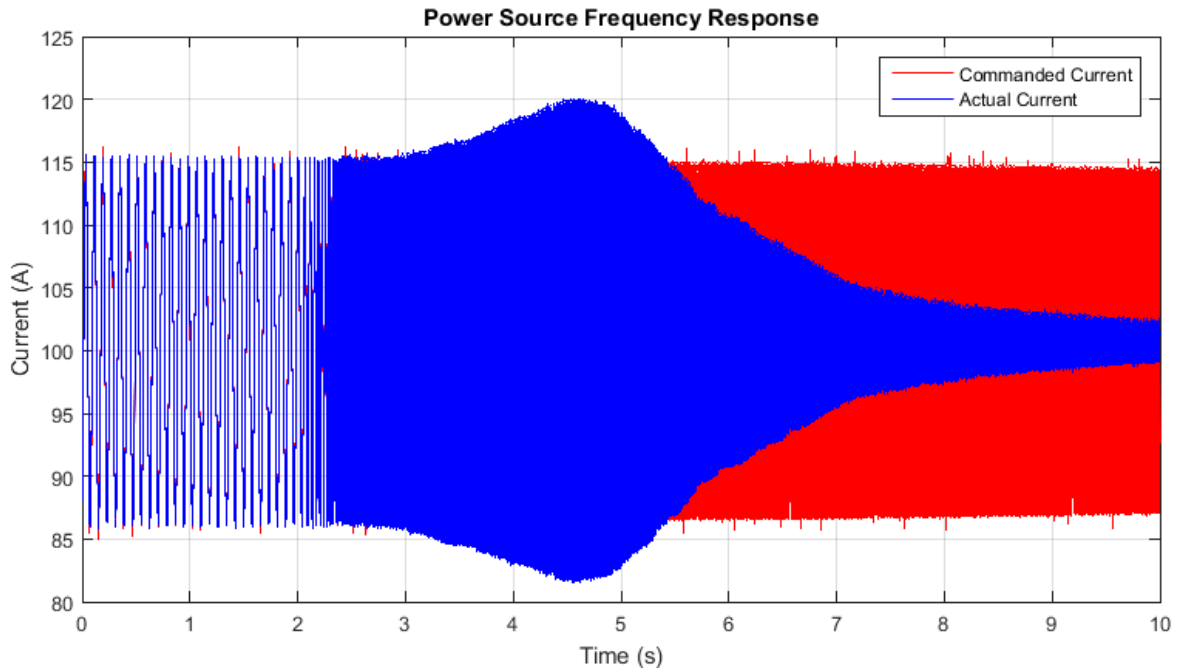


Figure 45: Time domain representation of welding power source frequency response. As the frequency is increased from 10Hz to 6kHz, the power source can no longer accurately track the control signal.

In Figure 45, the frequency increases from left to right. At just after 2s, the frequency becomes high enough that individual periods cannot be distinguished without zooming in. It can be seen that as frequency increases, the welding power source begins to supply more current than commanded. However, just after 4.5s, the welding current's amplitude begins to diminish with further increase in frequency. By the end of the experiment, when the frequency is maximized, the welding current's amplitude is significantly less than commanded.

6.3.2.2.2. Discrete Frequency Test

Although data collected from the current transducer and function generator did not contain significant amounts of noise, the DAQ system's limited bandwidth led to poor quality data at high frequencies. The poor quality arises because when only a few samples are taken over one period of the sinusoidal signal, the peaks and troughs are represented differently

depending on where the samples were taken within each period. An example of raw data collected in the 7kHz test can be seen in Figure 46.

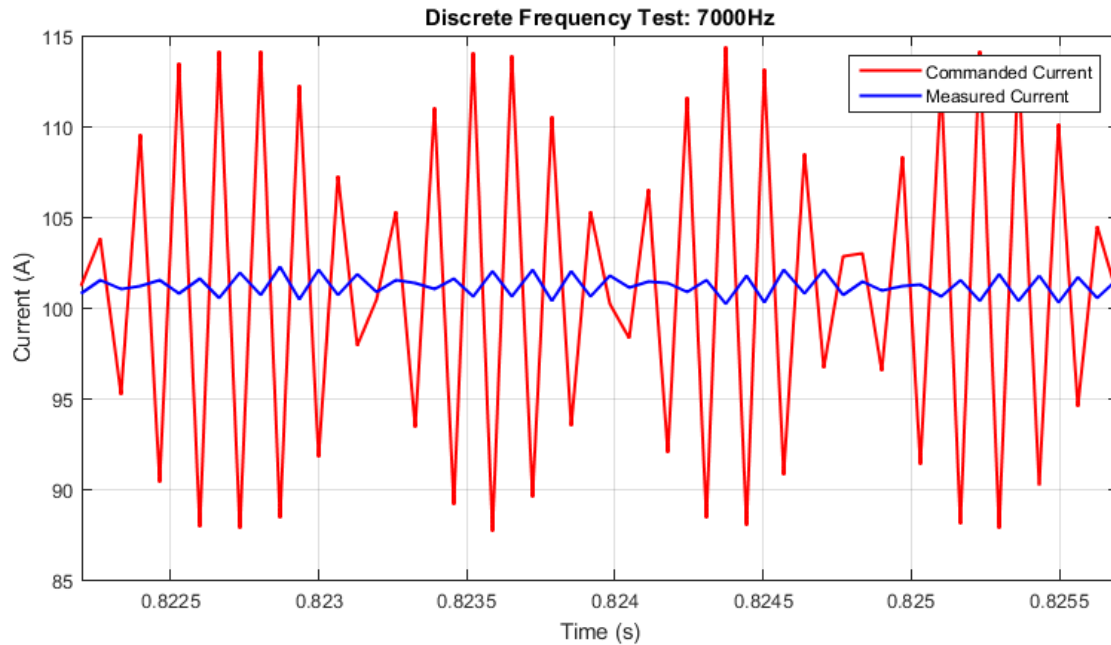


Figure 46: Example of raw data from 7kHz welding power source test.

As seen in Figure 46, the data sampled from the current transducer (measured current) and the function generator (commanded current) are not smooth, sinusoidal signals.

Because accurate measurements would be impossible to obtain from the raw data, the Levenberg-Marquardt NLLS model fitting technique was employed. Figure 47 shows an example of raw data compared to the models for both commanded and measured current.

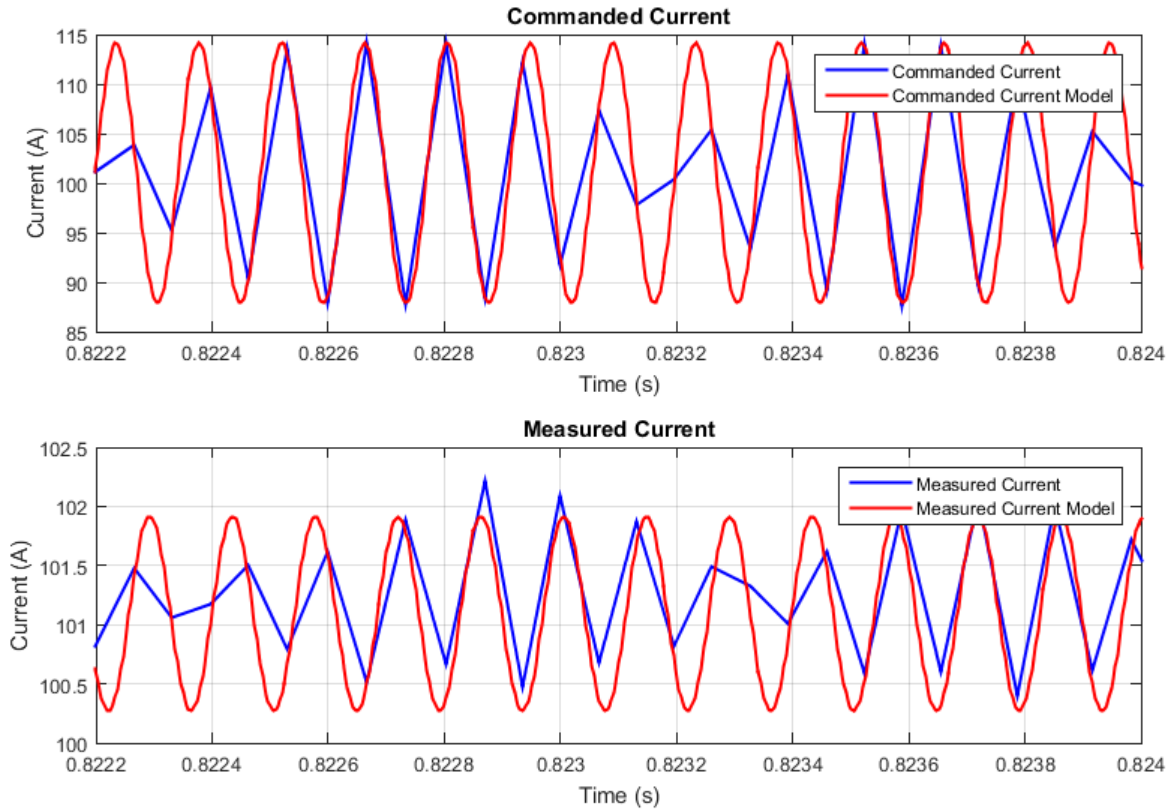


Figure 47: Comparison of raw data with models for commanded and measured current.

As seen in Figure 47, the models appear to coincide with the raw data. If the models accurately represent the raw data, they can be used to obtain much more accurate measurements. A Bode plot created using measurements from the models will be the best possible Bode plot in a least-squares sense.

The same NLLS algorithm was used to model the commanded and measured current data for each of the 33 different frequencies tested. An example of one of the modeled discrete frequency tests can be seen in Figure 48.

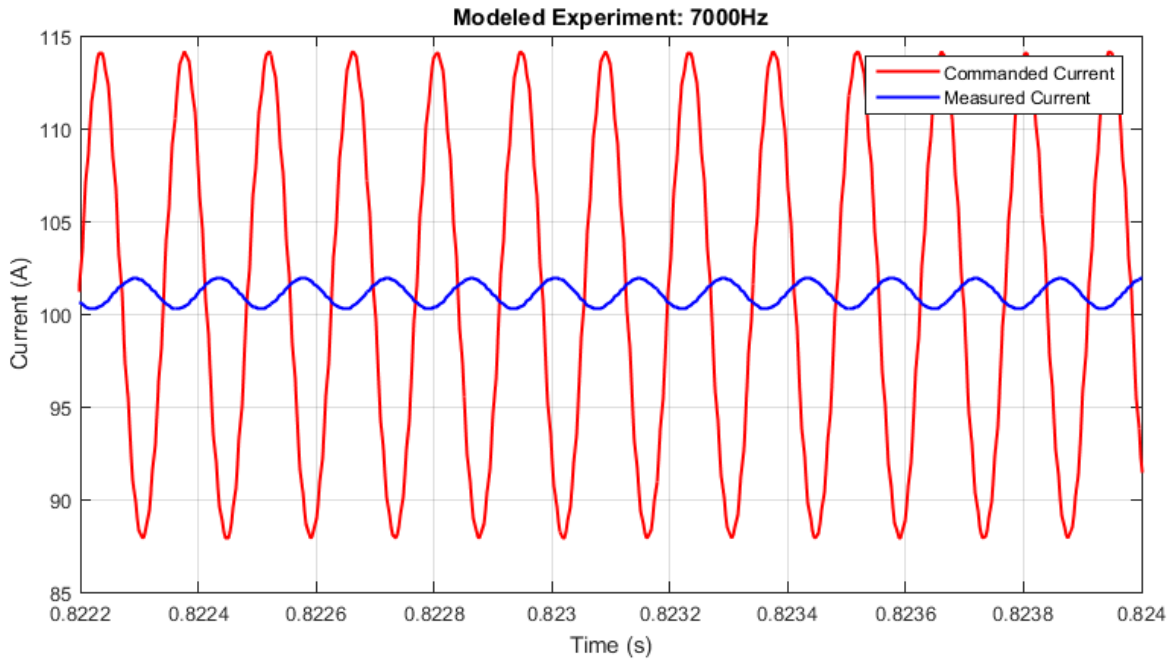


Figure 48: Modeled discrete frequency test.

As seen in Figure 48, the measured current lags the commanded current and the amplitude of its superimposed sine wave is greatly suppressed at 7kHz, which is to be expected.

Once models were made for all of the data, amplitude and phase values were obtained from the models and a Bode plot was generated. The Bode plot can be seen in Figure 49.

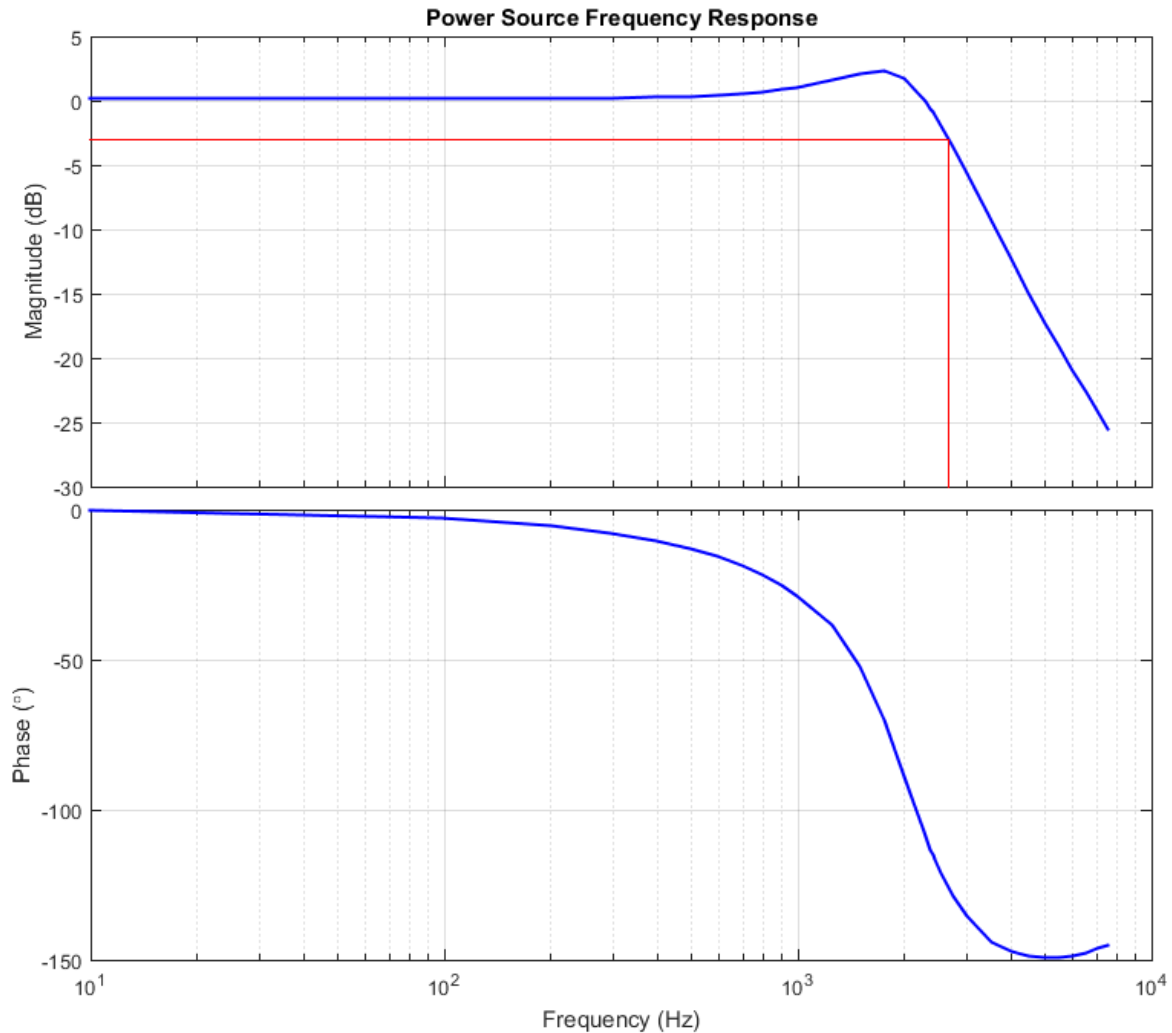


Figure 49: Bode plot showing the welding power source's frequency response. The red line shows the power source's corner frequency at 2.66kHz, indicating that the power source can track a 2.66kHz control signal with reasonable accuracy.

As seen in Figure 49, the welding power source can easily track the commanded current at low frequencies without any lag (phase shift) or decrease in amplitude. At about 20Hz, a slight lag can be seen in the phase plot. The lag slowly increases until about 1kHz where it begins to rapidly increase (decrease in phase) to a -150° phase.

The magnitude plot shows that welding power source's current amplitude can closely follow the commanded amplitude until about 500Hz. The frequency domain analysis shows the same phenomenon as the time domain frequency response representation where the welding

current amplitude increases from about 500Hz to 1500Hz. After about 1500Hz, the welding current amplitude decreases at about 40dB per decade.

The red line in Figure 49 shows the 3dB drop point occurs at about 2.66kHz, indicating the welding power source has a 2.66kHz bandwidth.

6.4. Video Imaging System

To allow post welding process data analysis, a video imaging system was installed. Because the features of interest are electrode extension and droplet transfer, a shadowgraph imaging system was selected. A schematic of the shadowgraph imaging system can be seen in Figure 50.

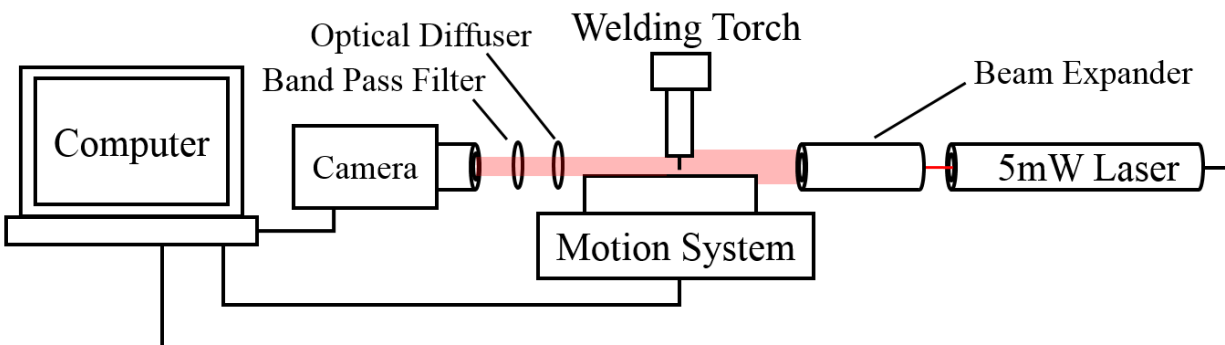


Figure 50: Shadowgraph imaging system schematic.

As seen in Figure 50, all the features of interest (e.g. contact tip position, substrate position, electrode extension, droplet transfer, etc.) cast a shadow from the laser light on the camera lens. When using a monochrome camera, the image will appear white wherever the light passes through unhindered and black (or dark grey) wherever a feature blocks the light.

The first apparent problem with this method is the laser light intensity's Gaussian distribution. The Gaussian distribution causes the center of the image to be excessively bright compared to the outside portions, and the limited dynamic range of the camera is insufficient for capturing the large range of light intensity. This problem is solved, however, by placing an

optical diffuser (ground glass window) in front of the camera lens. Optical diffusers diffuse or scatter the incident light beam, which minimizes or eliminates bright spots and creates a beam of more uniform intensity.

The next apparent problem is when the arc starts, extreme light intensity from the arc will completely saturate the image. The solution is to place an optical band pass filter in front of the camera lens that only allows the laser light to pass through. If a narrow band-width filter is used, only a small portion of light in the welding arc's light spectrum can pass through the filter. The small amount of welding arc light that does pass through the filter is overwhelmed by the laser light. An expanded laser beam makes an excellent light source because a laser can be chosen that outputs a particular wavelength (λ). The band pass filter must simply be selected with a center wavelength equal to the laser's wavelength.

With the equipment properly selected to produce a clear shadowgraph image of the welding process, all that was needed was a high-speed camera to obtain a video of the welding process. The high-speed camera used was a Photron[®] FASTCAM[®] SA-Z (S/N 1020248317). The SA-Z was capable of taking monochrome videos at 20,000fps (frames per second) with full 1024x1024 pixel resolution or up to 2.1million fps with reduced pixel resolution. Once a video was recorded, it could be processed frame by frame to determine features such as electrode extension, arc length, droplet detachments, and droplet diameter.

6.4.1. Imaging System Design and Validation

Before an effective imaging system can be made, the optical spectrum of the welding arc must be measured. Depending on the composition of the electrode, work piece/substrate, and shielding gas, a welding arc can emit many different light wavelengths of various intensities. It is important to find ranges of wavelengths in the arc light spectrum that have low intensities.

The wavelength regions of low intensities are where the wavelength for the laser and band pass filter should be selected. If the arc emits high intensity light at the same wavelength as the laser and band pass filter, the arc light will pass through the filter and saturate the image.

Typically, welding arcs emit lower intensity light in the region around 632.8nm wavelengths. Because 632.8nm is a common wavelength exploited in welding imaging systems, a laser and band pass filter were obtained based on 632.8nm wavelengths. The laser was a JDSU® 1125 HeNe (helium-neon) 5mW laser (S/N T8068953).

However, because the actual wavelengths emitted by a welding arc can vary significantly depending on electrode and work piece composition and shielding gas composition, the imaging system design still required validation. The procedure and results of validating the imaging system design are discussed in this section.

6.4.1.1. Procedure

The first task in validating the imaging system design was to analyze the arc spectrum. The arc spectrum was analyzed using an Ocean Optics® HR4000 optical spectrum analyzer (S/N HR4C6183). Before the spectrum analyzer was used, its calibration was verified by connecting it to an Ocean Optics calibration device with a fiber optic cable. A spectrum was obtained from the calibration device and compared to the known spectrum.

Once the calibration was verified, the fiber optic cable connected to the spectrum analyzer was pointed at the GMAW wire electrode. The electrode was ER70S-6 wire, and 98% Ar, 2% O₂ shielding gas was used. The welding arc was then started and a light spectrum was captured.

After capturing the arc light spectrum, the laser used in the imaging system was analyzed. Aiming the spectrum analyzer's fiber optic cable at the expanded laser beam, another spectrum was captured.

Lastly, the optical band pass filter was analyzed. To analyze the band pass filter's frequency (or wavelength) response, the filter was placed in front of a white light source (incandescent light bulb). The spectrum analyzer's fiber optic cable was then aimed at the white light source with the filter directly between the fiber optic and the white light source. Once the components were in proper alignment, a spectrum was captured.

All the captured spectra were then analyzed in MATLAB to validate the imaging system design.

6.4.1.2. Results and Discussion

The resulting spectrum from the calibration device compared to the calibration device's theoretical spectrum can be seen in Figure 51.

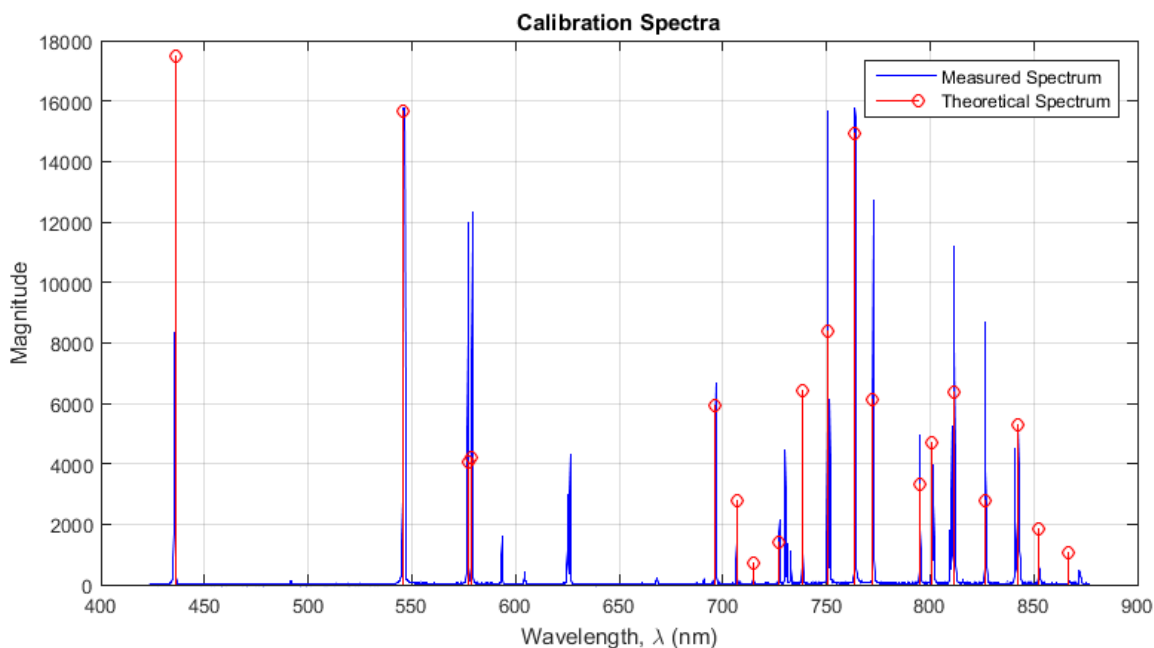


Figure 51: Spectrum analyzer calibration test. Measured spectrum has peaks at wavelengths that correspond with theoretical spectrum.

The units on the y-axes of all spectra measured with the spectrum analyzer are arbitrary and only represent relative light intensity. It can be seen that the relative magnitudes of the spectra in Figure 51 do not closely match. In addition, there appears to be additional peaks in the calibration spectrum that do not exist in the theoretical spectrum. However, the important factor is the wavelength. It can be seen that nearly all the peaks in the calibration spectrum have corresponding peaks in the theoretical spectrum at nearly identical wavelengths. The fact that the wavelengths of the two spectra appear to be in agreement indicates that the spectrum analyzer was sufficiently calibrated.

Figure 52 shows the welding arc light spectrum.

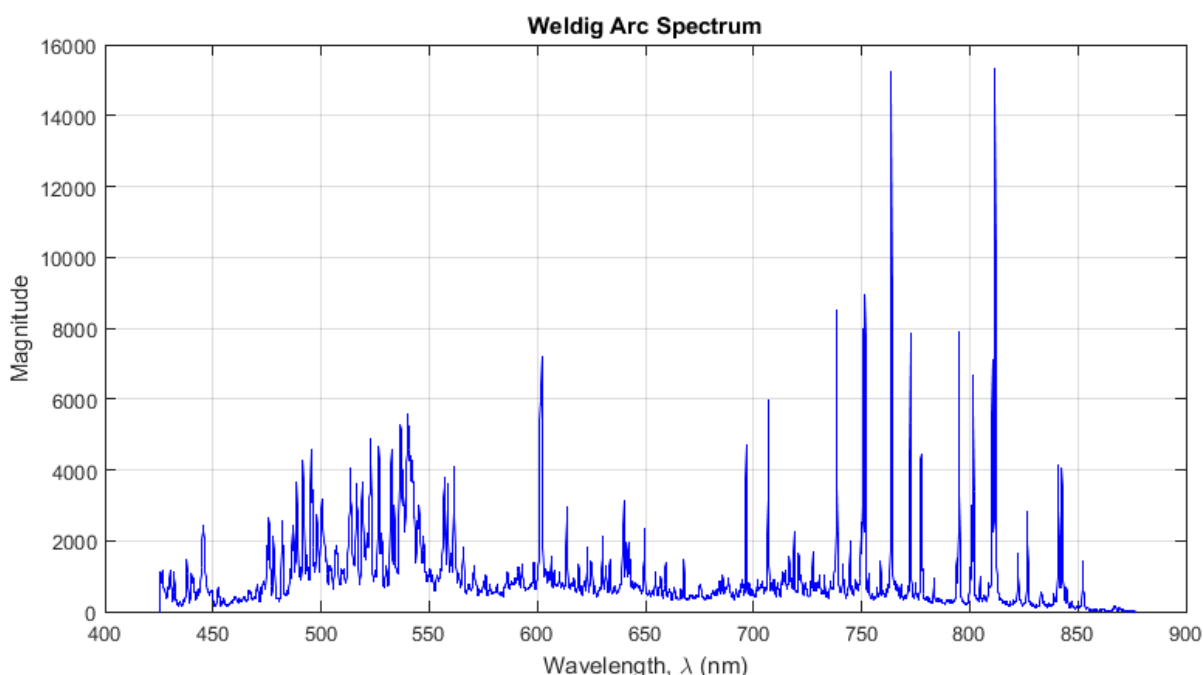


Figure 52: GMAW arc light spectrum with ER70S-6 wire and 98% Ar, 2% O₂ shielding gas. Regions where the wavelengths have low magnitudes are optimal wavelengths around which video imaging systems can be designed.

As seen in Figure 52, the welding arc light contains many different wavelengths at various intensities. Although there are locations in the spectrum that would be optimal to design the imaging system around (e.g. ~675nm), the availability and cost of lasers and band pass filters

at certain wavelengths is a limiting factor. It can be seen that in the region around 632.8nm, only relatively small spikes occur in the welding arc spectrum, indicating that the commonly available 632.8nm laser and band pass filter should be sufficient.

Figure 53 shows the imaging system's laser light spectrum.

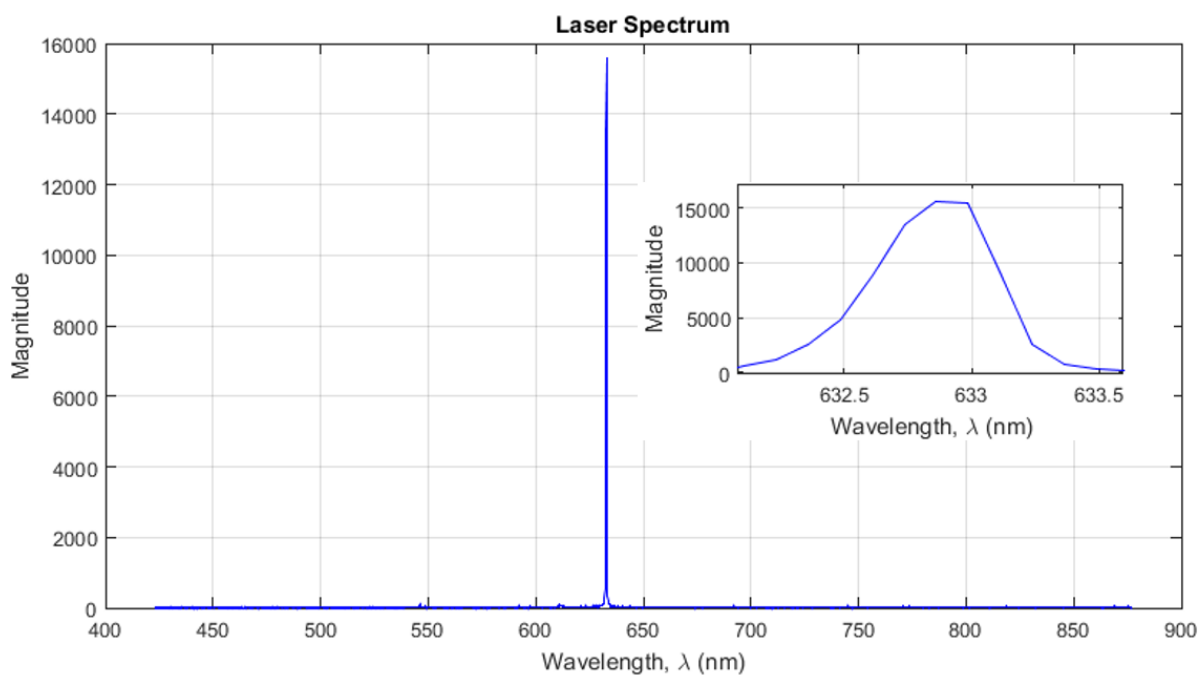


Figure 53: Imaging system laser light spectrum (including zoomed in image). The center wavelength is at approximately 632.8nm.

As seen in Figure 53, the laser has a very narrow bandwidth. The close up shown in Figure 53 shows that the laser light is centered at about 632.8nm as expected.

Figure 54 shows the frequency (or wavelength) response of the optical band pass filter.

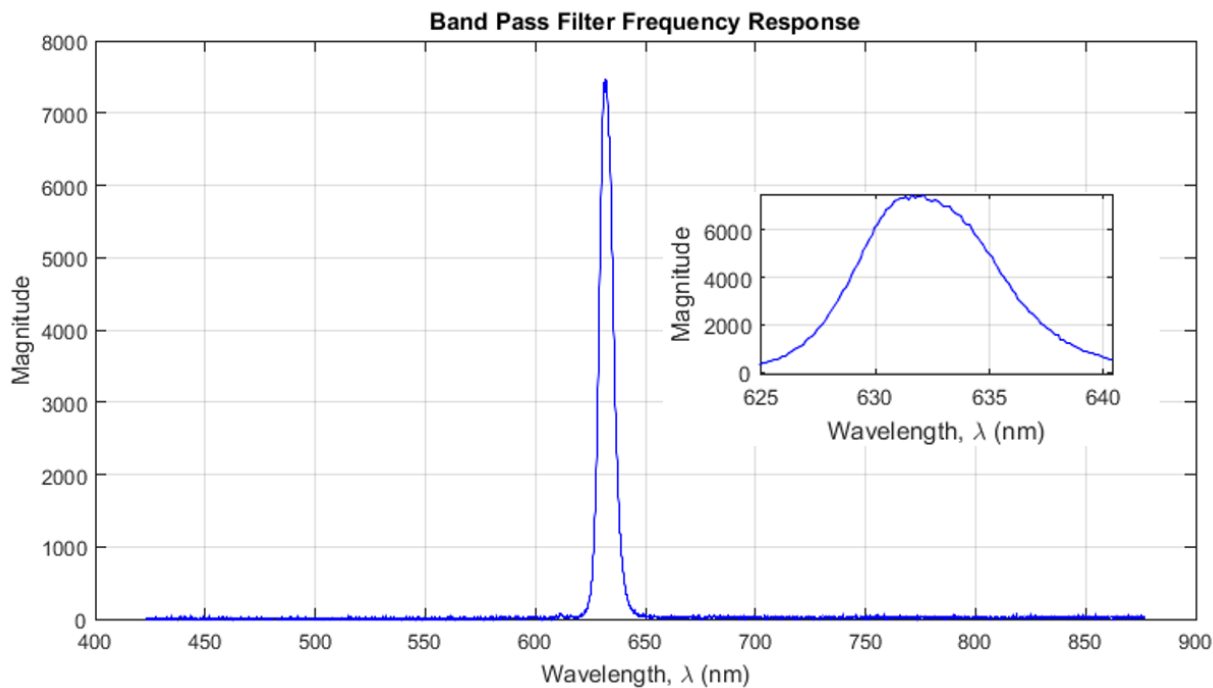


Figure 54: Optical band pass filter frequency (or wavelength) response. The center wavelength is at approximately 632nm.

As mentioned in the procedure section, Figure 54 was obtained by capturing the spectrum of white light passed through the band pass filter. Because white light contains nearly equal proportions of all wavelengths (at least over the wavelength range of interest), the wavelengths that pass through the filter represent the filter's frequency response.

Figure 54 shows that the filter has a relatively narrow band width. The close up shows that the filter has about a 632nm center wavelength.

Figure 55 shows the spectra of the entire imaging system including arc, laser, and filter spectra.

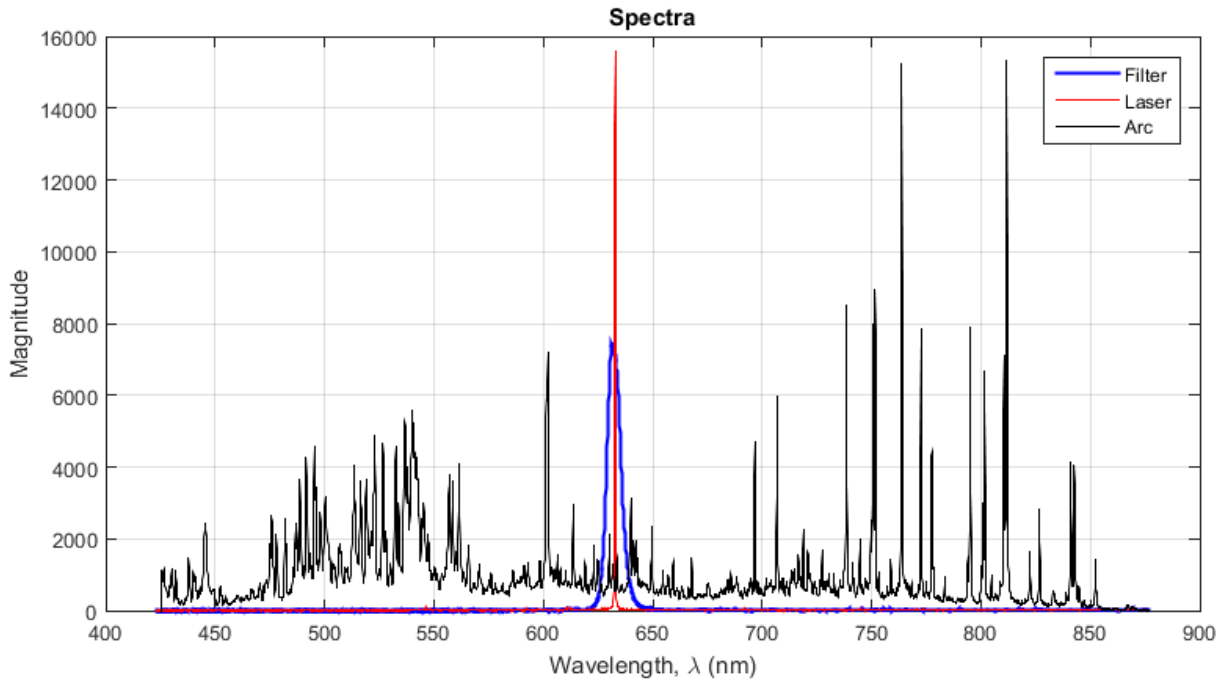


Figure 55: Spectra of imaging system including arc, laser, and filter spectra. No large spikes from the arc spectrum occur within the filter's pass band.

As seen in Figure 55, the laser emits wavelengths within the band pass filter's pass band. A relatively small proportion of arc light with wavelengths inside the pass band is allowed to pass through the filter and be seen by the camera. However, the arc light that can pass through the filter is of low magnitude and is overwhelmed by the laser light.

An example of a raw image taken during a weld can be seen in Figure 56.

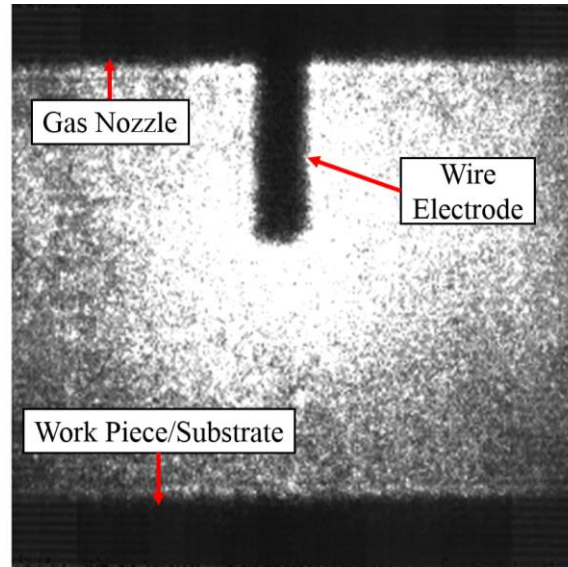


Figure 56: Raw image taken with the imaging system showing the GMAW gas nozzle, the wire electrode, and the top of the substrate.

Figure 56 shows that features of interest such as the electrode extension and the locations of the contact tip (relative to the gas nozzle) and substrate can be seen clearly.

6.4.2. Post Process Video Analysis

After raw images are captured in a video by the high-speed camera, the video can be processed frame by frame to obtain quantitative information about the welding process.

To perform post process analysis, a video processing algorithm was written in MATLAB (see Appendix D). The basic flow of the algorithm is as follows:

- 1) Extract a frame, which is a greyscale (black and white) image, from the video file.
- 2) Convert the greyscale image to a binary image based on a predetermined threshold. Converting to a binary image involves setting all the pixels with values above the threshold to white and all the pixels with values below the threshold to black. The resulting image is black or white instead of a greyscale.
- 3) Filter the image to remove white pixels from black background and black pixels from white background.

- 4) To measure the electrode extension, count the number of black pixels between the predefined location of the contact tip and the first white pixel below the contact tip. Repeat the pixel count for three locations across the width of the electrode and average the three pixel counts.
- 5) If the actual contact-tip-to-work distance (CTWD) is known, it can be related to the number of pixels between the contact tip and the substrate (work piece) in the image to determine actual measurements of the parameters.
- 6) Stitch processed frames back into a new video.

Figure 57 shows a comparison of raw images extracted from a video and the corresponding processed images.

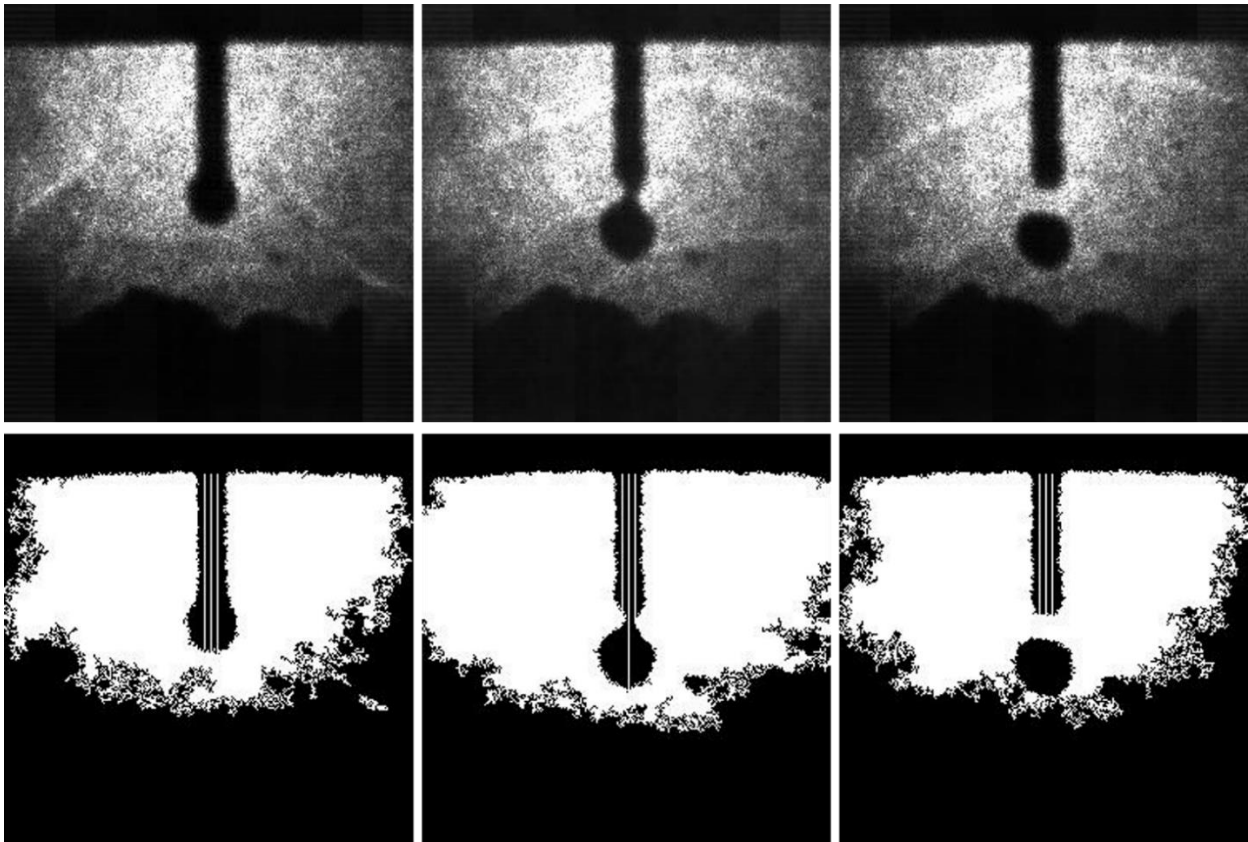


Figure 57: (Top) Raw images from high-speed video. (Bottom) Processed images from video showing electrode extension tracking.

As seen in Figure 57, the video processing algorithm is effective at increasing the contrast between the electrode and the background. It can also be seen that the algorithm effectively tracks the electrode extension, which is shown by the three white lines on the electrode in the images.

6.5. Three-Axis Motion System

To allow the work piece to be properly positioned relative to the welding torch, a 3-axis motion system was assembled. Because precise alignment was required between the video imaging system, the torch, and the 200W 532nm arc stabilizing laser, it was not practical to have a moving torch. The 3-axis motion system was built to move the work piece under a fixed torch. An Aerotech[®] linear stage was used for the motion system's x-axis, and two Velmex BiSlides[®] were used for the y and z-axes. Figure 58 shows the 3-axis motion system assembly.

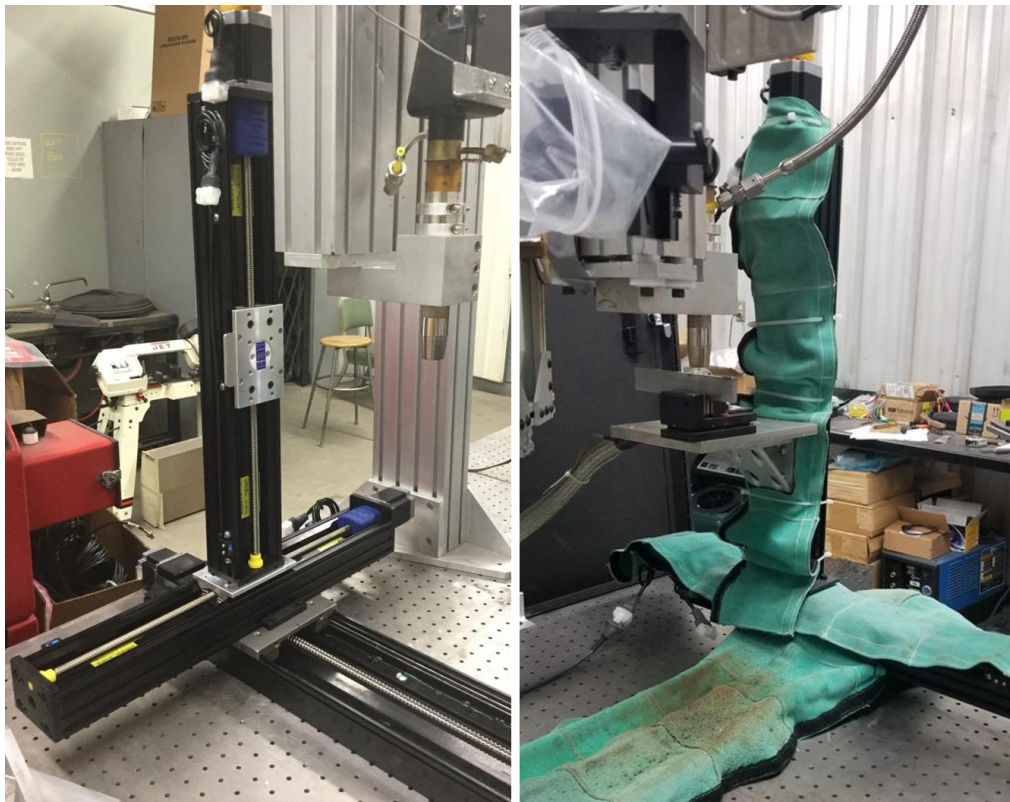


Figure 58: Three-axis motion system: (left) linear axes only and (right) linear axes configured for welding.

In Figure 58, the image on the left shows the assembly of linear axes, and the image on the right shows the motion system outfitted for welding with a work piece platform and spatter shields over the lead screws. The work piece platform was configured such that the GMAW torch was 90° to the work piece. The linear axes were all driven by stepper motors connected to the lead screws.

Motion was controlled using a Galil[®] DMC-4143 motion controller (S/N BV-7894). The Galil controller acted as both the controller and driver/amplifier for the stepper motors driving the axes. Communication was established between the Galil controller and the computer using a USB connection. One method of controlling motion was to send individual motion commands from the computer to the Galil controller, which immediately executed the command. The other motion control method was to load a motion program onto the Galil controller and trigger program execution with the computer.

A C++ class was developed to control motion for welding applications through the Galil controller. In addition, a new C++ project was created to control the motion system with the computer's keyboard. Keyboard control would allow the work piece to be easily repositioned below the torch for each experiment. Appendix E contains the C++ code for controlling the motion system.

6.6. High Frequency Arc Starter

The high frequency arc starter used in GLADiS was a Liburdi A200 Arc Starter. Figure 59 shows a simplified version of the high frequency arc starter's circuit diagram.

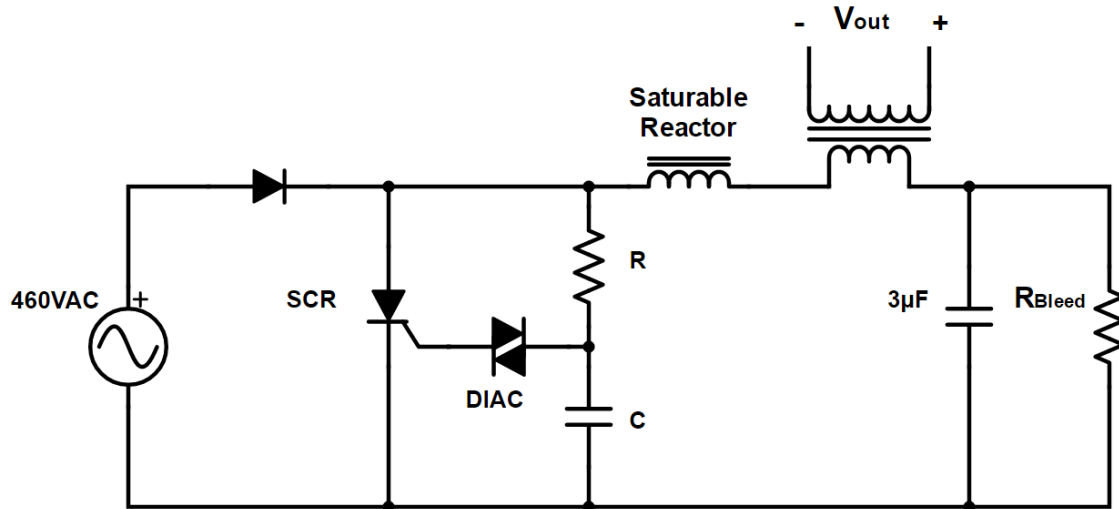


Figure 59: High frequency arc starter circuit diagram.

As seen in Figure 59, the high frequency arc starter is powered by a 460VAC source (the Liburdi Pulsweld P200-004 power source). The power source's positive half cycle charges the $3\mu\text{F}$ capacitor up to around 900V and starts an RC timing circuit. On the negative half cycle, the RC timing circuit has charged up, which triggers an SCR (silicon-controlled rectifier) through a DIAC (diode alternating current). When the SCR is triggered, the $3\mu\text{F}$ capacitor discharges through the primary winding of a step up transformer, generating about 10kV on the secondary winding, which is connected to the welding circuit. A small ferrite core inductor acts as a saturable reactor that holds off the discharge current for a small amount of time. The small amount of time ensures that the SCR gate has fully spread across its width and will not fail when hit by the discharge current.

The high frequency arc starter was designed to operate on 60Hz power. Because the high frequency arc starter's timing starts over on every positive half cycle, the high frequency arc starter generates a 10kV pulse every 60^{th} of a second. Although the pulses do not come at high frequency (60Hz), the pulses are extremely short and have a high frequency content.

6.6.1. DAQ Protection Circuit

Having the high frequency arc starter connected to the welding circuit meant that the voltage across the arc gap could be up to 10kV. However, the isolation input module for the DAQ's ADC that is responsible for measuring arc voltage could only protected up to $240V_{RMS}$. Therefore, a protection circuit was required to ensure that the high frequency arc starter's 10kV pulses could not be seen by the input module.

6.6.1.1. Circuit Design

Although instrumentation to measure the high frequency arc starter's actual output was not available, the frequency content of the high frequency arc starter's voltage pulses was known to be extremely high (higher than frequencies of interest in the welding process). The high frequency content indicated that a low-pass filter could be used to suppress the high frequency arc starter pulse while allowing voltages of interest to pass. However, the low-pass filter had to be designed to not absorb any energy from the high frequency arc starter so that the energy could be dissipated in the arc gap. In other words, the filter had to have a high input impedance at high frequencies. Therefore, an RL type filter was chosen instead of an RC type, which would have low input impedance to high frequencies. A circuit diagram of the filter design can be seen in Figure 60.

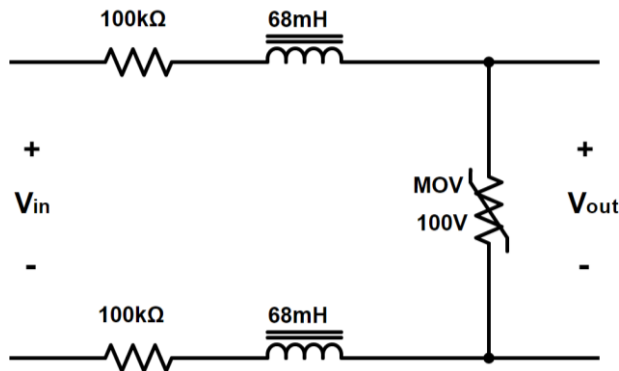


Figure 60: Protection circuit diagram. The $100k\Omega$ resistors and $68mH$ inductors provide high impedance to the high frequency arc starter, and the MOV ensures V_{out} never exceeds 100V.

The resistors and inductors used to implement the circuit shown in Figure 60 were chosen to have high voltage ratings. Large inductance values were chosen to block the high frequency, and 100k Ω resistors were added to provide extra impedance looking into the circuit. The analog input isolation module that would eventually be used to measure the arc voltage had a rated input impedance of 650k Ω to 700k Ω . Therefore, the size of the resistors added to the protection circuit were limited to 100k Ω to minimize voltage suppression caused by the voltage divider with the input module's input impedance.

The last component added to the protection circuit was a MOV (metal-oxide varistor). The basic operation of a MOV is simple: below the MOV's varistor voltage, the MOV acts like an open circuit; above the MOV's varistor voltage, it acts like a short circuit. Because the open circuit voltage of the welding power source was rated at 75V (actual open circuit voltage measured to be 60V), it was known that nothing above 75V would be of interest. The MOV was chosen with a varistor voltage of 100V, which was above the 75V open circuit voltage, but below the 240V_{RMS} limit of the input module. Any voltage spikes above 100V that might make it through the RL circuit would be quickly shorted circuited by the MOV.

6.6.1.2. Circuit Test

To test the protection circuit's pulse blocking ability, it was connected directly to the high frequency arc starter's output. Two electrodes were connected to the high frequency arc starter's output and positioned about 1/8in apart to simulate the arc gap. An inexpensive DMM (digital multimeter) was connected to the protection circuit's output to simulate the DAQ's input module. Upon energizing the high frequency arc starter, two observations were made: 1) the DMM survived, and 2) a spark appeared between the electrodes. These two observations indicated that the protection circuit successfully blocked the high voltage pulses from reaching

the DMM, and the circuit did not absorb energy from the high frequency arc starter, allowing the arc to start. The experiment was repeated with a 9V battery connected in series with the high frequency arc starter to test the protection circuits ability to pass lower frequency/voltage signals. Results showed the DMM was able to read the 9V signal and survive the arc start.

6.6.1.3. Voltage Measurement

The last step in implementing the protection circuit for voltage measurement was to design the complete voltage measurement system including the protection circuit and analog input module. The goal was to scale the input voltage range of interest, 0V-60V, to the input module's positive range, 0V-10V, using a voltage divider. However, the voltage divider design was complicated by the input module's relatively low input impedance. To properly design a voltage divider, the impedances of all components including the protection circuit and input module had to be taken into account. Figure 61 shows a circuit diagram of the primary resistances in the voltage measurement circuit.

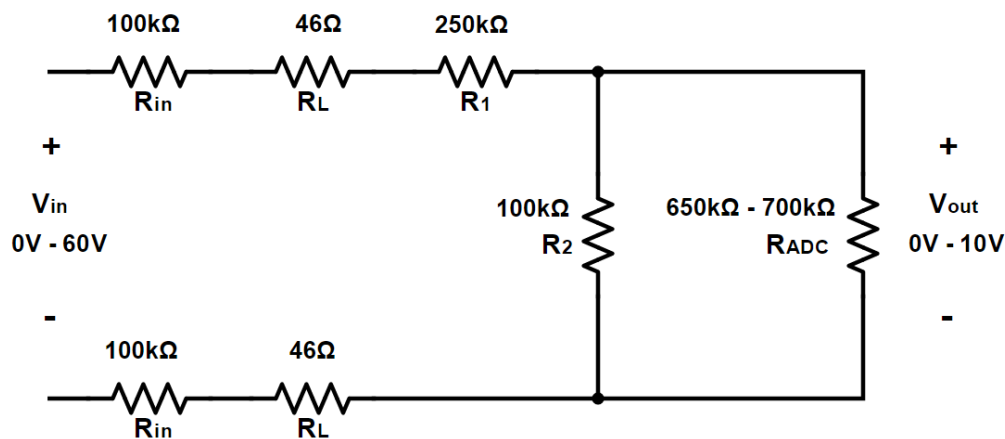


Figure 61: Arc voltage measurement resistance diagram.

In Figure 61, the R_{in} resistors are the two resistors in the protection circuit, the R_L resistors represent the inductors' resistance (non-ideal inductors), R_{ADC} is the input module's input impedance, and R_1 and R_2 are the voltage divider resistors to be designed. For

calculations, R_{ADC} was assumed to be $675k\Omega$. Because it was desired to have a high input impedance, a resistance of $100k\Omega$ was chosen for R_2 . With all other resistances known and the voltage scale factor known, a resistance for R_1 could be calculated using the voltage divider formula:

$$V_{out} = \frac{V_{in} \left(\frac{R_2 R_{ADC}}{R_2 + R_{ADC}} \right)}{2R_{in} + 2R_L + R_1 + \left(\frac{R_2 R_{ADC}}{R_2 + R_{ADC}} \right)} \quad (12)$$

$$R_1 = \frac{V_{in}}{V_{out}} \left(\frac{R_2 R_{ADC}}{R_2 + R_{ADC}} \right) - 2R_{in} - 2R_L - \left(\frac{R_2 R_{ADC}}{R_2 + R_{ADC}} \right) \quad (13)$$

$$R_1 = \frac{60V}{10V} \left(\frac{100k\Omega(675k\Omega)}{100k\Omega + 675k\Omega} \right) - 2(100k\Omega) - 2(46\Omega) - \left(\frac{100k\Omega(675k\Omega)}{100k\Omega + 675k\Omega} \right)$$

$$R_1 = 235k\Omega$$

Because the input module's actual input impedance during operation was unknown, a resistance of $250k\Omega$ was used for R_1 . A test with the voltage measurement circuit connected to the welding circuit showed that the power source's $60V$ open circuit voltage was scaled down to exactly $10V$ through the voltage measurement circuit. A photo of the voltage measurement/protection circuit can be seen in Figure 62.

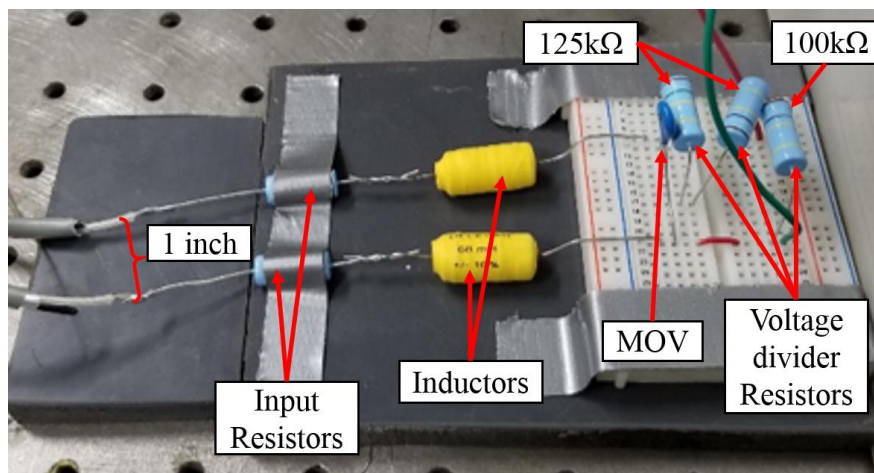


Figure 62: Arc voltage measurement and protection circuit. The distance between the wires/components on the input side up to the inductors is set to at least 1in to avoid arcing between wires.

It can be seen in Figure 62 that two 125kΩ resistors in series were used as R₁. It can also be seen that a 1in separation distance was used between the wires and components on the input side of the circuit up to the inductors. The large separation distance was to ensure that the high frequency arc starter's voltage pulses could not arc between voltage measurement wires.

With the component values known, a transfer function could be derived from the circuit diagram in Figure 63.

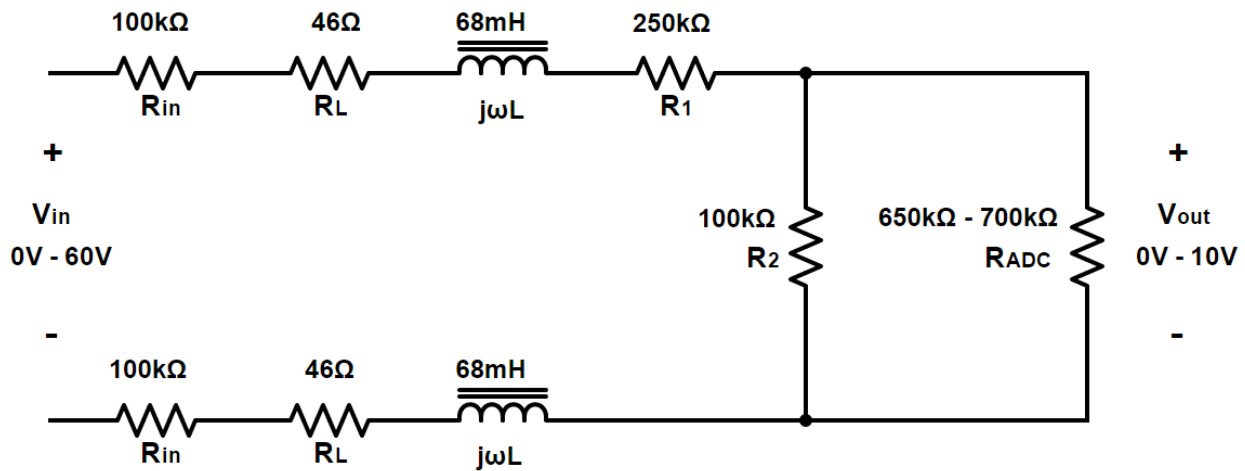


Figure 63: Arc voltage measurement and protection circuit diagram.

In the time domain, the input/output relationship is as follows:

$$\frac{V_{out}}{V_{in}} = \frac{\left(\frac{R_2 R_{ADC}}{R_2 + R_{ADC}}\right)}{2j\omega L + 2R_{in} + 2R_L + R_1 + \left(\frac{R_2 R_{ADC}}{R_2 + R_{ADC}}\right)} \quad (14)$$

Transforming (14) into the frequency (Laplace) domain results in the following:

$$h(s) = \frac{\left(\frac{R_2 R_{ADC}}{R_2 + R_{ADC}}\right)}{2sL + 2R_{in} + 2R_L + R_1 + \left(\frac{R_2 R_{ADC}}{R_2 + R_{ADC}}\right)} \quad (15)$$

or:

$$h(s) = \frac{R_{eq1}}{2sL + R_{eq2}} \quad (16)$$

where:

$$R_{eq1} = \frac{R_2 R_{ADC}}{R_2 + R_{ADC}} \quad (17)$$

and:

$$R_{eq2} = 2R_{in} + 2R_L + R_1 + \frac{R_2 R_{ADC}}{R_2 + R_{ADC}} \quad (18)$$

In pole-zero form, the transfer function becomes

$$h(s) = \frac{\frac{R_{eq1}}{2L}}{s + \frac{R_{eq2}}{2L}} \quad (19)$$

Plugging in the component values, the final transfer function is

$$h(s) = \frac{6.40(10^5)}{s + 3.95(10^6)} \quad (20)$$

Looking at the transfer function in (20), it can be seen that the circuit's corner frequency is 3.95Mrad/s or 629kHz. The DC gain (found by setting s to 0) is 0.16 which, when multiplied by 60V, results in 9.6V which meets the design specification. A Bode plot of the voltage measurement/protection circuit can be seen in Figure 64.

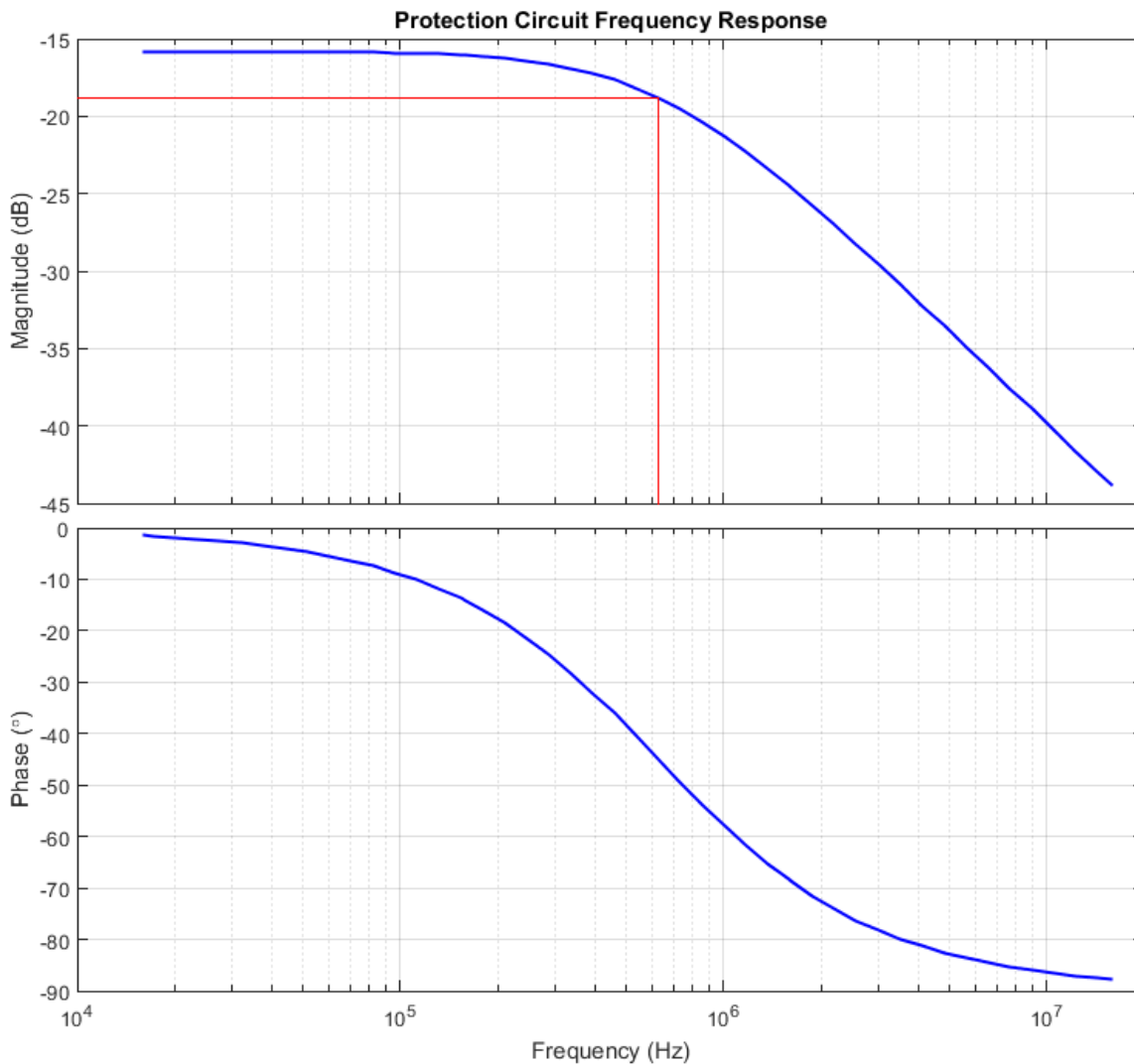


Figure 64: Bode plot showing the voltage measurement/protection circuit's frequency response. The DC gain is -15.8dB which scales the welding power source open-circuit voltage to ADC levels. The corner frequency is 629kHz

Figure 64 shows that the circuit exhibits the proper gain (-15.8dB) at low frequencies with little phase shift. It also shows the corner frequency (3dB drop) at 629kHz. Because the circuit was experimentally shown to effectively block the arc starter voltage pulse and not absorb excessive arc starter energy, it is likely that the pulse's main frequency content is greater than 1MHz. The corner frequency is high enough that it is unlikely that any voltage signals of interest in the welding process would be excessively suppressed by the circuit.

6.6.2. High Frequency Arc Starter Connection

Two options exist for connecting the high frequency arc starter to the welding circuit. It can be connected to the positive side (torch side) or the negative side (work piece side).

6.6.2.1. Positive Connection

The arc starter was initially connected to the positive side as shown in Figure 65.

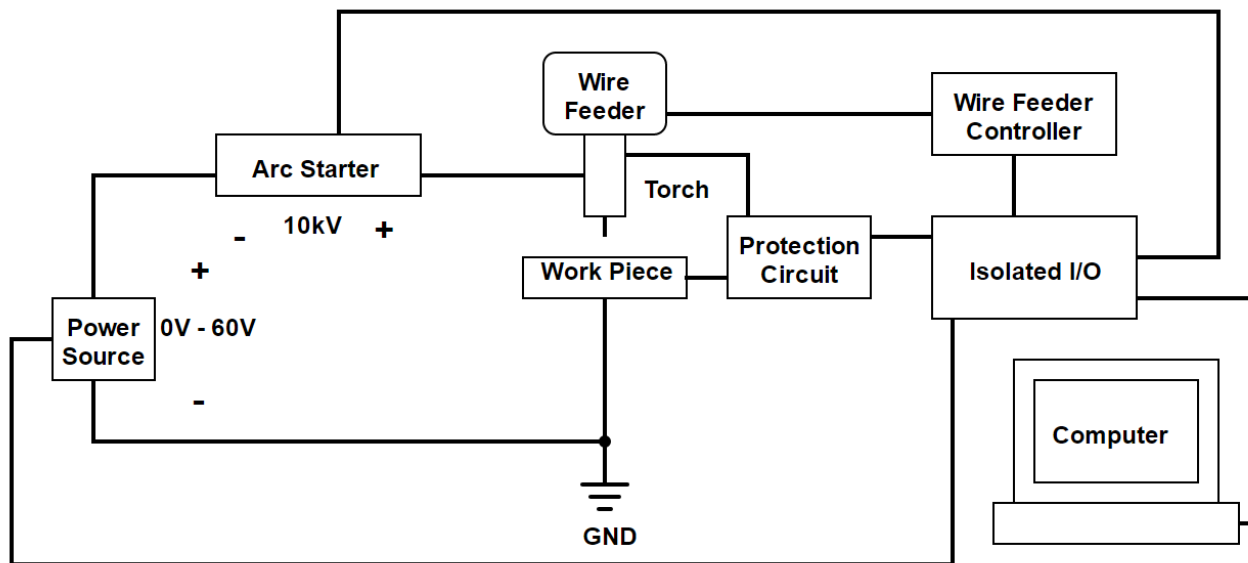


Figure 65: High frequency arc starter connection to positive side of welding circuit.

The high frequency arc starter was tested at both polarities on the positive side of the welding circuit, but the polarity shown in Figure 65 (positive side connected to welding torch) proved to be more effective. However, the connection in Figure 65 was highly problematic. When the high frequency arc starter was energized, its energy was often dissipated at one of seven locations other than the welding arc:

1. Inside the wire feeder
2. Inside the electronics enclosure housing the isolated I/O
3. On the 3-axis motion system
4. On a junction between air and water cooled positive welding leads

5. On the wire spool
6. Through the WFS encoder
7. Inside the wire feeder controller

Solutions were designed and implemented for the first five locations:

1. The wire feeder/torch assembly was insulated from the grounded frame to which it was connected as seen in Figure 66.

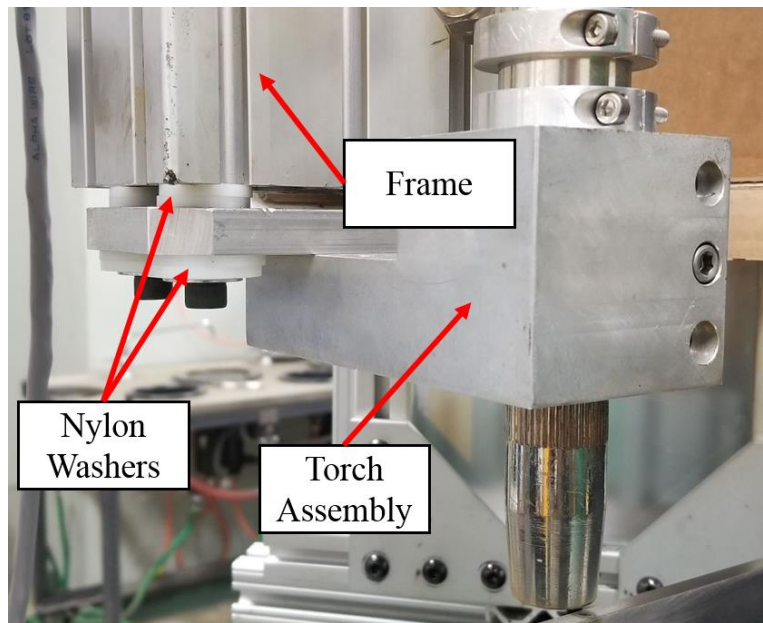


Figure 66: Wire feeder/torch assembly insulated from frame using nylon washers.

2. Large inductors (68mH) and MOVs were placed on the connections between the isolated I/O and the wire feeder controller to increase the impedance seen by the high frequency arc starter pulse and provide surge protection.
3. The work piece was insulated from the motion system as seen in Figure 67.

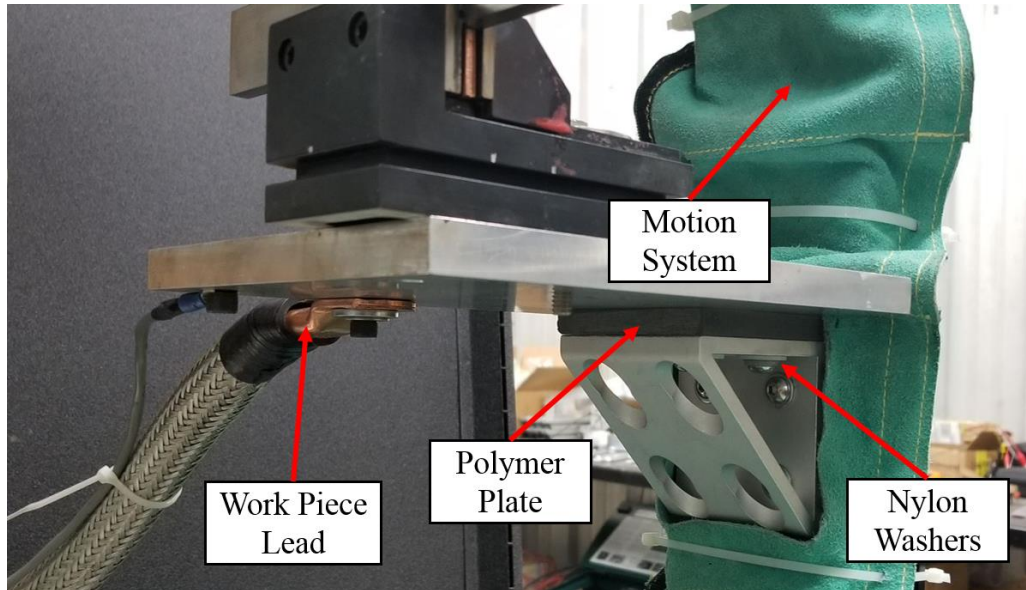


Figure 67: Work piece insulated from motion system using a polymer plate and nylon washers.

4. The junction between air and water cooled welding leads was rebuilt to provide extra clearance between the conductor and metal fasteners on the fixture to prevent arcing.
5. Extra insulation was added around the wire where it entered the wire conduit to prevent arcing between the wire/conduit and the metal frame holding the wire spool as seen in Figure 68.

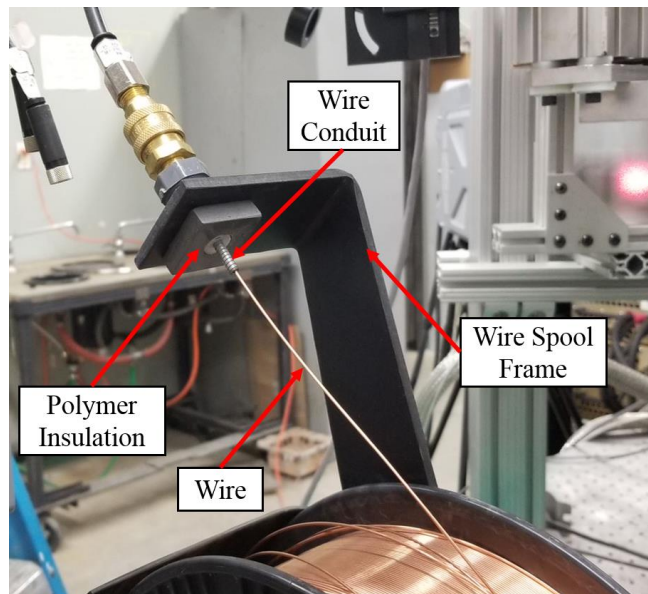


Figure 68: Insulation between wire/wire conduit and wire spool frame.

The WFS encoder was destroyed by the high frequency arc starter and removed from the system. The only way to prevent the high frequency arc starter from dissipating its energy in the last location (inside the wire feeder controller) was to disconnect the wire feeder from the wire feeder controller. The problem with the wire feeder was that the wire electrode, which was connected to the high frequency arc starter, was in contact with the wire feeder's drive wheels, which were connected to the wire feeder motor, which was connected to the wire feeder controller. There was not sufficient insulation anywhere between the electrode and the wire feeder controller to prevent the high frequency arc starter voltage from reaching the wire feeder controller.

With the wire feeder disconnected and the other five solutions in place, the high frequency arc starter could effectively arc between the wire electrode and the work piece. However, as soon as the wire feeder was connected to the wire feeder controller, all the high frequency arc starter's energy was consumed inside the wire feeder controller, and the arc would not light.

6.6.2.2. Negative Connection

Because the high frequency arc starter could not work in conjunction with the wire feeder when connected to the positive side of the welding circuit, it was moved to the negative side as seen in Figure 69.

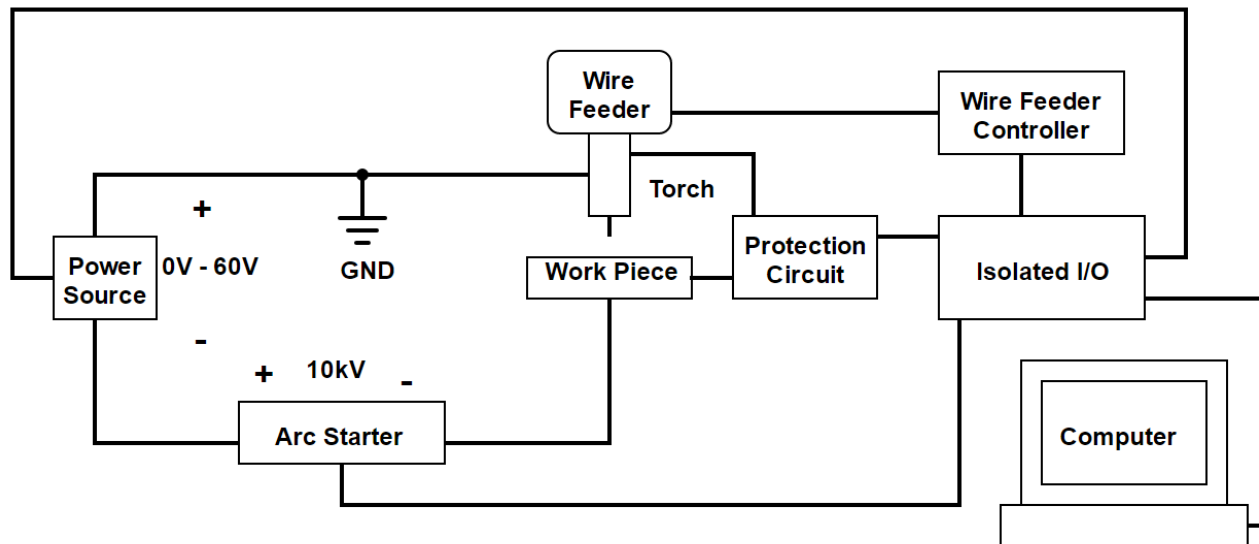


Figure 69: High frequency arc starter connection to negative side of welding circuit.

As seen in Figure 69, the positive side of the welding circuit was earth grounded. It was assumed that if the positive side was held to ground, there would be no voltage difference between the electrode/torch/wire feeder and the wire feeder controller. The configuration with the high frequency arc starter connected to the negative side is closer to the high frequency arc starter's intended connection to a GTAW system.

Experimentation showed that with the new configuration, the high frequency arc starter was able to start the arc with all system components connected.

6.6.3. Electromagnetic Interference

With the high frequency arc starter functioning, a new set of problems emerged. High voltages and electromagnetic interference (EMI) from the high frequency arc starter caused a number of problems with devices both connected to and isolated from the system. Energizing the high frequency arc starter could cause computer crashes and, almost always, caused connection losses between the computer and the USB connected Galil motion controller. EMI

also caused the laser power supply, which was completely isolated from the system, to shut down every time the high frequency arc starter was energized.

The high-frequency/high-voltage signal from the high frequency arc starter is of high enough frequency to be efficiently emitted by the welding leads, which act as antennas. If allowed to propagate into the room, EMI from the welding leads can scramble serial communications, and in some cases, can actually damage electronic devices. Most EMI prevention techniques rely on shielded signal cables to prevent EMI from entering cables that carry control signals. Another solution is to install shielding on the EMI source (the welding leads) to prevent EMI from being emitted [53]. EMI shielding on the welding leads, with proper grounding, is a proactive solution to minimize the amount of EMI that is emitted into the room.

6.6.3.1. EMI Shielding and Grounding

Implementing EMI shielding and grounding techniques began with installing an earth ground in the lab floor. The earth ground was installed by fixing a terminal strip to a cast iron drain pipe as seen in Figure 70.



Figure 70: Earth ground. The test frame, positive welding lead, all of the EMI shielding, and the Galil controller body were attached to earth ground.

The test frame/table, positive welding lead, all the EMI shielding, and the Galil controller body were connected to the earth ground. Connecting the shielding to earth ground allows absorbed EMI to be dissipated in the earth ground.

Shielding was then installed on the welding leads as seen in Figure 71.

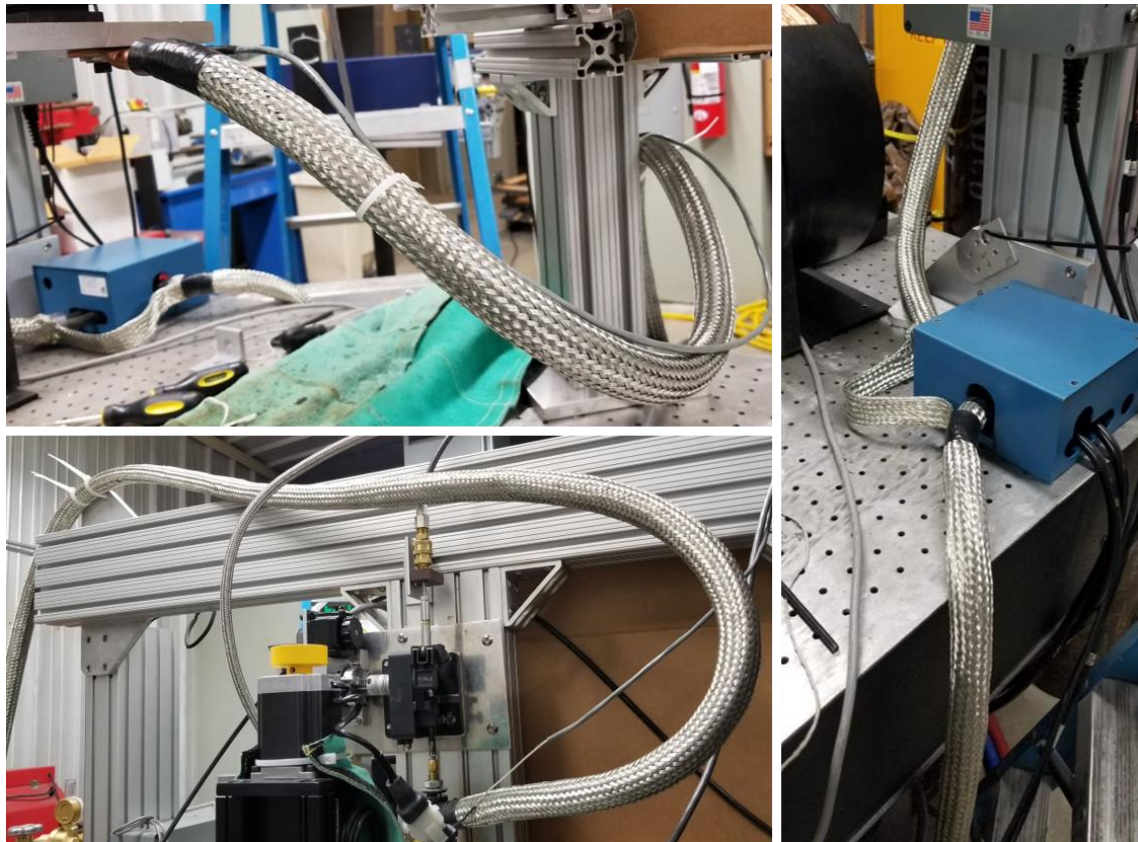


Figure 71: Shielding on welding leads. All shielding was connected to the earth ground.

Before installing shielding, the welding leads were run through clear plastic tubing. The plastic tubing was used to increase the distance between the copper conductors in the welding leads and the shielding and to make the distance constant. Because the shielding was connected to earth ground, the voltage difference between the shielding and copper conductor would be around 10kV when the high frequency arc starter was energized. An electric field created by 10kV potential separated only by the thickness of the welding lead insulation would be too strong for the insulation to withstand over many arc starts. Therefore, plastic tubing was added

to both increase the distance, and provide extra insulation between the conductor and the shielding. Clear plastic tubing was used because it does not contain air pockets within the plastic, which could break down under the intense electric field.

Once the welding leads were pulled through the clear plastic tubing, braided shielding was installed over the tubing. An important aspect of proper shielding was to connect one end of the shielding to earth ground. Connecting the shielding to ground ensured that absorbed EMI could be drained into the earth ground. Only one end of the shielding was connected to ground to eliminate the possibility of ground loops forming in the shielding.

Although shielding the welding leads prevented EMI from being emitted, parts of the welding circuit, such as the work piece, could not be effectively shielded. To prevent the remaining EMI from interfering with connections and communications, shielding was installed on cables that connected the various devices. Additional noise reduction was achieved by installing ferrite chokes (RF chokes) on the same cables. Figure 72 shows cables with shielding and ferrite chokes installed.

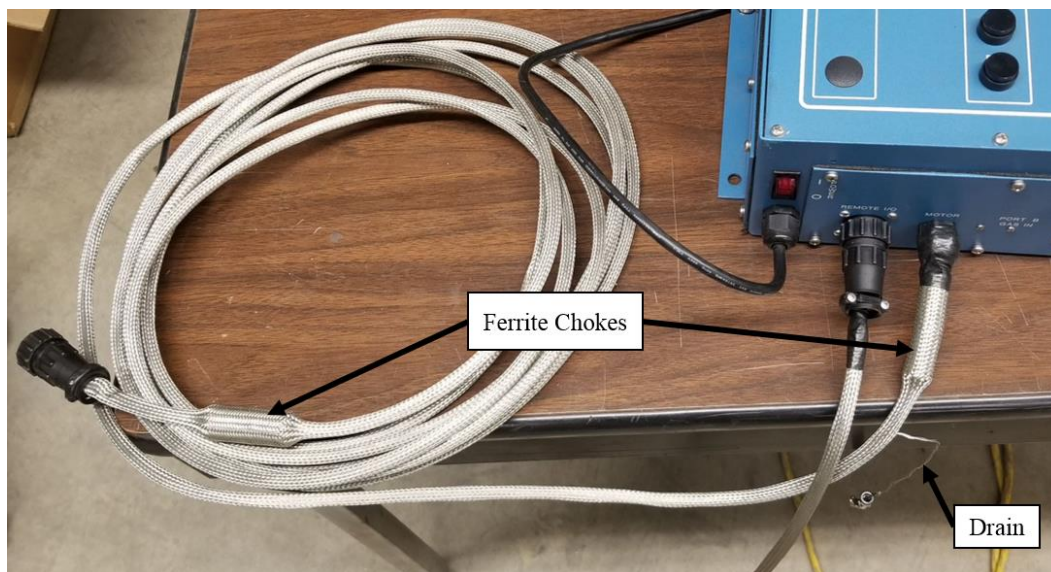


Figure 72: Ferrite chokes and shielding installed on cables. Shielding was installed over the ferrite chokes and drain was not routed through a ferrite choke to ensure EMI induced currents could flow unimpeded to earth ground.

As seen in Figure 72, the shielding was installed over the ferrite chokes. Ferrite chokes provide impedance to high frequency signals that pass through the center of the choke. If the shielding goes through the ferrite choke rather than over it, the choke will impede the flow of EMI induced currents to ground. For the same reason, the drain (wire that connects the shield to ground) does not pass through the ferrite choke as shown in Figure 72.

6.6.3.2. Software Solution

Shielding and grounding was effective at keeping EMI from interfering with most of the electronics and communications in the lab. However, several devices were still affected by the high frequency arc starter's EMI. One such device was the Galil motion controller. Roughly 30% of arc starts using the high frequency arc starter caused the Galil to momentarily disconnect and reconnect to the computer. The main problem with the loss of connection was that upon reconnection, the Galil would connect to a different USB port number (e.g., ttyUSB0 or ttyUSB1). Because a specific USB port number was hard coded in the C++ code controlling the Galil, a change in port number would cause a complete loss of connection. Multiple solutions were tested, including moving the Galil controller under the optical bench and using an optical USB cable, but nothing was effective.

The final solution was to write a new piece of code that could search through the computer's USB ports looking for the port number to which the Galil was connected. Once the port number was found, the code could then reconnect to the Galil using the new USB port number. The code used to reconnect to the Galil motion controller can be found in Appendix D in the motion control code.

6.6.3.3. Laser Proximity and Mounting

Another piece of equipment effected by the high frequency arc starter was the 200W 532nm laser. Even with shielding and grounding implemented, the laser would immediately shut off when the high frequency arc starter was energized. Although the laser's main console and optical head were completely insulated from the table and welding system, the laser was still highly susceptible to the high frequency arc starter.

The solution was to mount the laser on a separate platform as far as possible from the welding system. The laser's power cord was also run from another room in the laboratory. Although the laser was still slightly affected, the failure rate was reduced to about 5%.

6.6.4. Wire Feeder

It was originally assumed that the wire feeder and wire feeder controller would not be in danger of being damaged by the high frequency arc starter because they were connected to ground. However, part way through experimentation, the high frequency arc starter permanently damaged the wire feeder controller.

Although steady-state analysis indicated that the wire feeder controller would not be damaged by the high frequency arc starter, transient analysis could explain why the wire feeder controller was damaged. The welding electrode was connected to earth ground by 20ft of 000AWG welding cable, which has an associated self-inductance. The self-inductance of a cylindrical, nonmagnetic conductor is given by the following equation [54]:

$$L_s = 0.002l \left\{ \ln \left[\left(\frac{2l}{D} \right) \left(1 + \sqrt{1 + \left(\frac{D}{2l} \right)^2} \right) \right] - \sqrt{1 + \left(\frac{D}{2l} \right)^2} + \frac{\mu_r}{4} + \frac{D}{2l} \right\} \quad (21)$$

where:

L_s = self-inductance of conductor (μH)

l = conductor length (609.6cm)

D = conductor diameter (1.0405cm)

μ_r = conductor material relative permeability (for copper: $\mu_r = 0.99999$ [55])

Plugging the parameter values into (21) shows that the welding cable has an inductance of about $8.5\mu\text{H}$. Although $8.5\mu\text{H}$ is not a large inductance, at high frequency arc starter frequencies likely greater than 1MHz, the impedance created by $8.5\mu\text{H}$ could be significant. Figure 73 shows a comparison of a simplified welding circuit from both a steady-state and a transient prospective.

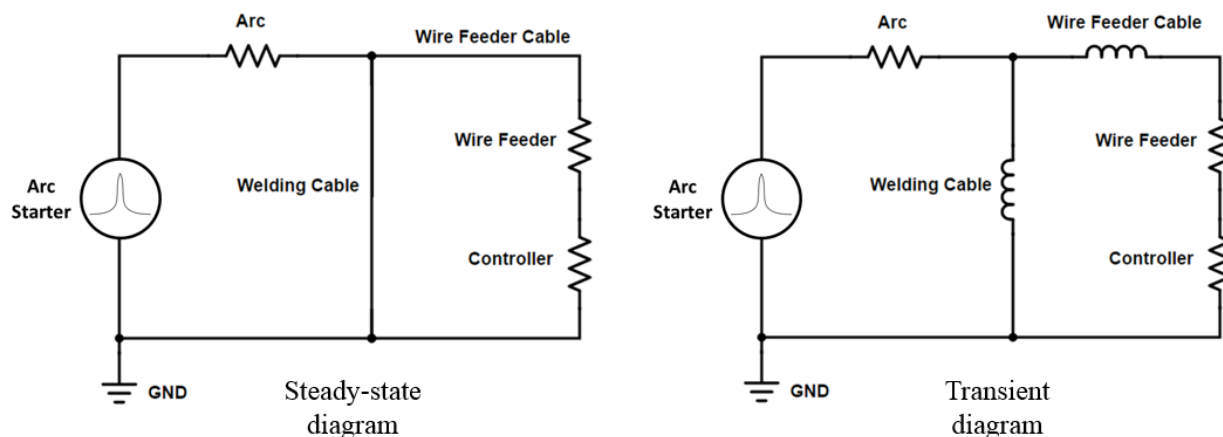


Figure 73: Comparison of steady-state and transient circuit diagrams. The self-inductance of the welding cables only becomes apparent in the transient diagram.

As seen in Figure 73, both diagrams show two paths from the arc starter to earth ground: through the welding cable or through the wire feeder and wire feeder controller. The wire feeder and wire feeder controller are shown as resistors for a simplified analysis. In the steady-state diagram, it can be seen that the welding cable is a short circuit in parallel with the wire feeder and wire feeder controller, and, therefore, no current would ever pass through the wire feeder and wire feeder controller. All the high frequency arc starter's energy would be dissipated across the arc, represented by another resistor (also simplified). Although the welding cable's self-

inductance still exists, it is negligible at low frequencies and can be ignored in the steady-state diagram.

The transient diagram is more representative of the actual welding circuit at high frequencies. It can be seen in the transient diagram that at high frequencies, the welding cable's self-inductance creates a current divider between the welding cable and the wire feeder/wire feeder controller. Some of the high frequency arc starter's energy would dissipate through the wire feeder and wire feeder controller. The portion of the high frequency arc starter's energy that dissipated in the wire feeder controller during experimentation is most likely why the controller was damaged.

6.6.4.1. Insulated Wire Feeder

With the wire feeder controller permanently damaged, a new wire feeding system had to be obtained. An additional CWT wire feeder controller was available to operate the same wire feeder, but it would most likely have been damaged in the same manner as the original CWT wire feeder controller. Therefore, a new wire feeder was built specifically to withstand the high frequency arc starter's pulse by simply insulating the connection between the wire feed motor and the wire feeder. The new wire feeder was built using a stepper motor connected to a polymer-bodied wire feeder as shown in Figure 74.

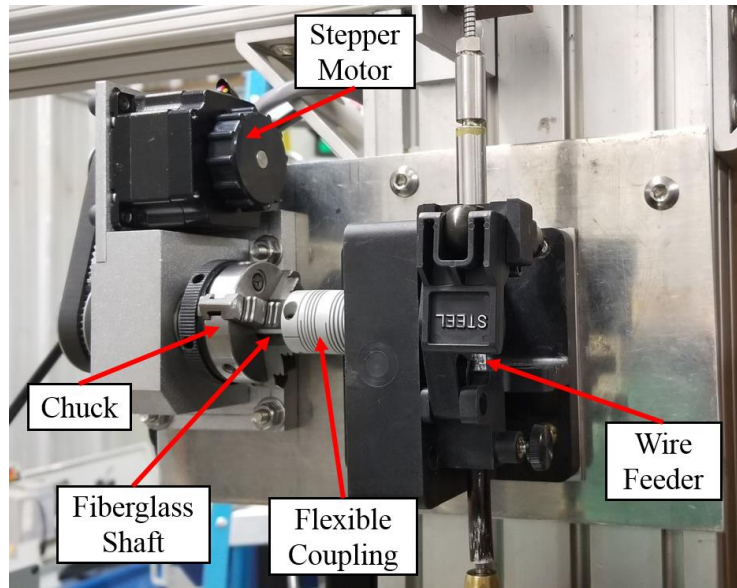


Figure 74: Custom built wire feeder. The motor is insulated from the wire feeder by the fiberglass shaft.

As seen in Figure 74, the wire feeder is connected to the stepper motor through a flexible coupling. One end of the coupling is connected to the drive roller on the wire feeder, and the other end is connected to a fiberglass shaft. The fiberglass shaft insulates the stepper motor from the wire feeder, which is the main purpose of the design. The other end of the fiberglass shaft is connected to a chuck, which is connected to the stepper motor through a gear reduction belt drive.

6.6.4.2. Insulated Wire Feeder Control

Once the insulated wire feeder was built, a means of controlling it had to be established. The easiest way to control the stepper motor was to use the fourth axis on the Galil motion controller. Once connected to the Galil controller, the stepper motor could be controlled similar to the 3-axis motion system.

The main problem using the Galil controller to control the wire feeder was being able to trigger precisely timed wire feed after energizing the high frequency arc starter. As soon as the high frequency arc starter was energized, the Galil controller would lose connection with the

computer. Using the automatic reconnection code was suitable for reconnecting the Galil controller to the computer, but the code could take 100ms or more to reestablish the connection. In experimentation, it was found that the wire feed needed to start within 40ms or less of the arc starting. Therefore, it was not possible to start the arc, reestablish the connection to the Galil controller, and start the wire feed in the desired time frame using the standard USB connection.

The solution was to exploit the Galil controller's digital I/O to trigger wire feed. Using different motion programming techniques, a motion program could be loaded onto the Galil controller prior to starting the arc. The motion program was written to execute only when an input pin on the digital I/O was toggled high. With this method, a USB connection loss between the computer and the Galil controller would not affect the wire feeding routine because the wire feeding program was already loaded on the Galil controller, and its execution was triggered independently from the USB connection.

The Galil controller's digital input pin was connected to a digital output isolation module controlled by the computer. A 5V signal from the output module was provided by the computer's power supply.

Initial tests showed that the new technique operated properly. However, when tested with the high frequency arc starter, it was found that the high frequency arc starter caused the Galil controller to crash (not just lose connection). Further investigation showed that the high frequency arc starter caused excess noise in the computer's power supply, which was connected to the Galil controller's digital I/O. The noise was strong enough to crash the Galil controller. However, the problem was solved by using a 9V battery as the digital signal voltage source instead of the computer's power supply. Tests showed that when using the 9V battery as the

voltage source, the wire feed routine operated properly with the high frequency arc starter. A circuit diagram of the wire feed trigger can be seen in Figure 75.

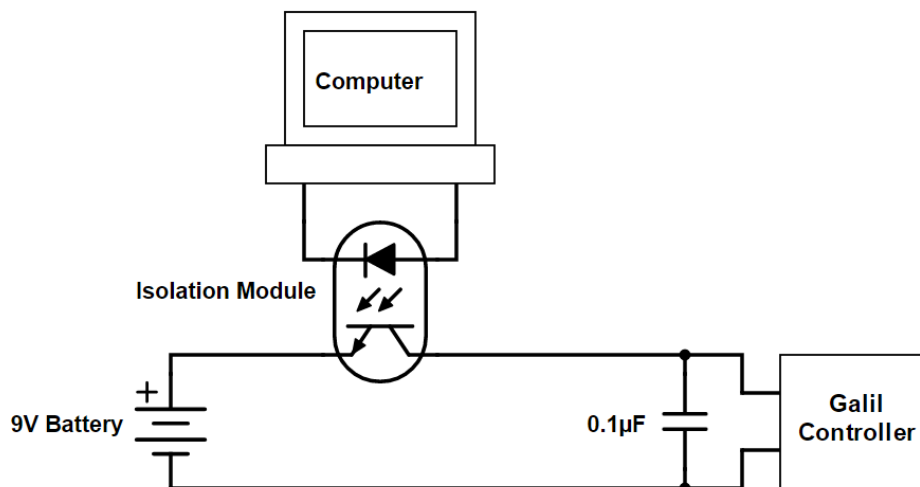


Figure 75: Wire feed trigger circuit diagram. When the computer energizes the isolation module, 9V is applied to the Galil controller's digital input, triggering wire feed. A 0.1µF capacitor was added to filter out EMI.

Although the connection carrying the digital signal from the 9V battery/digital output isolation module to the digital input pin on the Galil controller was shielded with the drain grounded, more extensive testing showed that EMI from the high frequency arc starter was strong enough to prematurely trigger the wire feed routine. Therefore, additional shielding was installed on the connection, and ferrite chokes were added to both ends. In addition, a 0.1µF capacitor was connected between the positive digital signal and the 0V reference directly before the connection to the Galil controller as shown in Figure 75. The EMI prevention techniques can be seen in Figure 76.

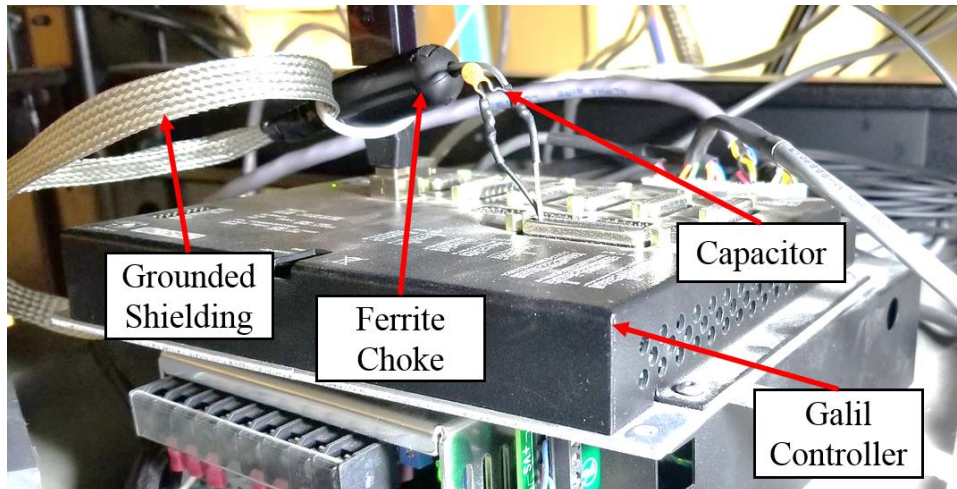


Figure 76: EMI prevention at Galil controller. The ferrite choke and 0.1 μ F capacitor were installed close to the Galil controller to filter out as much EMI as possible.

After installing the EMI prevention seen in Figure 76, unintentional wire feed starts were eliminated.

6.7. Laser

The laser used in GLADiS was an IPG Photonics® GLPN-200-R 200W 532nm laser (S/N JC000883). It was composed of two parts, main console and optical head, which were connected by a fiber optic and wire cable as seen in Figure 77.

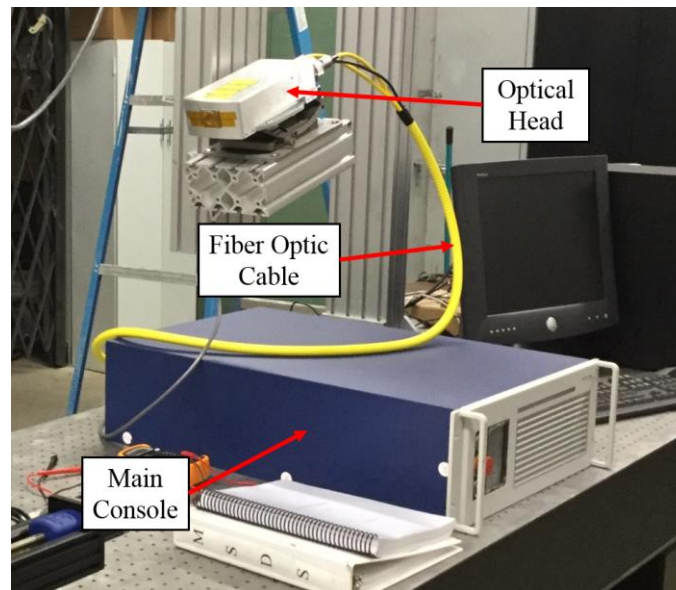


Figure 77: Laser console and optical head connected by a fiber optic and wire cable.

The main console held the power supply and lasing cavity, which delivered infrared (IR) radiation (1064nm laser beam) to the optical head. The optical head housed a second harmonic generator (SHG) which converted the IR laser beam into a green (532nm) laser beam.

According to the laser's specifications, the laser beam had a 0.6mm diameter at the optical head's output window, with a full angle beam divergence of 10mrad. The optical head was mounted on a pitch and rotate stage to allow more precise aiming of the laser beam.

The laser used a quasi-CW (quasi-continuous-wave) operation mode to produce maximum peak power without producing excessive heat in the optical head. Although the optical head was air cooled, the main console had to be liquid cooled by an IPG Photonics chiller.

The laser was controlled by the computer through an RS-232 interface. A C++ class (see Appendix F) was created to turn the laser on and off, adjust the laser power, and read the laser power.

To keep the optical head safe from weld spatter and heat from the arc, it was desired to have the optical head placed at least 15in away from the arc (much further than 15in if it was to be used in conjunction with the arc starter). However, the laser beam's 10mrad divergence resulted in a large spot size at extended distances away from the output window. For example, at 15in away from the output window, the spot size can be calculated as illustrated in Figure 78.

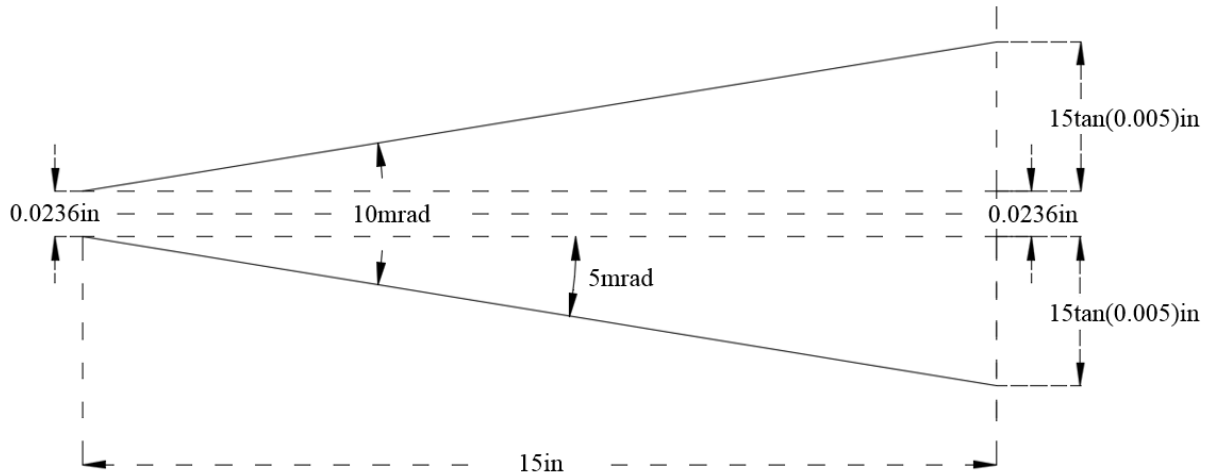


Figure 78: Laser beam divergence illustration. Even over a short distance, a 10mrad beam divergence results in a much larger spot size than the original beam diameter.

Note that the divergence angles in Figure 78 are exaggerated to improve the illustration's clarity. Using the initial beam diameter (0.6mm or 0.0236in) and the divergence angle, the beam diameter at 15in away from the output window can be calculated as follows:

$$D_f = D_i + 2(l)\tan(\theta) \quad (22)$$

where:

D_f = final beam diameter

D_i = initial beam diameter

l = distance between initial and final diameters

θ = half angle beam divergence

Plugging values into (22) yields:

$$D_f = 0.0236in + 2(15in)\tan(0.005) = 0.174in$$

Notice that over a 15in distance, the laser beam's diameter has increased to more than seven times larger than the initial diameter. Also, the laser beam must impinge upon the work

piece at an angle to avoid hitting the welding torch, which further increases the spot size in contact with the work piece.

Although it was unknown how the beam diameter would affect the welding process, it was speculated that focusing the beam would improve the laser's arc stabilizing ability. A plano-convex (PCX) lens with a 250mm focal length was obtained to focus the laser beam. A focal length of 250mm was selected to allow the lens to be placed at least 250mm (9.8in) from the welding arc to protect the lens. The lens material was selected to be fused silica. Fused silica has a high transmission at 532nm (greater than 90%), almost no thermal expansion, and excellent thermal shock resistance, making it ideal for focusing a high powered 532nm laser beam. The lens had a coating to eliminate reflection of 532nm wavelength light.

Because the laser beam had a measureable divergence, the lens could not simply be placed 9.8in (focal length) away from the work piece to minimize the spot size. When attempting to focus a diverging beam, the point where the beam focuses has to be calculated using the lens equation (23). The actual position of the lens and optical head relative to the work piece was calculated using the lens equation as illustrated by Figure 79.

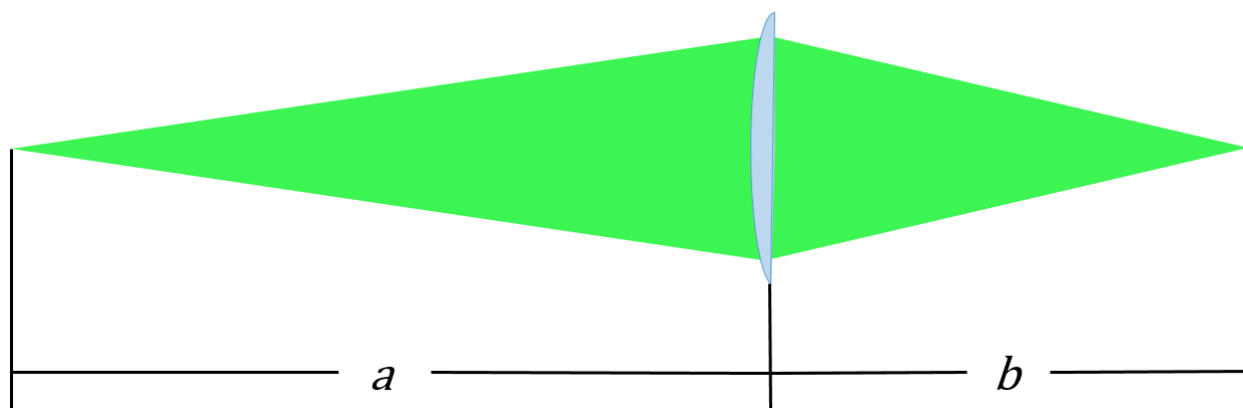


Figure 79: Illustration of lens equation.

The lens equation is given by:

$$\frac{1}{f} = \frac{1}{a} + \frac{1}{b} \quad (23)$$

where:

f = lens focal length

a = distance from initial focus point to lens

b = distance from lens to focus point

It can be seen in (23) that if a is less than f , b has to be negative, and if b is less than f , a has to be negative. Therefore, a and b both have to be greater than f to properly fulfill (23) and focus the laser beam.

To design the laser optics configuration, the distance between the work piece and the lens was selected to be 15in. Using the specified f of 9.8in and selected b of 15in, a could be calculated with (23) as follows:

$$\frac{1}{a} = \frac{1}{f} - \frac{1}{b} \Rightarrow a = \frac{1}{\frac{1}{f} - \frac{1}{b}} = \frac{bf}{b-f} = \frac{(15in)(9.8in)}{15in - 9.8in} = a = 28.3in$$

Because the beam diameter is not zero at the optical head's output window, a begins somewhere inside the optical head and is not the distance from the output window to the lens. The distance inside the optical head where a begins could be calculated using the beam divergence and the initial beam diameter as follows:

$$l_a = \frac{D_i}{2\tan(\theta)} \quad (24)$$

where:

l_a = length from output window to location where a begins within the optical head

D_i = initial beam diameter

θ = half angle beam divergence

Plugging actual values into (24) yields:

$$l_a = \frac{0.0236in}{2\tan(0.005)} = 2.36in$$

Therefore, the output window was to be placed a distance of $a - l_a$ from the lens:

$$a - l_a = 28.3in - 2.36in = 25.9in$$

A schematic of the final laser and optics setup can be seen in Figure 80.

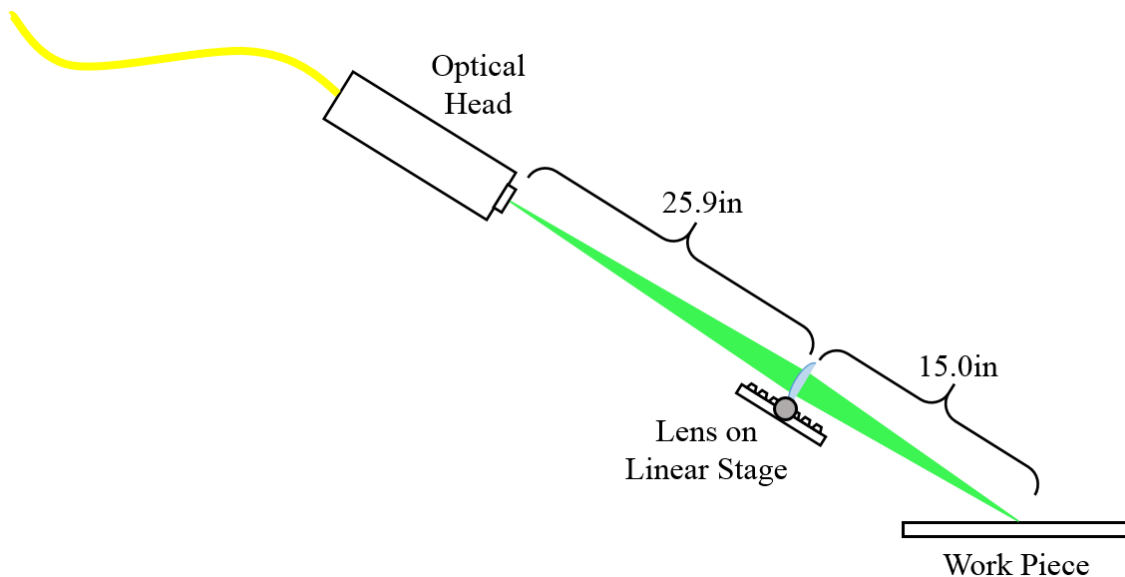


Figure 80: Laser and optics setup schematic. The lens was mounted on a linear stage to allow spot size adjustment.

As seen in Figure 80, the PCX lens was mounted on a linear stage to allow spot size adjustment and fine tuning of the lens position. Initial tests showed that the laser and optics setup was effective at focusing the laser beam on the work piece.

6.8. Summary

With each piece of equipment operational, the whole system (GLADiS) could be assembled. A block diagram of GLADiS can be seen in Figure 81.

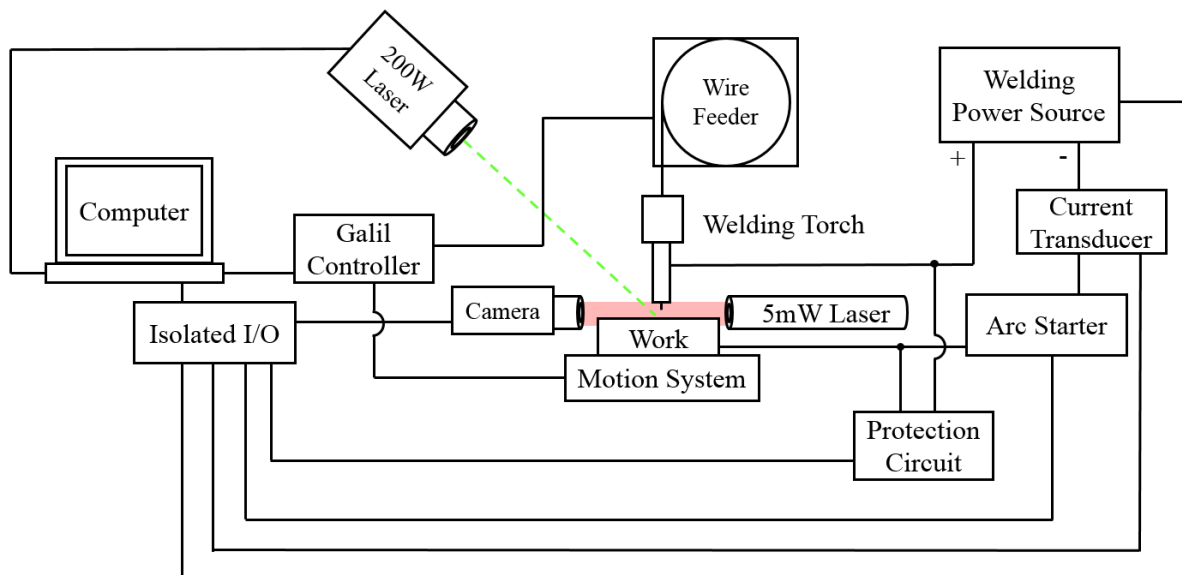


Figure 81: GLADiS block diagram.

The block diagram in Figure 81 represents the configuration with the insulated wire feeder controlled by the Galil controller. The controlled outputs included welding current, WFS, laser power, work piece position, and camera triggering. The process inputs were the welding current and the power source voltage. High-speed videos were stored in the high-speed camera and used for post process data analysis.

7. Continuous Weld Beads

With each piece of equipment operational and individually characterized, the system could be configured to produce welds. Before attempting to implement SiDD, the system was characterized by producing continuous weld beads, similar to a conventional GMAW processes. Characterizing the system involved depositing continuous weld beads using a variety of parameters to determine system attributes such as parameter limits, droplet detachment characteristics, and overall system behavior.

In addition to producing single, continuous weld beads, the system's ability to additively manufacture single bead width walls with standard, continuous deposition techniques was tested. To test the nature of droplet detachment, current pulsing strategies were also investigated.

7.1. Experimental Methods

Throughout experimentation, two types of consumables were used: shielding gas and wire. The only type of shielding gas used was 98% Ar, 2% O₂. The 98% Ar, 2% O₂ shielding gas is optimal for spray transfer or pulsed GMAW because it reduces surface tension and facilitates droplet detachment.

Two types of copper coated wire were tested: ER70S-3 and ER70S-6. The difference between wires is that ER70S-6 can have nearly double the concentration of manganese (Mn) and silicon (Si) compared to ER70S-3. Mn and Si act as deoxidizers and allow ER70S-6 to be used for welding steels with moderate amounts of scale and/or rust. However, as the molten tip of the electrode solidifies, the larger concentration of deoxidizers can cause an excessive buildup of oxides on the electrode tip. The buildup of oxides on the electrode tip can act as an insulator, making subsequent arc starts more difficult.

7.1.1. Arc Initiation and Termination

Before continuous welds could be made efficiently, an arc initiation technique had to be developed. For depositing continuous weld beads, a standard short circuiting arc start was sufficient. Because typical GMAW processes use CV power supplies, arcs are automatically started by the sudden spike in current when the wire short circuits to the work piece. However, GLADiS's power source was CC. With a CC power source, there is no spike in current when the wire shorts circuits to the work piece.

To perform a short circuiting arc start with the CC power source, an arc starting procedure had to be developed in the C++ control code. The basic steps for the arc starting procedure implemented in the control code are listed below:

1. Set current to a value high enough to instantly melt the wire electrode when a short circuit is made with the work piece
2. Enable the power source/welding arc
3. Begin feeding wire with the wire feeder at the desired WFS
4. Use voltage sensing to determine when the wire short circuits to the work piece
5. After waiting 35ms for the wire to melt and arc to start, reduce current to prevent wire from melting back to the contact tip

The arc starting procedure's five steps were coded into the welding process control program and tested until optimal parameters (e.g., starting current and wait time) were obtained. The section of code that controlled the arc starting procedure can be seen in Appendix G.

As discussed in the consumables section, a layer of oxide (usually SiO_2) is often left on the end of the wire electrode after a weld. If the oxide layer is thick enough, the electrical insulation it creates between the wire and the work piece can prevent a short circuiting arc start.

To facilitate arc starting, a wire sharpening arc termination procedure was developed. Wire sharpening techniques use a pulse of current at the termination of the arc to force remaining molten droplets off the end of the wire electrode. When the end of the wire solidifies after a weld, the oxide layer is much thinner if a droplet is not present.

To create a wire sharpening procedure, a current pulse was simply added at the end of the welding control code. Different current pulse heights and times were tested until optimal parameters were obtained to leave a sharp point on the electrode. See Appendix G for the code used in the wire sharpening/arc termination procedure.

7.1.2. Parameter Space

Once the welding arc could be started automatically, tests could be conducted to determine the system's parameter space. The parameter space consisted of many combinations of parameters (i.e., current, WFS, etc.) that resulted in a stable welding arc. The first weld tests were conducted at constant current, WFS, and CTWD. The tests were configured to determine the range of welding currents at various WFSs. The range of current for each WFS was found by starting at the minimum possible current and stepping the current up in 2A increments to the maximum possible current.

The minimum current was determined by observing the lowest current that could maintain the arc without short circuiting the wire to the work piece. The maximum current was determined by observing the electrode extension. The level of current that caused a near zero electrode extension was selected as the maximum current. The stable current range was determined for WFSs from 100ipm to 150ipm in 5ipm increments.

7.1.3. Wall Construction

Once the parameter space was determined, a set of parameters was selected to build the first wall specimen using layers of continuous weld beads. During the parameter space test, it was found that a 140ipm WFS at 190A produced an exceptionally stable arc and a uniform weld bead using 0.045in ER70S-3 wire. Before starting the wall build, a welding travel speed had to be found. A travel speed was found by testing various travel speeds and selecting the fastest travel speed that produced a uniform weld bead. A fast travel speed was selected because it would result in a thinner wall.

The wall was built by depositing continuous weld beads on top of one another until a wall was formed. Each layer was deposited in the opposite direction as the previous layer to mitigate start and end geometric effects.

7.1.4. Pulsed Current

The next step was to investigate droplet detachment behavior by developing pulsing parameters to obtain ODPP (one-drop-per-pulse). Pulsing parameters were developed using the following procedure [56].

- 1. Calculate the volume of wire melted per second and the volume of each droplet at nominal spray transition parameters, and calculate the theoretical droplet frequency:**

$$V_m = \frac{\pi(WFS)D^2}{4(60\text{ }^S/min)} \quad (25)$$

$$V_d = \frac{\pi D^3}{6} \quad (26)$$

$$DF = \frac{V_m}{V_d} \quad (27)$$

where:

V_m = volume melted per second (in^3/s)

WFS = nominal wire feed speed at spray transition (ipm)

D = wire diameter (in)

V_d = volume of each droplet (in^3)

DF = droplet frequency (Hz)

Typical spray transition parameters for ER70S-3 (or ER70S-6) were known to be about 220A welding current at 375ipm WFS. The nominal spray transition parameters were used in (25), (26), and (27) as follows:

$$V_m = \frac{\pi(375 \text{ in}/\text{min})(0.045 \text{ in})^2}{4(60 \text{ s}/\text{min})} = 9.94(10^{-3}) \text{ in}^3/\text{s}$$

$$V_d = \frac{\pi(0.045 \text{ in})^3}{6} = 4.77(10^{-5}) \text{ in}^3$$

$$DF = \frac{9.940(10^{-3}) \text{ in}^3/\text{s}}{4.771(10^{-5}) \text{ in}^3} = 208 \text{ Hz}$$

2. Approximate the melting rate control linear relationship for pulsed GMAW:

$$m = \frac{I_{DC}}{MR} \quad (28)$$

where:

m = melting rate control linear relationship

I_{DC} = DC spray transition current (nominally 220A for 0.045in ER70S-3)

MR = melting rate = DC spray transition WFS (nominally 375ipm for 0.045in ER70S-3)

The melting rate control linear relationship is found by using (28) as follows:

$$m = \frac{220 \text{ A}}{375 \text{ in}/\text{min}} = 0.587 \text{ A} \cdot \text{min}/\text{in}$$

3. Calculate a constant, C , using (29). Let $t_p = 1/DF$:

$$C = I_{DC}^2 t_p \quad (29)$$

where:

t_p = peak time, initially set to inverse of drop frequency

C = constant

The constant can be calculated using (29) as follows:

$$C = (220A)^2 \left(\frac{1}{208Hz} \right) = 232A^2 \cdot s$$

4. Calculate I_p by adding 50A to I_{DC} , and calculate t_p using (30):

$$t_p = \frac{C}{I_p^2} \quad (30)$$

where:

I_p = pulsing parameter peak current (A)

t_p = pulsing parameter peak time (s)

I_p and t_p can be calculated as follows:

$$I_p = 220A + 50A = 270A$$

$$t_p = \frac{232A^2 \cdot s}{(270A)^2} = 3.19(10^{-3})s$$

$$t_p = 3.19ms$$

5. Calculate the total pulse time using (31):

$$t_t = \frac{V_d(m)(60^S/m)}{A(I_{ave})} \quad (31)$$

where:

t_t = total pulse time (s)

A = cross-sectional area of wire electrode (in^2)

I_{ave} = intended operating current of wire electrode (about 160A)

Note that the goal of pulsed GMAW is to exploit the benefits of spray transfer, but at average currents and WFSs closer to short circuiting transfer. Therefore, the average current (I_{ave}) is selected from the wire manufacturer's range of rated currents for short circuiting transfer. Because the average current is based upon short circuiting transfer, the WFS for the final pulsing parameters is also based upon short circuiting transfer at the selected average current. For a 160A current, the nominal rated WFS is 150ipm.

The total pulse time is calculated as follows:

$$t_t = \frac{4.77(10^{-5})\text{in}^3(0.587 A \cdot \text{min}/\text{in})(60 S/m)}{1.59(10^{-3})\text{in}^2(160A)} = 6.60(10^{-3})s$$

6. Calculate background time using (32):

$$t_b = t_t - t_p \quad (32)$$

where:

t_b = pulsing parameter background time (s)

t_b is calculated as follows:

$$t_b = 6.60(10^{-3})s - 3.19(10^{-3})s = 3.41(10^{-3})s$$

$$t_b = 3.41ms$$

7. Calculate the background current using (33):

$$I_b = \frac{(I_{ave}t_t) - (I_p t_p)}{t_b} \quad (33)$$

where:

I_b = pulsing parameter background current (A)

I_b is calculated as follows:

$$I_b = \frac{(160A)(6.60(10^{-3})s) - (270A)(3.19(10^{-3})s)}{3.41(10^{-3})s} = 57.1A$$

Once a working set of pulsing parameters was calculated using the seven steps above, a C++ code was written to implement the parameters and produce a weld.

Welds were monitored using the high-speed camera. High-speed video images from the camera were used to optimize the pulsing parameters. Parameter optimization involved tuning the peak parameters to obtain ODP. For instance, if multiple drops detached on a single pulse, the peak time and/or peak current was reduced; if a drop did not detach on every pulse, the peak time and/or peak current was increased. Welds were made using both ER70S-3 and ER70S-6 to compare the difference.

Once optimal pulsing parameters were obtained, the maximum travel speed was found by increasing the travel speed until the weld bead was no longer uniform in width. A new wall was manufactured using the pulsed GMAW operation mode at the maximum travel speed. Similar to the wall made using constant, non-pulsed current mode, each layer was deposited in the opposite direction as the previous layer.

An additional wall was built without alternating the deposition direction to demonstrate the start and end geometric effects.

7.2. Results and Discussion

Results of the continuous weld bead tests would provide invaluable information going forward. Each test would produce valuable data and help generate a sense of the system's overall behavior.

7.2.1. Arc initiation and Termination

Through trial and error experiments, it was found that a starting current of 475A for a 35ms duration resulted in a robust short circuiting arc start. Figure 82 shows frames from the high-speed camera capturing a short circuiting arc start.

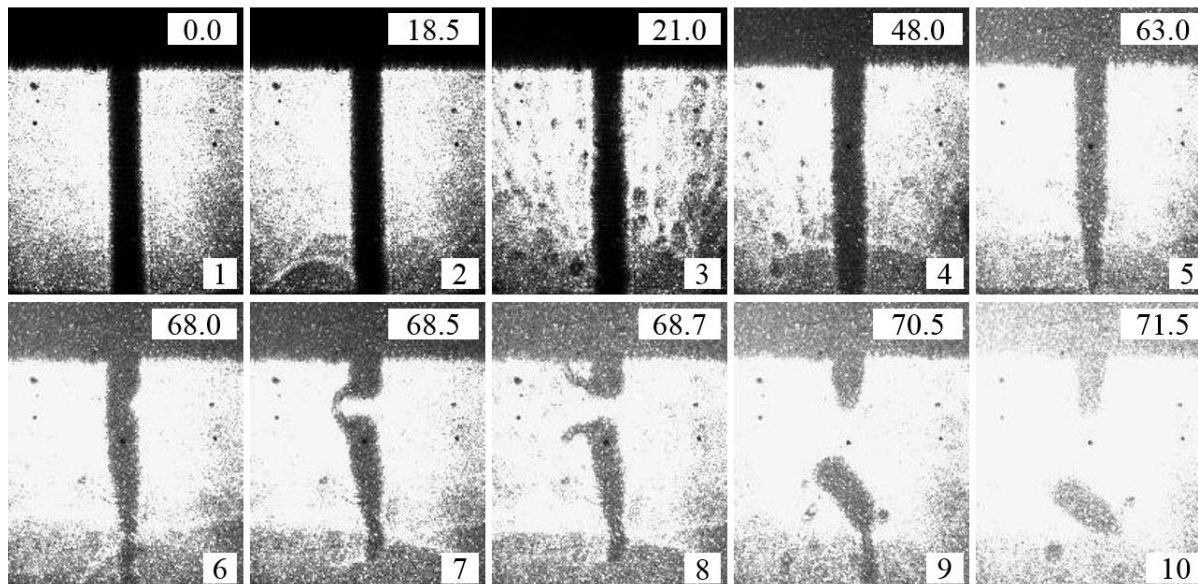


Figure 82: Short circuiting arc start. The number in the top right-hand corner of each frame is the time stamp in milliseconds (ms), and the number in the bottom right-hand corner of each frame is frame number.

A time stamp in milliseconds for each frame is given in the top right-hand corner of each frame in Figure 82. It can be seen that the short circuiting arc start duration is just over 70ms. The number in the lower right-hand corner of each frame represents the order in which the frame was taken. Frame 1 shows the wire electrode just before it makes contact with the work piece. By frame 2, the wire has made contact and resistive heating is initiated as indicated by the

thermal gradient line seen to the left of the wire in frame 2. Frame 3 shows metal vapors evaporating from the wire/work piece interface. In frame 4, slight necking begins to occur at the wire/work piece interface. Frame 5 shows the end of the wire continuing to neck down and beginning to melt. By frame 6, the wire begins necking closer to the contact tip while the lower portion turns into a liquid column. Frames 7 and 8 show the wire being ripped apart by intense electromagnetic forces generated by the 475A starting current. Frames 9 and 10 show portions of the wire being ejected as spatter as the arc is initiated.

The violent nature of a short circuiting arc start, as shown by Figure 82, demonstrates why noncontact arc starting techniques are vital to achieving fine geometric resolution. Noncontact arc starting techniques would allow the arc to be initiated without a high starting current and spatter. However, for system characterization with continuous weld beads, the short circuiting arc starting procedure was effective.

The arc termination (wire sharpening) technique was also tested. It was found that a current pulse of 475A for an 18ms duration was effective at reducing the oxide layer on the end of the electrode after a weld. Much of the arc starting technique's robustness could be attributed to the wire sharpening technique used at the end of each weld.

7.2.2. Parameter Space

The data from the parameter space test including voltage, current, and WFS was plotted in 3-D and is shown in Figure 83. Note that the parameter space was found for a CTWD of 5/16in.

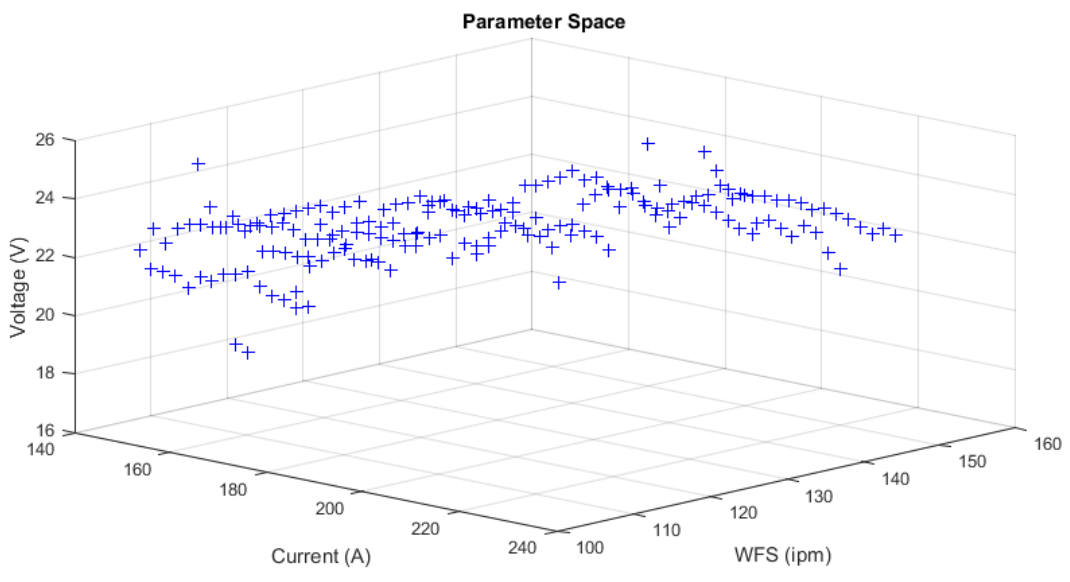


Figure 83: Parameter space, raw data. Data was taken using 0.045in diameter ER70S-3 wire and 98% Ar, 2% O₂ shielding gas.

The blue crosses in Figure 83 represent each data point that was measured. All data points shown represent a set of working parameters that will result in a stable arc. To make the data in Figure 83 easier to visually interpret, a surface (polynomial model) was fit to the data and is shown in Figure 84.

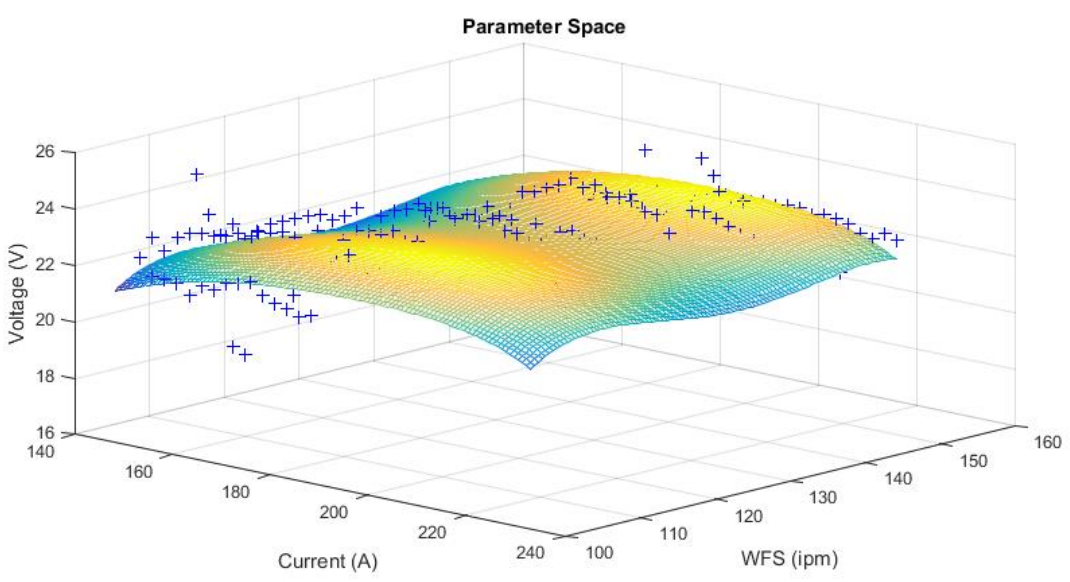


Figure 84: Parameter space with polynomial model. Data was taken using 0.045in diameter ER70S-3 wire and 98% Ar, 2% O₂ shielding gas.

The surface in Figure 84 shows the trend of the data making up the parameter space. Any set of parameters that lie on the surface should result in a stable welding arc.

7.2.3. Wall Construction

The first wall additively manufactured by GLADiS using standard GMAW deposition is shown in Figure 85.

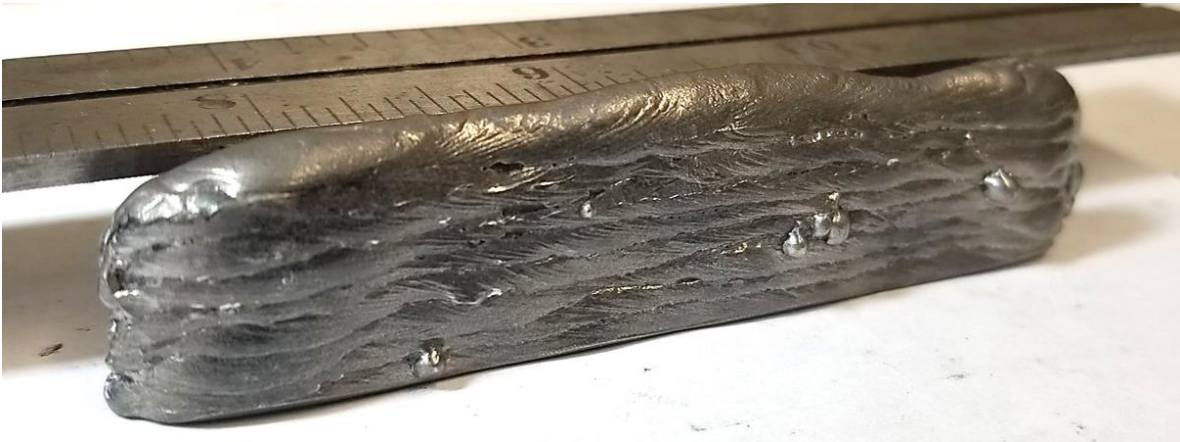


Figure 85: First wall specimen made with continuous weld beads and constant, non-pulsed current.

The wall shown in Figure 85 is about 3in long, 1in tall, and about 1/4in thick. It can be seen that the height is not uniform and the width deviates on both ends. Though the resolution and thickness may be suitable for some applications, it can be seen that standard GMAW deposition is incapable of producing small features with high geometric accuracy.

7.2.4. Pulsed Current

The pulsing parameters calculated using the 7-step process outlined in the experimental methods section are summarized in Table III. Also included in Table III are the final pulsing parameters after tuning with the high-speed camera

Table III: Calculated and tuned pulsing parameters to achieve ODPP: peak current (I_p), peak time (t_p), background current (I_b), and background time (t_b).

Parameter	I_p (A)	t_p (ms)	I_b (A)	t_b (ms)	WFS (ipm)
Initial Values	270	3.19	57.1	3.41	150
Tuned Values	290	3.40	57.1	3.41	150

As seen in Table III, while the background parameters remained the same, the peak parameters had to be slightly adjusted to achieve ODPP. Both the peak current and peak time were increased to ensure a single droplet was detached with each pulse.

Observation of high-speed video footage showed that the most important factor in detaching droplets was to match the droplets' natural oscillation with the current pulses. As a droplet clung to the end of the electrode, it had an oscillation in the vertical direction. If a current pulse was applied while the droplet was in an upward portion of the oscillation, the droplet would not detach. However, if the pulse was applied while the droplet was in a downward portion of the oscillation, it would easily detach. The indication was that droplet momentum was dominant over the electromagnetic force trying to detach the droplet. Only when the downward droplet momentum was favorable with the electromagnetic force could the droplet be detached.

Figure 86 shows high-speed camera frames during a weld using the optimized pulsing parameters.

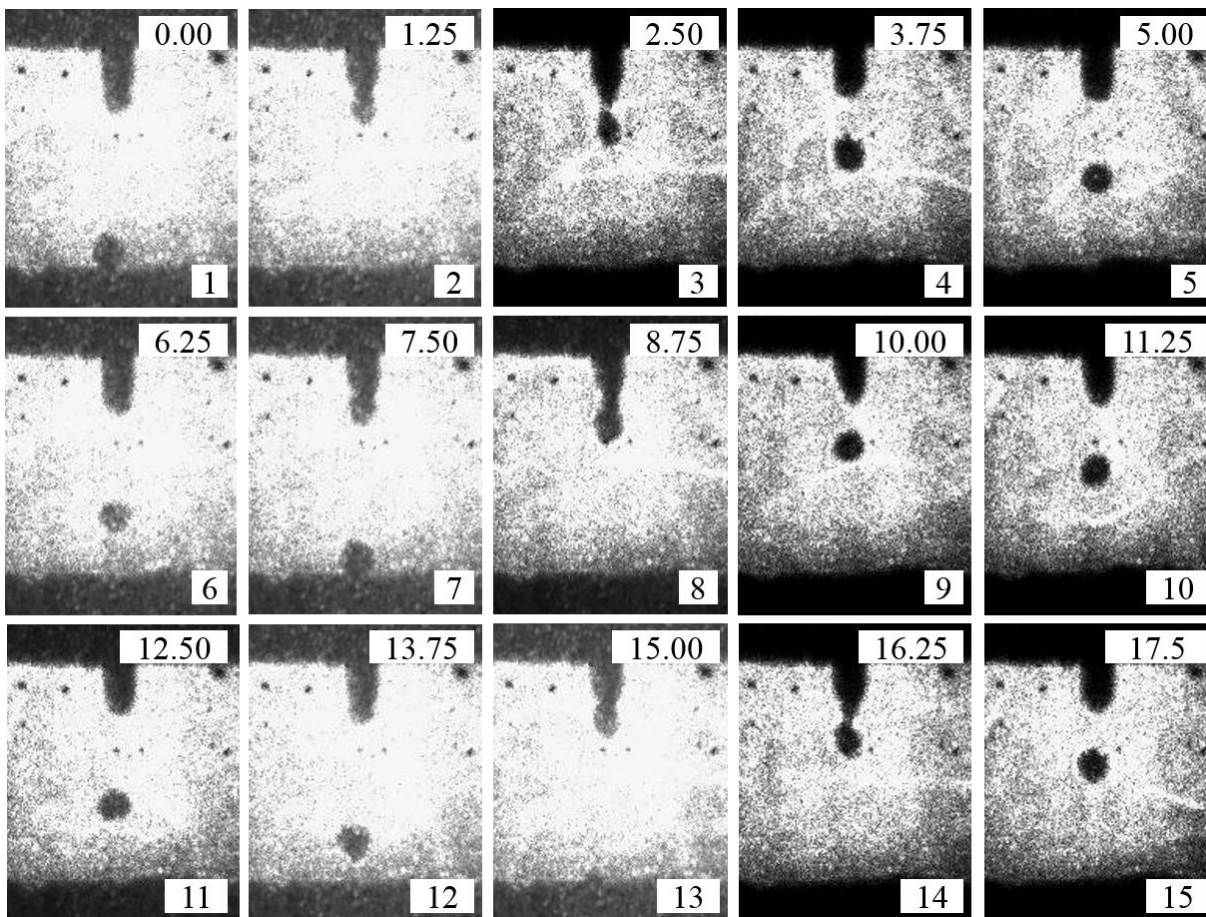


Figure 86: Pulsed GMAW achieving ODPP. The number in the top right-hand corner of each frame is the time stamp in milliseconds (ms), and the number in the bottom right-hand corner of each frame is frame number.

Each frame in Figure 86 has a number in the bottom right-hand corner denoting the time sequence and a time stamp (milliseconds) in the top right-hand corner. The frames were taken at 40,000 frames per second, but only every 50th frame was selected for Figure 86. Therefore, the time step between each frame shown is 1.25ms. Current pulses can be visually detected by comparing the frames' relative brightness. For example, comparing frames 13 and 14, it can be seen that frame 13 is much brighter, meaning that frame 13 was taken during a current pulse.

It can be seen that the frames begin on a current pulse. Frame 2 shows the beginning of a droplet being pinched off the wire electrode. Frame 3 shows the detached droplet immediately after the pulse. Frames 4 and 5 show the droplet being transferred across the arc during the

background current. Frames 6, 7, and 8 show another current pulse forming a droplet and beginning to pinch it off the electrode. Frames 9, 10, and 11 show the detached droplet transferring across the arc. The process repeats once again through the remaining frames.

Although the system achieved ODPP operation, a transient phenomenon was observed in the high-speed footage immediately after the arc start. The transient was in the form of a droplet that would not detach from the electrode tip. The first droplet to form on the electrode after the short circuiting arc start would continuously grow until gravity finally pulled it off the electrode. The droplet could last for as many as 10 pulses without being detached. However, once gravity pulled the drop from the electrode, subsequent drops were detached on every pulse. The same phenomenon was observed for all pulsing parameter tests, and the exact cause is unknown.

Figure 86 shows that ODPP parameters were successfully attained using the 7-step parameter calculation technique and tuning with ER70S-3 wire. However, when the same test was conducted with ER70S-6, ODPP parameters could not be attained. In addition, uniform weld beads could not be made with the ER70S-6. High-speed video footage showed that a number of droplets exploded as they were pinched off the electrode. Although the reasons are unknown, it was speculated that the ER70S-6 wire had gas pockets, inclusions and/or other internal imperfections that caused the droplets to explode.

Figure 87 shows the wall built using the ODPP pulsing parameters at the maximum travel speed of 15ipm for ER70S-3 wire.



Figure 87: Wall built with continuous weld beads using ODPP pulsing parameters with ER70S-3 wire and 98% Ar, 2% O₂ shielding gas.

The wall shown in Figure 87 is about 3.5in long, 0.5in tall, and 3/16in thick. It can be seen that considerable amounts of spatter was produced by the process. Although a 3/16in wall thickness would be suitable for some applications, it can be seen that pulsed GMAW would not be sufficient for building components with fine geometric detail.

Figure 88 shows an image of the wall built using ODPP pulsing parameters without alternating deposition direction between layers.

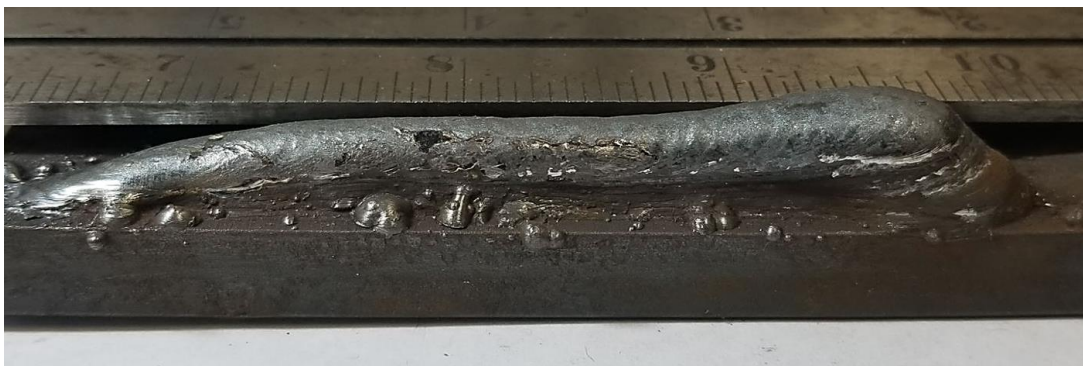


Figure 88: Wall built without alternating deposition direction. The wall was built with continuous weld beads traveling from right to left with ER70S-3 wire and 98% Ar, 2% O₂ shielding gas.

The wall in Figure 88 was built from right to left (all arc starts on the right). It can be seen that the wall slopes down significantly from the end where each layer started. With each subsequent layer, the effect is magnified with further weld metal build up at the start. It can be seen that standard deposition strategies, such as pulsed GMAW, used for AM have to take extra measures to achieve consistent geometry.

7.3. Summary

Continuous weld bead tests provided much needed information about how the system operated. While the short circuiting arc starting and wire sharpening techniques were effective, they demonstrated why noncontact arc starting techniques would be vital to the success of improved deposition strategies. Short circuiting arc starts produced excessive spatter in addition to starting the system in a state of transience, making controlled droplet detachment impossible.

The parameter space test provided valuable insight on the system's stability. It also provided a set of parameters to build a baseline wall specimen to which future specimens could be compared.

The process of developing and tuning pulsing parameters to achieve ODPP provided possibly the most useful information. Observing high-speed footage of droplet detachment and its relation to welding current provided a foundation for achieving single droplet deposition (SiDD).

8. Single Droplet Deposition

Achieving SiDD is the most crucial aspect of bridging the gap between WAAM process' high deposition rate, low geometric resolution and powder-based AM process' low deposition rate, high geometric resolution. SiDD is also a possible solution to the residual stress problems inherent to continuous weld bead WAAM components. This section describes the experiments performed to achieve SiDD and presents the experimental results.

8.1. Experimental Methods

SiDD process parameter development was conducted using ER70S-6 wire and 98% Ar, 2% O₂ shielding gas. The substrate (work piece) material used was 1/4in cold-rolled low carbon steel. Weld metal was deposited on the 1/4in edge of the substrate material.

Before attempts could be made to detach single droplets of weld metal, it was vital to implement an alternate arc starting method. As discussed in the continuous weld bead section, the short circuiting arc starting technique produced spatter (which is a multitude of droplets) and started the system in a transient state that made quick transition to stable droplet detachment difficult. Prior to the development of a noncontact arc starting technique, steel wool was used as a fuse. To start an arc using steel wool, a small wad of steel wool was placed between the wire electrode and the work piece, making sure that the steel wool is in contact with both. When a regular welding current was applied, the steel wool would melt/vaporize like a fuse and the arc would start. Using steel wool would allow the arc to start at normal welding current (or background current) without the need for a high starting current.

Using steel wool fuse arc starting, experiments could be performed to detach single droplets of weld metal. To reduce the number of variables, initial tests were conducted without wire feed. Because a single droplet of weld metal represents only a small length of wire, setting

the CTWD at 0.75in reduced the chances of melting the wire back to the contact tip. Welding parameters were initially set to correspond to a single cycle of the pulsing parameters developed in the continuous weld bead section. Parameters were adjusted based on high-speed camera footage until a single droplet could be detached from the stationary electrode.

Once parameters were obtained to deposit a single droplet, wire feed was added to the deposition process. A wire feeding sequence/routine was developed by using the high-speed camera to observe the amount of wire melted and the melting rate during a SiDD test. The high-speed camera was then used to tune the wire feed sequence to match the melting rate and length of melted wire. C++ code used to obtain SiDD can be found in Appendix H.

A final test was conducted to test the influence shielding gas had on the SiDD process. The SiDD process was executed with and without shielding gas for comparison.

8.2. Results and Discussion

It was found that steel wool was effective at starting the welding arc at low currents and without spatter. However, after multiple tests, it became clear that steel wool was not a practical solution for depositing the large numbers of droplets required to build a component. The main limitation was the amount of time required to place a small amount of steel wool between the electrode and work piece. In addition, high-speed footage showed that remaining steel wool, not consumed by the arc, influenced electric fields on the work piece. The high electric field strength on the sharp tips of the steel wool fibers could cause droplets to transfer in a lateral direction through the arc instead of axially straight down to the work piece.

It was found that the pulsing parameter background current of 57A was too low to initiate the arc, so a slightly higher current of 75A was used upon arc initiation. Once the arc was initiated after 75ms of 75A current, the current was dropped to 50A to form a droplet. A low

background current of 50A ensured that electromagnetic forces would not prematurely detach a droplet. After 100ms of 50A background current, a sufficiently sized droplet was formed. A 4ms pulse of 345A current was found to effectively detach the droplet. After the current pulse, the arc was terminated to prevent additional droplets from forming. Note that a wire sharpening procedure was not necessary because the current pulse was sufficient to detach a droplet without melting additional wire. Figure 89 shows the arc voltage and current that produced single drop deposition.

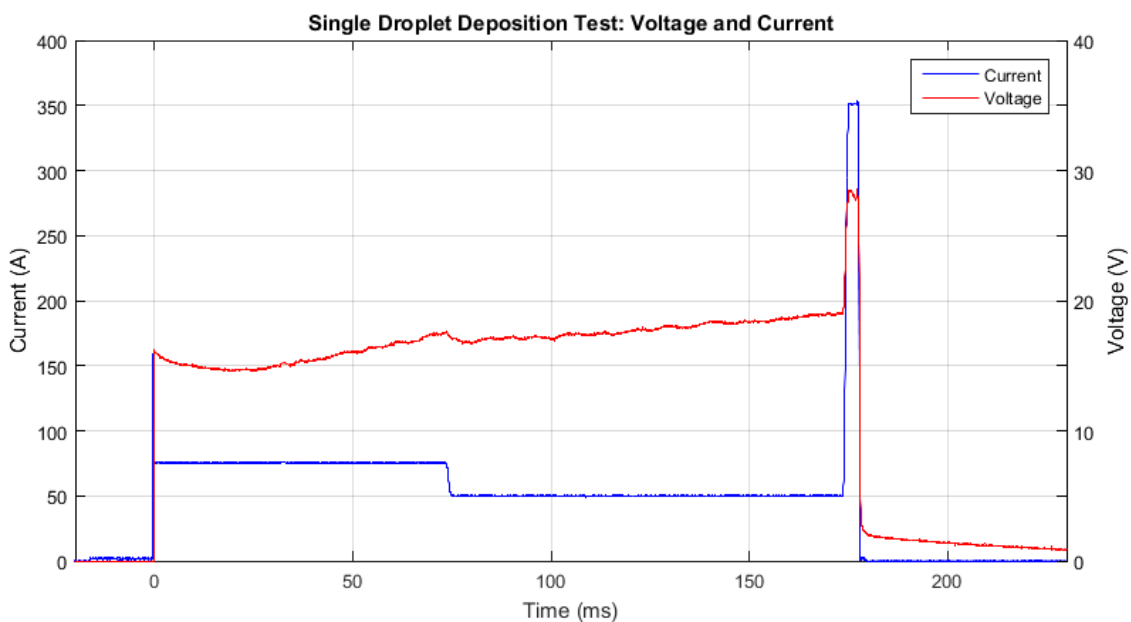


Figure 89: Voltage and current from SiDD test. Left-hand y-axis is the welding current and right-hand y-axis is the arc voltage. A droplet is formed over the first 175ms of background current, and is detached by the current pulse.

In Figure 89, the left-hand y-axis is the welding current and the right-hand y-axis is the arc voltage. Notice that because the welding power source is CC, the current does not vary throughout the deposition process, except when commanded. A high bandwidth welding power source, such as the 2.66kHz bandwidth welding power source used in the present research, is required to produce the current sequence shown in Figure 89.

It can be seen that the voltage is about 0V before the arc is started because the wire is short circuited to the work piece through the steel wool. Once the arc is initiated, indicated by a sudden increase in current, the steel wool melts/vaporizes, and the arc voltage jumps up to about 15V. Upon arc initiation ($t = 0\text{ms}$), there is a slight transience for about 20ms where the arc voltage decreases. However, once the arc becomes stable, the arc voltage increases throughout the remainder of the deposition process, with exception to the point where the current is reduced from 75A to 50A. The steady increase in arc voltage is caused by the increasing arc length as the wire electrode melts into a droplet and the length of solid electrode extension decreases (recall that there is no wire feed for this test). It can be seen that the arc is immediately terminated following the droplet detachment pulse.

Figure 90 shows high-speed frames taken during and after the droplet detachment pulse.

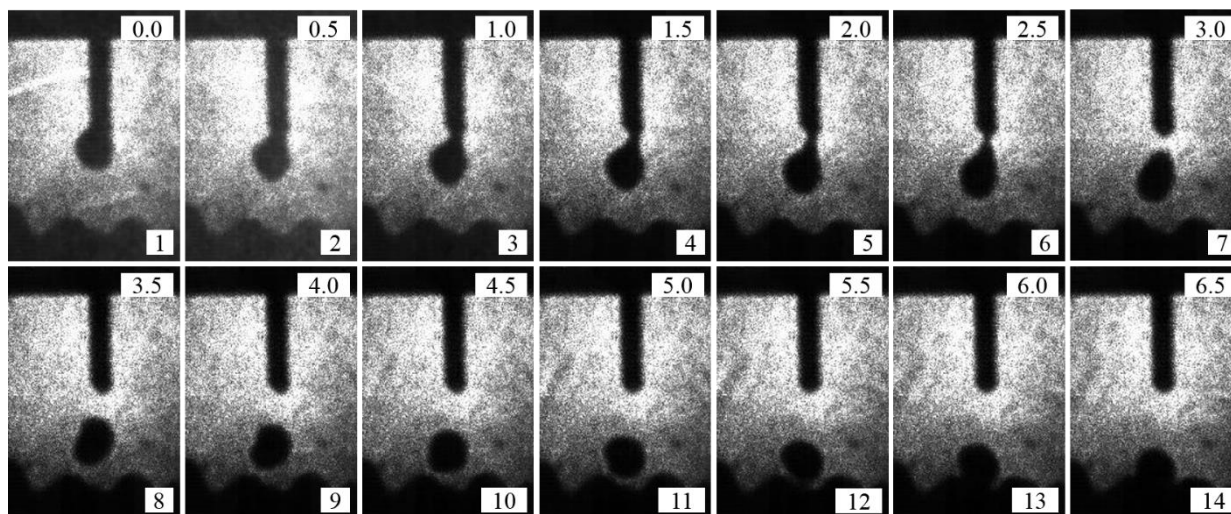


Figure 90: Droplet detachment. The number in the top right-hand corner of each frame is the time stamp in milliseconds (ms), and the number in the bottom right-hand corner of each frame is frame number.

The frames in Figure 90 were taken on 0.5ms intervals. Frames 1, 2, and 3 show the final 1.5ms of the current pulse. It can be seen that the current pulse provides just enough energy to accelerate the droplet in the downward direction and begin necking the droplet/wire interface.

After the current pulse is over (frames 4 through 14), the droplet has sufficient downward momentum to break free from the wire electrode and travel to the work piece.

The next step was to add wire feed to the process. Tuning the wire feeder to match the melting rate and length of melted wire presented several problems. First, when the wire feeder was commanded to start feeding wire from a dead stop, a 100ms delay was observed before the wire began to feed. As seen in Figure 89, the entire deposition process lasted only about 180ms from arc initiation to arc termination. Therefore, if wire was to be fed during the deposition period, the command to initiate wire feed had to be issued before the arc was actually started. The next problem was that the wire feeder continued to feed wire after the wire feed stop command was issued (see wire feeder step response in Figure 37). Therefore, the command to stop wire feed had to be issued at some point during the deposition process.

To tune in the proper wire feeding routine, data from the wire feeder step response test was used in addition to high-speed camera footage. It was found that starting a 130ipm WFS 40ms before the arc was started, and sending the wire feed stop command about 90ms before the arc was terminated was an effective wire feeding routine. A series of high-speed camera frames illustrating the SiDD test with wire feed can be seen in Figure 91.

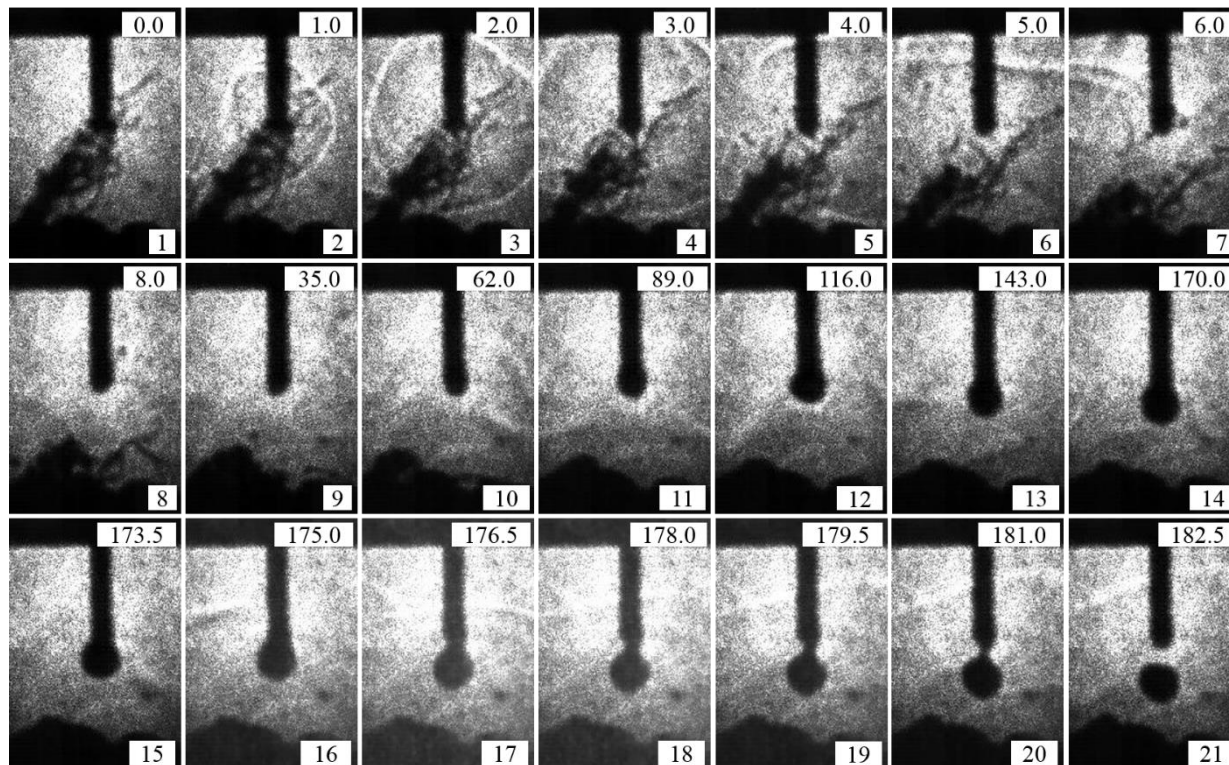


Figure 91: SiDD test with wire feed using steel wool fuse arc starting. The number in the top right-hand corner of each frame is the time stamp in milliseconds (ms), and the number in the bottom right-hand corner of each frame is frame number.

Note that in Figure 91, the frames do not represent evenly spaced time intervals. They were chosen to represent the SiDD test from start to finish. Frames 1 through 7 take place over 6ms and show the arc starting using the steel wool technique. Frame 1 shows the setup directly before the arc is enabled. In frame 2, thermal gradient lines can be seen as the arc is initiated. Frames 8 through 14 take place over about 162ms and show the droplet begin to form on the wire electrode. It can also be seen that the wire is being fed forward as indicated by the decreased arc length. Frames 15 through 21 take place over about 9ms and show the droplet detaching from the wire electrode. Frame 15 shows the droplet directly before the 345A current pulse is applied. The current pulse lasts 4ms from frame 16 to frame 19. Frame 20 shows that the droplet has sufficient downward momentum to continue moving in a downward direction

after the current pulse. By frame 21, the droplet has broken free from the surface tension holding it to the wire electrode.

Figure 92 shows droplets deposited on the edge of a 0.25in thick steel substrate.

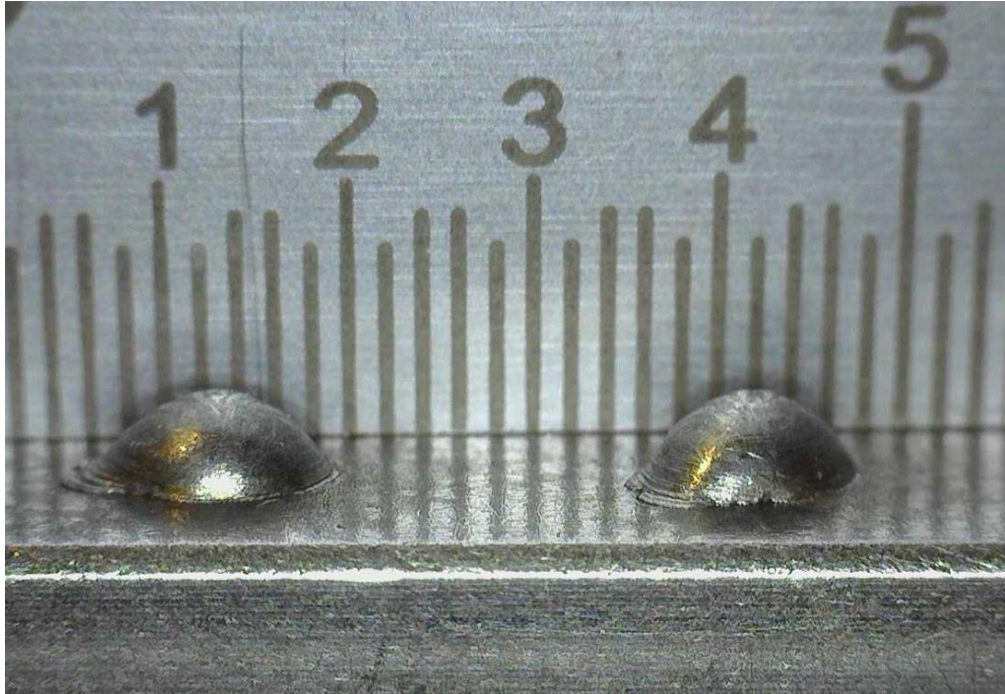


Figure 92: Single droplets deposited using SiDD. The droplets are about 0.1in in diameter.

In Figure 92, the ruler in the background is graduated in 0.02in increments with the numbers representing 0.1in increments. It can be seen that the individual drops have a diameter of about 0.1in.

To analyze the thermal input of SiDD, the power and total energy dissipated by the welding arc during a SiDD test was found. The power and total energy during a SiDD test can be seen in Figure 93.

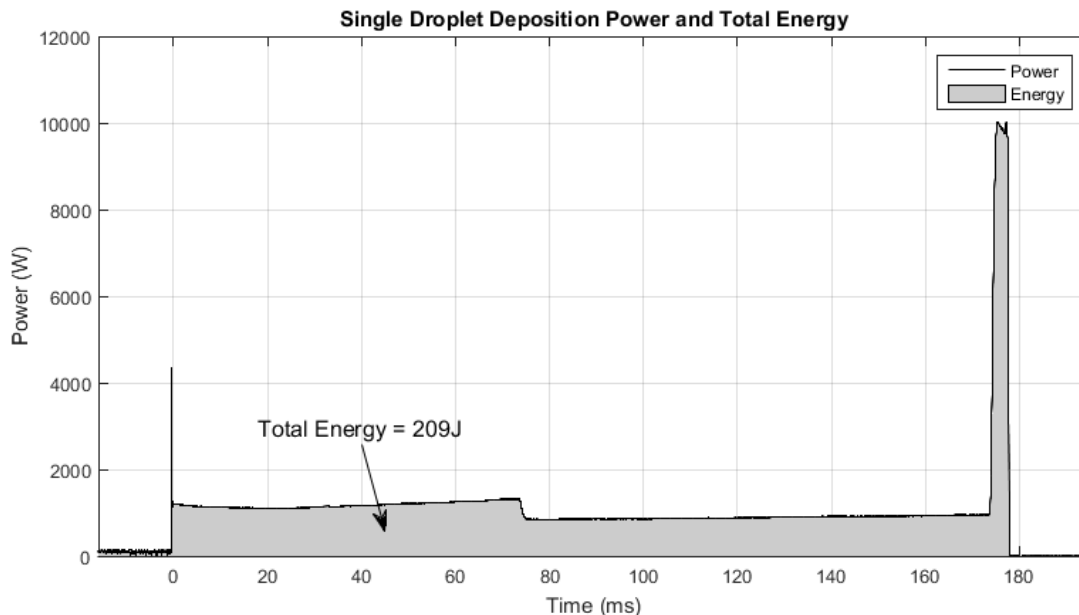


Figure 93: Power and total energy dissipated by the welding arc in SiDD. Power is equal to the arc voltage multiplied by the arc current; total energy is the area under the power curve and was found to be 209J.

The power was calculated by multiplying the arc voltage and the arc current (welding current) data in Figure 89. The total energy was found by numerically integrating the power curve using the trapezoidal integration function in MATLAB. The total energy was found to be 209J. For comparison, a continuous weld at typical process parameter values of 150A arc current and 20V arc voltage that lasted for 180ms would have a total energy of 540J.

It was inferred from the low total energy that the cooling rate of each droplet deposited using SiDD was extremely high. In fact, the droplets could be handled almost immediately after being deposited. The high cooling rate exists because the molten droplets are small enough that substrate's heat sinking ability quickly pulls all the heat from the droplets. In addition, the substrate itself is not excessively heated by the welding arc because the energy dissipated by the arc was only 209J. Because a large, fluid weld pool is not present on the substrate, the droplets appear to sit on the surface rather than wet out into a pool. The 200ms arc forms a pool on the substrate just large enough to create sufficient fusion between the droplet and the substrate.

The next test of the SiDD strategy was to determine the importance of shielding gas as it related to droplet detachment. Tests showed that the shielding gas composition played a highly significant role in droplet detachment. In fact, droplets could not be detached from the wire electrode when no shielding gas was present. High-speed video footage showed that the forces in the arc actually lifted the droplet upwards when no shielding gas was applied. The same exact welding parameters were then used to effectively detach droplets under an envelope of 98% Ar, 2% O₂ shielding gas.

8.3. Summary

Results of the SiDD tests showed that it was possible to detach a single droplet from the wire electrode. SiDD was made possible by an alternate arc starting method and tight control over the welding current.

Although steel wool was an effective alternate arc starting method, it proved to be impractical due to excessive time required to implement. In addition, non-melted/non-vaporized steel wool fibers appeared to have an effect on droplet placement on the work piece. However, SiDD was not possible using short circuiting arc starts, making steel wool a viable alternative for initial tests.

Provided that 98% Ar, 2% O₂ shielding gas was used, the current sequence in Figure 89 proved to be highly reliable at detaching single droplets. If no shielding gas was used, the droplet detaching current pulse actually lifted the droplet upwards rather than pulling it to the work piece.

Proving that SiDD was possible was a major breakthrough. If SiDD could be applied to AM, it would be possible to produce fine geometric features and, potentially, reduce residual stresses in manufactured components.

9. Noncontact Arc Starting

Experiments had shown that SiDD was not possible using traditional short circuiting arc starting techniques. As illustrated in Section 7.3.1, Figure 82, short circuiting arc starts generate excessive spatter, and the high starting currents required can set the system in a long-lasting initial transient. As observed in the pulsed current tests, the transient state caused by the short circuiting arc start made controlled single droplet detachment impossible.

The solution to the short circuiting arc starting problems for the initial SiDD tests was to use steel wool as a fuse to start the arc. Although the steel wool technique was effective for developing SiDD process parameters, it was not a practical solution. To ensure sufficient electrical contact between the wire electrode, steel wool, and the work piece, the work piece had to be cleaned, and the end of the wire clipped to remove oxides. A small piece of steel wool then had to be cut and carefully placed between the wire and the work piece in a manner that would not allow the shielding gas to blow the steel wool away. The process of using steel wool as an arc starting medium took approximately 60s per drop. A specimen build consisting of hundreds of droplets could take many hours using the steel wool technique.

The final solution was to use a noncontact arc starting technique. Noncontact arc starting techniques have been used extensively for manual GTAW processes where tungsten inclusions must be avoided. GTAW typically uses high frequency arc starters to generate an extremely high voltage capable of breaking down the air gap between the electrode and work piece. However, high frequencies and high voltages generated by high frequency arc starters can destroy electronics connected to the system, which is why they are generally only used in manual GTAW applications.

In attempt to avoid the problems inherent to high frequency arc starters, two other noncontact arc starting techniques and a lift starting technique were investigated before moving on to the high frequency arc starter. A total of five different arc starting techniques were investigated: photoemission/laser, alternate plasma source via PAW pilot arc, lift start, high frequency arc starter, and a high frequency arc starter/laser hybrid technique.

9.1. Photoemission/laser

The first noncontact arc starting technique to be investigated was a using a laser to generate sufficient photoemission to light the arc. The theory was that if sufficient numbers of electrons were emitted from either the cathode or the anode via photoemission, the power source's open circuit voltage would start a flow electrons and the arc would initiate.

9.1.1. Experimental Methods

Initial tests were performed using a GTAW torch with a pure tungsten electrode to simplify the experiment. A code was written to energize the welding torch to open circuit voltage and wait until an arc start was detected. After an arc start was detected (as indicated by an increase in current), the arc would be sustained for a few seconds before being terminated.

As seen in Figure 94, the laser was focused on the welding cathode, which was the tungsten electrode in the DCEN configuration.

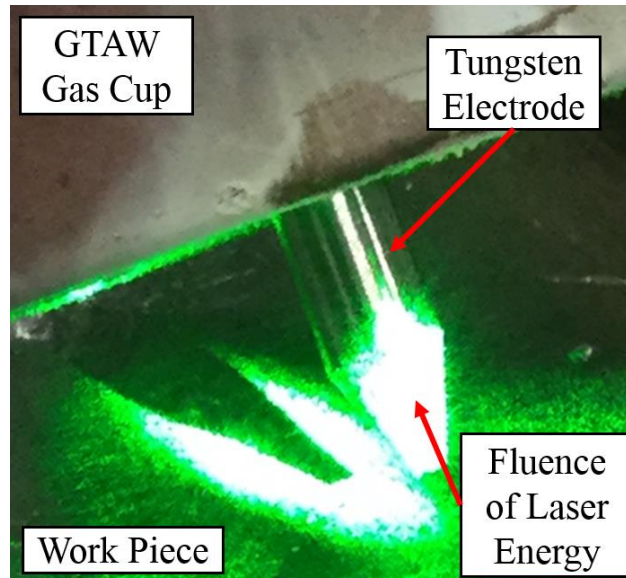


Figure 94: Laser focused on GTAW pure tungsten electrode. The center of the laser beam is focused near the tip of the tungsten electrode.

By observing the shadow on the work piece cast by the tungsten electrode, it can be seen that the center of the laser beam is on the electrode near the tip. Because the laser power distribution is Gaussian, the center of the beam is where most of the laser power exists.

With the electrode at open circuit voltage, waiting for an arc start, the laser was energized and the laser power slowly increased to the maximum 200W output. Even at the maximum laser power, the arc did not start.

The same experiment was then repeated with a graphite coating on the tungsten electrode. Graphite was applied to the tungsten electrode's surface in attempt to increase photoemission and ionization of the arc gap. With graphite added to the electrode surface, the arc started successfully.

Before moving on to a GMAW torch, the same tests (with and without graphite) were conducted with the laser focused on the work piece (the anode) directly under the electrode. Once again, the arc could only be started when graphite was applied to the work piece surface where the laser was focused.

Next, the GTAW torch was replaced with GLADiS's GMAW torch and the same four experiments were repeated: with and without graphite and with the laser focused on the anode and cathode. Because the GMAW torch was configured as DCEP, the cathode was the work piece and the anode was the wire electrode. The CTWD was set at 0.5in and ER70S-6 wire and 98% Ar, 2% O₂ shielding gas were used. With the GMAW torch, the arc could only be started when the laser was focused on the cathode (work piece) with graphite added to the cathode surface.

9.1.2. Results and Discussion

Tests with the GTAW torch showed that photoemission from a metal surface (either work piece or electrode) was not sufficient for starting the welding arc. Even with laser power up to 200W, no arc could be started. However, when graphite was added to the surfaces of the electrode and work piece, the laser produced enough photoemission and/or ionization in the arc gap from the graphite to start the arc.

It was observed that the arc started more effectively when the laser was focused on the cathode (tungsten electrode) with a graphite coating on the cathode. In fact, it was found that laser powers as low as about 20W were able to start arcs when the laser was focused on the cathode and graphite was added.

Test results with the GMAW torch were nearly identical to the results found in the GTAW torch tests. However, the GMAW configuration was more particular about the polarity on which the laser was focused. With GMAW, it was found that arcs could only be started with the laser focused on the cathode (work piece) with graphite added. Focusing the laser on the anode (wire electrode) often resulted in melting the wire electrode before an arc could be started.

The fact that graphite had to be added to start arcs using the laser made the laser arc starting technique an impractical solution. Even with the addition of graphite, reliable arc starts could not be achieved.

9.2. PAW Pilot Arc

The next proposed solution to produce noncontact arc starts without using a high frequency arc starter was to use the pilot arc from a PAW torch. Figure 95 shows a schematic of a typical PAW torch.

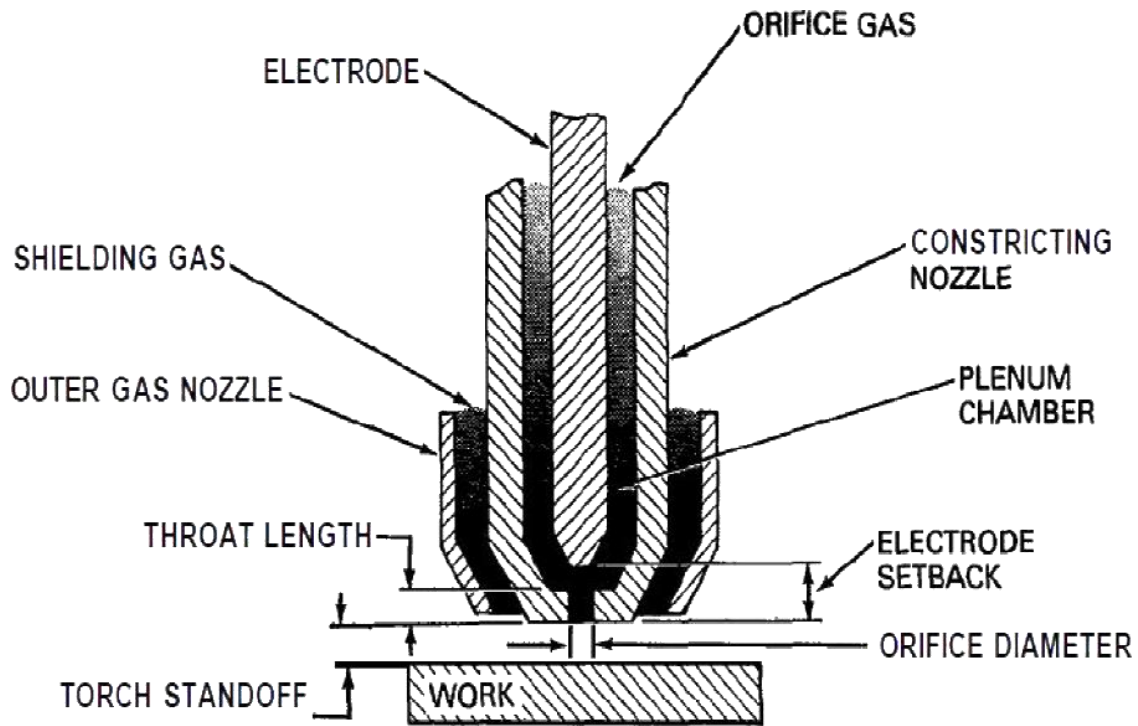


Figure 95: Schematic of PAW torch [3].

As seen in Figure 95, a PAW torch consists of three main components: an outer gas nozzle to direct shielding gas flow, a constricting nozzle to direct orifice gas flow, and a tungsten electrode. PAW can operate in two distinct modes: transferred arc and nontransferred arc. In transferred arc mode, the arc transfers from the electrode directly to the work piece. In nontransferred mode, the arc is established between the electrode and the constricting nozzle,

and high-pressured orifice gas forces the arc plasma through the constricting nozzle's orifice. The arc between the electrode and the constricting nozzle is often referred to as the pilot arc.

The idea was that if a PAW torch was aimed between GLADiS's wire electrode and the work piece, plasma from the PAW pilot arc would present sufficient ionization in the arc gap for the main arc to start.

The pilot arc itself is started using a high frequency arc starter built into the PAW power source. However, because the pilot arc circuit is completely contained within the PAW torch and power source, it was speculated that GLADiS's electronic components would not be affected by the PAW high frequency arc starter.

9.2.1. Experimental Methods

The first step was to position the PAW torch such that the pilot arc would be between the wire electrode and the work piece. The PAW torch was mounted on a 3-axis rack and pinion mount that would allow precise positioning and adjustments. One of the computer's digital outputs was then configured to control the PAW pilot arc. The SiDD code was then modified to trigger the PAW pilot arc. Addition code had to be written to predict if the main arc had actually been started by the pilot arc. The arc start prediction code simply monitored the main arc current; if the current increased above 60A, the arc was considered to be started. High-speed camera footage was used to fine-tune the timing of events (e.g., pilot arc start time and wire feed start time) within the welding control code. C++ code used to obtain SiDD with PAW pilot arc starts can be found in Appendix H.

Once the timing and torch position were fine-tuned, experiments were performed to characterize the performance of the SiDD strategy using PAW pilot arc noncontact arc starts. The CTWD was set at 0.5in and ER70S-6 wire and 98% Ar, 2% O₂ shielding gas was used. A

piece of 1/4in cold-rolled low carbon steel was used as the substrate, with depositions made on the 1/4in edge. After depositing a series of individual droplets, the system's ability to deposit sequential droplets to form a weld bead was tested. Lastly, the system's wall building ability was tested by depositing multiple layers, one droplet at a time.

9.2.2. Results and Discussion

The first major observation made while testing the PAW pilot arc's ability to initiate the main GMAW arc was that the PAW pilot arc itself was incapable of lighting the main arc unless the pilot arc was in physical contact simultaneously with both the wire electrode and the work piece. Because of the pilot arc's small size and the PAW torch's large size, it was difficult to maintain contact between the pilot arc, wire electrode, and work piece simultaneously.

However, it was found that if the pilot arc was triggered after the GMAW process was at open circuit voltage, the PAW high frequency arc starter, in addition to the pilot arc, would start the main GMAW arc. Essentially, if multiple droplets were to be deposited, the pilot arc would have to be shut off and restarted every drop as opposed to leaving the pilot arc operating continuously.

High-speed camera footage showed that the PAW power source had a delay of 107ms before actually starting the pilot arc on command. Because the wire feed also had a considerable delay time, the wire feed and pilot arc commands had to be closely synchronized. If the pilot arc started too soon, the lack of wire feed could cause the wire to melt back to the contact tip. If the pilot arc started too late, the wire feeder could drive the wire into the work piece and short circuit before the main arc initiated. The best timing solution was to send the pilot arc on command 30ms before the wire feed command. By the time the wire started to move, the pilot arc would start and initiate the main arc.

Other than adding the pilot arc on command 30ms before the wire feed command and an arc start prediction function, the control code used was identical to the original code for SiDD using steel wool arc starting. Figure 96 shows high-speed frames taken during a SiDD test using PAW pilot arc starting.

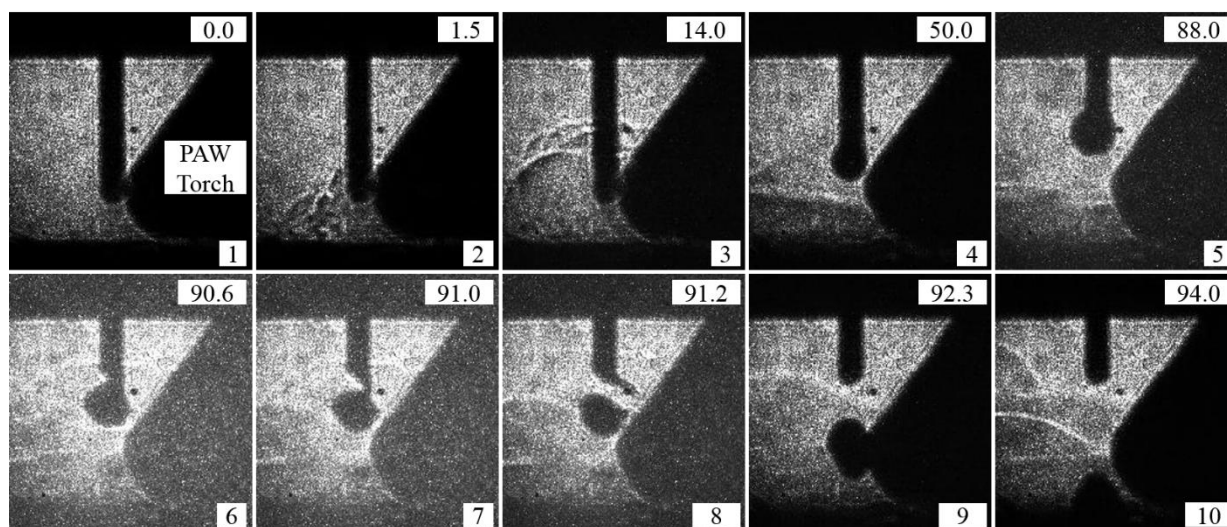


Figure 96: SiDD with PAW pilot arc start. The number in the top right-hand corner of each frame is the time stamp in milliseconds (ms), and the number in the bottom right-hand corner of each frame is frame number.

The frames in Figure 96 do not represent evenly timed frames, but rather represent different stages throughout the process. The black mass on the right-hand side of each frame is the PAW torch. Frame 1 shows the system before the arc is initiated. In frame 2, thermal gradient lines can be seen, which signify the pilot arc starting. Frame 3 shows the main GMAW arc starting as evident by the thermal gradient lines seen above the tip of the PAW torch. Frames 4 and 5 show a molten droplet forming during the background current time period. Frames 6, 7, and 8 were taken during the 4ms, 345A current pulse and show the droplet detaching from the wire electrode. Frames 9 and 10 show the droplet transferring to the work piece through the arc gap.

Figure 97 shows five droplets deposited using SiDD with PAW pilot arc starts.

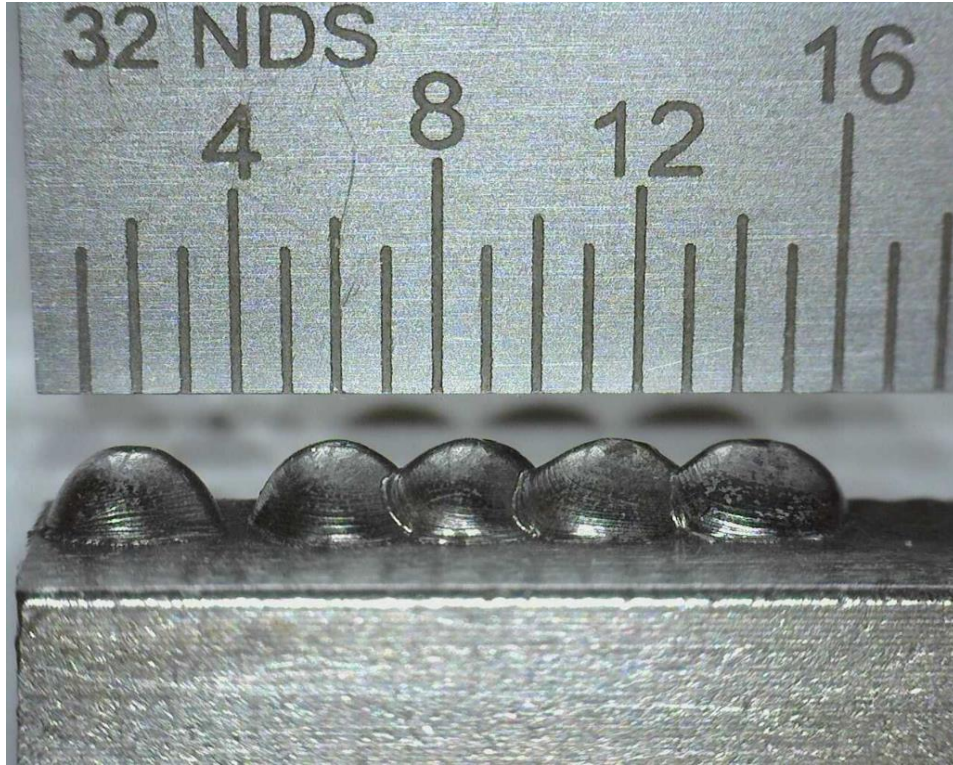


Figure 97: Droplets deposited using SiDD with PAW pilot arc starts.

In Figure 97, the ruler in the background is graduated in 1/32in increments. Using the steel wool starting technique, depositing five drops would have taken around 5 minutes. Using the PAW pilot arc technique, the five drops in Figure 97 took about 1.5 minutes to deposit. As the deposition process itself takes less than 200ms, the majority of time spent depositing droplets using PAW pilot arc starting was spent cleaning the work piece surface with a wire brush. Cleaning the work piece surface was not completely necessary, but it made the PAW pilot arc starting technique more robust (i.e., fewer failed arc starts).

Once the system was consistently depositing single droplets, a series of droplets was deposited to form a weld bead as seen in Figure 98.



Figure 98: Weld bead deposited using SiDD with PAW pilot arc starts. The weld bead was made by depositing one drop at a time from left to right using ER70S-6 wire and 98% Ar, 2% O₂ shielding gas.

The ruler shown in Figure 98 is graduated in 0.02in (1/50in) increments with the numbers marking 0.1in increments. The droplets in Figure 98 were deposited at a CTWD of 0.5in and with a drop spacing (i.e., distance between each droplet) of 0.07in. It can be seen that the weld bead has a relatively high aspect ratio (tall and narrow) due to the low heat input of each droplet. Although high aspect ratio welds are undesirable from a weld joining prospective, for AM a high aspect ratio weld can be beneficial. High aspect ratio weld beads would allow high aspect ratio features to be built on a component. The weld bead shown in Figure 98 measured 0.06in tall, 0.08in wide, and 1in long.

The next step was to investigate the feasibility of depositing layers on top of one another to form a wall. Figure 99 shows two layers deposited using SiDD with PAW pilot arc starts.



Figure 99: Two layers deposited using SiDD with PAW pilot arc starts. Both layers were deposited one drop at a time from right to left using ER70S-6 wire and 98% Ar, 2% O₂ shielding gas.

To deposit a second layer, the work piece was lowered 0.06in to compensate for the first layer height. As seen in Figure 99, the system was capable of depositing multiple layers using the SiDD technique with PAW pilot arc starts. The second layer was more uniform than the first layer, likely because of different heat sinking conditions. The first layer was deposited on the substrate, which is a relatively large heat sink. The second layer was deposited on the first layer, which is a smaller heat sink.

Throughout PAW pilot arc start testing, it was found that the PAW pilot arc starting technique was not highly robust, with a failure rate of about 10%. If the work piece was not cleaned before depositing a droplet, the failure rate was even higher.

It was also found that the PAW power source's high frequency arc starter produced enough EMI to cause connection failures between the computer and the Galil motion controller.

The last problem with the PAW pilot arc starting technique was the presence of the PAW torch in proximity to the main arc. Because the PAW had to be placed close to the GMAW arc gap (within about 0.1in), the minimum CTWD that could be used was 0.5in. A 0.5in CTWD was required to allow the PAW torch to fit between the work piece and the GMAW gas nozzle. For the arc to consistently start, the initial electrode extension had to be about 0.4in to set a 0.1in

arc gap. Although a 0.5in CTWD and a 0.4in initial electrode extension appeared to be effective, restrictions caused by inserting the PAW torch in close proximity to the GMAW electrode and work piece would be a limiting factor for future investigation of droplet coalescence and electrode extension.

9.3. Lift Start

Another alternative arc starting procedure investigated was lift arc starting. Lift arc starting is commonly used in GTAW applications where the possibility of tungsten inclusions is not of great concern. Attempting lift arc starting was the last effort to avoid using a high frequency arc starter.

In a lift arc start, the electrode begins in contact with the work piece. Immediately after the arc is enabled and current begins flowing through the electrode, the work piece and electrode are separated. Typically, the electrode is lifted away from the work piece, but GLADiS has a stationary torch, requiring the work piece to be moved. If the welding power source has sufficient inductance, the current will attempt to maintain its flow, and a large voltage can be generated at the arc gap. Upon separation of the wire electrode and work piece, the generated voltage can cause electric field emission in the arc gap that is created between the electrode and the work piece and start the arc. Though lift starting is not a noncontact arc starting technique, it can have the same benefits as noncontact arc starting without the problems associated with conventional short circuiting arc starts and high frequency arc starters.

9.3.1. Experimental Methods

For the lift start tests, ER70S-3 wire and 98% Ar, 2% O₂ shielding gas were used. Lift starts were tested by using the original SiDD control code used with steel wool arc starts. The original code was slightly modified to move the work piece down 0.05in for the lift start, and the

timing of events was modified as necessary to achieve an arc start. To simplify the tests, wire feed was removed from the code and the CTWD was increased to 0.6in to keep the wire from melting back to the contact tip. The wire electrode was manually adjusted to be in contact with the work piece for each test. The lift start C++ code can be found in Appendix H.

9.3.2. Results and Discussion

Although several lift start tests were successful, the lift starting technique proved to be unreliable. The welding power source did not have sufficient inductance to consistently repeat lift starts. The only way to achieve a lift start was to clip the end of the wire electrode and clean the work piece to get sufficient electrical contact. Even with clean surfaces and good electrical contact, the lift start method was unreliable.

The best way to achieve a more reliable lift start would be to add more inductance to the power source. However, more inductance would reduce the power source's frequency response and could make droplet detachment pulses less effective.

9.4. High Frequency Arc Starter

Because all other attempts at starting the welding arc proved to be inadequate, a high frequency arc starter was connected to the welding circuit. Recall that high frequency arc starters generate tremendously high voltages to break down shielding gas in the arc gap to start the arc. As previously mentioned, high frequency arc starters can be highly problematic in computer automated systems. Extremely high voltages generated by high frequency arc starters can destroy electronics connected to the welding circuit, and EMI generated by high frequency arc starters can cause communication failures with electronics in proximity to the welding circuit. However, high frequency arc starters have been used extensively in manual GTAW applications and have been proven effective at starting welding arcs.

9.4.1. Experimental Methods

Refer back to the arc starter portion of the equipment section (Section 6.6) for details on setting up the high frequency arc starter.

Once the arc starter was operational, it was integrated into the SiDD control code. Because the arc starter generated considerable EMI, the code had to be modified by adding an arc starting routine and arc start prediction algorithm.

Once the modified code was written, SiDD tests were performed. Original process parameters established during the steel wool arc start SiDD tests were modified based on test results to improve the deposition process reliability.

A new code was then written to control the wire feeder to automatically adjust the wire to the proper arc length before initiating the arc. The new code worked by feeding wire forward and sensing power source voltage to determine the location of the work piece. Once the work piece was found, as indicated by a sudden drop in power source open-circuit voltage, the wire feed was reversed to the desired arc length.

Tests were performed using no wire feed, wire feed from the CWT wire feeder, and wire feed from the custom built insulated wire feeder. All tests were performed using a CTWD of 5/16in and with ER70S-3 wire.

9.4.2. Results and Discussion

Initial arc starting tests showed that the arc starter was effective at starting arcs. However, the time between issuing the arc starter enable command and the arc actually initiating could range from about 7ms to 200ms. The large discrepancy in arc starting time made wire feed with the CWT wire feeder impossible. Recall that the CWT wire feeder took about 100ms to start feeding wire after the wire feed command was issued. Because of the wire feed delay time,

the wire feed had to be started a specific time (40ms) before the arc was started. Using the high frequency arc starter, however, meant that the arc start time could fall anywhere in a 193ms window. Therefore, it was impossible to know when to start the wire feed. Due to the difficulties feeding wire with the CWT wire feeder, initial tests were performed without wire feed. The CWT wire feeder was used exclusively for positioning the wire before each deposition test.

As discussed in the arc starter portion of the equipment section, part way through testing, the arc starter destroyed the CWT wire feeder controller. The new insulated wire feeder behaved much differently from the CWT wire feeder. The insulated wire feeder had a much faster response time to wire feed commands. In fact, it took the insulated wire feeder less than 40ms to begin wire feed after receiving the command. The insulated wire feeder was fast enough that the wire feed command could be issued after an arc start was detected, which made it possible to feed wire during a SiDD test.

Another benefit of the insulated wire feeder was that it was controlled by a stepper motor. A wire feed command could consist of a WFS and a wire feed distance. Because a distance could be specified, there was no need to have a separate wire feed stop command perfectly timed with arc termination within the deposition code.

An additional arc starter issue was that noise from the arc starter made it difficult to predict when the welding arc had actually started. Previously, an arc start was detected by sensing when the arc current was above 60A. However, a noise spike from the arc starter imposed on the arc current signal could easily exceed 60A and trigger a false arc start indication, which resulted in a failure to start the arc. To improve arc starting reliability, an arc starting

routine and arc start prediction algorithm was written in the C++ control code. A flow chart of the high frequency arc starting sequence can be seen in Figure 100.

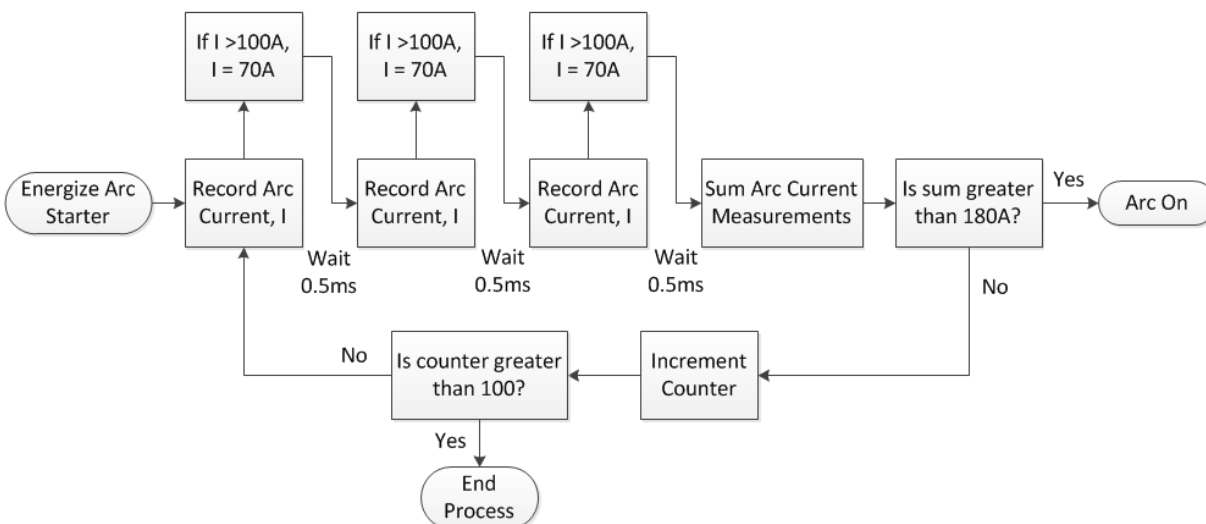


Figure 100: High frequency arc starting sequence flow chart.

The high frequency arc starting sequence in Figure 100 takes three current measurements and checks if the average is greater than 60A (sum of three measurements is greater than 180A). If the average is greater than 60A, the arc is considered to be on; if the average is below 60A, the arc is considered to be off. Three measurements are taken because the probability of noise spikes landing on all three measurements are extremely low. Each measurement is tested to see if the current exceeds 100A. Because the starting current is 75A, a measured current above 100A is known to be a noise spike. The current measurements have to be checked because if a noise spike exceeds 180A, the average current will appear to be greater than 60A and a false arc start indication is triggered. Any current measurements that exceeded 100A were set to 70A so that an arc start would not be falsely indicated.

Notice that the high frequency arc starting sequence in Figure 100 only allows the arc starter to run for 100 iterations, or 150ms. Limiting the run time to 150ms prevents the arc

starter from continuously running for extended periods of time while something is preventing an arc start. Throughout testing, the high frequency arc starting sequence code proved to be effective at starting arcs and correctly predicting arc starts.

For the high frequency arc starting tests, the SiDD code was modified to increase droplet detachment reliability by increasing the peak current to 350A and increasing the peak time to 4.5ms. The section of code used for testing SiDD with the high frequency arc starter can be found in Appendix H.

Two major arc starting limitations were found during testing for the high frequency arc starter to work: 1) the work piece had to be cleaned and the wire electrode clipped, and 2) the initial arc gap had to be small (about 0.04in). If the work piece and the tip of the wire electrode were not completely cleaned, the arc starter would arc between the electrode and work piece, but the main arc would not start. If the arc gap was much greater than 0.04in, the arc starter would not arc between the electrode and the work piece.

Although the first limitation had an easy solution (brush the work piece and clip the wire), it was not a practical solution. Having to clean the work piece and clip the wire for each deposited droplet greatly reduced the process deposition rate. In fact, it took about 30s to deposit each droplet.

The second limitation was easily solved by writing code to automatically position the wire before each drop. The code was written to, first, enable the main arc at a low current of about 1A. Enabling the main arc would cause the open circuit voltage to be present. Wire could then be fed forward while monitoring the arc voltage. When the wire made contact with the work piece, a short circuit would be created, and the arc voltage would drop to 0V. Once the drop in voltage was sensed, the main arc could be disabled to stop the current, and the wire feed

could be reversed. Wire could be fed in reverse until the desired arc gap length was created. The C++ code used to automatically position the wire can be found in Appendix H.

An additional modification was made to the SiDD current sequence. Previously, the arc was terminated immediately following the 350A current pulse. The modification was to add 15ms of a low, 40A, background current after the pulse as seen in Figure 101.

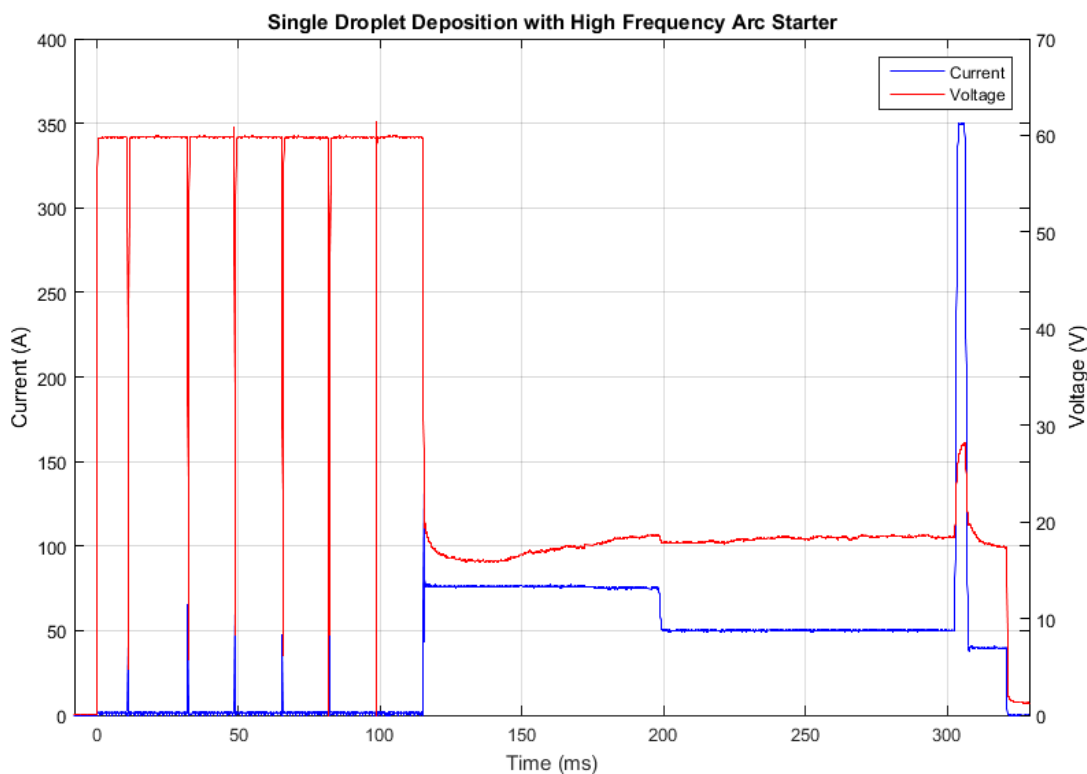


Figure 101: Arc current and voltage during SiDD with high frequency arc starting. After the power source is enabled at $t = 0$, the arc starter pulses seven times to initiate the arc.

The additional background current seen after the current pulse in Figure 101 kept the arc on as the droplet transferred and fused to the work piece. Keeping the arc on appeared to improve deposited droplets' form and make subsequent arc starts more reliable.

Figure 101 shows that the high frequency arc starter may make multiple attempts to initiate the main welding arc. Starting at $t = 0$ when the power source is enabled, the arc voltage is at open circuit voltage (about 60V) before the arc starts. During the period of open circuit

voltage, multiple current and voltage spikes can be seen. Measuring the time between spikes shows that they occur about every $1/60^{\text{th}}$ of a second. Recall that the arc starter generates voltage pulses at 60Hz, which explains the spikes seen in Figure 101. It can be seen that the arc starter pulses about seven times before the arc is started. The number of arc starter pulses that occurred before the arc start was mainly dependent on the work piece/electrode cleanliness.

9.5. Arc Starter/laser Hybrid Arc Starting Technique

Although the arc starter was effective at starting arcs, the deposition rate was highly limited by the cleaning process required for each drop. In addition, the process could not be automated because cleaning the electrode and work piece required pausing the process between each droplet deposition.

In attempt to eliminate the cleaning process, an arc starter/laser hybrid arc starting technique was developed. The hybrid technique used the exact same control code used for SiDD with high frequency arc starting. However, the hybrid technique included the laser, which was focused on the cathode (work piece) directly beneath the wire electrode.

9.5.1. Experimental Methods

The laser and focusing lens were set to aim directly below the wire electrode. Because the laser beam came in at an angle, the work piece height had to be held constant for each test. The focusing lens was adjusted to achieve the minimum possible spot size.

With the laser in place, the same SiDD process with the high frequency arc starter was executed. The laser power was varied from 10W to 100W over a variety of tests to determine the optimal laser power. Wire was fed for each test using the insulated wire feeder.

Once the optimal laser power was selected, a new control code was written that integrated the SiDD code with the automatic wire and work piece positioning code. The new

code was used to test the hybrid arc starting technique's ability to run in an automated environment. Appendix H contains the fully automated SiDD code.

9.5.2. Results and Discussion

The high frequency arc starter/laser hybrid arc starting technique proved to be highly effective at starting the arc. In fact, no cleaning was required between drops for the technique to be effective. The only limitation was that the CTWD had to be at least 0.25in to allow the laser to clear the GMAW gas nozzle.

Although the arc was found to start at any laser power above 25W, the optimal laser power was found to be 50W. With laser power lower than 50W, the arc occasionally failed to start, and with laser power above 50W, the laser added enough heat to widen the deposited droplets (i.e., decrease the weld bead aspect ratio). Laser powers above 100W caused excessive melting of the wire electrode during the automatic wire positioning process, which fed the wire directly in the laser's path.

Using 50W of laser power, the new code with both SiDD and automatic wire and work piece positioning was tested. The code was written to deposit a series of droplets to form a weld bead without stopping between drops. Video frames of the new automated SiDD process can be seen in Figure 102.

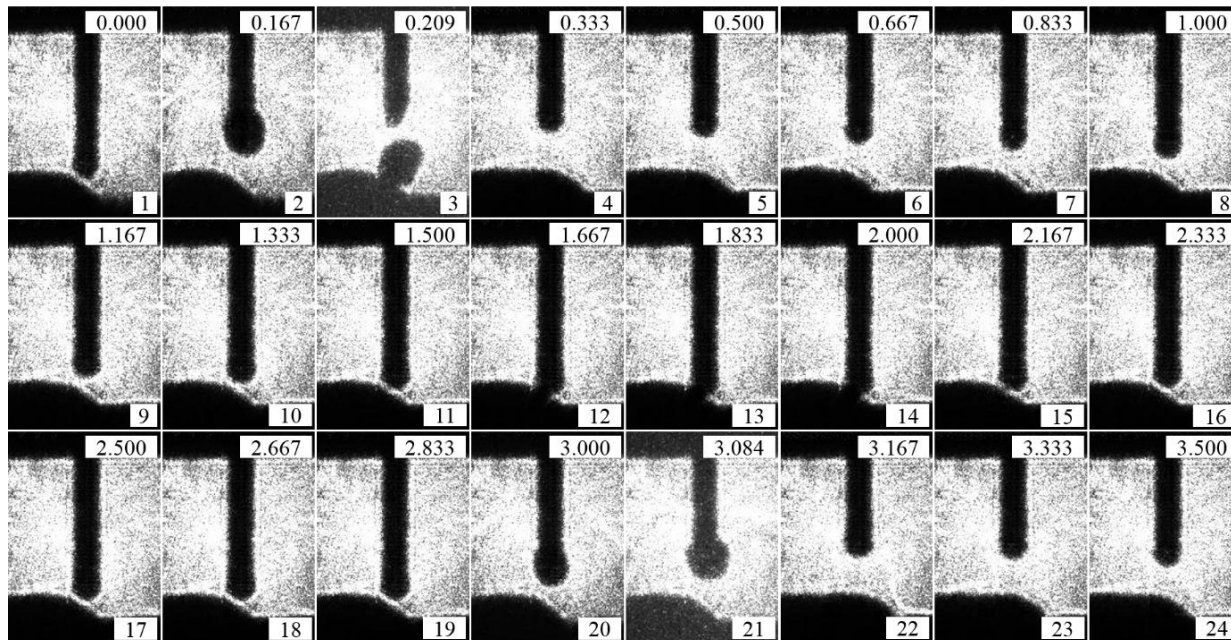


Figure 102: Video frames of automated SiDD with hybrid arc starting. The number in the top right-hand corner of each frame is the time stamp in seconds (s), and the number in the bottom right-hand corner of each frame is frame number.

With exception to frames 2 and 21, the time step between frames in Figure 102 is 167ms (six frames per second). Frames 2 and 21 were added to show more detail during the droplet deposition process. As seen in Figure 102, frame 1 shows a starting arc gap of 0.05in. Note that because the camera is not perpendicular to the work piece, the arc gap appears smaller than it actually is. Frames 2, 3, and 4 show the droplet formation, detachment, and fusion to the work piece. Two different mechanisms are occurring in frames 5 through 9: 1) the 3-axis motion system repositions the work piece for the next drop, and 2) the automatic wire positioning routine begins feeding the wire towards the work piece. Frames 10 through 18 show the progression of the automatic wire positioning routine as the wire is fed forward until contact with the work piece is made and then reversed until the proper arc gap length is achieved. Frame 19 represents the point where the process begins to repeat itself. Because frame 2 was added

separately from the timed frames, frame 19 occurs 3s after frame 1, making 3s the drop period with the automated process. Frames 20 through 24 show the process repeating itself.

Figure 103 shows a weld bead made with the automated SiDD process.



Figure 103: Weld bead made using automated SiDD with hybrid arc starting. The weld bead was made by depositing one drop at a time from left to right using ER70S-3 wire and 98% Ar, 2% O₂ shielding gas.

The bead in Figure 103 is made up of 16 individual droplets. The new automated process takes about 3s per drop, making the total deposition time for the bead in Figure 103 48s. Using the high frequency arc starter without the laser, the same bead would have taken about 480s or 8 minutes to deposit.

The most prominent problem that occasionally occurred with hybrid arc starts was that upon arc starting, molten metal on the tip of the wire electrode could bridge the 0.04in initial arc gap and short circuit. If a short circuit occurred, the SiDD process was simply shorted out, and the wire would be fused to the work piece. A short circuit could not be detected by the arc start prediction algorithm because the current signal appeared the same whether or not a short circuit had occurred. Although the same phenomenon occasionally occurred with the high frequency arc starting technique, it was not a major problem because the process was not automated. With the automated process, wire fused to the work piece presented a problem because the work piece

was automatically repositioned after each drop. If the wire was fused to the work piece when the work piece was being repositioned, equipment could potentially be damaged.

To solve the short circuiting issue, the arc start prediction algorithm was modified. An additional section was added to check the arc voltage after the current signal indicated an arc start. If the voltage was found to be less than 3V, the code would predict that a short circuit occurred (regular welding voltage would be closer to 15V). If a short circuit was predicted, the process would terminate before repositioning the work piece.

The number of short circuits that occurred was also reduced by increasing the initial arc gap length to 0.05in. The addition of the laser allowed the larger arc gap to be used for arc starting.

9.6. Summary

Achieving a noncontact arc starts proved to be one of the most difficult aspects of setting up GLADiS. However, noncontact starts were an integral part of the SiDD process. In fact, SiDD was highly impractical without the addition of noncontact arc starting.

It was found that photoemission alone produced by a 200W, 532nm laser was insufficient for starting arcs. The only way to achieve an arc start using the laser alone was to add graphite to the anode and/or cathode surfaces. While laser power of 200W on clean metal surfaces could not start the arc, a laser power of only about 20W was required when graphite was added.

The PAW pilot arc starting technique proved to be effective at starting arcs. The technique allowed the SiDD process to be tested for its ability to deposit weld beads and multiple layers. However, precise PAW torch placement was necessary, and the pilot arc starting technique was unreliable with a 10% failure rate. SiDD using PAW pilot arc starting was a slow process, about 18s per drop, because of work piece cleaning required before each drop.

Although the lift start arc starting technique showed some promise, it was too unreliable. More extreme cleaning of both the work piece and wire electrode tip was required to have even a chance for a successful arc start. It was speculated that the power source's inductance was too low for lift starting, and adding extra inductance would reduce the power source's frequency response.

All arc starting techniques tested were attempts to avoid the use of a high frequency arc starter because of its known influence on electronic components. When the arc starter was connected to the welding circuit, it proved to be even more problematic than expected (see Section 6.6). Once the high frequency arc starter was connected and all protection circuits, shielding, and grounding installed, the high frequency arc starter proved to be an effective arc starting technique. However, even the high frequency arc starter was highly susceptible to oxides on the work piece and electrode tip. In fact, to achieve arc starts with the high frequency arc starter, more rigorous cleaning than that required for PAW pilot arc starts had to be performed. The drop rate using the high frequency arc starter was about 30s per drop.

The high frequency arc starter/laser hybrid arc starting technique proved to be, by far, the best arc starting technique. It was a robust process, exhibiting very few failures. The hybrid arc starting technique was the only arc starting technique effective enough to automate the SiDD process. Using the hybrid technique, drop rates of 3s per drop were achieved.

10. Electrode Extension and Droplet Coalescence

With GLADiS fully operational, tests could be performed to investigate the possibility of improving droplet/substrate coalescence by minimizing the electrode extension. Recall that minimizing the electrode extension should allow the same length of wire to be melted with increased welding current. More current is required to melt the same length of wire because the wire does not experience as much resistive heating with a minimized electrode extension. With increased welding current, a larger weld pool should form on the substrate because current is the primary source of melting. A larger weld pool on the substrate would result in improved droplet/substrate coalescence.

10.1. Experimental Methods

To test the electrode extension/droplet coalescence relationship, three droplets were deposited on the edge of a 0.25in thick, low carbon steel specimen for two different electrode extensions. Drops were made using SiDD with the high frequency arc starter alone. The laser was not used to assist arc starts because the added thermal energy from the laser beam could alter the results.

For the first specimen, a CTWD of 5/16in and a long electrode extension was used. The voltage and current were measured throughout each drop. In addition, the high-speed camera was used to video each drop to allow the actual electrode extension to be measured.

After the long electrode extension droplets were made, the high-speed camera was used to determine the minimum achievable CTWD. The minimum CTWD was determined by finding the required clearance for a droplet to detach from the electrode without short circuiting to the substrate.

The CTWD was then set to 3/16in, the minimum value determined. The main reason the CTWD had to be minimized was that the high frequency arc starter could not start the arc unless the initial arc gap was around 0.04in. If a long CTWD was used, a long electrode extension had to be used to create a small arc gap.

Because the theory derived from the Lesnewich equation (1) indicated that more current would be required to melt the same length of wire, the same wire feeding routine was used for all tests. Test drops were made using SiDD at the short CTWD. The high-speed camera was used to monitor the electrode extension before and after each test drop. High-speed footage was then used to adjust the background current so that the same length of wire was melted as measured in the long electrode extension tests. In other words, the system was tuned to melt the same length of wire for both electrode extensions tested. To achieve the same length of wire melted, the current was adjusted.

With the current adjusted for the short electrode extension tests, three more droplets were deposited. Once again, voltage, current, and high-speed video data were collected for each drop.

Once all six droplets were deposited, they were cross-sectioned, polished, and etched to expose the fusion zones. The fusion zone areas were then measured to determine if more melting had occurred in the short electrode extension drops. The electrode extension tracking video processing algorithm was used on the high-speed video footage to determine the actual electrode extensions for each test.

10.2. Results and Discussion

When adjusting the current to match lengths of wire melted between electrode extensions, an important observation was made. It was clear that the background current had to be increased for the short electrode extension to melt the same length of wire. Thus, the

experimental results appeared to agree with the theory. To achieve the same wire length melted, the background current had to be increased by 5A. A 5A increase in background current corresponds to a 3A increase in the average current throughout the deposition process.

The actual electrode extension (ℓ_e) was measured for each test using the electrode extension tracking algorithm on the high-speed camera footage. Figure 104 shows example frames of the electrode extension tracking algorithm at work.

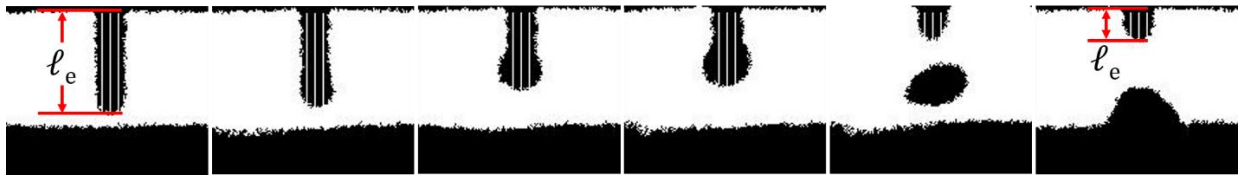


Figure 104: High-speed camera frames processed using electrode extension tracking algorithm.

The three vertical white lines shown on the electrode extension in Figure 104 show that the algorithm is tracking the electrode extension. Each white line is a location where the electrode extension is measured. After measuring all three locations, the lengths are averaged to find the electrode extension.

The measured electrode extensions for each test, as well as the average electrode extension for each CTWD are shown in Table IV. Also included in Table IV is the average current for the two different CTWDs.

Table IV: Measured electrode extensions.

Drop Number	Electrode Extension, ℓ_e (in)	
	5/16in CTWD	3/16in CTWD
1	0.268	0.130
2	0.261	0.142
3	0.264	0.136
Average	0.264	0.136
Average Current	66A	69A

As seen in Table IV, the short electrode extension was about half as long as the longer electrode extension. The results was an average current that was 3A higher to melt the same

length of wire. The relationship between electrode extension and welding current to melt a given length of wire electrode is shown in Figure 105.

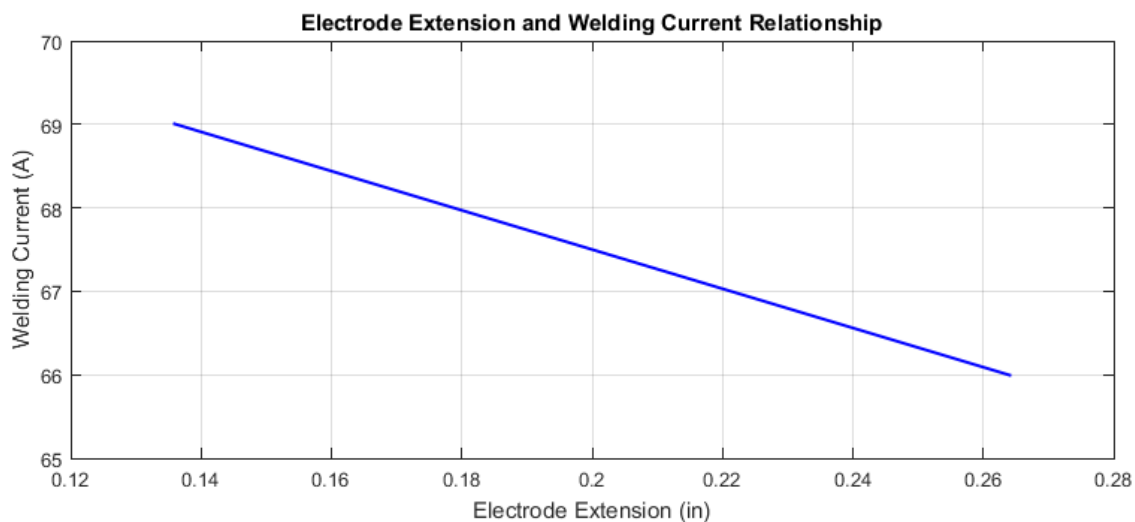


Figure 105: Relationship between electrode extension and welding current. To melt a given length of wire electrode, as electrode extension decreased, welding current increased.

Although the initial results appeared to confirm the theory, whether or not the additional 3A of average current improved droplet/substrate coalescence still had to be investigated. The best way to determine the coalescence was to measure the droplets' fusion zone size. A top view (xy-plane) of the specimens can be seen in Figure 106.

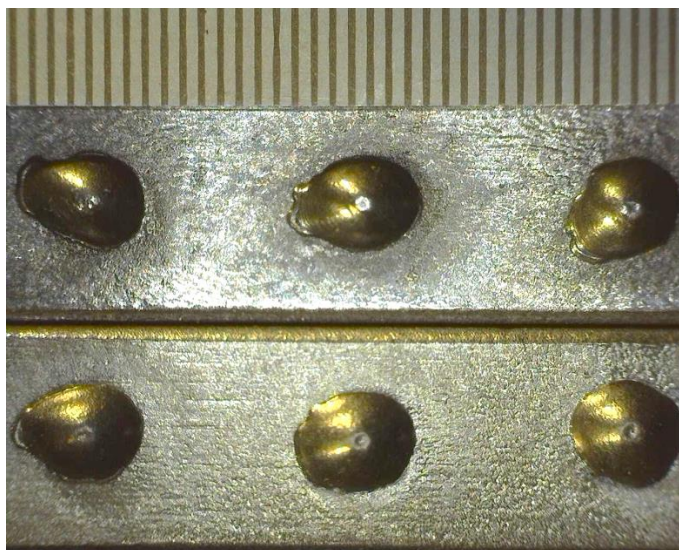


Figure 106: Droplets deposited at electrode extensions of (top) 0.264in and (bottom) 0.136in.

In Figure 106, the ruler on the top of the image is graduated in 0.02in increments. The droplets on the top were deposited with the long electrode extension (0.264in), and the droplets on the bottom were deposited with the short electrode extension (0.136in).

Initial fusion zone analysis was performed by using photo measurement software to measure the area each droplet covered in Figure 106. The area found represents the area on the xy-plane that is the droplet/substrate interface. It was found that the droplet/substrate interface for the short electrode extension droplets was about 7% larger than the long electrode extension droplets. The larger area indicates that the additional current used for the short electrode extension created a larger weld pool on the substrate, allowing the droplets to wet out to a larger diameter.

The next step was to cross-section the droplets and measure the area of the fusion zone in the xz-plane. Figure 107 shows a representative cross-section of a droplet and its fusion zone.

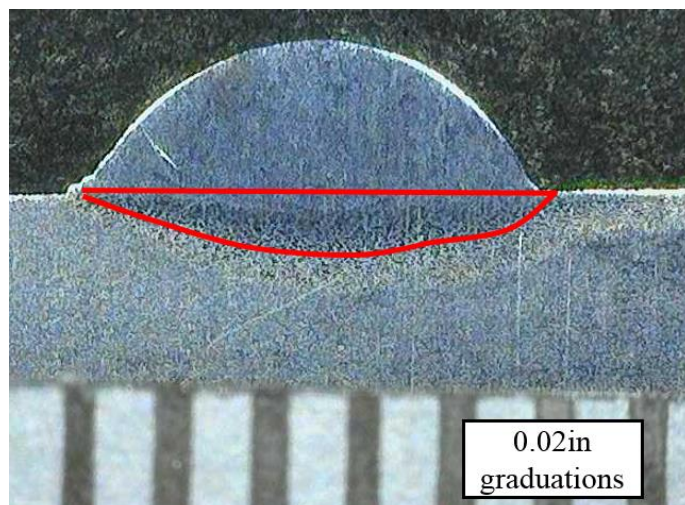


Figure 107: Cross-section of droplet fusion zone. Cross-section was taken through the center of the droplet.

Each droplet was cross-sectioned, and the fusion zone areas were found using photo measurement software as illustrated in Figure 107. Because the specimens were mounted in polymer mounts prior to cross-sectioning, it was difficult cross-section the droplets directly in

their centers. Off-centered cross sections would show a smaller fusion zone area and introduce error in area measurements. To minimize the measurement error, the length of each droplet cross-section was compared to its corresponding diameter in Figure 106 and scaled appropriately. Although measurement error still existed, approximate fusion zone areas could be determined. Figure 108 shows the relationship between fusion zone cross-sectional area and electrode extension, and the relationship between fusion zone cross-sectional area and welding current.

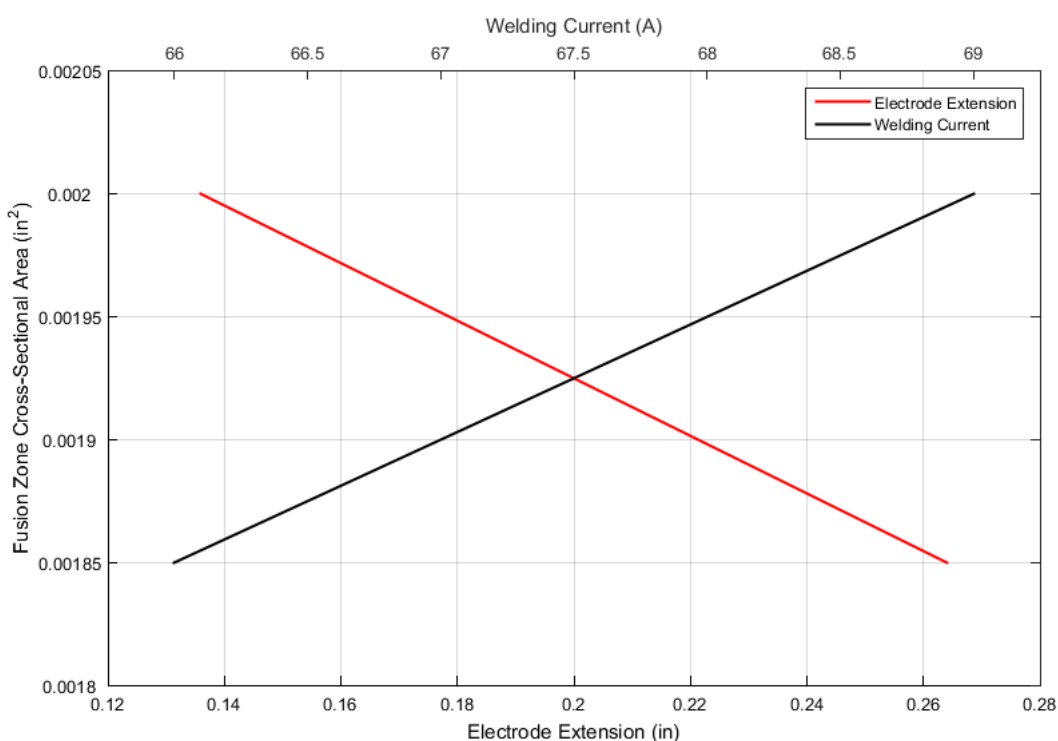


Figure 108: Relationship between fusion zone cross-sectional area, electrode extension, and welding current. The y-axis is the fusion zone cross-sectional area, the bottom x-axis is the electrode extension, and the top x-axis is the welding current.

In Figure 108 the red line represents the relationship between fusion zone cross-sectional area and electrode extension, and the black line represents the relationship between fusion zone cross-sectional area and welding current. To melt a given length of wire electrode, as electrode

extension increased, the fusion zone cross-sectional area decreased. As welding current increased, the fusion zone cross-sectional area increased.

Measuring the cross-sectional areas of each droplet fusion zone showed that the average fusion zone area in the short electrode extension droplets was 8% greater than the long electrode extension droplets. The 8% increase in fusion zone area agreed with the droplet/substrate interface area measurements that showed a 7% increase.

10.3. Summary

Initial observations confirmed that short electrode extensions allowed the same length of wire to be deposited at a higher current. Reducing the electrode extension from 0.264in to 0.136in allowed 5A of current to be added to the background current, resulting in a 3A increase in average current, thus confirming the theory derived from the Lesnewich equation (1).

Examination of droplets deposited at both electrode extensions showed that increased current at a short electrode extension increased the fusion zone cross-sectional area by 7%-8%. Improved coalescence at higher currents was expected, as current is the primary parameter that causes melting.

If lack of fusion is a problem in weld metal deposited using SiDD, decreasing the electrode extension would be a viable solution to improve droplet/substrate coalescence.

11. Specimen Builds and Parameter Tuning

With control code developed to achieve SiDD and noncontact arc starting techniques tested, linear wall specimens could be made to test the system's AM capabilities. Wall specimens were built by depositing weld beads on top of one another to form a single bead width wall. A schematic of depositing a single layer can be seen in Figure 109.

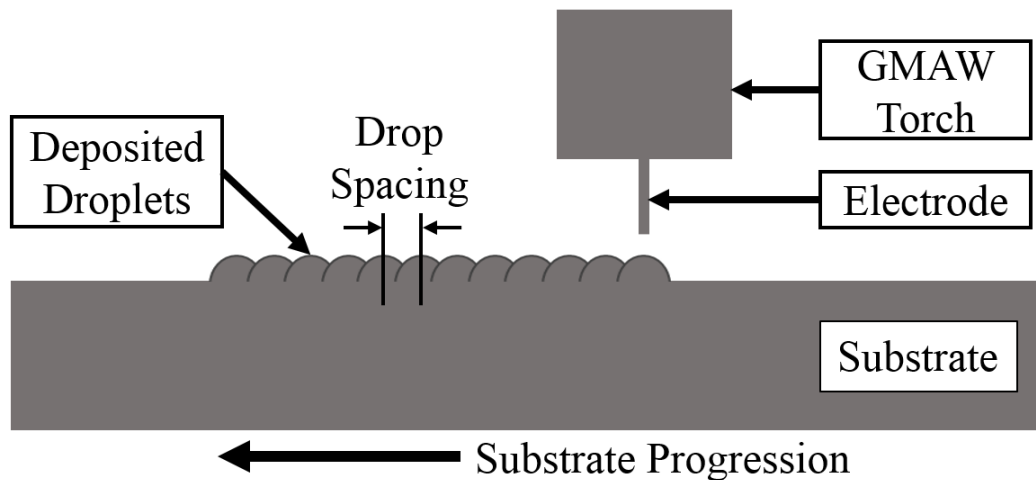


Figure 109: Schematic of depositing a single layer using SiDD.

As seen in Figure 109, after a droplet is deposited, the substrate is progressed in the direction of wall progression. The distance the substrate moves between each droplet deposition is the drop spacing. After a layer is deposited, the substrate is lowered a distance equal to a single layer height, and a new layer is deposited atop the previous layer.

11.1. Experimental Methods

Specimens were made using three different arc starting techniques: PAW pilot arc starts, high frequency arc starts, and the arc starter/laser hybrid arc starting technique. Four specimens were built with the high frequency arc starting technique to test various parameters.

11.1.1. PAW Pilot Arc Start Specimen (PAWS1)

The first wall specimen manufactured by GLADiS was deposited using the PAW pilot arc starting technique. The specimen was denoted as PAWS1 (PAW specimen number 1). For each layer deposited, the CTWD was set at 0.5in, and 0.045in diameter ER70S-6 wire was used. Layers were deposited by executing the SiDD with PAW pilot arc starting code (found in Appendix H) to deposit each droplet. Once a droplet was deposited, the substrate/work piece was cleaned with a wire brush, the wire manually repositioned to the proper arc gap length, and the substrate jogged 0.07in (drop spacing) in the direction of wall progression. The process was then repeated until the desired number of droplets was deposited. After a layer was complete, the substrate was lowered 0.05in to maintain a 0.5in CTWD.

The specimen's first layer was made up of 19 droplets, and the number of droplets in each successive layer was reduced by one so that droplets did not have to be deposited on the ends of previous layers. Depositing droplets on the end of previous layers required manual substrate positioning. Occasionally, when an error occurred with a droplet deposit, an additional droplet was placed over the location where the error occurred. Half way through the build, the specimen's top surface was ground flat to keep the specimen height consistent for the duration of the build. The deposition process was repeated until six layers were deposited.

11.1.2. Arc Starter Specimen 1 (HFS1)

The next specimen, HFS1 (high frequency arc starter specimen number 1), was built using the high frequency arc starting technique. Because the CWT wire feeder was still operational, no wire feed during droplet deposition was used to make the specimen. Repositioning the wire before each deposit was the wire feeder's only function. A CTWD of 0.3125in (5/16in) was selected, and 0.045in diameter ER70S-3 wire was used. HFS1 was built

by executing the SiDD with high frequency arc starting code found in Appendix H. After executing the deposition code, the wire electrode was clipped and the substrate cleaned with a wire brush. The automatic wire and substrate positioning code (also found in Appendix H) was then executed to prepare for the next drop. The drop spacing was set at 0.073in in the direction of wall progression. Once each layer was deposited, the substrate was lowered to maintain a constant CTWD.

HFS1 was the largest specimen built. Each layer was composed of about 50 droplets, and 10 layers were deposited. Height inconsistencies due to droplets not landing directly beneath the electrode were not corrected with grinding, but rather low spots were manually filled in by positioning the low spot below the torch and executing the SiDD code. Rather than reducing the number of drops on each layer, the substrate was manually positioned at the specimen's ends to build up the specimen ends. This technique allowed nearly square ends to be made on the specimen rather than tapered ends that result from reducing the number of droplets in each successive layer.

11.1.3. Arc Starter Specimen 2 (HFS2)

After HFS1 was built, the high-speed camera was used to optimize the drop spacing, which was adjusted to 0.068in. In addition, since the CWT wire feeder controller had been rendered non-operational, the insulated wire feeder was in place. With the insulated wire feeder, it was possible to feed wire during the deposition process. A wire feeding routine was developed to feed 0.05in of wire at 55ipm. Using wire feed during the deposition process allowed the CTWD to be reduced to 0.1875in (3/16in) without the risk of melting wire back to the contact tip. Because the CTWD was reduced, the electrode extension was also reduced. The shorter

electrode extension required adjusting the background current to a higher value to melt an equivalent volume of wire. Once again, 0.045in diameter ER70S-3 wire was used.

Other than the changing the drop spacing and CTWD and adding wire feed, the code and methods used to produce HFS2 were identical to those used for HFS1. To save build time, the size of HFS2 was reduced to 16 droplets per layer and 7 layers tall. Once again, no grinding was performed to alter the geometry during the build.

11.1.4. Arc Starter Specimen 3 (HFS3)

HFS3 was built using the same parameters, code, and methods as HFS2. However, if a significant height inconsistency was observed during the HFS3 build, a belt sander was used to grind down the top surface to make it a uniform height. A height inconsistency was usually caused by a droplet deviating from the path straight down from the electrode to the work piece, and instead, landing atop the previous droplet. Grinding was only implemented on two layers throughout the build.

11.1.5. Arc Starter Specimen 4 (HFS4)

Once again, HFS4 was built using the same parameters, code, and methods used for HFS2 and HFS3. The only difference was that HFS4 was ground on each layer, regardless of height consistency.

11.1.6. Arc Starter/laser Hybrid Specimen (HS1)

The last specimen produced, HS1 (hybrid specimen number 1), was built using the arc starter/laser hybrid arc starting technique. The HS1 build used the same parameters and methods as HFS3 (grinding only when needed), but at a 0.3125in CTWD to allow room for the laser beam to clear the gas nozzle. Besides the addition of the laser beam, the main difference in the HS1 build was that it used the automated SiDD code, found in Appendix H, to deposit each layer.

The substrate was manually lowered after each layer to maintain the correct CTWD. Because of the laser beam, no cleaning was required between drops.

For the previous specimens, in attempt to build square ends, the substrate was manually positioned to deposit droplets on the ends. Manual positioning was required because the standard drop spacing did not work on the ends of the specimens. Because HS1 was built using automated SiDD for each layer, manual positioning was not practical. Therefore, the number of drops was reduced on each layer to avoid running into the ends of previous layers. If manual substrate positioning was not used at the ends of each layer, droplets would often not land on the wall specimen, and would instead land on the substrate next to the wall specimen. The first layer was composed of 22 droplets and the droplet number in subsequent layers was reduced appropriately. A total of eight layers were deposited.

11.2. Results and Discussion

After each specimen was manufactured, they could be compared in terms of geometric consistency, surface finish, and build time.

11.2.1. PAW Pilot Arc Start Specimen (PAWS1)

The specimen manufactured using SiDD with PAW pilot arc starting (PAWS1) can be seen in Figure 110.

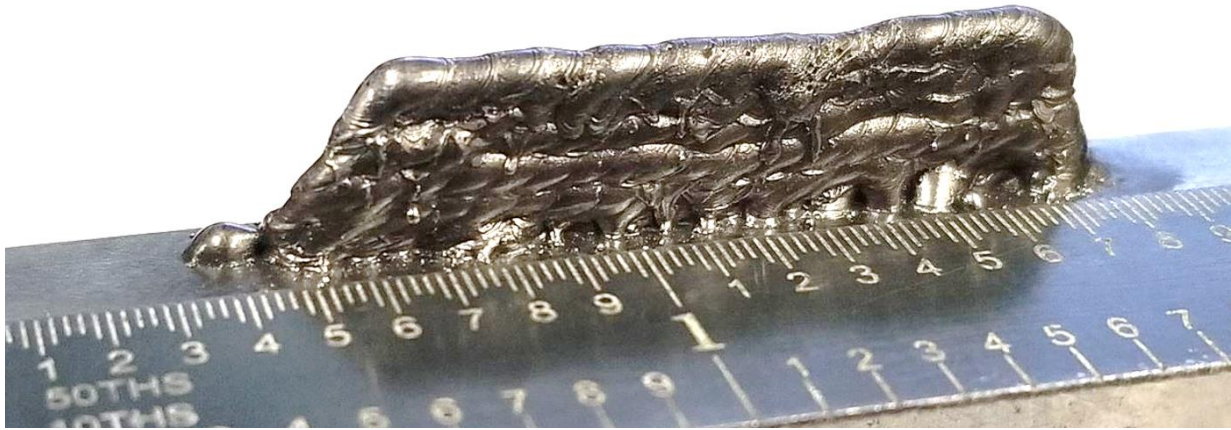


Figure 110: PAWS1 specimen manufactured using SiDD with PAW pilot arc starting using ER70S-6 wire and 98% Ar, 2% O₂ shielding gas.

The wall shown in Figure 110 is about 1.25in long, 0.3in tall, and 0.095in thick (ruler is graduated in 0.02in increments). It can be seen that the PAWS1 specimen height is not completely consistent across the length. The left-hand side of the specimen is angled due to the droplet number reduction for each layer.

It can be seen that the surface finish is relatively rough, caused by what appears to be spatter on the sides of the wall. High-speed video footage showed that some of the droplets, similar to the pulsed current test, exploded as they were detached from the wire electrode. Once again, the exploding droplets were likely due to impurities and/or the additional oxidizers present in the ER70S-6 wire.

Because the substrate/specimen had to be cleaned before each drop, the build time was about 0.5hr. The high-speed camera was used to measure the amount of wire melted for each droplet. From the amount of wire melted and the build time, the deposition rate was calculated to be about 0.017lb/hr.

11.2.2. Arc Starter Specimen 1 (HFS1)

Figure 111 shows the first specimen produced with SiDD using the high frequency arc starter (HFS1).



Figure 111: HFS1 specimen manufactured using SiDD with high frequency arc starting using ER70S-3 wire and 98% Ar, 2% O₂ shielding gas.

The ruler in Figure 111 is graduated in 0.0625in (1/16in) increments. HFS1 is 3.2in long, 0.5in tall, and about 0.1in thick. It can be seen that the ends of the specimen are relatively square which was achieved by manually positioning the substrate to fill in the ends with SiDD. It can be seen that the height is not completely uniform across the length, with a large number of high and low spots. If an additional layer was to be added, low spots would first have to be filled by manually positioning the substrate and depositing droplets in the low spots. The low spot filling procedure was performed after nearly every layer throughout the build.

It can be seen that the surface of HFS1 is relatively rough. However, the roughness was not caused by exploding droplets because ER70S-3 wire was used. The roughness was mostly caused by the drop spacing, which caused droplets to not land directly beneath the electrode.

Droplets already on the substrate affect the electric field behavior near the substrate surface. For instance, strong electric fields can form on sharp points and or edges. Electric fields have an effect on the arc and, therefore, on droplets transferring through the arc. Because the location where new droplets land on the substrate is highly affected by electric fields, the location of previously deposited droplets affect the location where new droplets land.

If the drop spacing is too large, previously deposited droplets will pull new droplets towards themselves as the new droplets transfer across the arc. Because the new droplets are attracted to previously deposited droplets, and the same excessive droplet spacing is applied for each drop, the horizontal distance between the electrode and the last deposited droplet increases with every iteration. In as few as three drops, the horizontal distance can become far enough that a new droplet will not be attracted to the last droplet and will transfer straight down to the substrate, leaving a void between the newest droplet and the previous droplet. The same phenomenon will then occur through the subsequent droplets. The excessive droplet spacing phenomenon is shown schematically in Figure 112.

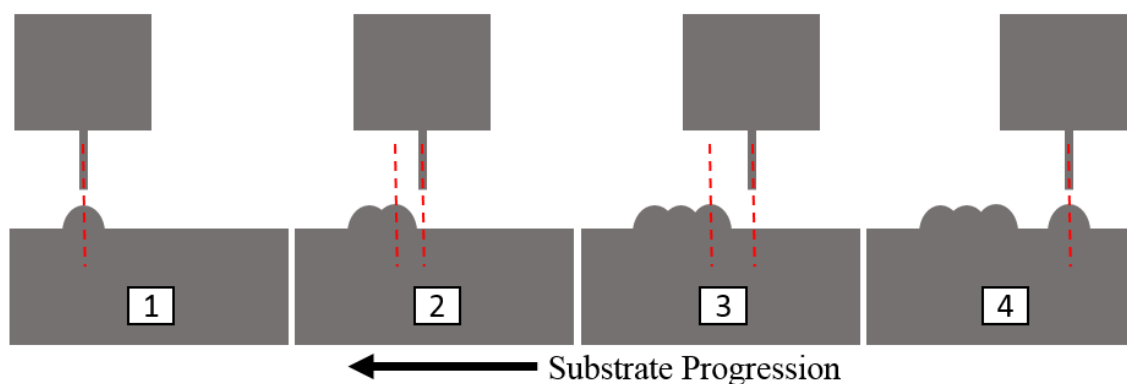


Figure 112: Effects of excessive drop spacing. Detaching droplets are attracted to previously deposited droplets. If excessive drop spacing is used, the horizontal distance detaching droplets travel increases with every drop.

In Figure 112, the dotted red lines show the horizontal distance between the electrode and where the droplet actually lands. As seen, the first droplet lands directly under the electrode. By

the next droplet, the drop spacing is too large and the next droplet travels to the left, landing beside the previous drop. The same behavior occurs with the third droplet, but the horizontal space is even larger. By the fourth droplet, the horizontal space is so large that the droplet is no longer attracted to the previous drop and falls straight down to the substrate. It can be seen that a void exists between the fourth droplet and the series of previous droplets.

Figure 113 shows a comparison of weld beads (single layer walls) made with the 0.073in drop spacing used for HFS1 and a 0.070in drop spacing.



Figure 113: Drop spacing comparison. A drop spacing of 0.070in produced a more uniform weld bead compared to the drop spacing of 0.073in.

As seen in Figure 113, a drop spacing of 0.070in (only three thousandths of an inch smaller) produced a much more uniform weld bead. It can be seen that the surface roughness of a wall made with the 0.073in drop spacing would be excessive, which was observed in the HFS1 specimen.

Because the wire had to be clipped and the substrate cleaned between each drop, HFS1 had a significant built time. At about 30s per drop, the 500 drop specimen took about 4.2hr to build. The deposition rate was decreased from the PAWS1 specimen and was calculated to be about 0.010lb/hr.

11.2.3. Arc Starter Specimen 2 (HFS2)

Figure 114 shows the HFS2 specimen made with optimal drop spacing and no grinding.



Figure 114: HFS2 specimen manufactured using SiDD with high frequency arc starting using ER70S-3 wire and 98% Ar, 2% O₂ shielding gas.

The ruler seen in Figure 114 is graduated in 0.0625in (1/16in) increments. HFS2 is 1in long, 0.35in tall, and 0.085in thick. Testing showed that the optimal drop spacing was 0.068in. It can be seen that optimal drop spacing greatly improved the height uniformity. In fact, no low spots had to be filled when optimal drop spacing was used. However, some deviation in height across the specimen's length can still be seen.

Another benefit of optimal drop spacing was that the surface finish was much smoother than the HFS1 specimen.

Because drop spacing was the only parameter to change between HFS1 and HFS2, the deposition rate was the same (0.010lbs/hr). However, since HFS2 was much smaller, the built time was reduced to about 1hr.

11.2.4. Arc Starter Specimen 3 (HFS3)

Figure 115 shows the HFS3 specimen made with optimal drop spacing and occasional grinding.



Figure 115: HFS3 specimen manufactured using SiDD with high frequency arc starting using ER70S-3 wire and 98% Ar, 2% O₂ shielding gas.

The ruler seen in Figure 115 is graduated in 0.02in (1/50in) increments. HFS3 is 1in long, 0.35in tall, and 0.085in thick. During the HFS3 build, only two layers exhibited a high spot that was ground flat. It can be seen that grinding the high spots on two layers considerably improved the height consistency of the final product. Only slight deviation in height across the specimen's length can be seen.

The surface finish was also slightly improve by the grinding process. HFS3 had the smoothest surface finish yet to be seen.

The build time was increased by only a couple of minutes over HFS2 due to the short time spent grinding. The slight increase in overall build time had a negligible effect on deposition rate.

11.2.5. Arc Starter Specimen 4 (HFS4)

Figure 116 shows the HFS4 specimen made with optimal drop spacing and grinding on every layer.



Figure 116: HFS4 specimen manufactured using SiDD with high frequency arc starting using ER70S-3 wire and 98% Ar, 2% O₂ shielding gas.

The ruler seen in Figure 116 is graduated in 0.0625in (1/16in) increments. HFS2 is 1in long, 0.35in tall, and 0.08in thick. As seen in Figure 116, grinding each layer flat resulted in a specimen with nearly perfect height consistency across its length. The only anomalies were three droplets that veered off to the side and landed on the substrate surface during the second layer deposition.

Grinding each layer also further improved the surface finish, even compared to HFS3.

Similar to HFS3, the grinding step added a few minutes to the overall built time.

Compared to the time it took to deposit each layer, the grinding time was negligible and had little effect on the deposition rate.

11.2.6. Arc Starter/laser Hybrid Specimen (HS1)

The final specimen to be manufactured using the arc starter/laser hybrid arc starting technique can be seen in Figure 117.



Figure 117: HS1 specimen manufactured using SiDD with laser hybrid arc starting using ER70S-3 wire and 98% Ar, 2% O₂ shielding gas.

The ruler seen in Figure 117 is graduated in 0.0625in (1/16in) increments. HS1 is 1.5in long, 0.4in tall, and 0.1in thick. Similar to HFS3, only two layers in HS1 had high spots to grind down. It can be seen in Figure 117 that the HS1's height is consistent over the specimen's length.

HS1 exhibited the best surface finish of all the specimens. It was found that the laser caused droplets to land directly beneath the electrode nearly every time, which was likely due to laser arc stabilization. With a stabilized arc, the droplets had a very small side-to-side variation in position, which resulted in a smooth surface finish.

Compared to the previous specimens, HS1 had a short built time. The HS1 specimen took 7.4 minutes to deposit 148 droplets, 36 more droplets than HFS2, HFS3, and HFS4. The

deposition rate was calculated to be 0.10lb/hr, which was 10 times faster than the standard high frequency arc starting technique. If optimized for speed, the SiDD process with hybrid arc starting could potentially be much faster. The SiDD process could be optimized for speed by increasing the substrate travel speed between droplet depositions, increasing the WFS in the automatic wire positioning sequence, and reducing or eliminating wait times in the process control code.

11.3. Summary

It was found that all noncontact arc starting methods were effective at building wall specimens. Tests showed that grinding down high spots on layers greatly improved both the surface finish and geometric consistency. Grinding each layer regardless of high spots further improved the surface finish and geometric consistency. However, a major factor that determined the resulting surface finish and geometric consistency was the drop spacing. Use of the optimal drop spacing proved to greatly affect the resulting specimen appearance.

Another major factor in improving specimen appearance and increasing the deposition rate was the addition of the laser. Using the high frequency arc starter/laser hybrid technique made automation possible and increased the deposition rate by about 10 times compared to using the high frequency arc starter without the laser. In addition to increasing the deposition rate, laser arc stabilization further improved surface finish and geometric consistency.

A summary of each specimen build and a qualitative ranking of surface finish and geometric consistency can be seen in Table V.

Table V: Summary of specimen builds.

Specimen	Grinding	Drop Spacing (in)	Surface Finish	Geometric Consistency	Deposition Rate (lb/hr)
PAWS1	as required	0.070	5	5	0.017
HFS1	none	0.073	6	6	0.010
HFS2	none	0.068	4	4	0.010
HFS3	as required	0.068	3	3	0.010
HFS4	each layer	0.068	2	2	0.010
HS1	as required	0.068	1	1	0.100

The surface finish and geometric consistency columns in Table V represent the ranking of each specimen relative to the others with 1 being the best and 5 being the worst. For example specimen HS1 is ranked first (number 1) for having the best surface finish and geometric consistency, and specimen HFS1 is ranked last (number 5) for having the worst surface finish and geometric consistency.

12. Specimen Metallurgical Analysis

As a final test, one of the build specimens was cross-sectioned and analyzed to determine some of its metallurgical properties. The HSF4 specimen was chosen as a representative sample of all the specimens.

12.1. Macrographs

Two cross-sections were taken from opposite ends of the HFS4 specimen. The cross-sections were polished down to 0.25 micron diamond paste and etched using 3% nital. Macrographs were taken of both cross-sections. A macrograph of HFS4's first cross-section can be seen in Figure 118.

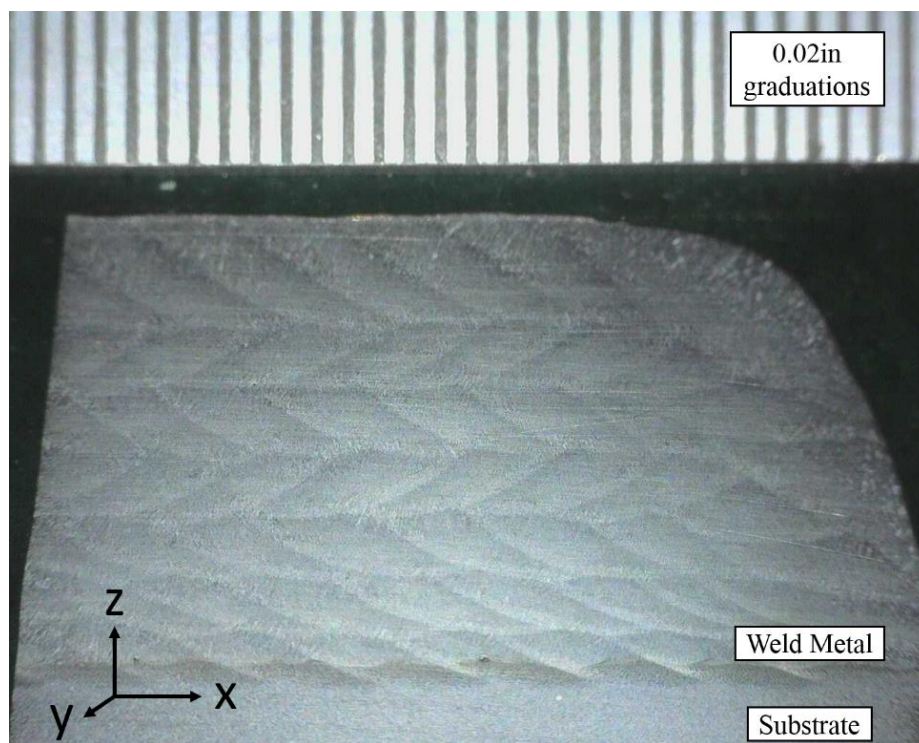


Figure 118: Macrograph of HFS4 cross-section number 1. Individual droplets and layers can be seen in the macrograph. No significant voids can be seen.

In Figure 118, the ruler in the top of the image is graduated in 0.02in increments. The axes in the bottom left-hand corner of the macrograph indicates the orientation. The x-axis is along the specimen's length and is the direction each layer was deposited. The y-axis is along

the specimen's thickness and perpendicular to the build direction. The z-axis is along the specimen's height.

It can be seen that the lower portion of the macrograph shows the substrate, and the upper portion shows the weld metal. The macrograph clearly shows each of the seven layers and the individual droplets in each layer. The build direction along the x-axis can also be seen. For example, it can be seen that the top layer was deposited left to right because each droplet appears to overlap the droplet to its left. The opposite is true for the second layer down from the top.

Fusion between individual droplets appears complete, as no voids, pores, or inclusions can be seen in the macrograph of the first cross-section.

HFS4's second cross-section macrograph can be seen in Figure 119.

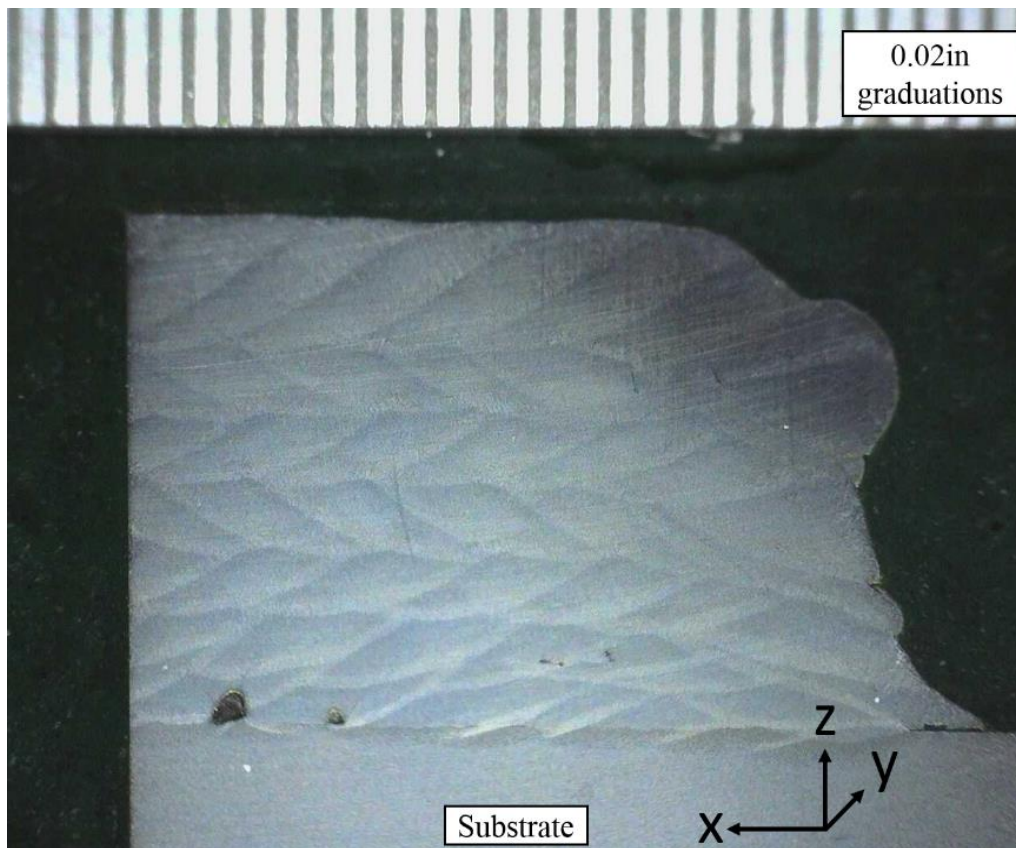


Figure 119: Macrograph of HFS4 cross-section number 2. Voids can be seen at the substrate/weld metal interface, and smaller voids can be seen in the weld metal.

The cross section in Figure 119 was taken from the opposite end and opposite side as the first cross section as indicated by the axes in the bottom right-hand corner. It can be seen that the second macrograph shows several small voids in the specimen. The easiest void to identify in the macrograph is the lack of fusion seen on the right-hand side at the weld metal/substrate interface. The voids are more easily characterized at higher magnification.

12.2. Voids

A micrograph of the largest void in the HFS4 specimen can be seen in Figure 120.

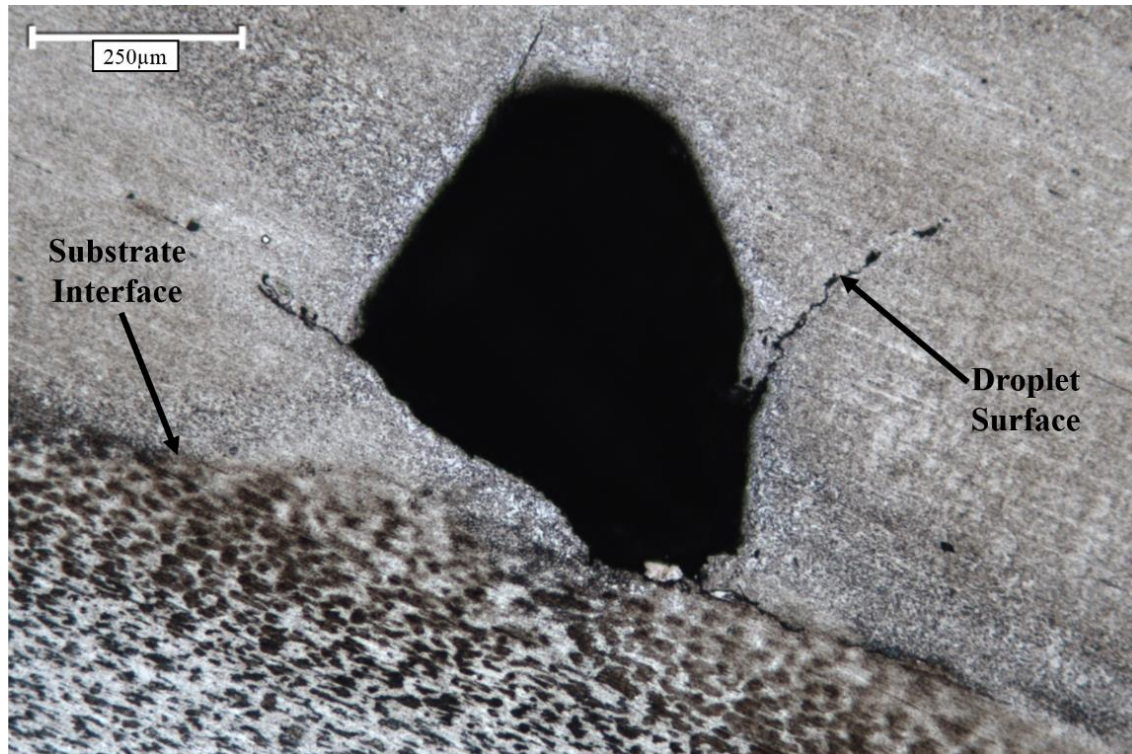


Figure 120: Largest HSF4 specimen void at substrate interface (10x magnification). The void was likely caused by lack of fusion between droplets and the substrate.

The scale bar in Figure 120 is 250 microns (μm) or about 10^{-6} in, making the void about 600microns (0.6mm) or 0.024in across at the widest point. Notice that the void occurred at the substrate/weld metal interface. The micrograph was taken at a slight angle with the substrate on the bottom and the weld metal on the top.

The void appears to be created by a lack of fusion between the droplet and the substrate/previous droplet. As illustrated in Figure 120, there appears to be a lack of fusion around the circular surface of a neighboring droplet.

Another void along the substrate/weld metal interface is shown in Figure 121.

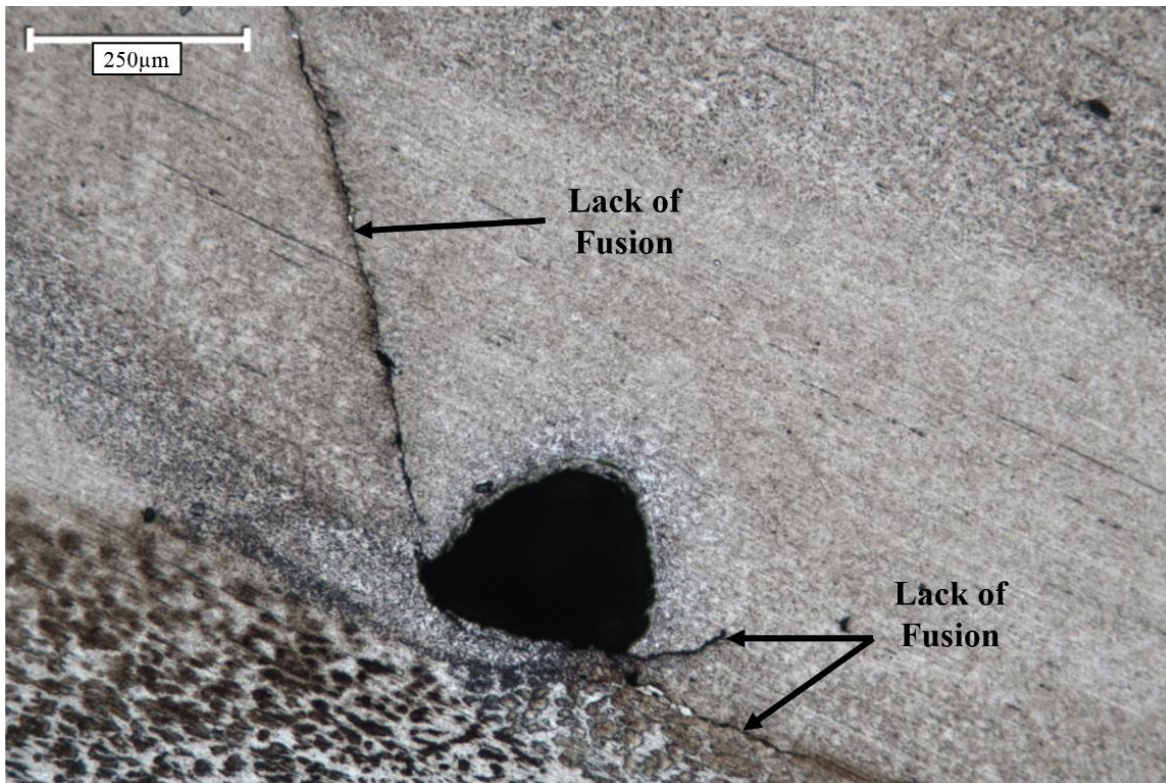


Figure 121: Smaller HSF4 specimen void at substrate interface (10x magnification). The void was likely caused by lack of fusion between droplets and the substrate.

The void shown in the micrograph in Figure 121 appears to be similar in nature to the void in Figure 120. It appears that the void exists where a droplet did not fully fuse to the substrate/previous droplet.

A void within the weld metal (not next to the substrate) is shown in Figure 122.

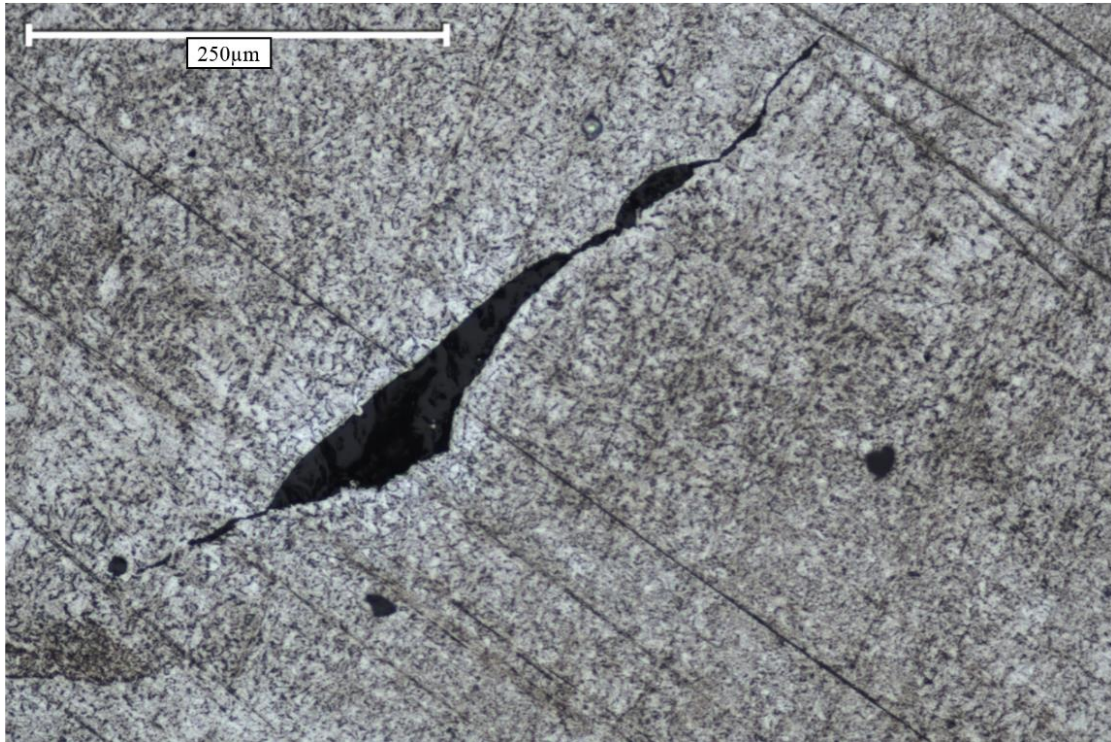


Figure 122: HSF4 specimen void within the weld metal (10x magnification). The void was likely caused by lack of fusion between droplets.

As seen in Figure 122, the void within the weld metal appears to be a lack of fusion between droplets. Looking at the scale bar, it can be seen that the void is about 500 microns or 0.02in long.

It was found that most voids were found at the substrate/weld metal interface. The cause of voids at the interface was likely due to the substrate's increased heat sinking abilities compared to the wall specimen's heat sinking abilities. Because the substrate represented a larger heat sink, complete fusion between droplets and the substrate was less likely.

Although several voids were present in the specimen, overall the specimen exhibited excellent density. The largest void found was less than a millimeter in size. In addition, because components are generally removed from the substrate after being built, voids that occur at the substrate/weld metal interface may be insignificant.

12.3. Microstructure

Three representative micrographs were taken at the substrate/weld metal interface, the middle layers, and the top layer. Figure 123 shows a micrograph taken at the substrate/weld metal interface at 10x magnification.

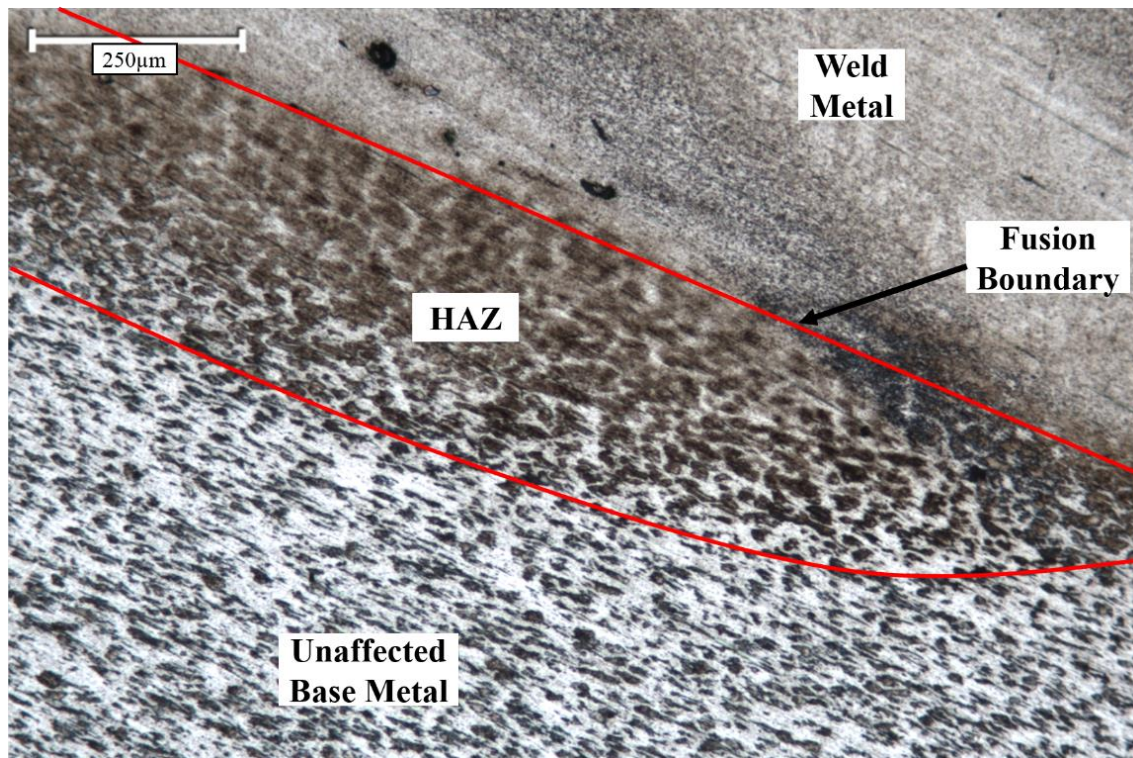


Figure 123: Microstructure of substrate/weld metal interface (10x magnification).

The microstructure in Figure 123 is divided into three regions: the unaffected base metal (substrate), HAZ (heat affected zone), and the weld metal. It can be seen that the unaffected base metal has a microstructure of coarse ferrite and pearlite grains. The grains are elongated, which is characteristic of cold rolling. In various regions of the HAZ, the microstructure significantly changes due to recrystallization and/or grain growth. The microstructure in the weld metal is composed of much finer grains. In fact, the grain structure in the weld metal cannot be resolved at the 10x magnification in Figure 123. In the weld metal just above the fusion boundary, small voids and/or inclusions can be seen.

Figure 124 shows a micrograph taken of the weld metal at 50x magnification.

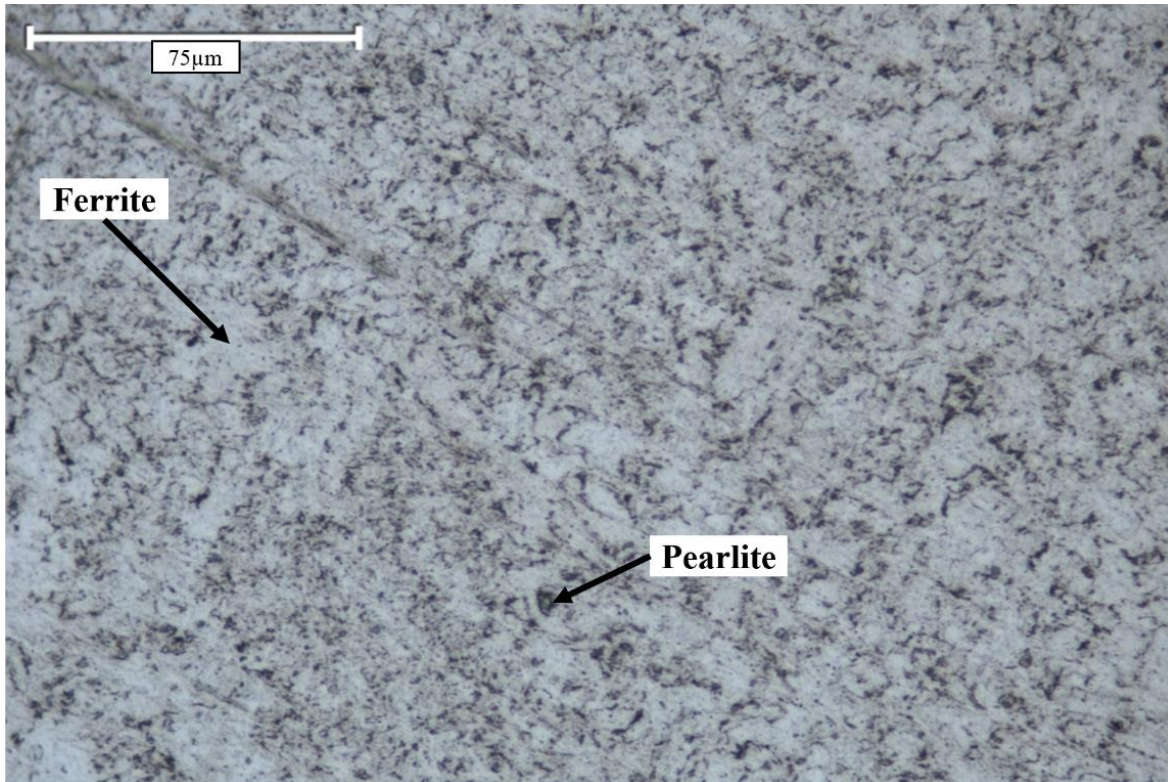


Figure 124: Microstructure of weld metal in middle layers (50x magnification). The microstructure in the middle layers is composed of equiaxed ferrite and pearlite grains that are 5 to 10 microns in size.

Notice that the scale bar in Figure 124 is 75 microns. It can be seen that the weld metal has a microstructure composed of relatively equiaxed ferrite and pearlite grains. The grain size is on the order of 5 to 10 microns. The small grain size is due to the high cooling rates and low heat input of the SiDD process. A small grain size indicates that the weld metal will have a much higher strength and toughness compared to the base material as given by the Hall-Petch relationship.

Microstructure analysis produced no evidence of grains growing and persisting from one layer to the next layer. In addition, because each droplet solidified towards its center, there was no evidence of grains growing and persisting from one droplet to the next droplet within a single layer.

The weld metal in Figure 124 was deposited in the specimen's middle layers and is representative of how the bulk composition of a component manufactured by GLADiS would appear. However, weld metal in middle layers was reheated by subsequent layers, altering the microstructure. Figure 125 shows weld metal from the top layer, which was not reheated by subsequent layers.

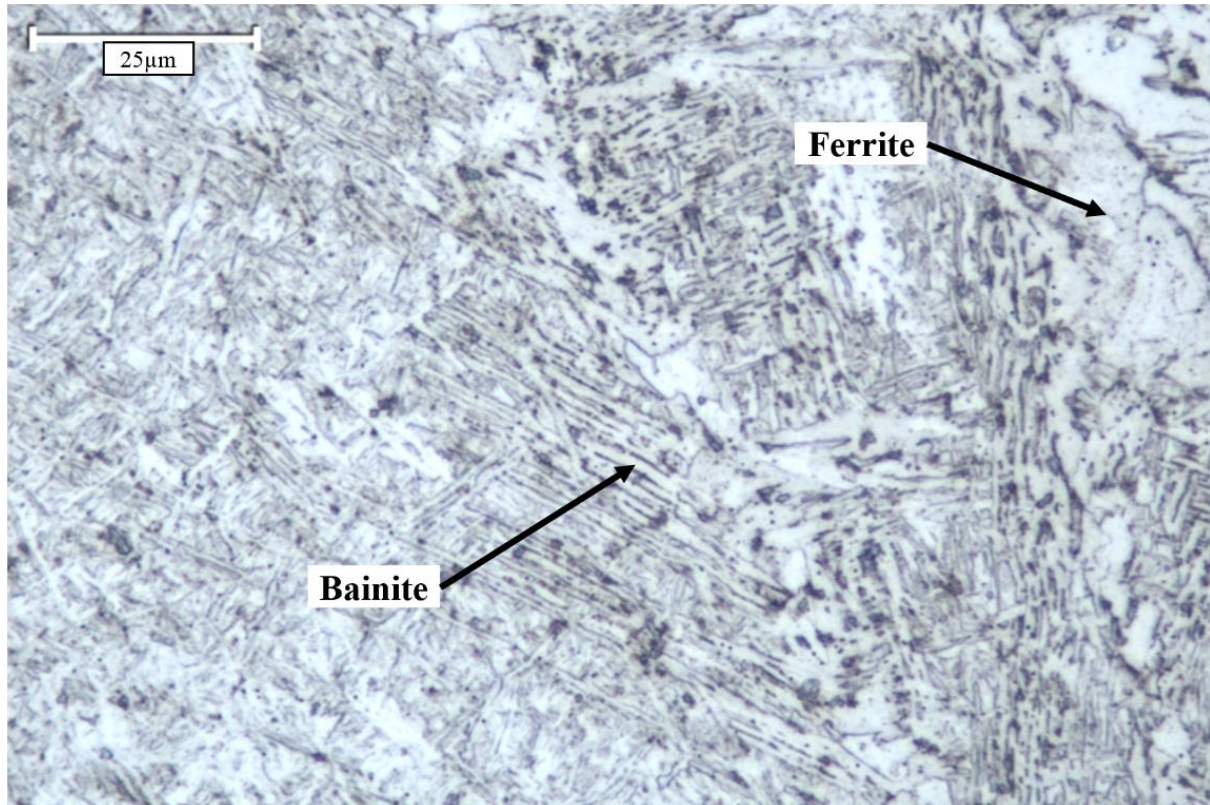


Figure 125: Microstructure of weld metal in top layer (100x magnification). The top layer microstructure is composed mostly of bainite and ferrite.

The micrograph in Figure 125 was taken at 100x, and the scale bar is 25 microns. It can be seen that the top layer's microstructure has additional features compared to the middle layers. In addition to ferrite, it appears that bainite formed in the top layers. Bainite is a non-equilibrium microstructure that exhibits improved strength and toughness properties. Bainite forms when cooling rates are too fast for equilibrium transformations (e.g., austenite to ferrite), but too slow for martensitic transformation. Bainite is composed of layers of cementite and dislocation-rich

ferrite. The large dislocation concentration is one of the attributes that gives bainite excellent strength properties.

Upon reheating, carbon becomes highly mobile and begins to diffuse to regions of lower carbon concentration. In addition, reheating causes the high concentration of dislocations in the ferrite to annihilate. Therefore, in layers below the top layer, reheating by subsequent layers causes dissolution of the previous layer into a stable, equilibrium structure as seen in Figure 124.

12.4. Summary

The HFS4 specimen built by GLADiS exhibited classic metallurgical properties. Although several voids were found, the largest was less than a millimeter in size, and overall, relatively few voids existed.

The micrographs indicated that the weld metal deposited using the SiDD technique exhibited an extremely fine-grained microstructure. Compared to conventional AM techniques, components built using GLADiS would be expected to have excellent strength and toughness in the as-built condition, without post-process heat treating.

13. Process Parameter Ranking

Throughout the process of building specimens, parameters were constantly tuned to achieve more optimal results. A list of key parameters was compiled and ranked in order of importance. They are welding current, shielding gas composition, drop spacing, laser power, electrode composition, and electrode extension.

13.1. Welding Current

Welding current was found to be the most important parameter. To achieve SiDD, a specific current routine had to be followed. First, a relatively high starting current was required to establish the arc and attain stable operating conditions. A lower background current was then required to grow a droplet and ensure premature droplet detachment did not occur. A current pulse of a specific amplitude and time was then required to detach the droplet. If the pulse was too long or high, multiple droplets could be detached; if the pulse was too short or low, the droplet would not detach.

13.2. Shielding Gas Composition

The next most important parameter was the shielding gas composition. It was found that a shielding gas of 98% Ar, 2% O₂ was required to achieve SiDD. Without an Ar rich environment, the current flux distribution localizes on the bottom of the droplet, and electromagnetic forces lift the droplet upwards. A downward acting electromagnetic force is required for controlled droplet transfer.

13.3. Drop Spacing

Although it did not affect the SiDD process, drop spacing was found to be the most important parameter in determining a specimens' geometric quality (accuracy and surface finish). If too short a drop spacing was used, droplets would pile on top of one another and often

deviate to the side. If too long a drop spacing was used, a weld bead of poor uniformity was made as shown in Figure 113 of Section 11.2.2. Adjusting the drop spacing by only a few thousandths of an inch was the difference between inadequate drop spacing and optimal drop spacing.

13.4. Laser Power

Another important parameter was laser power. Although the laser was not needed to produce specimens, it increased the production speed by about 10 times compared to using a high frequency arc starter without the laser. Using the laser allowed the SiDD technique to be automated because electrode and substrate cleaning was not required between drops.

The laser also provided arc stabilization and allowed specimens to be built with better geometric accuracy and surface finish. Droplets tended to land more consistently at the location where the laser was focused on the substrate.

Although laser benefits could be realized at a wide range of laser power, it was found that 50W was optimal. Powers below 50W were less reliable at arc starting, and powers above 50W added excessive thermal energy and changed the shape of deposited droplets/weld beads.

13.5. Electrode Composition

Electrode composition was found to be another important factor in determining specimen geometric quality. The ER70S-6 wire was found to produce parts with a rougher surface finish. The rough surface finish was due to spatter ejecting when a molten droplet of ER70S-6 exploded. Switching to ER70S-3 wire allowed specimens to be produced with a much better surface finish.

13.6. Electrode Extension

It was found that using a short electrode extension improved droplet/substrate coalescence. Cutting the electrode extension in half resulted in a 7%-8% increase in fusion zone cross-sectional area. However, specimen analysis showed that few lack of fusion voids existed, and most of those that did exist were at the substrate interface, where lack of fusion is likely not a problem.

14. Conclusions

The goal of this research was to bridge the gap between powder-based processes (low deposition rate, high geometric resolution) and wire-based processes (high deposition rate, low geometric resolution) using GMAW WAAM. The result: some of the thinnest (if not the thinnest) walls that have ever been manufactured using GMAW WAAM were built, exhibiting consistent surface finish and sound metallurgical microstructures.

14.1. Single Droplet Deposition

It was found that SiDD could be achieved by using the proper welding current sequence. After arc starting with a relatively high starting current, a low background current could form a droplet, and a current pulse could detach the droplet from the electrode. SiDD could only be achieved using an alternative arc starting method to the traditional short circuiting arc start used by GMAW. In addition, it was highly important to use the 98% Ar, 2% O₂ shielding gas. Without an Ar rich shielding environment, droplets could not be detached in a controlled manner.

14.2. Noncontact Arc Starting

It was found that photoemission from a metal surface generated by a 200W, 532nm laser was insufficient for starting the welding arc with the welding power source's open-circuit voltage. Starting the arc with the laser required coating the cathode surface with graphite and focusing the laser on the cathode.

The next noncontact arc starting technique investigated, PAW pilot arc starts, proved to be effective at starting the main welding arc. However, the PAW torch had to be placed in close proximity to the arc gap. Intrusion of the PAW torch in the arc area prevented the ability to achieve short electrode extensions. Because the work piece had to be cleaned before each

deposition test, SiDD with PAW pilot arc starting was produced an impractically long SiDD cycle time.

A brief investigation of lift start arc starting revealed that the welding power source did not have high enough inductance to reliably start the arc. To achieve an arc start by lift starting, the work piece had to be extremely clean and the wire electrode clipped to remove insulating layers on the electrode tip.

The first three arc starting techniques were attempts to avoid using a high frequency arc starter. When they proved to be inadequate, a high frequency arc starter was implemented. Many of GLADiS's electrical conductors had to be shielded, and an earth ground had to be installed to which the shielding could be connected. Circuit protection filters were required to protect electronics connected to the system. Extra insulation had to be installed on all devices connected to the welding circuit.

The final step in bullet-proofing the system to the arc starter was to custom build an insulated wire feeder that could withstand the high frequency arc starter. The insulated wire feeder was controlled by the Galil controller, which was susceptible to communication failures when the arc starter was energized. Once the insulated wire feeder was built, a triggering mechanism was developed to allow wire feed to be commanded, even after an arc starter induced connection loss to the Galil controller.

Tests showed that SiDD with high frequency arc starts was effective, but was not robust. To start the arc, the work piece had to be cleaned and the wire clipped, resulting in a slow deposition rate of about 30s per drop.

The last noncontact arc starting technique investigated was the high frequency arc starter/laser hybrid technique. It was found that hybrid technique was extremely effective at

starting the welding arc. Using 50W of laser power focused on the cathode eliminated the need to clean the work piece and clip the wire, which greatly increased the deposition rate compared to noncontact arc starting techniques without the laser.

14.3. Electrode Extension and Droplet Coalescence

It was found that more current was required to melt the same length of wire when using a short electrode extension. The average current for the SiDD process with a 0.136in electrode extension was 3A higher than the average current with a 0.264in electrode extension. Analyzing droplets deposited at both electrode extensions showed that the 3A increase in average current at the short electrode extension resulted in a 7%-8% increase in fusion zone area. The results agreed with the theory derived from the Lesnewich equation (1).

14.4. Specimen Builds and Parameter Tuning

Throughout the specimen builds, four parameters were found to greatly affect the specimens' resulting geometric accuracy and surface finish: electrode composition, drop spacing, interlayer grinding, and laser power.

Specimen PAWS1 was built with PAW pilot arc starts. It was built with ER70S-6 wire, near optimal drop spacing (0.07in), interlayer grinding only when needed, and no laser. The surface was relatively rough due to spatter from exploding droplets. Exploding droplets were only observed when using ER70S-6 wire. Because the drop spacing was not optimal, the geometric accuracy was reduced. In addition, the slow speed of the PAW pilot arc starting technique resulted in a slow deposition rate of 0.02lb/hr.

The HFS1 specimen was the first specimen built with the high frequency arc starting technique. It was built with ER70S-3 wire, 0.073in drop spacing, no interlayer grinding, and no laser. Although there was no spatter from the ER70S-3 wire, the specimen's surface was

relatively rough due to the excessive drop spacing. Also, because no interlayer grinding was performed, low spots had to be filled. Due to excessive cleaning required between drops, the deposition rate was reduced to 0.01lb/hr.

HFS2 was built with ER70S-3 wire, optimal drop spacing (0.068in), no interlayer grinding, and no laser. Using the optimal charge spacing of 0.068in greatly improved the specimen's surface finish and geometric accuracy. However, because no interlayer grinding was performed, high spots could be seen in the finished component and the geometric accuracy was slightly reduced. Similar to HFS1, the deposition rate was 0.01lb/hr.

HFS3 was built with using the same parameters and techniques as HFS2, but with the addition of interlayer grinding only when needed. HFS3 was similar to HFS2, but the geometric accuracy and surface finish was improved by adding intermittent interlayer grinding. Interlayer grinding added only an insignificant amount of time to the building process, and the deposition was calculated to be 0.01lb/hr.

HFS4 was built, once again, using the same parameters and techniques as HFS2 and HFS3, but interlayer grinding was performed on every layer. The result was a specimen with better surface finish and geometric accuracy than the previous specimens. The deposition rate was the same as the previous high frequency arc starting specimens.

The last specimen, HS1, was built using the high frequency arc starter/laser hybrid technique. Except for the addition of the laser, the build parameters were the same as HFS3 with intermittent interlayer grinding. The HS1 specimen had the best surface finish and geometric accuracy, which was accredited to laser arc stabilization. The laser allowed the process to be automated, which increased the deposition rate to 0.1lb/hr, 10 times greater than the high frequency arc starting technique without the laser.

14.5. Specimen Analysis

Specimen analysis showed complete fusion between individual droplets, with few voids and/or inclusions. Metallography analysis showed that the SiDD process produced weld metal with a small grained microstructure. Grains in the middle layers were about 5 to 10 microns in diameter. In addition, no evidence was found of grains growing and persisting from one layer to the next layer, and no evidence was found of grains growing a persisting from one droplet to the next droplet within a single layer.

14.6. Process Parameter Ranking

Various parameters used for building specimens with SiDD were ranked in order of most important to least important. The ranking is as follows:

1. Welding current: SiDD could not be achieve without the proper welding current routine.
2. Shielding gas composition: without the use of an Ar rich shielding gas, droplets could not be detached from the electrode.
3. Drop spacing: a specimen's geometric accuracy and surface finish was highly dependent on the drop spacing. Only the optimal drop spacing of 0.068in could produce a geometrically accurate specimen with a smooth surface.
4. Laser power: using a laser to assist the arc starter allowed the SiDD process to be automated. The result was a deposition rate increase of about 10 times. The laser also provided arc stabilization which allowed specimens to be produce with better geometric accuracy and surface finish.

5. Electrode composition: It was found that ER70S-6 wire produced spatter when molten droplets exploded due to possible imperfections in the wire. ER70S-3 wire did not produce spatter.
6. Electrode extension: It was found that decreasing the electrode extension improved droplet/substrate coalescence by allowing more welding current to be used to melt the same length of wire.

14.7. Future Work

The present research encompassed concepts from a variety of engineering fields. Although many of these concepts were exploited, they were not extensively studied. Each individual concept that was briefly investigated in the present research could provide the topic for future research projects. This section presents suggestions for future research projects and investigations.

14.7.1. Specimen Metallurgical and Mechanical Analysis

Because the present research's scope mainly focused on the process of building small features with GMAW, little work was performed to evaluate the specimens' metallurgical and mechanical properties. Future work should more thoroughly investigate the metallurgical and mechanical properties of specimens produced using the SiDD process. Mechanical tests, such as a tensile test, should be performed to determine the weld metal's actual strength and toughness properties. Specimens could be produced with various process parameters, such as various levels of heat input, to test the effects of processing parameters on deposited weld metal. In addition, a large number of specimens should be produced so that results from metallurgical and mechanical tests present a statistically significant data set.

14.7.2. Residual Stress and Droplet Placement

Specimens built in the present research were made by sequentially depositing droplets next to each other to form weld beads. The weld beads were stacked in layers to produce a wall. Although the heat input was low using SiDD, the manner in which the droplets were deposited could lead to excess heat buildup in a specific location, and therefore, residual stress.

Future work should investigate randomized or strategic placement of droplets on a build plane to distribute heat input and mitigate residual stress. Residual stress tests should be performed on specimens made with different droplet placement strategies to compare.

14.7.3. Closed-loop Control

Experimentation performed in the present research was accomplished using open-loop control. After an experiment was performed, voltage, current, and high-speed video data were analyzed. Observations made in the data analysis were used to adjust the process parameters. The process was then executed using the new parameters, and more observations were made. It was an iterative process that resulted in a working set of parameters for a given set of conditions.

Often times, the conditions in a real world system change. For example, a high spot on a build plane would cause the CTWD to be shorter in that location. If set process parameters are used, the change in conditions could alter the process's functionality.

Future work should investigate the use of a closed-loop control technique, such as feedback control, to control process parameters. Closed-loop control could be used to maintain a precise electrode extension, or it could be used to control droplet diameter. The result would be a system that was more robust to changing conditions.

Feedback of process parameters could be provided by several different techniques. One technique would be to use the voltage and current measurements to estimate features such as the

electrode extension. For example, dividing the power source voltage by the welding current would result in a measurement of dynamic resistance, which could be used to estimate the electrode extension to use for feedback.

Another feedback sensing technique would be to use arc light sensing [14]. Sensing the arc light could be used to obtain an estimate of the electrode extension and, possibly, the droplet diameter.

Possibly the most accurate feedback sensing technique for controlling electrode extension and droplet diameter would be to use a high-speed camera from which frames could be extracted and processed in real-time. High-speed camera frames could be used to measure the electrode extension and droplet diameter with a reasonably high degree of accuracy.

14.7.4. Pulsing Power Source and Arc Starting

The high frequency arc starter used in the present research was a relatively simple pulsing power source that supplied voltage pulses at regular intervals (60Hz). Characteristics of the voltage pulses, such as amplitude, duration, and shape, were not adjustable. Test results showed that the high frequency arc starter was not the best arc starting technique because it could only start the arc if the work piece and electrode tip were cleaned, and it could only arc over a 0.04in arc gap. In addition, the high frequency arc starter supplied multiple voltage pulses until the arc was started, making the arc starting time irregular.

Arc starting could be greatly improved by designing a pulsing power source with modern power electronics that could supply precisely controlled voltage pulses. Having the ability to precisely control characteristics of a pulse would allow a pulse to be optimized for arc starting. The pulsing power supply would have to be capable of supplying peak controllable voltages of at least 10kV over a $5\mu\text{s}$ – $10\mu\text{s}$ duration to generate sufficient field emission to start the arc. Arcs

could be started over larger arc gaps if higher peak voltages (20kV – 50kV) could be achieved. Different controllable pulse shapes, such as ramp or step changes in the pulse waveform, could be investigated to determine the pulse shape effect on arc starting.

Although the pulsing power source could use either voltage or current control, it would potentially be more beneficial for arc starting to precisely control the voltage. Controlling the voltage would allow more precise control over the electric field that generates field emission in the arc gap.

14.7.5. Laser Arc Stabilization and Photoemission/laser Arc Starting

Although test results indicated that laser arc stabilization allowed droplets to be deposited with higher accuracy, extensive research could be performed to more thoroughly analyze the effect of a laser on a welding arc. For example, it was found that the 532nm laser used in testing took approximately 15s to reach its power set-point on command. Therefore, the laser was not turned off between droplet depositions when depositing a single layer. Because the laser ran continuously, the laser power had to be reduced to 50W to minimize heat input from the laser.

It is possible that laser arc stabilization could be improved by increasing the laser power. If a laser was obtained that could reach its power set-point within a several milliseconds, the laser could be pulsed at a much higher power during the time duration in which the arc is on in the SiDD process (less than 200ms). The average laser power could be reduced, while much higher laser power over a short time period could be used to stabilize the arc.

Another possible benefit to having a laser capable of generating high-powered pulses is that it could potentially be used for starting the welding arc. Tests in the present research showed that 200W of laser power was insufficient for starting the welding arc without the

addition of graphite. However, using a pulse of much higher laser power could potentially generate sufficient photoemission and even metal evaporation in the arc gap and start the arc.

14.7.6. Wire Electrode Diameter and Composition

The present research investigated the use of two different wire electrode compositions: ER70S-6 and ER70S-3. Both wires were composed of mild steel, but with varying concentrations of deoxidizers. The same SiDD process could possibly be applied to different metals and alloys other than mild steel. SiDD with various stainless steel alloys, aluminum alloys, and titanium alloys could be investigated. Metallurgical and mechanical properties of SiDD weld metal composed of various alloys could be analyzed.

In addition to testing SiDD with various wire compositions, the effects of wire diameter could also be investigated. Only 0.045in diameter wire was investigated in the present research.

14.7.7. Custom Contact Tip

The contact tips used in the present research were standard, off the shelf contact tips. It is generally assumed that the wire electrode makes contact with the contact tip at the end of the contact tip. The point of contact between the wire electrode and the contact tip is the point where current is conducted into the wire electrode. However, a problem with conventional contact tips is that the actual location of contact between the wire electrode and the contact tip can be uncertain.

To allow wire to easily pass through the contact tip, the contact tip's inside diameter is slightly larger than the wire electrode's outside diameter. If the wire electrode is straight, it could potentially rattle around the inside the contact tip, instantaneously changing the point of contact. Because the true electrode extension is measured from the point of contact to the end of

the electrode, the true electrode extension could be instantaneously changing a distance equal to the contact tip's length (1in to 2in).

In addition, the contact surfaces between the wire electrode and the contact tip can change over time as the contact tip wears. Contact tip wear could cause the point of contact to shift over time.

Because part of the present research focused on reducing the electrode extension, it may be important to investigate the production and implementation of a custom contact tip. A custom contact tip could be made with tighter tolerances and/or out of an alternative material to ensure a stable point of contact at the contact tip's end. Having a stable point of contact at the contact tip's end would allow the true electrode extension to be precisely measured and controlled.

14.7.8. Automatic Geometry Correction

During the HFS1 build, it was found that low spots could be manually filled by positioning the torch over the low spot and using SiDD to fill it. Future work could investigate the feasibility of using a device, such as a profilometer, to automatically locate low spots on the build plane. If the location of low spots could be determined, the system could be programmed to automatically reposition the torch and fill them.

14.7.9. Substrate Release Mechanism

Specimen metallurgical analysis showed that several voids existed at the substrate/weld metal interface. The voids were characterized as lack of fusion due to high heat sinking conditions on the substrate.

A future study could explore the possibility of exploiting the low heat input of SiDD and the high heat sinking conditions on the substrate to develop a substrate release mechanism. It may be possible to extend the electrode extension on the first layer to allow current reduction and

further reduce fusion to the substrate. With reduced fusion, it could be possible to break the weld metal off the substrate surface with a light blow from a hammer.

14.7.10. Geometric Capabilities

The present research's scope was limited to building simple geometries (i.e., single bead width, linear walls). A future study could investigate the prospect of producing components with complex geometric features using SiDD. Research could include finding geometric limits of depositing weld metal in the flat position with simple motion systems, as well as geometric limits of depositing weld metal using robotic torch positioning and/or substrate turntables.

14.7.11. Integrating Conventional GMAW AM and SiDD

The benefit of using conventional GMAW deposition for AM is that high deposition rates can be achieved when building large components without small features. In contrast, the benefit of using SiDD is that small features could be produced at lower deposition rates. However, the same system could be used to achieve both SiDD and conventional GMAW deposition. Therefore, it could be possible to quickly build large components that exhibited small features by integrating conventional GMAW deposition and SiDD on a single system. Integrating the two deposition techniques into one system would allow large portions of a component to be built at around 22lb/hr [8] and small features to be built using SiDD.

15. References Cited

- [1] E. Winick, "MIT Technology Review: 10 Breakthrough Technologies 2018," Massachusetts Institute of Technology, March 2018. [Online]. Available: <https://www.technologyreview.com/lists/technologies/2018/#3-d-metal-printing>. [Accessed 16 May 2018].
- [2] D. Ding, Z. Pan, D. Cuiuri and H. Li, "Wire-feed additive manufacturing of metal components: technologies, developments and future interests," *International Journal of Advanced Manufacturing Technology*, vol. 81, pp. 465-481, 2015.
- [3] American Welding Society, Inc., *Welding Handbook, Volume 2 - Welding Processes, Part 1* (9th Edition), R. L. O'Brien, Ed., Miami: American Welding Society, Inc., 2004.
- [4] K. Mumtaz and N. Hopkinson, "Selective Laser Melting of thin wall parts using pulse shaping," *Journal of Materials Processing Technology*, vol. 210, no. 2, pp. 279-287, 2010.
- [5] K. Mumtaz and N. Hopkinson, "Top surface and side roughness of Inconel 625 parts processed using selective laser melting," *Rapid Prototyping Journal*, vol. 15, no. 2, pp. 96-103, 2009.
- [6] K. P. Karunakaran, A. Bernard, S. Suryakumar, L. Dembinski and G. Taillandier, "Rapid manufacturing of metallic objects," *Rapid Prototyping Journal*, vol. 18, no. 4, pp. 264-280, 2012.
- [7] K. M. Taminger and R. A. Hafley, "Electron Beam Freeform Fabrication for Cost Effective Near-Net Shape Manufacturing," in *NATO/RTO AVT-139 Specialists' Meeting on Cost Effective Manufacture via Net Shape Processing*, Amsterdam; Netherlands, 2006.
- [8] S. W. Williams, F. Martina, A. C. Addison, J. Ding, G. Pardal and P. Colegrove, "Wire + Arc Additive Manufacturing," *Materials Science and Technology*, vol. 32, no. 7, pp. 641-647, 2016.
- [9] NORSK TITANIUM, "Technology," Norsk Titanium US Inc., 2018. [Online]. Available: <http://www.norsktitanium.com/technology>. [Accessed 1 June 2018].
- [10] K. Kussmaul, F. -W. Schoch and H. Luckow, "High Quality Large Components 'Shape Welded' by a SAW Process," *Welding Journal*, vol. 62, pp. 17-24, 1983.

- [11] B. W. Shinn, D. F. Farson and P. E. Denney, "Laser stabilisation of arc cathode spots in titanium welding," *Science and Technology of Welding and Joining*, vol. 10, no. 4, pp. 475-481, 2005.
- [12] Y. M. Zhang, E. Liguio and R. Kovacevic, "Active metal transfer control by monitoring excited droplet oscillation," *Welding Journal*, vol. 77, no. 9, pp. 388-s - 395-s, 1998.
- [13] A. Lesnewich, "Control of melting rate and metal transfer in gas-shielded metal-arc welding: part 1 - control of electrode melting rate," *Welding Journal*, vol. 8, pp. 343s-353s, 1958.
- [14] R. B. Madigan, *Control of Gas Metal Arc Welding Using Arc Light Sensing*, Golden, CO: Colorado School of Mines, 1994.
- [15] L. A. Jones, P. Mendez, D. Weiss and T. W. Eagar, "Dynamic Behavior of Gas Metal Arc Welding," in *Iron and Steel Technology*, Pohang, Korea, 1997.
- [16] L. A. Jones, T. W. Eagar and J. H. Lang, "Magnetic forces acting on molten drops in gas metal arc welding," *Journal of Physics D: Applied Physics*, vol. 31, no. 1, pp. 93-106, 1998.
- [17] Y. M. Zhang and P. J. Li, "Modified Active Control of Metal Transfer and Pulsed GMAW of Titanium," *Welding Research Supplement*, pp. 54-61, 2001.
- [18] S. Subramaniam, D. R. White, J. E. Jones and D. W. Lyons, "Experimental Approach to Selection of Pulsing Parameters in Pulsed GMAW," *Welding Journal*, vol. 78, pp. 166-s - 172-s, 1999.
- [19] A. F. Ribeiro and J. Norish, "Rapid Prototyping Process Using Metal Directly," in *Seventh Annual Solid Freeform Fabrication Symposium*, Austin, TX, 1996.
- [20] M. D. McAninch and C. C. Conrardy, "Shape melting - a unique near-net shape manufacturing process," *Welding Review International*, vol. 10, no. 1, pp. 33-40, 1991.
- [21] C. M. Weber and B. M. Dingman, *Robotic Manufacture of Near Net Shape Components by the Shape Melting Process*, San Diego: Babcock & Wilcox, 1988.
- [22] Y. Zhang, Y. Chen, P. Li and A. T. Male, "Weld deposition-based rapid prototyping: a preliminary study," *Journal of Materials Processing Technology*, vol. 135, pp. 347-357, 2003.

- [23] G. C. Anzalone, C. Zhang, B. Wijnen, P. G. Sanders and J. M. Pearce, "A Low-Cost Open-Source Metal 3-D Printer," *IEEE Access*, vol. 1, pp. 803-810, 2013.
- [24] +MFG, "Projected Benefits During Product Life Cycle," +MFG, 2016. [Online]. Available: <http://plus-mfg.com/projected-benefits-during-product-life-cycle/>. [Accessed 24 July 2018].
- [25] +MFG, "+1000K Arc Metal Deposition Machine," 2015. [Online]. Available: <http://plus-mfg.com/wp-content/uploads/2015/03/1000K-Features-3.19.15.pdf>. [Accessed 24 July 2018].
- [26] J. Xiong, G. Zhang and W. Zhang, "Forming appearance analysis in multi-layer single-pass GMAW-based additive manufacturing," *International Journal of Advanced Manufacturing Technology*, vol. 80, no. 9-12, pp. 1767-1776, 2015.
- [27] C. Doumanidis and Y.-M. Kwak, "Multivariable adaptive control of the bead profile geometry in gas metal arc welding with thermal scanning," *International Journal of Pressure Vessels and Piping*, vol. 79, pp. 251-262, 2002.
- [28] J. Xiong and G. Zhang, "Adaptive control of deposited height in GMAW-based layer additive manufacturing," *Journal of Materials Processing Technology*, vol. 214, pp. 962-968, 2014.
- [29] J. Xiong, Z. Yin and W. Zhang, "Closed-loop control of variable layer width for thin-walled parts in wire and arc additive manufacturing," *Journal of Materials Processing Technology*, vol. 233, pp. 100-106, 2016.
- [30] J. Xiong, G. Zhang, Z. Qiu and Y. Li, "Vision-sensing and bead width control of a single-bead multi-layer part: material and energy savings in GMAW-based rapid manufacturing," *Journal of Cleaner Production*, vol. 41, pp. 82-88, 2013.
- [31] P. Kazanas, P. Deherkar, P. Almeida, H. Lockett and S. Williams, "Fabrication of geometrical features using wire and arc additive manufacture," *Proceedings of the Institution of Mechanical Engineers, Part B: Journal of Engineering Manufacture*, vol. 226, pp. 1042-1051, 2012.
- [32] J. Xiong, Y. Lei, H. Chen and G. Zhang, "Fabrication of inclined thin-walled parts in multi-layer single-pass GMAW-based additive manufacturing with flat position deposition," *Journal of Materials Processing Technology*, vol. 240, pp. 397-403, 2016.

- [33] K. Furukawa, "New CMT arc welding process - welding of steel to aluminium dissimilar metals and welding of super - thin aluminium sheets," *Welding International*, vol. 20, no. 6, pp. 440-445, 2006.
- [34] Y.-A. Song, S. Park, D. Choi and H. Jee, "3D welding and milling: Part I - a direct approach for freeform fabrication of metallic prototypes," *International Journal of Machine Tools and Manufacture*, vol. 45, no. 9, pp. 1057-1062, 2005.
- [35] B. D. DeRuntz, "Assessing the Benefits of Surface Tension Transfer Welding to Industry," *Journal of Industrial Technology*, vol. 19, no. 4, pp. 1-8, 2003.
- [36] Lincoln Electric, *Waveform Control Technology: Surface Tension Transfer (STT)*, Cleveland: The Lincoln Electric Company, 2005.
- [37] E. K. Stava, "Waveform control speeds root pass," *Welding Design & Fabrication*, vol. 74, no. 2, p. 39, 2001.
- [38] T. F. Costa and L. O. Vilarinho, "Influence of Process Parameters During the Pipe Welding of Low-Carbon Steel Using RMD (Regulated Metal Deposition) Process," in *21st Brazilian Congress of Mechanical Engineering*, Natal, RN, Brazil, 2011.
- [39] Miller Electric Mfg. Co., *PipeWorx Welding System*, Index No. PWS/2.0 ed., Appleton, Wisconsin: Miller Electric Mfg. Co., 2014.
- [40] J. Feng, H. Zhang and P. He, "The CMT short-circuiting metal transfer process and its use in thin aluminium sheets welding," *Materials and Design*, vol. 30, no. 5, pp. 1850-1852, 2009.
- [41] P. S. Almeida and S. Williams, "Innovative Process Model of Ti-6Al-4V Additive Layer Manufacturing Using Cold Metal Transfer (CMT)," in *Proceedings of the twenty-first annual international solid freeform fabrication symposium, University of Texas at Austin*, Austin, TX, 2010.
- [42] J. Ding, P. Colegrove, J. Mehnert, S. Ganguly, P. S. Almeida, F. Wang and S. Williams, "Thermo-mechanical analysis of Wire and Arc Additive Layer Manufacturing process on large multi-layer parts," *Computational Materials Science*, vol. 50, pp. 3315-3322, 2011.
- [43] S. Selvi, A. Vishvakshnan and E. Rajasekar, "Cold metal transfer (CMT) technology - An overview," *Defence Technology*, vol. 14, no. 1, pp. 28-44, 2018.

- [44] A. S. Haselhuhn, B. Wijnen, G. C. Anzalone, P. G. Sanders and J. M. Pearce, "In Situ Formation of Substrate Release Mechanisms for Gas Metal Arc Weld Metal 3-D Printing," *Journal of Materials Processing Technology*, vol. 226, pp. 50-59, 2015.
- [45] D. Yang, G. Wang and G. Zhang, "Thermal analysis for single-pass multi-layer GMAW vased additive manufacturing using infrared thermography," *Journal of Materials Processing Technology*, vol. 244, pp. 215-224, 2017.
- [46] H. Zhao, G. Zhang, Z. Yin and L. Wu, "Three-dimensional finite element analysis of thermal stress in single-pass multi-layer weld-based rapid prototyping," *Journal of Materials Processing Technology*, vol. 121, pp. 276-285, 2012.
- [47] H. H. Zhao, H. C. Li, G. J. Zhang, Z. Q. Yin and L. Wu, "Numerical simulation of temperature field and stress distributions in multi-pass single-layer weld-based rapid prototyping," *Reviews on Advanced Materials Science*, vol. 33, no. 5, pp. 402-409, 2013.
- [48] X. Bai, H. Zhang and G. Wang, "Modeling of the moving induction heating used as secondary heat source in weld-based additive manufacturing," *International Journal of Advanced Manufacturing Technology*, vol. 77, pp. 717-727, 2015.
- [49] X. Bia, H. Zhang and G. Wang, "Improving prediction accuracy of thermal analysis for weld vased additive manufacturing by calibrating input parameters using IR imaging," *International Journal of Advanced Manufacturing Technology*, vol. 69, pp. 1087-1095, 2013.
- [50] J. Xiong, Y. Lei and R. Li, "Finite element analysis and experimental validation of thermal behavior for thin-walled parts in GMAW-based additive manufacturing with various substrate preheating temperatures," *Applied Thermal Engineering*, vol. 126, pp. 43-52, 2017.
- [51] H. Zhao, G. Zhang, Z. Yin and L. Wu, "A 3D dynamic analysis of thermal behavior during single-pass multi-layer weld-based rapid prototyping," *Journal of Materials Processing Technology*, vol. 211, pp. 488-495, 2011.
- [52] A. F. Alhuzaim, *Investigation in the use of plasma arc welding and alternative feedstock delivery method in additive manufacture*, Butte, MT: ProQuest Dissertations Publishing, 2014.
- [53] W. Tuttle, Interviewee, *EMI prevention techniques*. [Interview]. 7 May 2018.

- [54] F. W. Grover, *Inductance Calculations*, New York: Dover Publications, 2009.
- [55] D. K. Cheng, *Field and Wave Electromagnetics*, Reading, Massachusetts: Addison-Wesley Publishing Company, 1992.
- [56] M. D. McAninch, *Evaluation of the Gas Metal Arc Welding Process Using Wrought and Rapidly Solidified Strip Consumables*, Columbus, OH: The Ohio State University, 1990.

16. Appendix A: Analog and Digital I/O Control Code

16.1. I/O PCI Card Control

The following code was the C++ class used to control the analog and digital I/O.

```
// Class for operating the I/O PCI cards

#include "dacqdev.h"

dacqdev::dacqdev() // constructor
{
    dev_filename="/dev/comedi1"; // create DAC device file name
    dev_filename_ai = "/dev/comedi0"; // create ADC device file name
    // Upon reboot, devices can swap comedi numbers
    // (i.e., comedi1 becomes comedi0 and comedi0 becomes comedi1)

    device = comedi_open(dev_filename.c_str()); // open a DAC comedi device
    device_ai = comedi_open(dev_filename_ai.c_str()); // open a ADC comedi device

    if(!device) // if DAC device could not be opened, print out an error
    {
        comedi_perror(dev_filename.c_str());
        is_available=false; // device not available
        printf("Warning - I/O Card Not Found\n");
    }
    else // if DAC device opened, report a success
    {
        printf("I/O Card Found\n");
        is_available = true; // device available
        configure(); // configure I/O cards (see configure function below)
    }

    if(!device_ai) // if ADC device could not be opened, print out an error
    {
        comedi_perror(dev_filename_ai.c_str());
        is_available_ai = false; // device not available
        printf("Warning - AI Card Not Found\n");
    }
    else // if ADC device opened, report a success
    {
        printf("AI Card Found\n");
        is_available_ai = true; // device available
        configure(); // configure I/O cards (see configure function below)
    }
}

dacqdev::~~dacqdev() // destructor
{
    //printf("in dacqdev destructor\n");
    comedi_close(device); // close DAC device
    comedi_close(device_ai); // close ADC device
}

void dacqdev::configure() // configure DAC and ADC devices
{
```

```

if(is_available==false) return; // if DAC device not available, exit program
if (is_available_ai == false) return; // if ADC device not available, exit program

#define SUBD_AI 0 /* analog input */
#define SUBD_AO 0 /* analog output */
#define SUBD_DIO 1 /* digital input */

// When reading is out of range (oor), set to NAN (not a number):
comedi_set_global_oor_behavior(COMEDI_OOR_NAN);

// analog output (DAC)
//ranges:      0      1      2      3      4      5
//all channels: [-10,10] [-5,5] [-2.5,2.5] [0,10] [0,5] [0,2.5]
ao_range=3; // set analog output range to 0V-10V
// get range information to print to screen:
ao_range_info = comedi_get_range(device, SUBD_AO, 0, ao_range);
// determine maximum valid data value for DAC:
ao_maxdata = comedi_get_maxdata(device, SUBD_AO, 0);

// there are 3 banks of 8 bits DIO (digital input/output)
// setting the direction of a bit in a bank sets the entire bank that direction
// the channels are addressed 0-23
comedi_dio_config(device, SUBD_DIO, 0, COMEDI_OUTPUT);
comedi_dio_config(device, SUBD_DIO, 8, COMEDI_INPUT);
comedi_dio_config(device, SUBD_DIO, 16, COMEDI_INPUT);
comedi_dio_config(device, SUBD_DIO, 20, COMEDI_INPUT);

// analog input (ADC)
//ranges:      0      1      2      3
//all channels: [0 V,10 V] [0 V,5 V] [0 V,2.5 V] [0 V,1.25 V]
ai_range=1; // set analog input range to 0V-5V to match isolation module output
// get range information to print to screen:
ai_range_info = comedi_get_range(device_ai, SUBD_AI, 0, ai_range);
// determine maximum valid data value for ADC:
ai_maxdata = comedi_get_maxdata(device_ai, SUBD_AI, 0);

// print DAC and ADC range information:
printf("[0,%d] -> [%g,%g]\n", ao_maxdata, ao_range_info->min, ao_range_info->max);
printf("[0,%d] -> [%g,%g]\n", ai_maxdata, ai_range_info->min, ai_range_info->max);
}

bool dacqdev::ready() // function to check if DAC device is available
{
    return is_available;
}

// function for controlling analog output (DAC). Enter the desired output channel
// and the desired output voltage (value)
void dacqdev::ao(int channel,double value)
{
    if(is_available==false) return; // only execute if device is available

    // scale value to proper DAC form (10.0 is from the range above):
    lsampl_t data = (lsampl_t)(value/10.0*(double)ao_maxdata);
    // don't let the data value go outside DAC acceptable range:
    if(data<0) // minimum scaled value is 0

```

```

        data=0;
        if(data>4095) // maximum scaled value is 4095
            data=4095;

        // set DAC output to desired value:
        comedi_data_write(device, SUBD_A0, channel, ao_range, ao_aref, data);
    }

// function for controlling analog input (ADC). Enter the desired input channel
double dacqdev::ai(int channel)
{
    lsampl_t data; // create variable of type lsampl_t
    if(is_available_ai==false) return 0.0; // only execute if device is available

    //channel=channel - 1; Channel number printed on PCB does not match comedi channel
number
    unsigned int ai_delay = 900; //allow input to settle after switching channels
    // read from the desire input channel:
    comedi_data_read_delayed(device_ai, SUBD_AI, channel, ai_range, ai_aref, &data,
ai_delay);
    // convert comedi value to physical value:
    double physical_value = comedi_to_phys(data, ai_range_info, ai_maxdata)*2.0;
    // comedi_to_phys is multiply by 2 to compensate for isolation module gain of 1/2
    // (SCM5B41-03 Module)

    return physical_value;// return the physical value;
}

// function for controlling digital output. Enter the desired output channel
// and desired logic state (Boolean value)
void dacqdev::dout(int channel, bool value)
{
    if(is_available==false) return; // only execute if device is available
    lsampl_t data=(lsampl_t)value; // create variable of type lsampl_t and set it to
desired logic state
    // the allowable channels here are defined by bank output direction under
configure above
    // set digital output to desired logic state:
    comedi_data_write(device, SUBD_DIO, channel, 0, 0, !data);
}

// function for controlling digital input. Enter the desired input channel
bool dacqdev::din(int channel)
{
    if(is_available==false) return false; // only execute if device is available
    lsampl_t data; // create variable of type lsampl_t
    // the allowable channels here are defined by bank input direction under configure
above
    // read logic state from desired input channel:
    comedi_data_read(device, SUBD_DIO, channel, 0, 0, &data);
    return (bool)data; // return logic state
}

```

16.2. DAQ Function

The following C++ code is the data acquisition (DAQ) function that operated as a separate thread to the process control code.

```
int DAQ_FLAG = 1; // use to turn off DAQ thread
char weld_data[1000]; // character string that holds data file name

void DAQ_thread()// this function collects data from the weld process
{
    Timer et; // create an instance of the elapsed timer
    wire_dev wire; // create an instance of the wire feeder control device
    welder_dev welder; // create an instance of the welder control device
    dacqdev dacq; // create an instance of the DAQ device
    //laser_dev laser; // create an instance of the laser control device

    ofstream data_file (weld_data); // create a data file using given file name

    if (data_file.is_open())// make sure file is open
    {
        data_file << "Time,Current,Voltage" << endl; // headers for each column

        et.start(); // start timer

        while(DAQ_FLAG) // take data for as long as DAQ_FLAG = 1
        {
            // measure parameters and write them to file in csv format:
            data_file << et.getElapsedTimeInMicroSec() << ","
            << welder.get_current() << "," << welder.get_voltage() << endl;

        }

        et.stop(); // stop timer

        data_file.close(); // close data file

        cout << "DAQ complete" << endl; // print to screen that DAQ is complete

    }
    else cout << "unable to open file" << endl; // if file could not open
}

////////// To use DAQ function as a thread enter the following: ///////////*
// create file name to which data will be written:
sprintf(weld_data, "/home/gladis/Documents/WeldData/data.csv");
thread (DAQ_thread).detach(); // create and start DAQ thread

////////// Process control code goes here //////////

DAQ_FLAG = 0;// turn off DAQ thread */
```

17. Appendix B: Wire Feeder

17.1. Wire Feeder Control Code

The following code is the C++ class used to control the CWT wire feeder.

```
// code to control wire feeder (CWT wire feeder)
// wire feeder class uses dacqdev class to controll wire feeder

#include "wiredev.h"
#include <math.h>

wire_dev::wire_dev() // constructor
{}

wire_dev::~wire_dev() // destructor: turn off wire feed
{
    dac_dev.dout(3, false); // digital out module 3 is wire forward
    dac_dev.dout(4, false); // digital out module 4 is wire reverse
}

// function to set WFS. Enter desired WFS in ipm
void wire_dev::set_wfs(double wfs)
{
    // scale the wfs to the max voltage into the wire feeder
    wfs=(wfs+0.52081)/31.61273; // derived from calibration

    dac_dev.ao(2,wfs); // write to DAC channel 2
}

// function to read WFS from encoder
double wire_dev::get_wfs()
{
    double wfs = dac_dev.ai(0); // Read from ADC channel 1
    if(isnan(wfs)) // set NaNs to 0.0
    {
        wfs = 0.0;
    }

    return wfs; // return value from encoder
    // actual WFS is determined in post processing
}

// function to control forward wire feed. Enter "true" for forward,
// enter "false" for wire feed off
void wire_dev::fwd(bool onoff)
{
    dac_dev.dout(4, onoff); // digital out module 4 is wire forward
}

// function to control reverse wire feed. Enter "true" for reverse,
// enter "false" for wire feed off
void wire_dev::rev(bool onoff)
{
    dac_dev.dout(6, onoff); // digital out module 6 is wire reverse
}
```

17.2. Wire Feeding System Calibration

The following MATLAB code was used to process encoder data and to process all of the wire feeding system calibration data.

```
% Dale Brush
% Wire Feeder Calibration Test
% November 16, 2017

clear,clc,close all

i = 0; % indexing variable
for k = 20:20:300; % test all WFSs
i = i+1; % increment indexing variable

file = sprintf('wfs_%.0fipm.csv',k); % create file name

data = csvread(file,1,0); % extract data from file

t = data(:,1)'/1e6; % Time data converted to seconds
v = data(:,2)'; % WFS data from encoder
cmd = data(:,3)'; % Commanded WFS from analog output

cmd_mean(i) = mean(cmd); % store average command value for each WFS test

err = isnan(v); % find NaNs in data
v(err) = 0.16; % set NaNs to logic 0 value

v = detrend(v,0); % remove DC from encoder data

% Find zero crossings:
cnv = v .* circshift(v,[0 1]);% multiply signal by shifted signal
zx = find(cnv < 0);% find where the product is less than zero

% Interpolate zeros:
for k1 = 2:size(zx,2)-1
    ixrng = zx(k1)-2:zx(k1)+2; % range of points around each zero crossing
    X = t(ixrng); % time data point in range
    Y = v(ixrng); % encoder signal points in range
    b = [ones(size(X)); X]'\Y'; % find linear regression parameters
    % Y = b(2)*X + b(1)
    Xi(k1-1) = -b(1)/b(2); % Set Y to 0 and solve for X to get zero crossing
end

% Calculate WFS
time = (diff(Xi))/60; % find time between each zero crossing
dist = 1/(2*98.67); % distance between edges
% 98.67 cycles/inch, 2 zero crossings/cycle -> 1/(2*98.67) inches/crossing

wfs = dist./time; % calculate wfs

wfs_mean(i) = mean(wfs);% store average WFS value for each WFS test
```

```

wfs_cmd = cmd*30; % calculate nominal commanded WFS

figure(1) % plot measured and commanded WFS
plot(Xi(1:end-1),wfs,'b'), hold on, grid on
plot(t,wfs_cmd,'r','linewidth',1.5)
ylim([0 350])
xlim([0 5])
title('Wire Feeder Calibration Test WFS Data')
xlabel('Time (s)'), ylabel('WFS (ipm)')
legend('Measured WFS','Commanded WFS (nominal)')

figure(2) % plot command voltage
plot(t,cmd,'r','linewidth',1.5), hold on, grid on
title('Wire Feeder Calibration Test Command Voltage')
xlabel('Time (s)'), ylabel('Voltage (V)'), xlim([0 5])
end

figure % plot average WFS vs. average command voltage
plot(cmd_mean,wfs_mean,'bx'), hold on, grid on
r = polyfit(cmd_mean,wfs_mean,1); % find LLS model parameters
wfs_fit = r(1)*cmd_mean + r(2); % build model
plot(cmd_mean,wfs_fit,'r') % plot model
title('Wire Feeder Calibration Test')
xlabel('Input Voltage (V)'), ylabel('WFS (ipm)')
legend('Measured Data','Linear Relationship','location','best')

% check model by calculating R^2 value
Rsqr = 1-sum((wfs_mean-wfs_fit).^2)/sum((wfs_mean-mean(wfs_mean)).^2);

txt = sprintf('wfs = %.3fV - %.3f',r(1),-r(2));
txt2 = sprintf('R^2 = %.4f',Rsqr);

text(2,285,txt)
text(2,265,txt2)

```

17.3. Step Response Analysis

The following MATLAB code was used to process the wire feeder's step response data.

```

% Dale Brush
% Wire Feeder Step Response
% November 16, 2017

clear,clc,close all

k = 9; % test all WFSs

file = sprintf('wfs_step%.0f.csv',k); % create file name

data = csvread(file,1,0); % extract data from file

```



```

t = data(:,1)'/1e6; % Time data converted to seconds
v = data(:,2)'; % WFS data from encoder
cmd = data(:,3)'; % Commanded WFS from analog output

err = isnan(v); % find NaNs in data
v(err) = 0.16; % set NaNs to logic 0 value

v = detrend(v,0); % remove DC from encoder data

% Find zero crossings:
cnv = v .* circshift(v,[0 1]);% multiply signal by shifted signal
zx = find(cnv < 0);% find where the product is less than zero

% Interpolate zeros:
for k1 = 2:size(zx,2)-1
    ixrng = zx(k1)-2:zx(k1)+2; % range of points around each zero crossing
    X = t(ixrng); % time data point in range
    Y = v(ixrng); % encoder signal points in range
    b = [ones(size(X)); X]'\Y'; % find linear regression parameters
    % Y = b(2)*X + b(1)
    Xi(k1-1) = -b(1)/b(2); % Set Y to 0 and solve for X to get zero crossing
end

% Calculate WFS
time = (diff(Xi))/60; % find time between each zero crossing
dist = 1/(2*98.67); % distance between edges
% 98.67 cycles/inch, 2 zero crossings/cycle -> 1/(2*98.67) inches/crossing

wfs = dist./time; % calculate WFS

wfs_cmd = cmd*32.0388 - 0.5277; % calculated commanded WFS

figure(1) % plot measured and commanded WFS
subplot(2,1,1)
plot(Xi(1:end-1),wfs,'b'), hold on, grid on
plot(t,wfs_cmd,'r','linewidth',1.5)

ylim([0 125])
xlim([0 7])
title('10ipm to 100ipm Step')
xlabel('Time (s)'), ylabel('WFS (ipm)')
legend('Measured WFS','Commanded WFS')

```

17.4. Time Domain Analysis

The following MATLAB code was used to process encoder data and create the time domain frequency response plot show in Figure 38.

```

% Dale Brush
% Wire Feeder Frequency Response Test
% Time domain Representation

```

```

% November 13, 2017

clear,clc,close all

data = csvread('weld_data.csv',1,0); % Read in data

t = data(:,1)'; % Time data in microseconds
v = data(:,2)'; % Encoder data (WFS)
cmd = data(:,3)'; % Function generator data (commanded WFS)

plot(t/1e6,v,'bo'), hold on, grid on
title('Encoder Output Signal')
xlabel('Time (s)'), ylabel('Output (V)')

T = mean(diff(t))/1e6; % determine sampling period
Fs = 1/T; % sampling frequency

err = isnan(v); % find locations where data is NAN
v(err) = 2; % set NANs to 2 to see where they occur
plot(t(err)/1e6,v(err),'rx') % plot the NANs

v(err) = 0.16; % set NANs to the logic 0 value

v = detrend(v,0); % remove DC offset from encoder signal
figure
plot(t/1e6,v,'b')

% Find zero crossings (x-intercepts):
cnv = v .* circshift(v,[0 1]); % multiply signal by shifted signal
zx = find(cnv < 0); % find where the product is less than zero

% Interpolate zeros:
for k1 = 2:size(zx,2)-1
    ixrng = zx(k1)-2:zx(k1)+2; % range of points around each zero crossing
    X = t(ixrng); % time data point in range
    Y = v(ixrng); % encoder signal points in range
    b = [ones(size(X)); X]'\Y'; % find linear regression parameters
    % Y = b(2)*X + b(1)
    Xi(k1-1) = -b(1)/b(2); % Set Y to 0 and solve for X to get zero crossing
end

hold on
plot(Xi/1e6,zeros(1,length(Xi)),'ko'), grid on
title('Processed Encoder Output Signal')
xlabel('Time (s)'), ylabel('Output (V)')
legend('Encoder signal','Zero crossings')
xlim([1 1.016])

% Calculate WFS
time = (diff(Xi)./1e6)/60; % find time between each zero crossing
dist = 1/(2*98.67); % distance between edges
% 98.67 cycles/inch, 2 zero crossings/cycle -> 1/(2*98.67) inches/crossing

wfs = dist./time; % calculate WFS

```

```

figure
plot(Xi(1:end-1)./1e6,wfs,'b'), hold on, grid on

wfs_cmd = cmd*32.0388 - 0.5277; % calculated commanded WFS

plot(t/1e6,wfs_cmd,'r','linewidth',1.15)
title('Wire Feeder Frequency Response')
xlabel('Time (s)'), ylabel('WFS (ipm)')
legend('Measured WFS','Commanded WFS','location','best')

```

17.5. Frequency Domain Analysis

The following MATLAB code was used to process encoder data, build NLLS models, and create a Bode plot of the wire feeder.

```

% Dale Brush
% Wire Feeder Frequency Response Test
% discrete frequency tests
% November 15, 2017

clear,clc,close all
tic
j = 0; % indexing variable
for k = [0.2,0.5:0.25:10.5,11,11.5,12,12.5]; % test all frequencies
    j = j+1 % increment indexing variable

    file = sprintf('wfs_%04dHz.csv',k*100); % create file name

    data = csvread(file,1,0); % read in corresponding file

    t = data(:,1)'/1e6; % Time data
    v = data(:,2)'; % Encoder data (WFS)
    cmd = data(:,3)'; % Function generator data (Commanded WFS)

    err = isnan(v); % find NaNs
    v(err) = 0.16; % set NaNs to logic 0 value

    v = detrend(v,0); % % remove DC offset from encoder signal

    % Find zero crossings:
    cnv = v .* circshift(v,[0 1]); % multiply signal by shifted signal
    zx = find(cnv < 0); % find where the product is less than zero

    % Interpolate zeros
    for k1 = 2:size(zx,2)-1
        ixrng = zx(k1)-2:zx(k1)+2;% range of points around each zero crossing
        X = t(ixrng); % time data point in range
        Y = v(ixrng); % encoder signal points in range
        b = [ones(size(X)); X]'\Y'; % find linear regression parameters
    end
end

```

```

    % Y = b(2)*X + b(1)
    Xi(k1-1) = -b(1)/b(2); % Set Y to 0, solve for X to get zero crossing
end

% Calculate WFS
time = diff(Xi)./60; % find time between each zero crossing
dist = 1/(2*98.67); % distance between edges
% 98.67 cycles/inch, 2 zero crossings/cycle -> 1/(2*98.67) inches/crossing

wfs = dist./time; % calculate WFS
wfs_cmd = cmd*32.0388 - 0.5277; % calculated commanded WFS

wfs_cmd = wfs_cmd'; % transpose commanded WFS data
t = t'; % transpose time data

wfs = wfs'; % transpose measured WFS data
t2 = Xi(1:end-1)'; % transpose time data for measure WFS

%%%%%%%%% Make initial guess by minimizing cost function %%%%%%%%%%%
w = 2*pi*k; % Set frequency to the nominal value for the test
r = @(W) res2(W,wfs_cmd,t); % function handle to calculate residuals
i = 0; % indexing variable

% calculate in-sample-error for a range of test frequencies
for x = w-2.5:0.1:w+2.5;
    i = i+1; % increment indexing variable
    freq(i) = x; % Store test frequencies
    res = r(x); % calculate residuals at each test frequency
    V(i) = res'*res; % calculate in-sample-error for each test frequency
end
% % % plot(freq,V), hold on % plot of in-sample-error = cost function
% % % title('Cost Function'), grid on
% % % xlabel('Frequency'); ylabel('In-Sample Error')
[val,loc1] = min(V); % find minimum of cost function
% frequency resulting in lowest in-sample-error = initial guess
Xo = freq(loc1); % initial guess for frequency
% % % plot(Xo,val,'rx')

%%%%%%%%%% Find Commanded WFS Model %%%%%%%%%%%

% Levenberg-Marquardt non-linear least-squares algorithm
[Xf_cmd, Ssq, CNT, Res, XY] = LMFnlsq(r,Xo); % Final parameter estimates

% Use final frequency parameter in LLS to find all final parameters
AA = [cos(Xf_cmd.*t), sin(Xf_cmd.*t), ones(numel(t),1)]; % A-matrix

theta = AA\wfs_cmd; % find B, C, and D
B = theta(1); C = theta(2); D = theta(3);

phs_cmd = atan(-C/B); % Find phase from C and B

A_cmd = B/cos(phs_cmd); % find amplitude from B and the phase
if A_cmd < 0 % make sure all amplitudes are positive, if not:
    A_cmd = A_cmd*-1; % make amplitude positive
    phs_cmd = phs_cmd - pi; % shift by pi, or 180 degrees

```

```

end

A_Cmd(j) = A_cmd; % store commanded WFS amplitudes
Phs_cmd(j) = phs_cmd; % store commanded WFS phases
K(j) = Xf_cmd/(2*pi); % build frequency vector in Hz

%%%%%%%%%%%%%%%%%%%%%%%%%%%%%%%%%%%%%%%%%%%%%%%%%%%%%%%%%%%%%%%%%%%%%%%% Find Measured WFS Model %%%%%%%%%%%%%%%%%%%%%%%%%%%%%%%%%%%%%%%%%%%%%%%%%%%%%%%%%%%%%%%%%%%%%%%%%
r2 = @(W) res2(W,wfs,t2); % new function handle to calculate residuals
% Levenberg-Marquardt non-linear least-squares algorithm
[Xf_meas, Ssq, CNT, Res, XY] = LMFnlsql(r2,Xo); % Final parameter estimates

% Use final frequency parameter in LLS to find all final parameters
AA2 = [cos(Xf_meas.*t2),sin(Xf_meas.*t2),ones(numel(t2),1)]; % A-matrix

theta2 = AA2\wfs; % find B, C, and D
B2 = theta2(1); C2 = theta2(2); D = theta2(3);

phs_meas = atan(-C2/B2); % Find phase from C and B

A_meas = B2/cos(phs_meas); % find amplitude from B and the phase
if A_meas < 0 % make sure all amplitudes are positive, if not:
    A_meas = A_meas*-1;% make amplitude positive
    phs_meas = phs_meas - pi; % shift by pi, or 180 degrees
end

A_Meas(j) = A_meas; % store measured WFS amplitudes
Phs_meas(j) = phs_meas; % store measured WFS phases

clear Xi
end

M = A_Meas./A_Cmd; % calculate Bode plot magnitude (change in amplitude)
Phs = Phs_meas - Phs_cmd; % calculate Bode plot phase

db = 20*log10(abs(M)); % convert magnitude to decibel scale
figure % plot magnitude
subplot(2,1,1), semilogx(K,db,'b','linewidth',1.5), hold on, grid on
xlim([0.28 12.5])
plot([3.512 3.512],[-30 -3],'r'), plot([0.1 3.512],[-3 -3],'r')
title('Magnitude'), xlabel('Frequency (Hz)'), ylabel('Magnitude (dB)')
% plot phase
subplot(2,1,2), semilogx(K,unwrap(Phs)*180/pi,'b','linewidth',1.5), grid on
xlim([0.28 12.5])
title('Phase'), xlabel('Frequency (Hz)'), ylabel('Phase (\circ)')
subtitle('Wire Feeder Frequency Response');
toc

```

18. Appendix C: Welding Power Source

18.1. Welding Power Source Control Code

The following code is the C++ class used to control the welding power source, arc starter, and shielding gas flow.

```
// C++ class to control welding power source, arc starter, and shielding gas
// welder class uses dacqdev class to control welding power source

#include "welderdev.h"
#include <math.h>

welder_dev::welder_dev() // constructor
{}

welder_dev::~welder_dev() // destructor: disable power source
{
    dac_dev.dout(0, 0); // digital out module 0 is the main arc enable
}

// function to set welding current. Enter desired welding current in amps
void welder_dev::set_current(double current)
{
    // scale the current to the max voltage into the power source (10V)
    current=current/400.0*10.0; // 400 amps @ 10 Volts, assuming 2 power sources
    dac_dev.ao(1,current); // write to DAC
}

// function to get welding current in amps
double welder_dev::get_current()
{
    double current = dac_dev.ai(2); // Read from ADC channel 2
    // ADC channel 2 is connected across resistor in LEM transducer circuit
    if(isnan(current)) // set NaNs to 0
    {
        current = 0.0;
    }
    // Resistor in LEM transducer circuit was sized for 600A max current
    // Current is multiplied by 1.0287 to compensate for non-exact resistor value
    current = current/10.0*600.0*1.0287; // [0 10]V -> [0 600]A
    return current; // return measured current in amps
}

// function to get welding voltage in volts
double welder_dev::get_voltage()
{
    double voltage = dac_dev.ai(3); // Read from ADC channel 3
    if(isnan(voltage)) // set NaNs to 0
    {
        voltage = 0.0;
    }
    voltage = voltage*6.18; // scale for voltage divider
    return voltage; // return measured voltage in volts
}
```

```

// function to enable/disable the power source. Enter "true" for arc on,
// Enter "false" for arc off
void welder_dev::arc(bool onoff)
{
    dac_dev.dout(0, onoff); // digital out module 0 is the main arc
}

// function to enable/disable the arc starter. Enter "true" to energize,
// Enter "false" to de-energize
void welder_dev::arc_start(bool onoff)
{
    dac_dev.dout(1, onoff); // digital out module 1 is the arc starter
}

// function to enable/disable the shielding gas. Enter "true" to turn on shielding,
// Enter "false" to turn off shielding
void welder_dev::arc_shielding(bool onoff)
{
    dac_dev.dout(2, onoff); // digital out module 2 is the shielding gas
}

```

18.2. Step Response Test

The following MATLAB code was used to process the welding power source step response data.

```

% Dale Brush
% Power Source Step Response
% January 29, 2018

clear,clc,close all

%% Step response test using function generator and oscilloscope %%

in_data = csvread('F0106CH1.CSV',0,3); % Function generator signal data
out_data = csvread('F0106CH2.CSV',0,3); % measured current data

t = in_data(:,1)*1000; % time in ms
cmd = in_data(:,2)*600/10; % Function generator signal
resp = out_data(:,2)*1.02*600/10; % measured current, properly scaled

plot(t,cmd,'r'), hold on, grid on
plot(t,resp,'b'), title('Power Source Step Response')
xlabel('Time (ms)'), ylabel('Current (A)')
legend('Commanded Current','Actual Current')

%% Step response test using analog output isolation module and DAQ %%

```

```

figure
data = csvread('ps_step2.csv',1,0); % read in data

t = data(:,1)./1e6; % Time in seconds
cmd = data(:,3)*600/10; % commanded current
resp = data(:,2)*1.015+2; % actual current (properly scaled)

%%% Scale axis and plot %%%
plot((t-4.0705)*1000+.1,cmd,'r','linewidth',1), hold on, grid on
plot((t-4.0705)*1000+.1,resp,'b','linewidth',1)
title('Output Module Controlled Step Response Test')
xlabel('Time (ms)'), ylabel('Current (A)')
xlim([.1 2.6]), ylim([20 220])

%%% plot ideal step input %%%
plot([.5 .5],[50.62 200.1],'k--','linewidth',1)
plot([.5 2.6],[200.1 200.1],'k--','linewidth',1)
plot([0 .5],[50.62 50.62],'k--','linewidth',1)

legend('Commanded Current','Actual Current','Ideal Step Input')

```

18.3. Variable Frequency Test

The following MATLAB code was used to generate the time domain representation of the welding power source's frequency response shown in Figure 45.

```

% Dale Brush
% Power Source Frequency Response Test
% Variable Frequency test
% November 27, 2017

clear,clc,close all

file = sprintf('PS_test.csv'); % create file name

data = csvread(file,1,0); % extract data from file

t = data(:,1)/1e6; % time data converted to seconds
I = data(:,2)*1.0287; % measured current adjusted for resistor value
cmd = data(:,3)*600/10; % commanded current from function generator

plot(t,cmd,'r'), grid on, hold on
plot(t,I,'b')
title('Power Supply Frequency Response')
legend('Commanded Current','Actual Current')
xlabel('Time (s)'), ylabel('Current (A)')

```


18.4. Discrete Frequency Test

The following MATLAB code was used to fit NLLS models to the data and create the welding power supply frequency response Bode plot.

```
% Dale Brush
% Power Source Frequency Response Test
% Create Bode Plot
% November 27, 2017

clear,clc,close all

j = 0; % indexing variable

% Fit models to each data set and obtain parameters for creating Bode plot
for k = [1, 10, 100:100:1000, 1250:250:2250, 2300:50:2500, 2750,
3000:500:7500];
    j = j+1 % increment indexing variable

    file = sprintf('PS_%04dHz.csv',k); % create file name

    data = csvread(file,1,0); % extract data from file

    t = data(:,1)/1e6; % time data converted to seconds
    I = data(:,2)*1.0287; % measured current adjusted for resistor value
    cmd = data(:,3)*600/10; % commanded current from function generator

    %%%%%%%%% Make initial guess by minimizing cost function %%%%%%%%%%%
    w = 2*pi*k; % Set frequency to the nominal value for the test
    r = @(W) res2(W,cmd,t); % function handle to calculate residuals
    i = 0; % indexing variable
    % calculate in-sample-error for a range of test frequencies
    for x = w-50:1:w+220;
        i = i+1; % increment indexing variable
        freq(i) = x;% Store test frequencies
        res = r(x);% calculate residuals at each test frequency
        V(i) = res'*res;% calculate in-sample-error for each test frequency
    end
    [val,loc1] = min(V);% find minimum of cost function
    Xo = freq(loc1); % initial guess for frequency

    %%%%%%%%%%%%%%% Find Commanded Current Model %%%%%%%%%%%%%%%
    % Levenberg-Marquardt non-linear least-squares algorithm
    [Xf_cmd, ~, ~, ~, ~] = LMFnlsql(r,Xo);% Final parameter estimates

    % Use final frequency parameter in LLS to find all final parameters
    AA = [cos(Xf_cmd.*t),sin(Xf_cmd.*t),ones(numel(t),1)]; % A-matrix

    theta = AA\cmd; % find B, C, and D
```

```

B = theta(1); C = theta(2); D = theta(3);

phs_cmd = atan(-C/B); % Find phase from C and B

A_cmd = B/cos(phs_cmd); % find amplitude from B and the phase
if A_cmd < 0 % make sure all amplitudes are positive, if not:
    A_cmd = A_cmd*-1;% make amplitude positive
    phs_cmd = phs_cmd - pi; % shift by pi, or 180 degrees
end

A_Cmd(j) = A_cmd; % store commanded amplitudes
Phs_cmd(j) = phs_cmd; % store commanded phases
K(j) = Xf_cmd/(2*pi); % build frequency vector in Hz

%%%%%%%%%%%%%%%%%%%%%%%%%%%%%%%%%%%%%%%%%%%%%%%%%%%%%%%%%%%%%%%%%%%%%%%% Find Measured Current Model %%%%%%%%%
r = @(W) res2(W,I,t); % new function handle to calculate residuals
% Levenberg-Marquardt non-linear least-squares algorithm
[Xf_meas, ~, ~, ~, ~] = LMFnlsql(r,Xo);% Final parameter estimates

% Use final frequency parameter in LLS to find all final parameters
AA2 = [cos(Xf_meas.*t),sin(Xf_meas.*t),ones(numel(t),1)]; % A-matrix

theta = AA2\I; % find B, C, and D
B = theta(1); C = theta(2); D = theta(3);

phs_meas = atan(-C/B); % Find phase from C and B

A_meas = B/cos(phs_meas); % find amplitude from B and the phase
if A_cmd < 0 % make sure all amplitudes are positive, if not:
    A_cmd = A_cmd*-1;% make amplitude positive
    phs_cmd = phs_cmd - pi; % shift by pi, or 180 degrees
end

A_Meas(j) = A_meas; % store measured amplitudes
Phs_meas(j) = phs_meas; % store measured phases
end

M = A_Meas./A_Cmd; % calculate Bode plot magnitude (change in amplitude)
Phs = Phs_meas - Phs_cmd; % calculate Bode plot phase

db = 20*log10(abs(M)); % convert magnitude to decibel scale
figure % plot magnitude
subplot(2,1,1), semilogx(K,db,'b','linewidth',1.5), hold on, grid on,
xlim([10 1e4])
plot([2662.4 2662.4],[-30 -3],'r'), plot([0.1 2662.4],[-3 -3],'r')
title('Magnitude'), xlabel('Frequency (Hz)'), ylabel('Magnitude (dB)')
% plot phase
subplot(2,1,2), semilogx(K,unwrap(Phs)*180/pi,'b','linewidth',1.5), grid on,
xlim([10 1e4])
title('Phase'), xlabel('Frequency (Hz)'), ylabel('Phase (\circ)')

subtitle('Power Supply Frequency Response');

```

19. Appendix D: Video Processing Algorithm

The following MATLAB code is the video processing algorithm used for post welding process analysis.

```

% Dale Brush
% Image Process
% January 16, 2018

clear,clc,close all

%%%%%%%%%%%%%%%%%%%%%%%%%%%%%%%%%%%%%%%%%%%%%%%%%%%%%%%%%%%%%%%%%%%%%%%% Process Raw Video %%%%%%%%%%
raw_vid = VideoReader('one_drop_wire_feed.avi'); % create video object
raw_vid.CurrentTime = 180; % Start reading frames at select time (seconds)

ctwd = 0.375; % contact tip to work distance (inches)
ctl = 25; % contact tip location (pixels)
bpl = 203; % base plate location (pixels)

ipp = ctwd/(bpl-ctl); % inches per pixel

j = 0;

%while hasFrame(raw_vid) % Process all frames
%                               ~ or ~
for k = 1:3000; % Process select number of frames
    j = j + 1;

    img_raw = readFrame(raw_vid); % Extract frame

    %    figure
    %    imshow(img_raw)

    img_bin = im2bw(img_raw,0.3); % convert grayscale image to binary image

    %    figure
    %    imshow(img_bin)

    img_filt1 = bwareaopen(~img_bin,150); % remove black specs from background

    %    figure
    %    imshow(img_filt1)

    img=bwareaopen(~img_filt1,50);% remove white specs from electrode extension

    % select locations across the electrode extension width to measure:
    m1 = 126; m2 = 130; m3 = 134;

    i = 0;
    np1 = 0; % number of pixels count
    % Count number of black pixels between contact tip location and first

```

```

% white pixel below at first location
while ~i && np1 < (bpl-ctl) % don't count below substrate
    np1 = np1+1; % pixel count
    i = img(ctl+np1,m1); % if i = 1, count will stop
    img(ctl+np1,m1) = 1; % set analyzed pixels to white for reference
end

i = 0;
np2 = 0; % number of pixels count
% Count number of black pixels between contact tip location and first
% white pixel below at second location
while ~i && np2 < (bpl-ctl) % don't count below substrate
    np2 = np2+1; % pixel count
    i = img(ctl+np2,m2); % if i = 1, count will stop
    img(ctl+np2,m2) = 1; % set analyzed pixels to white for reference
end

i = 0;
np3 = 0; % number of pixels count
% Count number of black pixels between contact tip location and first
% white pixel below at third location
while ~i && np3 < (bpl-ctl) % don't count below substrate
    np3 = np3+1; % pixel count
    i = img(ctl+np3,m3); % if i = 1, count will stop
    img(ctl+np3,m3) = 1; % set analyzed pixels to white for reference
end

np_ave = mean([np1,np2,np3]); % average number of pixels
np_max = max([np1,np2,np3]); % max number of pixels

% figure
% imshow(img)
% hold on
% plot([m1,m2,m3],29+[np1,np2,np3],'rx')

% Create image file to write the processed frame to
img_name = sprintf('img%d.jpg',j);
filename = ['F:\Research\GMAW_AM\video_process/images/',img_name];
imwrite(img,filename) % Write frame to image file

% (optional) Create image file to write the original frames to. Only
% necessary if any frames are removed from the processed frames and
% corresponding original frames are desired.

% img_name2 = sprintf('o_img%d.jpg',j);
% filename2='F:\Research\GMAW_AM\video_process/original_images/',img_name2];
% imwrite(img_raw,filename2) % Write frame to image file

le(j) = np_ave*ipp; % calculate actual electrode extension in inches
le_max = np_max*ipp; % calculate max electrode extension

% (optional) Throw out frames where electrode short circuited and cause
% inaccurate electrode extension calculation
% if le_max >= ctwd

```

```

%         j = j - 1;
%     end

end

mean(le) % Find the average electrode extension of all the frames

%%
%%%%%%%%%%%%%%%%%%%%%%%%%%%%%%%%%%%%%%%%%%%%%%%%%%%%%%%%%%%%%%%%%%%%%%%%%% Stich images back into video %%%%%%%%%%%
Vid_obj = VideoWriter('odpp1_process.avi'); % Create new video object
Vid_obj.FrameRate = 30; % Choose video frame rate

open(Vid_obj); % Open video object

for i = 1:2:2870 % Choose images to write into new video
    % Create filenames corresponding to processed images
    img_name = sprintf('img%d.jpg',i);
    filename = ['F:\Research\GMAW_AM\video_process/images/',img_name];

    im = imread(filename); % Read image

    writeVideo(Vid_obj,im); % Write image to video
end

close(Vid_obj) % close video object

% (optional) If original frames were written to image files, they too can
% be stitched into a video with frame corresponding to processed video

% Vid_obj2 = VideoWriter('original1.avi'); % Create new video object
% Vid_obj2.FrameRate = raw_vid.FrameRate; % Choose video frame rate
%
% open(Vid_obj2); % Open video object
%
% for i = 1:2:2870 % Choose images to write into new video
%     % Create filenames corresponding to original images
%     img_name2 = sprintf('o_img%d.jpg',i);
%     filename2='F:\Research\GMAW_AM\video_process/original_images/',img_name2];
%
%     im = imread(filename2); % Read image
%
%     writeVideo(Vid_obj2,im); % Write image to video
% end
%
% close(Vid_obj2) % close video object

```

20. Appendix E: Motion Control Code

Appendix E contains all the C++ code used to control the Galil controller for motion and wire feeding applications.

20.1. C++ class used for motion and wire feed control

The following code is the C++ class used by the main control code to control motion and wire feed with the insulated wire feeder.

```
// C++ class to control the Galil controller and motion system
#include "moddev.h"

GCon g = 0; //variable used to refer to a unique connection. A valid connection is
nonzero.

mo_dev::mo_dev() // constructor: connect to controller, apply settings
{
    connect(); // see connect function
}

mo_dev::~mo_dev() // destructor
{
    GCmd(g, "ST"); //stop all motion and programs
    if (g) GCclose(g); g = 0; //close g
}

// function to connect to controller and apply proper settings
void mo_dev::connect()
{
    // first part of code searches through USB ports looking for Galil
    // connection code was written to allow communication between the
    // Galil and the computer to be re-established after energizing the
    // arc starter
    // initialize structures:
    struct udev *udev;
    struct udev_enumerate *enumerate;
    struct udev_list_entry *devices, *dev_list_entry;
    struct udev_device *dev;

    int port_num = 0; // initially try port number 0
    char usb_port[100]; // character string for USB port name
    char galil_con[100]; // character string for Galil connection argument

    do { // check each port until Galil is found, then stop looking
        sprintf(usb_port,"ttyUSB%.1i",port_num); // create USB port name to analyze
        /* create the proper Galil connection argument based upon USB port number: */
        sprintf(galil_con,"/dev/ttyUSB%.1i -d --baud 115200 --subscribe ALL",port_num);

        port_num++; // increment port number incase current port is not the Galil
    } while (1);
}
```

```

/* Create the udev object */
udev = udev_new();
if (!udev) { // only continue if udev object can be created
    printf("Can't create udev\n");
    exit(1);
}

/* create a list of devices in the subsystem */
enumerate = udev_enumerate_new(udev);

/* look for device corresponding to the current USB port name */
udev_enumerate_add_match_sysname(enumerate, usb_port);
udev_enumerate_scan_devices(enumerate);
devices = udev_enumerate_get_list_entry(enumerate);

/* list devices with attributes */
udev_list_entry_foreach(dev_list_entry, devices) {
    const char *path;

    /* get the filename of the /sys entry for the device
    and create a udev_device object (dev) representing it */
    path = udev_list_entry_get_name(dev_list_entry);
    dev = udev_device_new_from_syspath(udev, path);

    /* Query device properties/attributes */
    dev = udev_device_get_parent_with_subsystem_devtype(dev, "usb",
"usb_device");
    if (!dev) {
        printf("Unable to find parent usb device.\n");
        exit(1);
    }

    /* Check if the device manufacturer is Galil */
    if(!strcmp(udev_device_get_sysattr_value(dev,"manufacturer"),"Galil")){
port_num to 4
    }
    udev_device_unref(dev); // release udev object
}

/* Free the enumerator object */
udev_enumerate_unref(enumerate);
udev_unref(udev);
}
while(port_num < 4); // only check USB ports 0 through 3
// At this point, the USB port to which the Galil is connected has been determined

/* connect to Galil controller using argument created above with proper USB port */
GOpen(galil_con, &g);

GCmd(g, "ST"); //stop all motion and programs

GCmd(g, "MT 2,2,2,2"); // set motor type to steppers

GCmd(g, "SH"); //Servo Here (turn on motors)

}

```

```

// function to check Galil connection status (0 = connected, 1 = not connected)
bool mo_dev::connection()
{
    GInfo(g, buf, sizeof(buf)); // get connection string
    /* extract part of the connection string to compare: */
    std::copy(buf + 14, buf + 21, cmpbuf);

    return strcmp(cmpbuf,"DMC4143"); // return status
}

// function to move 3-axis motion system (single move). Enter the desired
// axis, speed (ipm), and distance (inches)
void mo_dev::move(char *axis, double speed, double distance)
{
    // Each axis has a different number of steps per inch and speed and
    // distance are relative to the number of steps per inch
    if(!strcmp(axis,"X")) // check if it is the x-axis
    {
        spd = speed*steps_per_inch_x/60; // convert ipm to steps per second
        dist = distance*steps_per_inch_x; // convert inches to steps
    }
    if(!strcmp(axis,"Y")) // check if it is the y-axis
    {
        spd = speed*steps_per_inch_y/60; // convert ipm to steps per second
        dist = distance*steps_per_inch_y; // convert inches to steps
    }
    if(!strcmp(axis,"Z")) // check if it is the z-axis
    {
        spd = speed*steps_per_inch_z/60; // convert ipm to steps per second
        dist = distance*steps_per_inch_z; // convert inches to steps
    }
    // send speed value to Galil:
    sprintf(cmd,"SP %1.0f,%1.0f,%1.0f",spd,spd,spd);
    GCmd(g, cmd);
    // send distance value to controller:
    sprintf(cmd,"PR %1.0f,%1.0f,%1.0f",dist,dist,dist);
    GCmd(g, cmd);
    // execute motion command on commanded axis:
    sprintf(cmd,"BG %s",axis);
    GCmd(g, cmd); // begin
}

// Function to load motion program onto Galil controller. Program could be
// any desired motion paths. As written, this function writes a program
// using axis, speed, and distance arguments similar to the move function.
// Program will not execute until "execute" program is used
void mo_dev::load_program(char *axis, double speed, double distance)
{
    // Each axis has a different number of steps per inch and speed and
    // distance are relative to the number of steps per inch
    if (!strcmp(axis, "X")) // check if it is the x-axis
    {
        spd = speed*steps_per_inch_x / 60; // convert ipm to steps per second
        dist = distance*steps_per_inch_x; // convert inches to steps
    }
    if (!strcmp(axis, "Y")) // check if it is the y-axis
    {
        spd = speed*steps_per_inch_y / 60; // convert ipm to steps per second

```



```

        dist = distance*steps_per_inch_y; // convert inches to steps
    }
    if (!strcmp(axis, "Z")) // check if it is the z-axis
    {
        spd = speed*steps_per_inch_z / 60; // convert ipm to steps per second
        dist = distance*steps_per_inch_z; // convert inches to steps
    }
    // Build a string containing the motion program:
    string GP = "#A;"; // start of program

    sprintf(cmd, "SP %1.0f,%1.0f,%1.0f;",spd,spd,spd); // speed
    GP += cmd;

    sprintf(cmd, "PR %1.0f,%1.0f,%1.0f;",dist,dist,dist); // distance
    GP += cmd;

    sprintf(cmd, "BG %s;",axis); // begin command
    GP += cmd;

    sprintf(cmd, "AM %s;",axis); // halt operations until after move
    GP += cmd;

    GP += "EN;"; // end of program

    printf("%s\n",GP.c_str()); // print program to screen

    GProgramDownload(g,GP.c_str(),0); // download program onto Galil controller
}

// Function to execute current program loaded onto Galil controller.
void mo_dev::execute_program()
{
    GCmd(g, "XQ\r\n");
}

// Function to stop 3-axis motion system
void mo_dev::stop_motion()
{
    GCmd(g, "ST X,Y,Z"); //stop motion
}

// Function to stop all motion and wire feed
void mo_dev::stop()
{
    GCmd(g, "ST"); //stop all motion and wire feed
}

////////// Wire Feed ////////////
// The folling functions were used to control the new insulated
// wire feeder, which was connected to the Galil's forth axis.

// Function to feed wire forward at a constant feed until a stop
// command is issued. Enter WFS in ipm.
void mo_dev::wirefwd(double wfs)
{
    // create command using jog command:
    sprintf(cmd, "JG ,,,%1.0f",wfs*steps_per_inch_d/60);
}

```

```

    GCmd(g, cmd); // load command onto Galil
    GCmd(g, "BG D"); // begin wire feed
}

// Function to feed wire backward at a constant feed until a stop
// command is issued. Enter WFS in ipm.
void mo_dev::wirerev(double wfs)
{
    // create command using jog command:
    sprintf(cmd, "JG ,,,%1.0f", -wfs*steps_per_inch_d/60);
    GCmd(g, cmd); // load command onto Galil
    GCmd(g, "BG D"); // begin wire feed
}

// Function to stop the wire feed
void mo_dev::wirestop()
{
    GCmd(g, "ST D"); // stop motion on the D-axis
}

// Function to feed wire a given distance at a given WFS.
// Enter desired speed in ipm and desired distance in inches
void mo_dev::wirefeed(double speed, double distance)
{
    spd = speed*steps_per_inch_d/60; // convert ipm to steps per second
    dist = distance*steps_per_inch_d; // convert inches to steps

    sprintf(cmd, "SP ,,,%1.0f", spd); // speed
    GCmd(g, cmd); // load speed
    sprintf(cmd, "PR ,,,%1.0f", dist); // distance
    GCmd(g, cmd); // load distance

    GCmd(g, "BG D"); // begin wire feed
}

// Function to load a program to feed wire a given distance
// at a given WFS. Same as the wirefeed function above except
// that the program does not execute until triggered. This function
// allows a wire feeding program to be executed even after the arc
// starter causes a connection loss between the Galil and the
// computer. This is accomplished by triggering the wire feed using
// a digital input on the Galil rather than the USB connection.
void mo_dev::wire_prog(double speed, double distance)
{
    spd = speed*steps_per_inch_d/60; // convert ipm to steps per second
    dist = distance*steps_per_inch_d; // convert inches to steps

    string GP = "#A;\n"; // start of program

    // Use the "after input" (AI) command to halt program execution until
    // a digital input pin is toggled
    sprintf(cmd, "AI -1;\n"); // -1 = positive edge trigger, channel 1
    GP += cmd;

    // Set acceleration. Acceleration was tuned using high-speed
    // camera footage to match the wire burn off step response
    sprintf(cmd, "AC ,,,100000;\n"); // acceleration
    GP += cmd;
}

```

```

    sprintf(cmd, "SP ,,,%1.0f;\n", spd); // speed
    GP += cmd;

    sprintf(cmd, "PR ,,,%1.0f;\n", dist); // distance
    GP += cmd;

    sprintf(cmd, "BG D;\n"); // begin wire feed command
    GP += cmd;

    GP += "EN;"; // end of program

    GProgramDownload(g, GP.c_str(), 0); // download program to Galil

    GCmd(g, "XQ\r\n"); // execute program
    // program is immediately running on Galil, but waiting for
    // external trigger on digital input pin before wire feed
}

// Function to trigger wire feed program. Function uses dac_dev class
// to toggle digital output module and trigger wire feed
void mo_dev::wire_start(bool onoff)
{
    dac_dev.dout(7, onoff); // digital output 7 is the wire feed trigger
}

```

20.2. C++ Project for Jogging Motion System and Wire Feeder

The following code is the main C++ code used to jog the motion system and wire feeder using the computer's keyboard.

```

// Project used to control motion system and wire feeder with keyboard
#include <sys/types.h>
#include <sys/stat.h>
#include <fcntl.h> // access to Linux keyboard
#include <linux/input.h>
#include <iostream>
#include <unistd.h>
#include <string.h>
#include "gclib.h"
#include "gclibo.h"
#include <libudev.h>
#include <stdio.h>
#include <stdlib.h>
#include <locale.h>
#include <cstring> //strlen, etc.

using namespace std;

int main()
{

```

```

GCon g = 0; //variable used to refer to a unique connection. A valid connection is
nonzero.
char cmd[1000]; // initialize character string

double steps_per_inch_x = 64000; // number of steps to move 1 inch (x-axis)
double steps_per_inch_y = 128000; // number of steps to move 1 inch (y-axis)
double steps_per_inch_z = 256000; // number of steps to move 1 inch (z-axis)
double steps_per_inch_d = 8500; // number of steps to feed 1 inch (d-axis)

////////// Find Correct USB Port //////////
// first part of code searches through USB ports looking for Galil
// initialize structures:
struct udev *udev;
struct udev_enumerate *enumerate;
struct udev_list_entry *devices, *dev_list_entry;
struct udev_device *dev;

int port_num = 0; // initially try port number 0
char usb_port[100]; // character string for USB port name
char galil_con[100]; // character string for Galil connection argument

do { // check each port until Galil is found, then stop looking
analyze    sprintf(usb_port, "ttyUSB%.1i", port_num); // create USB port name to
port_num); // create the proper Galil connection argument based upon USB port number:
    sprintf(galil_con, "/dev/ttyUSB%.1i -d --baud 115200 --subscribe ALL",

    port_num++; // increment port number incase current port is not the Galil

    /* Create the udev object */
    udev = udev_new();
    if (!udev) { // only continue if udev object can be created
        printf("Can't create udev\n");
        exit(1);
    }

    /* create a list of devices in the subsystem */
    enumerate = udev_enumerate_new(udev);

    /* look for device corresponding to the current USB port name */
    udev_enumerate_add_match_sysname(enumerate, usb_port);
    udev_enumerate_scan_devices(enumerate);
    devices = udev_enumerate_get_list_entry(enumerate);

    /* list devices with attributes */
    udev_list_entry_foreach(dev_list_entry, devices) {
        const char *path;

        /* get the filename of the /sys entry for the device
        and create a udev_device object (dev) representing it */
        path = udev_list_entry_get_name(dev_list_entry);
        dev = udev_device_new_from_syspath(udev, path);

        /* Query device properties/attributes */
        dev = udev_device_get_parent_with_subsystem_devtype(dev, "usb",
"usb_device");

```

```

        if (!dev) {
            printf("Unable to find parent usb device.\n");
            exit(1);
        }

        /* Check if the device manufacturer is Galil */
        if (!strcmp(udev_device_get_sysattr_value(dev, "manufacturer"),
"Galil")){
            port_num = 4; // if it is the Galil, end the search by setting
port_num to 4
        }
        udev_device_unref(dev); // release udev object
    }

    /* Free the enumerator object */
    udev_enumerate_unref(enumerate);
    udev_unref(udev);
} while (port_num < 4); // only check USB ports 0 through 3
// At this point, the USB port to which the Galil is connected has been determined

/* connect to Galil controller using argument created above with proper USB port
GOpen(galil_con, &g);

GCmd(g, "ST"); //stop all motion and programs

GCmd(g, "MT 2,2,2,2"); // set motor type to steppers

GCmd(g, "SH"); //Servo Here (turn on motors)

////////////////////////////////////// Jog ////////////////////////////////////////

int code, value, stop_motion = 0; // initialize variables

while(!stop_motion) // program terminated by setting stop_motion to 1
{
    // open the keyboard (event2 is the keyboard)
    int kbd = open("/dev/input/event2", O_RDONLY);
    // O_RDONLY = open for read only

    if(kbd != -1) // check for successful keyboard open
    {
        cout << "Keyboard found" << endl; // print success
        cout << "Press \"e\" to exit" << endl; // pressing "e" ends program

        input_event ie; // initiate variable of type input_event

        while(read(kbd, &ie, sizeof(ie))){ // keyboard is in communication:
            {
                // record key code and value
                // code: which key was pressed/held/released
                // value: 1 = pressed, 0 = released, 2 = held
                code = ie.code; value = ie.value;

                if (value == 1) // key was pressed (value = 2 if key is held)
                {
                    // Check which key was pressed:

```

```

if (code == 103) //cout << "up" << endl; // up arrow
{ // jog x-axis forward at 20ipm
  sprintf(cmd,"JG %1.0f",20*steps_per_inch_x/60);
  GCmd(g, cmd);
  GCmd(g, "BG X");
}

if (code == 108) //cout << "down" << endl;// down arrow
{ // jog x-axis backward at 20ipm
  sprintf(cmd,"JG %1.0f",-20*steps_per_inch_x/60);
  GCmd(g, cmd);
  GCmd(g, "BG X");
}

if (code == 106)//cout << "right"<< endl;// right arrow
{ // jog y-axis forward (right) at 20ipm
  sprintf(cmd,"JG ,%1.0f",20*steps_per_inch_y/60);
  GCmd(g, cmd);
  GCmd(g, "BG Y");
}

if (code == 105) //cout << "left" << endl;// left arrow
{ // jog y-axis backward (left) at 20ipm
  sprintf(cmd,"JG ,%1.0f",-20*steps_per_inch_y/60);
  GCmd(g, cmd);
  GCmd(g, "BG Y");
}

if (code == 78) //cout << "plus" << endl; // plus key
{ // jog z-axis forward (up) at 20ipm
  sprintf(cmd,"JG ,,%1.0f",20*steps_per_inch_z/60);
  GCmd(g, cmd);
  GCmd(g, "BG Z");
}

if (code == 74) //cout << "minus" << endl; // minus key
{ // jog z-axis backward (down) at 20ipm
  sprintf(cmd,"JG ,,%1.0f",-20*steps_per_inch_z/60);
  GCmd(g, cmd);
  GCmd(g, "BG Z");
}

if (code == 33) //cout << "f" << endl; // f key
{ // feed wire forward at 20ipm
  sprintf(cmd,"JG ,,,%1.0f",20*steps_per_inch_d/60);
  GCmd(g, cmd);
  GCmd(g, "BG D");
}

if (code == 19) //cout << "r" << endl; // r key
{ // feed wire backward (reverse) at 20ipm
  sprintf(cmd,"JG ,,,%1.0f",-20*steps_per_inch_d/60);
  GCmd(g, cmd);
  GCmd(g, "BG D");
}
}

```

```

        if ((value == 0) && (code > 0)) // a key was released
        {
            GCmd(g, "ST"); //stop all motion and programs
        }

        if (code == 18) break; stop_motion = 1; // e key: end program

// Note that when a key is pressed, value = 1 upon the press and value = 2 as the key
// is held. Therefore when a key is pressed and held, the jog command is sent to the
// Galil controller only once when the key is first pressed and value = 1. Since
// value = 2 as the key is held, motion will continue until the key is released and
// value = 0. This simply means that the axis will move as long as the key is held,
// but the jog command is only sent once.

    }
    cout << "Closing Keyboard..." << endl;
    close(kbd); // close keyboard
}
}
cout << "Exiting..." << endl;
GCmd(g, "ST"); //stop all motion and programs
if (g) GCclose(g); g = 0; //close g
}

```

21. Appendix F: Laser Control Code

The following code is the C++ class used to control the laser.

```
// C++ class to control the laser

#include "laserdev.h"

#define BUF_SIZE 10000 // set buffer size
unsigned char sysbuf[BUF_SIZE]; // initialize system buffer
unsigned char localbuf[BUF_SIZE]; // initialize local buffer

int cport_nr=0; // communication port number 0

// setup and open the spectrum port
int bdrate=57600; // baud rate
int comports_open_success=false;

laser_dev::laser_dev() // constructor
{
    // check if communication has been established
    if(serial.RS232_OpenComport(cport_nr, bdrate))
    {
        comports_open_success=false;
        printf("Can not open comport\n");
        exit(-1);
    }
    comports_open_success=true;
}

laser_dev::~laser_dev() // destructor
{
    serial.RS232_CloseComport(cport_nr); // close port
}

// Function to set laser to ACC mode
// ACC (automatic current control) mode allows power to be set in percent
void laser_dev::acc_mode()
{ // send bytes that make up command: ACC
    serial.RS232_SendByte(cport_nr, 'A');
    serial.RS232_SendByte(cport_nr, 'C');
    serial.RS232_SendByte(cport_nr, 'C');
    // terminate with carriage return:
    serial.RS232_SendByte(cport_nr, '\r');

    usleep(50000);
}

// Function to set laser to APC mode
// APC (automatic power control) mode allows power to be set in watts
void laser_dev::apc_mode()
{ // send bytes that make up command: APC
    serial.RS232_SendByte(cport_nr, 'A');
    serial.RS232_SendByte(cport_nr, 'P');
    serial.RS232_SendByte(cport_nr, 'C');
    // terminate with carriage return:
    serial.RS232_SendByte(cport_nr, '\r');
}
```



```

        usleep(50000);
    }

    // Function to set percent power in ACC mode. Enter desired
    // laser power in percent: 0% ~= 0W, 100% ~= 200W
    void laser_dev::set_percent(int pwr)
    {
        acc_mode(); // set laser to ACC mode

        // SCS (set current set point) command
        sprintf(cmd, "SCS %.3i", pwr);
        // send each byte stored in cmd:
        serial.RS232_SendByte(cport_nr, cmd[0]);
        serial.RS232_SendByte(cport_nr, cmd[1]);
        serial.RS232_SendByte(cport_nr, cmd[2]);
        serial.RS232_SendByte(cport_nr, cmd[3]);
        serial.RS232_SendByte(cport_nr, cmd[4]);
        serial.RS232_SendByte(cport_nr, cmd[5]);
        serial.RS232_SendByte(cport_nr, cmd[6]);
        // terminate with carriage return:
        serial.RS232_SendByte(cport_nr, '\r');

        usleep(50000);
    }

    // Function to set power in APC mode. Enter desired
    // laser power in watts: 0.5W to 200W
    void laser_dev::set_watts(int pwr)
    {
        apc_mode(); // set laser to APC mode

        // SPS (set power set point) command
        sprintf(cmd, "SPS %.3i", pwr);
        // send each byte stored in cmd:
        serial.RS232_SendByte(cport_nr, cmd[0]);
        serial.RS232_SendByte(cport_nr, cmd[1]);
        serial.RS232_SendByte(cport_nr, cmd[2]);
        serial.RS232_SendByte(cport_nr, cmd[3]);
        serial.RS232_SendByte(cport_nr, cmd[4]);
        serial.RS232_SendByte(cport_nr, cmd[5]);
        serial.RS232_SendByte(cport_nr, cmd[6]);
        // terminate with carriage return:
        serial.RS232_SendByte(cport_nr, '\r');

        usleep(50000);
    }

    // Function to turn laser on
    void laser_dev::on()
    { // send bytes that make up command: EMON (emission on)
        serial.RS232_SendByte(cport_nr, 'E');
        serial.RS232_SendByte(cport_nr, 'M');
        serial.RS232_SendByte(cport_nr, 'O');
        serial.RS232_SendByte(cport_nr, 'N');
        // terminate with carriage return:
        serial.RS232_SendByte(cport_nr, '\r');
    }

```

```

        usleep(50000);
    }

    // Function to turn laser off
    void laser_dev::off()
    { // send bytes that make up command: EMOFF (emission off)
        serial.RS232_SendByte(cport_nr, 'E');
        serial.RS232_SendByte(cport_nr, 'M');
        serial.RS232_SendByte(cport_nr, 'O');
        serial.RS232_SendByte(cport_nr, 'F');
        serial.RS232_SendByte(cport_nr, 'F');
        // terminate with carriage return:
        serial.RS232_SendByte(cport_nr, '\r');

        usleep(50000);
    }

    // Function to get laser power in watts
    double laser_dev::get_power()
    {
        // flush RX and TX (recieve and transmit) buffers
        serial.RS232_flushRXTX(cport_nr);

        // Send ROP (read output power) command:
        serial.RS232_SendByte(cport_nr, 'R');
        serial.RS232_SendByte(cport_nr, 'O');
        serial.RS232_SendByte(cport_nr, 'P');
        // terminate with carriage return:
        serial.RS232_SendByte(cport_nr, '\r');

        int localidx=0; // initialize local index variable
        int n=0; // initialize variable for response string size

        for(unsigned int z=0;z<BUF_SIZE;z++) //clear the buffers
        {
            localbuf[z]=0;
            sysbuf[z]=0;
        }

        do // read and store response characters until a carriage return
        {
            // read response from laser:
            n = serial.RS232_PollComport(cport_nr, sysbuf, BUF_SIZE-1);
            if(n>0) // if there is a response:
            {
                for(unsigned int k=0;k<n;k++)
                { // read each byte in response
                    localbuf[localidx]=sysbuf[k];
                    localidx++;
                }
            }
        } // return when a carriage return is found
        while(localbuf[localidx-1]!='\r');

        int s = localidx-1; // number of bytes in response

        if(s<0) // s = -1 if no response

```

```
{
    printf("no response from instrument\n");
    return -1;
}

char Rval[(s-5)]; // buffer for return value
// The return values is a character string with the power in watts
// and 5 extra characters
// Example Response: ROP: 100.0
// Note that there is 5 characters before 100.0 including a space
// Response is not always 10 characters long (e.g. R0P: 100.0 vs. ROP: 99.9)
// but 5 characters always exist before the power value

// put bytes representing the power value into Rval
for(int i=0;i<(s-5);i++)
{
    Rval[i]=localbuf[(i+5)]; // start at 5th byte
}

double val = atof(Rval); // convert string to floating-point number (type double)

return val; // return measured power in watts
}
```

22. Appendix G: Continuous Weld Bead Code

22.1. Arc Initiation and Termination

The following code is the C++ code used for the short circuiting arc starting procedure.

```

//////////////////////////////////// Arc Starting Procedure //////////////////////////////////////
welder.arc_shielding(true); // turn on shielding gas
usleep((unsigned long)(2*1e6)); // shielding gas pre flow time
double I = 475.0; // starting current for short circuiting arc start
welder.set_current(I); // set power source to starting current
welder.arc(true); // enable power source/welding arc
usleep(0.1*1e6); // allow time for open circuit voltage to build

wire.fwd(true); // start wire feed

while (welder.get_voltage(>30.0){} // do nothing while wire is feeding

usleep((unsigned long)(35 * 1e3)); // wait 35ms after short circuit
welder.set_current(Ib); // set current to a lower welding current value
////////////////////////////////////

```

The following code is the C++ code used for the wire sharpening/arc termination procedure.

```

//////////////////////////////////// Weld termination //////////////////////////////////////
wire.fwd(false); // shut of wire feed (wire continues to feed, i.e., deceleration)

welder.set_current(475.0); // set current pulse height in A

usleep((unsigned long)(18 * 1e3)); // pulse time is 18ms

welder.arc(false); // disable welding arc
usleep((unsigned long)(2 * 1e6)); // shielding gas post flow time
welder.arc_shielding(false); // turn off shielding gas
////////////////////////////////////

```

22.2. Pulsed GMAW

The following is a section of C++ code used to produce a weld in pulsed GMAW mode.

```

//////////////////////////////////// Initailization //////////////////////////////////////
char y[] = "Y"; // initialize y-axis variable
char z[] = "Z"; // initialize z-axis variable
mo.load_program(y, 15, -6); // load motion program to Galil controller
// when executed, program will move 6 inches (-y direction) at 15ipm

wire.rev(false); // make sure wire is not moving in reverse
wire.fwd(false); // make sure wire is not moving forward
wire.set_wfs(150); // set WFS to 150 ipm
////////////////////////////////////

```

```

//////////////////////////////////// Arc Starting Procedure //////////////////////////////////////
welder.arc_shielding(true); // turn on shielding gas
usleep((unsigned long)(2*1e6)); // shielding gas pre flow time
double I = 475.0; // starting current for short circuiting arc start
welder.set_current(I); // set power source to starting current
welder.arc(true); // enable power source/welding arc
usleep(0.1*1e6); // allow time for open circuit voltage to build

wire.fwd(true); // start wire feed

dacq.dout(5, 1); // trigger camera

while (welder.get_voltage()>30.0){} // do nothing while wire is feeding

usleep((unsigned long)(35 * 1e3)); // wait 35ms after short circuit
welder.set_current(Ib); // set current to a lower welding current value
////////////////////////////////////

//////////////////////////////////// Welding Procedure //////////////////////////////////////

mo.execute_program(); // Start motion program

double Ib = 57.1; // background current (A)
double Ip = 290.0; // peak current (A)
double Tb = 3.41; // background time in ms
double Tp = 3.4; // peak time in ms

double Tstart = et.getElapsedTimeInMicroSec(); // acquire starting time
// Weld for 2 seconds:
while((et.getElapsedTimeInMicroSec()-Tstart)<(2*1e6)){

    welder.set_current(Ib); // set to background current
    usleep((unsigned long)(Tb*1e3)); // hold for background time
    welder.set_current(Ip); // set to peak current
    usleep((unsigned long)(Tp*1e3)); // hold for peak time

}

dacq.dout(5, 0); // reset camera trigger
mo.stop(); // stop motion

////////////////////////////////////

//////////////////////////////////// Weld termination //////////////////////////////////////
wire.fwd(false); // shut of wire feed (wire continues to feed, i.e., deceleration)

welder.set_current(475.0); // set current pulse height in A

usleep((unsigned long)(18 * 1e3)); // pulse time is 18ms

welder.arc(false); // disable welding arc
usleep((unsigned long)(2 * 1e6)); // shielding gas post flow time
welder.arc_shielding(false); // turn off shielding gas
////////////////////////////////////

```

23. Appendix H: Single Droplet Deposition Code

23.1. Single Droplet Deposition with Steel Wool Arc Starts

The following code is a section of the C++ code used to produce single droplet deposition using steel wool to start the arcs.

```
// create file name to which data will be written:
sprintf(weld_data, "/home/gladis/Documents/WeldData/data.csv");

thread (DAQ_thread).detach(); // create and start DAQ thread

wire.rev(false); // make sure wire is not moving in reverse

wire.fwd(false); // make sure wire is not moving forward

wire.set_wfs(130.0); // set WFS to 130ipm

welder.arc_shielding(true); // start shielding gas

double I = 75.0; // set starting current to 75A
welder.set_current(I); // set power source to starting current

usleep((unsigned long)(1*1e6)); // shielding gas pre-flow time

dacq.dout(5, 1); // trigger high-speed camera

wire.fwd(true); // start wire feed forward

usleep((unsigned long)(40*1e3)); // wait for wire feed delay time

welder.arc(true); // enable main arc

usleep((unsigned long)(75*1e3)); // leave starting current on for 75ms
welder.set_current(50); // drop to background current
usleep((unsigned long)(15*1e3)); // wait 15ms for wire feeder timing
wire.fwd(false); // turn off wire feed
usleep((unsigned long)(85*1e3)); // 85ms of more background current
welder.set_current(345); // set to peak current to detach droplet
usleep((unsigned long)(4*1e3)); // peak time is 4ms

welder.arc(false); // turn off main arc

usleep((unsigned long)(1*1e6)); // shielding gas post-flow time
dacq.dout(5, 0); // reset high-speed camera trigger
welder.arc_shielding(false); // turn off shielding gas

DAQ_FLAG = 0; // stop DAQ
```

23.2. Single Droplet Deposition with PAW Pilot Arc Starts

The following code is a section of the C++ code used to produce single droplet deposition using the PAW pilot arc to start the main arc.

```
// create file name to which data will be written:
sprintf(weld_data, "/home/gladis/Documents/WeldData/data.csv");
thread (DAQ_thread).detach(); // create and start DAQ thread

wire.rev(false); // make sure wire is not moving in reverse
wire.fwd(false); // make sure wire is not moving forward
wire.set_wfs(130.0); // set WFS to 130ipm

welder.arc_shielding(true); // start shielding gas

double I = 75.0; // set starting current to 75A
welder.set_current(I); // set power source to starting current

usleep((unsigned long)(1*1e6)); // shielding gas pre-flow time

dacq.dout(5, 1); // trigger high-speed camera

dacq.dout(1, 1); // pilot arc on (takes 0.107s to light)

usleep((unsigned long)(30*1e3)); // wait 30ms before wire feed

wire.fwd(true); // start wire feed forward

usleep((unsigned long)(40*1e3)); // wait for wire feed delay time

welder.arc(true); // enable main arc

while(welder.get_current() < 60.0){} // when current is more than 60A, arc has started

usleep((unsigned long)(75*1e3)); // leave starting current on for 75ms
welder.set_current(50); // drop to background current
usleep((unsigned long)(15*1e3)); // wait 15ms for wire feeder timing
wire.fwd(false); // turn off wire feed
usleep((unsigned long)(85*1e3)); // 85ms of more background current
welder.set_current(345); // set to peak current to detach droplet
usleep((unsigned long)(4*1e3)); // peak time is 4ms

dacq.dout(1, 0); // pilot arc off

welder.arc(false); // turn off main arc

usleep((unsigned long)(1*1e6)); // shielding gas post-flow time
dacq.dout(5, 0); // reset high-speed camera trigger
welder.arc_shielding(false); // turn off shielding gas

DAQ_FLAG = 0; // stop DAQ
```

23.3. Single Droplet Deposition with Lift Arc Starts

The following code is a section of the C++ code used to produce single droplet deposition using a lift start arc starting technique.

```
// create file name to which data will be written:
sprintf(weld_data, "/home/gladis/Documents/WeldData/data.csv");
thread(DAQ_thread).detach(); // create and start DAQ thread

char x[] = "X"; // initialize x-axis variable
char y[] = "Y"; // initialize y-axis variable
char z[] = "Z"; // initialize z-axis variable

welder.arc_shielding(true); // turn on shielding gas

double I = 75.0; // set starting current to 75A
welder.set_current(I); // set power source to starting current

usleep((unsigned long)(1 * 1e6)); // shielding gas pre-flow time

dacq.dout(5, 1); // trigger high-speed camera

welder.arc(true); // enable main arc
usleep((unsigned long)(5 * 1e3)); // pause 5ms to ensure current flow through wire

mo.move(z, 20.0, -0.05); // drop work piece 0.05in

while (welder.get_voltage() < 5.0){} // wait while wire is in contact with work piece
usleep((unsigned long)(7 * 1e3)); // wait 7ms and check again in case of noise
while (welder.get_voltage() < 5.0){} // check voltage again to ensure contact is broken

// start single droplet deposition current sequence
usleep((unsigned long)(70 * 1e3)); // starting current lasts for 70ms
welder.set_current(50); // drop to background current
usleep((unsigned long)(100 * 1e3)); // 100ms of background time
welder.set_current(345); // 345A current pulse
usleep((unsigned long)(4*1e3)); // 4ms peak time

welder.arc(false); // turn off main arc

usleep((unsigned long)(2 * 1e6)); // shielding gas post-flow time
dacq.dout(5, 0); // reset high-speed camera trigger
welder.arc_shielding(false); // turn off shielding gas

DAQ_FLAG = 0; // stop DAQ
```


23.4. Single Droplet Deposition with High Frequency Arc Starts

The following code is a section of the C++ code used to produce single droplet deposition using a high frequency arc starter.

```
// create file name to which data will be written:
sprintf(weld_data, "/home/gladis/Documents/WeldData/junk.csv");
thread (DAQ_thread).detach(); // create and start DAQ thread

mo.connect(); // establish connection with Galil controller
mo.wire_prog(55, 0.05); // create and download wire feed routine to Galil controller

welder.arc_shielding(true); // turn on shielding gas

double I = 75.0; // starting current (A)
welder.set_current(I); // set welding current to starting current

usleep((unsigned long)(1*1e6)); // allow time to set current

dacq.dout(5, 1); // trigger camera

welder.arc(true); // enable welding power source
usleep((unsigned long)(5*1e3)); // allow time for arc to enable
welder.arc_start(true); // enable arc starter
usleep((unsigned long)(1*1e3)); // allow time for arc starter to energize

int count = 0; // counter for arc starting routine
double I_sum = 0.0; // current summation for arc starting routine
double i1,i2,i3,i11,i22,i33; // variable for troubleshooting arc starting routine
// Arc starting routine and arc start prediction algorithm:
// check for 3 consecutive 60+ amp measurements (3 x 60 = 180) to ensure
// that noise does not appear to be an arc start. The routine can only go
// for 100 iterations (150ms) before exiting to prevent the arc starter
// from pulsing for extended periods of time when the arc won't start
while((I_sum < 180)&&(count < 100))
{
    count++; // increment counter
    I_sum = 0.0; // set current summation to 0
    i11 = i1; // store previous current measurement
    i1 = welder.get_current(); // get new current measurement
    if (i1 > 100.0) i1 = 70.0; // if current is over 100A, it is noise
    // noise spikes exceeding 180A trigger a false arc start indication
    I_sum += i1; // add new current measurement to current summation
    usleep((unsigned long)(0.5*1e3)); // wait half a millisecond
    i22 = i2; // store previous current measurement
    i2 = welder.get_current(); // get new current measurement
    if (i2 > 100.0) i2 = 70.0; // if current is over 100A, it is noise
    I_sum += i2; // add new current measurement to current summation
    usleep((unsigned long)(0.5*1e3)); // wait half a millisecond
    i33 = i3; // store previous current measurement
    i3 = welder.get_current(); // get new current measurement
    if (i3 > 100.0) i3 = 70.0; // if current is over 100A, it is noise
    I_sum += i3; // add new current measurement to current summation
    usleep((unsigned long)(0.5*1e3)); // wait half a millisecond
}
```

```

        printf("I_sum = %f\n",I_sum); // display current summation
    }

welder.arc_start(false); // After arc starting routine, turn off arc starter

printf("count = %i\n",count); // display number of routine iterations

if(count < 100)// if count is less than 100, the arc has started
{
    //////////////// Single droplet deposition routine ////////////////
    usleep((unsigned long)(35*1e3)); // pause for 35ms before wire feed

    mo.wire_start(true); // start wire feed

    usleep((unsigned long)(35*1e3)); // after 35ms, drop current to 50A
    welder.set_current(50); // set current to 50A
    usleep((unsigned long)(40*1e3)); // pause 40ms for CWT wire feeder
    //welder.fwd(false); // CWT feeder: stop wire feed
    usleep((unsigned long)(60*1e3)); // run low current for and additional 60ms
    welder.set_current(350); // set current to 350A to detach droplet
    usleep((unsigned long)(4.5*1e3)); // 350A pulse time is 4.5ms
    welder.set_current(40); // drop to low current as droplet transfers
    usleep((unsigned long)(15*1e3)); // keep low current for 15ms
}

welder.arc(false); // turn off welding arc
mo.wire_start(false); // reset wire feed trigger

usleep((unsigned long)(2*1e6)); // 2 second shielding gas post-flow
dacq.dout(5, 0); // Turn off camera trigger
welder.arc_shielding(false); // turn off shielding gas

// display arc start routine variables for troubleshooting
printf("i11 = %f, i22 = %f, i33 = %f\n",i11,i22,i33);
printf("i1 = %f, i2 = %f, i3 = %f\n",i1,i2,i3);
DAQ_FLAG = 0; // turn off DAQ thread

```

23.5. Automatic Wire Positioning

The following C++ code was used to automatically position the wire at the desired arc gap length and move the work piece/specimen before starting the arc. The follow code applies to the insulated wire feeder.

```

char x[] = "X"; //
char y[] = "Y"; // create variable for motion system
char z[] = "Z"; //

mo.connect(); // establish connection with Galil controller

////////////////////// Position Wire ////////////////////////
mo.move(y,10,-0.068); // move work piece for new drop

```

```

welder.set_current(1.0); // set welding current to 1A to allow full OC voltage
welder.arc(true); // enable welding power source
usleep((unsigned long)(0.1*1e3)); // allow time for OC voltage to build

mo.wirefwd(5.0); // jog wire forward
// if the voltage is more than 20V, the wire and wore piece are not in contact
while(welder.get_voltage()>20.0){} // do nothing while wire is feeding
// when the voltage drops below 20V, wire has made contact
welder.arc(false); // disable welding power source
mo.wirestop(); // stop wire feed

mo.wirefeed(5.0,-0.04); // retract wire 0.04in for optimal arc start
sleep(1); // give time to retract wire
////////////////////////////////////////////////////////////////////////////////////////////////////////////////////////////////

```

23.6. Automated Single Droplet Deposition

The following C++ code is the section of code that produced automated single droplet deposition using the arc starter/laser hybrid arc starting technique.

```

char x[] = "X"; //
char y[] = "Y"; // create variable for motion system
char z[] = "Z"; //

mo.connect(); // establish connection with Galil controller

welder.arc_shielding(true); // turn on shielding gas

usleep((unsigned long)(2*1e6)); // 2 second gas pre-flow time

for (int drop_num = 0; drop_num < 5; drop_num++) // set number of drops
{

    mo.wire_prog(55, 0.1); // download wire feed routine to Galil controller

    DAQ_FLAG = 1; // Allow DAQ to start
    // create file name to which data will be written:

    sprintf(weld_data, "/home/gladis/Documents/WeldData/data%i.csv", drop_num+1);

    thread (DAQ_thread).detach(); // create and start DAQ thread

    double I = 75.0; // starting current (A)
    welder.set_current(I); // set welding current to starting current
    usleep((unsigned long)(100*1e3)); // power source needs time to set current

    dacq.dout(5, 1); // trigger camera

    welder.arc(true); // enable welding power source
    usleep((unsigned long)(5*1e3)); // allow time for source to enable
    welder.arc_start(true); // enable arc starter
    usleep((unsigned long)(1*1e3)); // allow time for arc starter to energize

```

```

int count = 0; // counter for arc starting routine
double I_sum = 0.0; // current summation for arc starting routine
double i1,i2,i3,i11,i22,i33;// variable for troubleshooting arc starting routine
// Arc starting routine and arc start prediction algorithm:
// check for 3 consecutive 60+ amp measurements (3 x 60 = 180) to ensure
// that noise does not appear to be an arc start. The routine can only go
// for 100 iterations (150ms) before exiting to prevent the arc starter
// from pulsing for extended periods of time when the arc won't start
while((I_sum < 180)&&(count < 100))
{
    count++; // increment counter
    I_sum = 0.0; // set current summation to 0
    i11 = i1; // store previous current measurement
    i1 = welder.get_current(); // get new current measurement
    if (i1 > 100.0) i1 = 70.0; // if current is over 100A, it is noise
    // noise spikes exceeding 180A trigger a false arc start indication
    I_sum += i1; // add new current measurement to current summation
    usleep((unsigned long)(0.5*1e3)); // wait half a millisecond
    i22 = i2; // store previous current measurement
    i2 = welder.get_current(); // get new current measurement
    if (i2 > 100.0) i2 = 70.0; // if current is over 100A, it is noise
    I_sum += i2; // add new current measurement to current summation
    usleep((unsigned long)(0.5*1e3)); // wait half a millisecond
    i33 = i3; // store previous current measurement
    i3 = welder.get_current(); // get new current measurement
    if (i3 > 100.0) i3 = 70.0; // if current is over 100A, it is noise
    I_sum += i3; // add new current measurement to current summation
    usleep((unsigned long)(0.5*1e3)); // wait half a millisecond

    printf("I_sum = %f\n",I_sum); // display current summation
}

welder.arc_start(false); // disable arc starter

printf("count = %i\n",count); // display number of arc start iterations
printf("drop: %i\n",drop_num+1); // display current drop number

// Improve arc start prediction algorithm by checking arc voltage.
// If the voltage is less than 3V, the wire has likely short
// circuited to the work piece. A short would appear the same as an
// arc start when looking at the current measurements.
if(welder.get_voltage() < 3)
{
    count = 100; // set count to 100, which is a no-start
}
//welder.set_current(75);
if(count < 100) // Algorithm has predicted an arc start
{
    usleep((unsigned long)(35*1e3)); // pause for 35ms before wire feed

    mo.wire_start(true); // start wire feed routine

    usleep((unsigned long)(35*1e3)); // after 35ms, reduce current to 50A
    welder.set_current(50); // set current to 50A
    usleep((unsigned long)(100*1e3)); // wait 100ms for drop to grow
    welder.set_current(350); // detach drop with 350A pulse
    usleep((unsigned long)(4.5*1e3)); // pulse time is 4.5ms
    welder.set_current(40); // set current low during drop transfer
}

```

```

        usleep((unsigned long)(15*1e3)); // keep low current for 15ms
    }

    welder.arc(false); // disable welding power source
    mo.wire_start(false); // reset wire feed trigger

    usleep((unsigned long)(50*1e3)); // take data for an additional 50ms
    DAQ_FLAG = 0; // turn of DAQ thread

    ////////////////////////////////////// Position Wire //////////////////////////////////////
    if(count < 100)// only if algorithm has predicted arc start
    {
        mo.connect(); // establish connection with Galil controller
        mo.move(y,10,-0.068); // move work piece for new drop

        welder.set_current(1.0); // set current to 1A to allow full OC voltage
        welder.arc(true); // enable welding power source
        usleep((unsigned long)(0.1*1e3)); // allow time for OC voltage to build

        mo.wirefwd(5.0); // jog wire forward
        // if voltage is more than 20V, wire and wore piece are not in contact
        while(welder.get_voltage(>20.0){} // do nothing while wire is feeding
        // when the voltage drops below 20V, wire has made contact
        welder.arc(false); // disable welding power source
        mo.wirestop(); // stop wire feed

        mo.wirefeed(5.0,-0.05); // retract wire 0.05in for optimal arc start
        sleep(1); // allow time to retract wire
    }

    //////////////////////////////////////

    // if count is 100 or more, the algorithm predicted a no-start.
    // End program by setting the drop number high
    if(count >= 100)
    {
        drop_num = 100;
    }
}

usleep((unsigned long)(2*1e6)); // 2 second gas post-flow time
dacq.dout(5, 0); // Turn off camera trigger
welder.arc_shielding(false); // turn on shielding gas

}
// leave
return 0;

```

SIGNATURE PAGE

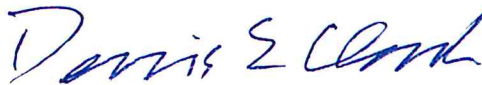
This is to certify that the thesis prepared by Dale Brush entitled "Control of Gas Metal Arc Welding Using Process Sensing and Laser Arc Stabilization for Additive Manufacturing" has been examined and approved for acceptance by the Department of Electrical Engineering, Montana Tech of the University of Montana, on this 29th day of November, 2018.



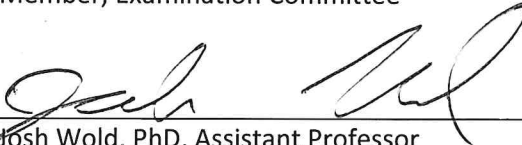
Bruce Madigan, PhD, Professor
Department of General Engineering
Chair, Examination Committee



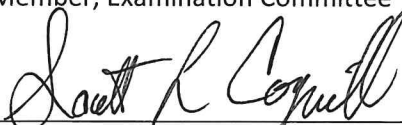
Dan Trudnowski, PhD, Professor and Dean
Department of the School of Mines & Engineering
Member, Examination Committee



Denis Clark, MS, Welding Engineer
Member, Examination Committee



Josh Wold, PhD, Assistant Professor
Department of Electrical Engineering
Member, Examination Committee



Scott Coguill, MS, Laboratory Director
Department of Mechanical and Civil Engineering
Member, Examination Committee